



THE UNIVERSITY OF
WAIKATO
Te Whare Wānanga o Waikato

Research Commons

<http://researchcommons.waikato.ac.nz/>

Research Commons at the University of Waikato

Copyright Statement:

The digital copy of this thesis is protected by the Copyright Act 1994 (New Zealand).

The thesis may be consulted by you, provided you comply with the provisions of the Act and the following conditions of use:

- Any use you make of these documents or images must be for research or private study purposes only, and you may not make them available to any other person.
- Authors control the copyright of their thesis. You will recognise the author's right to be identified as the author of the thesis, and due acknowledgement will be made to the author where appropriate.
- You will obtain the author's permission before publishing any material from the thesis.

Small-scale Turbulence and its Influence on Forest-scale Morphodynamics within a Coastal Mangrove Forest

A thesis

submitted in fulfilment

of the requirements for the degree

of

Doctor of Philosophy

In

Earth Sciences

at

The University of Waikato

by

Benjamin Kenneth Norris



THE UNIVERSITY OF
WAIKATO
Te Whare Wānanga o Waikato

2019

Abstract

Mangroves are coastal wetland ecosystems consisting of salt-tolerant trees and shrubs that inhabit the upper intertidal zone of estuaries, river banks and barrier islands. These trees grow in the intersection between the coastal ocean and land, and form a barrier against hazards such as waves, coastal flooding and erosion for many densely populated areas that often lack hard coastal defense structures. By damping tidal currents and waves, mangroves also facilitate sedimentation, and may contribute to coastal stability in the face of rising sea levels. The valuable ecosystem services provided by mangroves are the result of characteristic bio-physical feedbacks between the mangrove vegetation, hydrodynamics and sediment dynamics within intertidal zones (Chapter 1). This thesis focuses on understanding these bio-physical feedbacks, specifically: (i) how mangrove root density affects tidal current and wave dissipation, (ii) how mangrove root structures modify the flow field, and (iii) how mangrove roots facilitate sediment transport within forested areas.

Linking Mangrove Root Density and Turbulent Dissipation

The link between mangrove root density and turbulent dissipation was explored in a coastal mangrove forest that is exposed to an energetic wave environment. Measurements of turbulent kinetic energy (TKE) dissipation were collected over millimeter to centimeter scales within clusters of mangrove pneumatophore roots ('canopies') spanning regions from the unvegetated mudflat to the densely vegetated forest. High-resolution root geometries were reconstructed using a newly developed photogrammetric method. The frontal area density of the vegetation (a) was compared to the TKE dissipation rate estimates at the same height above bed. Mangrove tree (and hence, root) density was greatest along a narrow band between the mudflat and forest: the forest 'fringe'. Temporally variable turbulence was maximum in the fringe and was often elevated in the forest relative to the unvegetated mudflat. The largest dissipation rates ($4.5 \times 10^{-3} \text{ W kg}^{-1}$) were measured as breaking waves propagated over root canopies in very shallow water. Dissipation rates were reduced, but often remained intense (e.g., between $10^{-5} - 10^{-4} \text{ W kg}^{-1}$) under non-breaking waves at the fringe, likely indicating turbulent generation in pneumatophore wakes. Turbulence was positively correlated with

root density and wave height and was negatively correlated with water depth. Substrate grain size distributions in the fringe were larger (sandier) than those offshore and onshore, suggesting intense turbulence may winnow fine-grained sediments from the fringe.

Observations of Turbulence in Mangrove Root Canopies

High-resolution velocity measurements were collected within and above two dense canopies of mangrove pneumatophore roots in a wave-exposed mangrove forest. In both canopies, root density decreased steadily with height above bed owing to the variability in root heights and the tapered shape of the roots. Within the canopies, we consider turbulence within three zones: near the bed above the wave boundary layer, around the mean canopy height, and above the canopy. The near-bed turbulence was particularly intense (up to $6.5 \times 10^{-4} \text{ W kg}^{-1}$), likely owing to oscillatory wave-driven currents flowing past dense vegetation. Near the bed and around the mean canopy height, peaks in horizontal velocity power spectra at frequencies corresponding to Strouhal numbers of ~ 0.2 may indicate Von Kármán wake shedding in the lee of the pneumatophores. Furthermore, a recirculation zone was observed immediately behind a cluster of pneumatophores at intermediate heights. These coherent flow structures were associated with zones of enhanced Reynolds stresses (up to $5.3 \times 10^{-3} \text{ m}^2 \text{ s}^{-2}$), and eddy viscosities (up to $1.9 \times 10^{-3} \text{ m}^2 \text{ s}^{-1}$). Large near-bed stresses were associated with near-bed drag coefficients that are up to an order of magnitude larger than those expected in the absence of vegetation. Observed eddy viscosities are consistent with theoretical expectations, derived from scaling arguments using a standard mixing-length model. These results suggest that pneumatophore roots can contribute greatly to turbulent mixing (e.g., eddy viscosities were on average $O(10^{-4} - 10^{-3} \text{ m}^2 \text{ s}^{-1})$), and therefore may enhance the sediment entrainment occurring in mangrove forest fringes.

Understanding the Hydrodynamic and Morphodynamic Feedbacks in Mangroves

Field experiments were carried out within a wave-exposed coastal mangrove forest to quantify the change in bed level throughout a tidal cycle using high-resolution velocity and bed level measurements collected in situ. Experiments spanned the unvegetated mudflat, mangrove forest fringe and forest, where data were collected during single tidal cycles (flood-ebb) during a two-week period. Cross-wavelet

transforms of the velocity and bed level measurements were often highly correlated ($\geq 90\%$ squared coherence) over a range of frequencies, spanning those corresponding to short-period wind and swell waves to long-period infragravity waves. Bed level change events associated with short-period waves were more frequent in the mudflat and fringe, while those associated with long-period waves were much more frequent in the forest. Net bed level changes over single events were nearly normally distributed, indicating similar numbers of events resulting in accretion and erosion, regardless of the across-shore position. Still, bed level change events exceeding the observed net tidal elevation change occurred infrequently. This pattern suggests that the net tidal elevation change within the mangrove forest must be related to the frequency of these infrequent events. Large bed level changes were often associated with high bed shear stresses ($0.3 - 1.5 \text{ N m}^{-2}$) and turbulence of $O(10^{-3} \text{ W kg}^{-1})$, particularly on the mudflat and in the forest fringe. Across all experiments, the mudflat and forest site experienced net accretion (4.5 and 6.8 mm, respectively) while the fringe experienced net erosion (-9.5 mm). This work suggests a dynamic role for waves in mangroves: short-period waves stir sediment on the mudflat and forest fringe, while infragravity waves help advect entrained sediment inside the forest.

The concepts developed over this thesis are summarized briefly in Figure A.1, which presents a geomorphological feedback between the environment, mangrove roots, and sediment transport. Sediment is carried landward by the rising tide. Energetic turbulence that forms around mangrove roots may preferentially remove fines from the forest fringe. Suspended sediment may then be advected further into the forest to be deposited as current velocities weaken closer to slack tide.

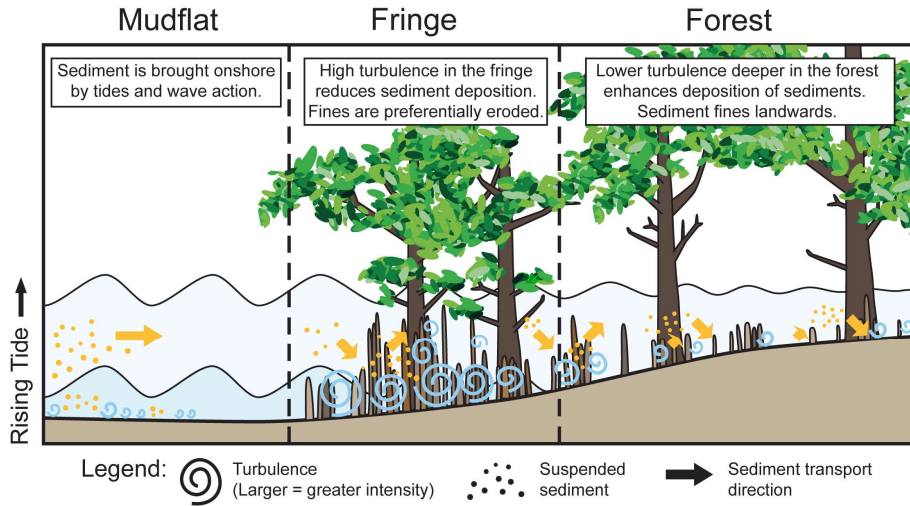


Figure A.1: A conceptual diagram of the bio-geomorphic feedback between mangrove root density, turbulence and sediment transport presented within this thesis. Larger symbols (spirals, arrows) denote greater effects of (turbulence, sediment transport). Note: the two illustrated water levels show the tide rising.

In every walk with nature one receives far more than he seeks.

-John Muir (1838 – 1914)

Acknowledgements

First and foremost, an enormous thank you to my supervisors, Dr. Julia Mullarney, Dr. Karin Bryan from the University of Waikato, and Dr. Stephen Henderson from the Washington State University, for your advice, guidance, technical assistance, and your support along this incredible journey. I truly believe that my success is due in large part to your persistence and patience with me. Thank you for encouraging me to push myself harder than I thought was possible. I consider myself very fortunate that you took me on as your graduate student, and I am grateful for all of the opportunities you have given me to grow personally and professionally.

Secondly, a big thank you to Dean Sandwell from the University of Waikato for his invaluable technical knowledge and creativity in deploying instruments in the field. I'll never forget the day we had to extract one of the Aquadopps from the mudflat at high tide. Dean and I both took several attempts to unscrew the instrument from its frame before Julia provided Dean a little extra 'ballast' so he could stay underwater long enough to pull the whole arrangement up off the bed. Suffice to say, we had quite the adventure together.

Moreover, Dean and Julia's insatiable up-beat attitude helped to carry our team through some difficult moments in the early days of my PhD career. The fieldwork was incredibly tough, but the struggle was definitely worth it: we collected an excellent dataset. A big thank you to Julia, Dean and Steve for battling the mud, mosquitos, wasps, hot sun, torrential rain, lightning, and sleep deprivation to make this thesis possible.

Of course, this project (as part of the larger Mekong Tropical Delta Study) would not have been possible if it weren't for the hard work of Chuck Nittrouer and Andrea Ogston from the University of Washington, Rich Nguyen from the Office of Naval Research (ONR), H.P. Võ Lương, Xuan Tien Nguyen Vinh, and Hoang Phong Nguyen from VNU University of Science (Ho Chi Minh City), who were instrumental in planning, organizing, and coordinating the challenging logistics of the experiments and for assistance in the field. To Daniel Culling, Aaron Fricke, Sergio Fagherazzi and William Nardin, thank you for your company in the field and also for keeping our spirits high. Special thanks must also go to the Mekong

Taxi Service (Dan and Aaron), who prevented the kiwi team from enduring many a stormy high tide in the mangrove forest.

Funding for this PhD research was provided by ONR (grant numbers N62909-14-1-N028 to JM and KB, N00014-14-10112 to SH, and N00014-12-1-0181, N00014-13-1-0075, N00014-13-1-0781, N00014-15-1- 2014, N0014-15-1-2011, N0014-13-1-0127, which supported AF and DC). This funding enabled the field research, trips to Vietnam to discuss logistics and findings with project collaborators, a trip to the United States to attend the American Geophysical Union (AGU) Ocean Sciences conference in 2016, and money to publish manuscripts and our articles in *Oceanography*.

Although a PhD is often a solitary experience, helpful advice and emotional support was readily available from my fellow students at the University of Waikato, especially my friends Dr. Shawn Harrison, Dr. Alex Port, Dr. Steve Hunt, Dr. Victor Godoi, Peter De Ruiter, Ben Stewart, Dr. Mariana Cussioli, Jonno Rau, John Mering, Joss Ratcliffe, John Montgomery, Dr. Paola Rodriguez, and everyone else in the Coastal Marine Group. It was a pleasure to work alongside you all, day by day in the office. I consider myself very lucky to have had the opportunity to get to know you; your company and companionship kept me going throughout my PhD. Also, a big thank you to my valued friend Dr. Erik Horstman, who helped me work through many complex concepts and eccentricities with my data, and who also frequently provided world-class baking.

Thank you as well to friends and family in New Zealand and the United States for all your support, especially Mom, Dad, Jon, Paul, Nick, Ryan, and the other wonderful people who have become my whānau in Hamilton.

Most importantly, thank you to my incredible wife Francesca, who did not even hesitate when I suggested that we uproot ourselves from California and move to New Zealand so I could work towards my PhD. Your emotional (and sometimes financial) support has been invaluable to me throughout this whole process. Thank you for your unrelenting support and encouragement through the difficult times; I'm not sure I could have done this without you by my side. I look forward to returning the favor, now that you're starting on your own PhD journey.

Table of Contents

Abstract	iii
Acknowledgements	ix
Table of Contents	xi
List of Figures	xv
List of Tables	xxiii
List of Symbols	xxv
Chapter 1: Background and Introduction.....	1
1.1 The Value of Mangroves	1
1.2 An Overview of Mangrove Characteristics	2
1.2.1 Global Distribution	4
1.2.2 Mangrove Environments.....	5
1.2.3 Physical Processes in Mangroves	6
1.3 Mangrove Hydrodynamics and Morphodynamics	8
1.3.1 Tidal-scale Flow.....	9
1.3.2 Wave Dissipation.....	11
1.3.3 Sedimentation.....	12
1.3.4 Turbulence	14
1.4 Research Objectives	15
1.5 Research Questions	15
1.6 Regional Setting: Field Site and Data Collection.....	16
1.7 Thesis Outline.....	22
Chapter 2: The Effect of Pneumatophore Density on Turbulence: A Field Study in a <i>Sonneratia</i> -dominated Mangrove Forest, Vietnam.....	25
Contribution of Authors	26
Abstract	27
2.1 Introduction	27
2.2 Background.....	30
2.3 Field Measurements.....	33
2.3.1 Field Site	33
2.3.2 Vegetation Sampling.....	34
2.3.3 Hydrodynamic Observations.....	35
2.4 Data Analysis.....	39
2.4.1 Dissipation rate of turbulent kinetic energy	39

2.4.2	Tide Intervals and Quadrat Subsampling	41
2.5	Results.....	44
2.5.1	Hydrodynamic and vegetation observations.....	44
2.5.2	Spatial Trends	50
2.6	Discussion	54
2.6.1	Dissipation rate magnitude	54
2.6.2	Canopy density effects on turbulence.....	56
2.6.3	Geomorphological implications	57
2.7	Conclusions.....	59
Chapter 3: Turbulence within Natural Mangrove Pneumatophore Canopies.....		61
Contribution of Authors.....		62
Abstract.....		63
3.1	Introduction.....	64
3.2	Field Experiments and Methods	68
3.2.1	Experimental Setup	68
3.2.2	Data Processing	72
3.2.3	Turbulent Dissipation Rate.....	74
3.2.4	Spectral Calculations	75
3.2.5	Reynolds Stress Calculation.....	77
3.3	Results.....	80
3.3.1	Vegetation Geometry.....	80
3.3.2	Offshore Conditions	81
3.3.3	Canopy Turbulence.....	82
3.3.4	Turbulence Characteristics	84
3.3.5	Canopy-Scale Currents.....	93
3.4	Discussion	95
3.5	Summary and Conclusions	98
Chapter 4: Hydrodynamically Driven Changes in the Bed Elevation within a Coastal Mangrove Forest.....		101
Contribution of Authors.....		102
Abstract:.....		103
4.1	Introduction.....	104
4.2	Methods.....	107
4.2.1	Field Site.....	107
4.2.2	Measurements.....	108
4.2.3	Sample Analysis and Data Quality Control.....	113

4.2.4	Data Analysis	113
4.3	Results	120
4.3.1	General Conditions during the Experiments.....	120
4.3.2	Bed Level Variability.....	124
4.4	Discussion.....	134
4.5	Conclusions	137
Chapter 5:	General Conclusions	139
5.1	Review of Major Concepts.....	139
5.2	Recommendations for Future Work	143
5.2.1	Species-dependent energy dissipation	143
5.2.2	Wake length scales.....	144
5.2.3	The establishment of young mangroves.....	145
5.3	Summary.....	146
Appendix A:	Calculation of wave and current velocities	148
Appendix B:	Spectral and structure function estimates of the TKE dissipation rate.....	149
Appendix C:	Estimation of ripple geometry	151
References	153

List of Figures

- Figure 1.1:** Mangrove roots, (a) prop roots of *Rhizophora* spp., (b) knee roots of *Bruguiera* spp., (c) buttress roots of *Xylocarpus* spp., and (d) pneumatophores of *Sonneratia* spp. Photo source for panels (a – c): http://www.mangrove.at/mangrove_roots.html 3
- Figure 1.2:** Global distribution of mangroves (Giri et al. 2011), with the Indo-West Pacific region highlighted as a red circle..... 4
- Figure 1.3:** Three main types of mangrove landforms: a) riverine, b) basin, and c) fringe. After Mazda & Wolanski, (2007)..... 5
- Figure 1.4:** Regional context of experiments: a) Mekong River Delta with the Sông Tiền and Sông Hậu distributaries identified. The white square shows approximately the extent of Cù Lao Dung in the Sông Hậu distributary channel (panel b). Photo sources are: Envistat (panel a) and Rapideye (panel b). 16
- Figure 1.5:** (a) to (c): example ‘flats to forest’ instrument configurations. (d): a ‘fine scale’ configuration. Three Vectrinos were deployed in a horizontal row amongst a cluster of pneumatophore roots. (e): Vectrino data logging station with the communications and power boxes, and a field laptop in a special water-resistant housing. (f): a HOBO U30 weather station deployed offshore on the mudflat in front of the mangrove forest in the SW. Scientists for scale (approximately 1.6 m with 0.2 m in the mud). 19
- Figure 1.6:** Illustration of the photogrammetric reconstruction method used to obtain high-resolution estimates of pneumatophore geometries. (a): a sample photo from one of the photo sets used to reconstruct vegetation geometry. In this image a 1 m² quadrat delineates features of interest. (b): The point cloud created from inputting the photo set into VisualSFM. Note that the quadrat has been removed from this reconstruction. (c): Pneumatophores represented as three-dimensional shapes from near the bed level (dark colors) to the top of the canopy (light colors). Each height ‘slice’ is represented here as a cylinder, where the cylinder diameter is the twice the mean of the radius of each slice as generated by the sector-slice algorithm (Liénard et al. 2016)..... 21
- Figure 2.1:** Overview map of Cù Lao Dung, located in the Sông Hậu distributary channel of the Lower Mekong Delta. Two main field sites are highlighted, the southwest and northeast (SW and NE), with insets depicting the locations of individual measurement and vegetation survey sites within the mudflat, mangrove fringe and forest. In SW inset, ‘Md’ stands for ‘mudflat’, ‘Fr’ for ‘fringe’ and ‘Fo’ for ‘forest’. Dotted lines in both insets denote the fringe zone of the forest. Vegetation type was digitized to differentiate between *Sonneratia* and other mangroves by comparing maps provided by Bullock et al., (2017), and Google Earth images. 32

- Figure 2.2:** (Panel a) a typical instrument deployment around one of the vegetation survey sites on the SW transect within the mangrove fringe. (Panel b) 3D point cloud generated by the structure-from-motion software created from approximately 200 photographs of the quadrat scene. (Panel c) Pneumatophores represented as 3D shapes with circular horizontal cross-section, and with elevation-dependent diameter and location, fitted to the 3D point cloud. 38
- Figure 2.3:** Example tidal divisions for low (LL), medium-low (ML), medium high (MH) and high (HH). Tidal sections are of equal length, beginning after the instruments are submerged then finishing at slack tide. Colors correspond to the same tidal stages in the subsequent figures. 42
- Figure 2.4:** (Panel a) Current vector map showing both the location of the collocated instrument and the quadrat deployment (circle and triangle). (Panel b) Quadrat reconstruction of pneumatophore diameters at the height slice of the velocity measurements. The triangle represents the location of the Vectrino Profiler. Squares denote the subsampling process according to the arrows in panel a. (Panel c) a single 20 cm² subsample of the vegetation proximal to the Vectrino Profiler. This particular example is the dark blue box (HH) in panel b. 43
- Figure 2.5:** Vertical profiles of currents and turbulent dissipation during 30 minutes on March 6th (HAB = ‘Height Above Bed’). Panels (a–c): Onshore current velocities measured at mudflat (a), fringe (b) and forest (c) locations. Raw velocities were averaged using a 30 second window and a 30% overlap, removing wave-frequency flows. Below-bed values and values corresponding to the wave boundary layer, have been removed (in black). (Panels d–f) TKE dissipation rates for the mudflat (d), fringe (e) and forest (f). Dissipation rates were calculated using a 30 second window of vertical velocities, per depth bin. Similarly to (a–c) below-bed and wave boundary layer values have been excluded (in black). Panels (g–i) show detailed view of times and elevations bounded by dashed boxes in (d–f). 46
- Figure 2.6:** Profiles of the frontal area density as a function of height above the bed, $a(z)$. Symbols on the un-vegetated mudflat represent surveys without pneumatophores ($a = 0 \text{ m}^{-1}$). The black bar shows a unit of 1 m^{-1} for reference. Quadrat locations (Tables 2.1 and 2.2) are denoted by symbols: open circle, square and diamond: mudflat deployments; open five-pointed star: Q1; cross: Q2; triangle: Q3a; asterisk: Q3b; closed circle: Q3c; closed square: Q4; downward-facing triangle: Q5; six-pointed star: Q6; closed diamond: Q7; left-pointing triangle: Q8; right-pointing triangle: Q9; closed five-pointed star: Q10; closed triangle: Q11; closed left-pointing triangle: Q12; closed right-pointing triangle: Q13. 48
- Figure 2.7:** (Panel a) Fringe location showing pronounced erosion near pneumatophores (e.g. scour pits around small clusters of stems in the

middle of the photo). (Panel b) Forest location, 94 m landward of the fringe, with no clear scour around pneumatophores. 49

Figure 2.8: Turbulent dissipation rates (Panel a), vegetation frontal area density (Panel b) and significant wave height (Panel c), with observations from all deployments binned at 10 m cross-shore intervals to emphasize spatial variability. Symbols and error bars respectively represent the mean and standard deviation of all observations within a 10-m bin. Panel (a): TKE dissipation, shown separately for each tidal stage. Panel (b): vegetation frontal area profiles surveyed at low tide, with values corresponding to current meter elevations presented. Panel (c): Significant wave heights, with all tidal stages combined. Error bars depict the range of H_s over the four tidal stages. 50

Figure 2.9: Dissipation rate (ε) versus wave breaking parameter ($\gamma = \text{wave height/water depth}$) for all four tidal stages. Each point represents ε and γ for a single measurement location, averaged from the start to the end of a single tidal stage. Most points fall below $\gamma < 0.3$ indicating minimal breaking, so that wake-induced turbulence provides the most likely source for high turbulent dissipation rates. For $\gamma > 0.3$, wave breaking likely contributes turbulence. 52

Figure 2.10: TKE dissipation rate (ε) versus vegetation frontal area (a) (Panel a) or solid volume fraction ϕ (Panel b) for 20 cm² quadrat subsamples. Open symbols correspond to values of $\gamma > 0.3$, closed symbols correspond to cases with $\gamma < 0.3$ (i.e. cases with minimal breaking)... 53

Figure 2.11: All measured TKE dissipation rates corresponding to the breaking condition, $\gamma > 0.3$ by across-shore position. Points are binned with horizontal distance at intervals of 10 m. 55

Figure 2.12: A conceptual diagram of the mangrove bio-geomorphic feedback mechanism presented in this chapter. Larger spirals mean higher intensity turbulence. Note: the two illustrated water levels show the tide rising..... 59

Figure 2.13: A conceptual diagram of the mangrove bio-geomorphic feedback mechanism presented in this paper. Larger spirals mean higher intensity turbulence. 59

Figure 3.1: Overview map of Cù Lao Dung, located in the Sông Hậu distributary channel in the lower Mekong Delta. (Panel a) Regional context of deployment region (red square). (Panel b) Deployment locations on the seaward edge of Cù Lao Dung; the horizontal turbulence array (HTA) experiment was deployed in the southwest, and the vertical turbulence array (VTA) in the northeast within 10 m of the mudflat/mangrove forest fringe boundary. The symbol ‘W’ denotes the location of the weather station in the southwest. Data sources are, Envistat (panel a) and Rapideye (panel b). 67

Figure 3.2: Experimental setup for the HTA experiment (panels a – b) and the VTA (panels c – d). Canopies in panel (a) and panel (c) were created

by tracing the 3D SFM reconstructions of the canopies in profile-view, and depict the height of canopy elements relative to the measurement positions. Thick dashed and solid lines respectively show the mean canopy height $\langle h_c \rangle$ and max canopy height h_{max} . Colored dotted lines are the normalized measurement height of the three Vectrinos. Canopy elements in blue boxes in panels (a) and (c) correspond to the subsampled elements depicted in the blue boxes in panels (b) and (d). Eye symbols show the viewing angle of the plan-view panels (a, c) relative to the profile view panels (b, d). In panels (b) and (d), triangles show the Vectrino positions. Light blue arrows show the mean current flow direction through the canopies. Pneumatophore basal diameters are represented by black circles. The x-axis scales of panels (a) and (c) are shown for reference in panels (b) and (d). 69

Figure 3.3: Photographs of the experimental set-up showing the locations of collocated sensors to the HTA (panel a) and VTA (panel b). The downward-looking ADV in panel a (unlabeled) was not used here, and the quadrat was removed prior to the experiment..... 71

Figure 3.4: Example wave-turbulence decomposition for a 10-minute data time series from the ADV deployed above the HTA on March 7th, 2015. Coherence squared between the vertical velocity component and the pressure signal (black line), and the 95% confidence level at 30 D.O.F., 0.19 (dashed red line). Grey circles show the wave band, or frequency components that are significantly coherent. (b) Power spectral density (PSD) of the vertical velocity component (S_{ww} , solid black line). Grey circles denote frequencies in the wave band. The solid red line represents the linear fit between f_{wc} and f_{hc} used for extracting the slope of the turbulent band (Section 3.3.4.2). The dotted line is $f^{-5/3}$, as indicated. 77

Figure 3.5: Grey curves are the variance-preserving cospectra (panel a) and integrated cospectra (ogive curves; panel b) of turbulent velocity components u' and w' from the HTA1 experiment at $x = 20$ cm, 0.018 m above the bed at 13:41 local time. The grey regions in (a) show the measurements with 95% confidence intervals for the cospectral estimates. Black curves in (a) and (b) show the model cospectra, the Kaimal curve, and thin vertical black lines show the cutoff wavenumber, k_c and the roll-off wavenumber, k_θ . The high-frequency end of the cospectra are blown up in the inset of panel (a) to aid comparison of the model and observations. Although raw cospectra were used in the model fit, spectra shown in the inset of panel (a) have been smoothed with a 10-point running mean to reduce noise for display. To compute the ogive curves, the cospectra were integrated from the Nyquist wavenumber nk to 0 to exclude wave frequencies... 78

Figure 3.6: Vertical profiles of vegetation statistics. (a) Number of stems per square meter, n ; (b), the mean stem diameter, d ; (c) the frontal area of the canopy, a ; and (d), the volume fraction occupied by the vegetation, ϕ . The red line is the total canopy (1 m²) measured at the HTA site; blue line, the total canopy (1 m²) measured at the VTA site.

The yellow and purple lines are the subsampled regions of the two canopies (Figure 3.2). Horizontal lines denote the maximum (solid line) and mean canopy heights for the HTA and VTA, dashed and dotted lines, respectively..... 81

Figure 3.7: Environmental conditions measured during the experiments. (a) Two-hour averaged wind speeds (dashed grey line) and directions (solid black line) during the two experiments. Grey bars designate the length of each of the horizontal turbulence array (HTA) experiments and the vertical turbulence array (VTA) experiment. Panels (b – g), hydrodynamic forcing conditions: water depth (panels b, c), peak period (panels d, e) and significant wave height (panels f, g) recorded by the ADV and pressure sensor collocated with the turbulence arrays. 82

Figure 3.8: 10-minute averages of wave (a, b) and current (c, d) magnitude and directions measured above the canopies at each experimental site. The magnitudes depicted for U_w are mean orbital velocities. Color corresponds to the tidal stage, with lighter blues the flood tide and darker blues the ebb tide. The compass in the lower right-hand corner of panels (a, b) shows the orientation of the across-shore (X) and along-shore (A) directions relative to north (N). 83

Figure 3.9: Time series of the TKE dissipation rate normalized by $|U^3|$, ($\hat{\epsilon}$), for the three positions of the HTA (panels a – c) and VTA (panels d – f). VTA dissipation rates were computed and averaged over 10-minute segments for each instrument. For the HTA, each segment is plotted against the across-shore position of the array. For the VTA, every third point in the profile is plotted as a marker w.r.t the normalized height above bed, z/h_{max} . Colors correspond to time elapsed after low tide and are consistent between subplots. 84

Figure 3.10: Power spectral densities of along-current velocity (S_{uu} , black line) averaged over a 1.5-hour period during the experiments. 95% confidence intervals shown at 10x actual size. The solid black line indicates a -5/3 slope. Panels (a – c) show velocity spectra from the array positions where high turbulence was observed in Figure 3.9: HTA1, $x = 20$ cm, HTA2 $x = 10$ cm, and the VTA, $z/h_{max} = 0.04$. Arrows highlight shedding frequency peaks of interest. Panels (d – f) show velocity spectra from the other array positions in these experiments; note the absence of peaks in frequency bands between 1 – 4 Hz. 86

Figure 3.11: Time series of slopes of fits to auto-spectra of along-current (S_{uu} , solid lines), across-current (S_{vv} , dashed lines) and vertical (S_{ww} , dotted lines) from the array positions where high turbulence was observed in Figure 3.9. Slopes were calculated by a linear fit over the frequency range $f_{wc} < f < f_{hc}$ Hz over 10-minute windows with >30 degrees of freedom. The thin horizontal black line indicates a -5/3 slope. 87

Figure 3.12: Time series of velocity ratios, u_{rms}/v_{rms} (light grey) and w_{rms}/u_{rms} (dark grey) for the array positions where high turbulence was observed

in Figure 3.9. Dotted and solid black lines are 10-point moving averages of the two ratios, respectively. The solid horizontal line corresponds to ratios of one..... 89

Figure 3.13: Time-averaged profiles of along-current and vertical velocities for the HTA experiments (a – c) and the VTA experiment (d – f). Note that the HTA experiments were not synoptic, and therefore panels a – c show mean velocities under different environmental conditions. 90

Figure 3.14: Time-averaged profiles of turbulence statistics for the HTA experiments: the vertical Reynolds stress $-\overline{u'w'}$, (panels a – c), and the eddy viscosity $\overline{\nu}_t$, (panels d – f). In panels (b, e), the dashed horizontal line denotes the mean canopy height $\langle h_c \rangle$. Note that the HTA experiments were not synoptic, and therefore panels a – c show turbulence statistics under different environmental conditions. 91

Figure 3.15: Time-averaged profiles of turbulence statistics for the VTA experiment: the vertical Reynolds stress $-\overline{u'w'}$, (panels a – c) and the time-averaged eddy viscosity $\overline{\nu}_t$, (panels d – f). 92

Figure 3.16: The depth and time-averaged squared friction velocity (u_*^2) scaled by the squared mean drift velocity $\langle U_d^2 \rangle$ for all experiments. Points shown are the mean value, with error bars of one standard deviation. Horizontal solid, dotted and dashed lines are the maximum and mean canopy heights of the HTA and VTA canopies, respectively. 96

Figure 4.1: Deployment location. Panel (a) Regional context of deployment region (red square) situated within the lower Mekong Delta. (b) Deployment locations (SW) on the seaward edge of Cù Lao Dung, shown in detail in panel (c), where white lines denote the relative position of the boundaries between the mudflat, fringe and forest. Fixed instruments are denoted with blue circles, and moveable array sites 1 – 3 with orange squares. Panels (d, e, f) photos of deployment configurations in each of the three environments, 1 m² quadrats for scale. Note, the mudflat ADCP is not shown in panel (d). Data sources are respectively, Envisat (a), Rapideye (b), Google Earth (c)..... 107

Figure 4.2: Method for estimating patches of pneumatophore roots from two of the flood tide experiments, March 11th, 2015 (panels a and b), and March 9th, 2015 (panels c and d). Panels (a, c) show the 10-minute averaged current direction measured by the ADCPs collocated with the Vectrinos as a grey sector. Current velocity magnitudes averaged 0.1 m/s during the March 11th, 2015 experiment, and 0.08 m/s during the March 9th, 2015 experiment. Panels (a, c) also show the dominant wave direction (to) colored by the wave orbital velocity. Panels (b, d) show a 20 cm² subsampled region of each quadrat survey around the Vectrino (yellow triangle). Pneumatophore basal diameters are depicted as black circles. The patch width D or individual root diameter d is shown in red for roots upstream of the Vectrinos..... 112

- Figure 4.3:** An example logarithmic fit (red line) to 10 min time-averaged velocity profiles (Equation 4.1). Data are from the mudflat site. The velocity measurements are normalized by the measurement closest to the bed. The r^2 of this example is 0.94 with p-val < 0.05. 116
- Figure 4.4:** Example raw data from the experiment conducted on March 6th, 2015 at Site 3 used to identify the bed level. Panel (a) Vectrino acoustic amplitude returns, where the maximum value of the amplitude (white) is compared to the reported averaged bed level (black) from panel (b). Panel (b) Reported instantaneous (black) and running median (red; 512-point window) of the bottom track of the Vectrino..... 118
- Figure 4.5:** Example cross wavelet transform of the across-shore velocity (u) and the bed level for three across-shore positions: the mudflat (a), fringe (b) and forest (c) during the experiment on 6th of March, 2015. The thick black contours designate the 5% significance level against red noise, and the shaded area denote the cone of influence, where edge effects become important. 119
- Figure 4.6:** Time series of water depth, the across-shore, depth-averaged velocity (\bar{u}), significant wave height (H_s), and suspended-sediment concentration (SSC). Note some instruments were part of the moveable arrays and so records from a single location do not cover the full two-week period. The length of each experiment (Table 4.1) is represented by the shaded areas in each panel. 121
- Figure 4.7:** Boxplots depicting trends in the mean near-bed across-shore velocity (\bar{u}), bed shear stress (τ_b) and turbulent kinetic energy dissipation rate (ϵ) for the mudflat, fringe and forest sites. Panels (a, c, e) are of the flood tide experiments, while panels (b, d, f) are of the ebb tide experiments. In panels (c, d), the asterisk ‘*’ denotes the average critical shear stress (τ_{cr}) for needed to entrain the characteristic sediment type for each area. 122
- Figure 4.8:** Example spectral density of the water depth from the 6th of March, 2015, computed for the mudflat, fringe and forest (light grey to dark grey lines)..... 124
- Figure 4.9:** Bed level time series for each experiment. Note, only the March 9th, 2015 experiment was contiguous across high tide (Table 4.1). For the March 9th experiment, only the bed level trace from the ‘middle’ Vectrino profiler is shown (see Figure 4.10 for details). 125
- Figure 4.10:** Bed level during the experiment on March 9th, 2015. Panel (a) time series of the bed level across a single flood-ebb tide transition, with high tide indicated as the vertical black line. The initial bed level, surveyed prior to the experiment, is shown by the horizontal black line. Breaks in each curve are gaps in the data record. The bed level traces have been smoothed using a 50-point running mean for display purposes. Panel (b) a map of the bed elevation change computed by differencing the bed elevation areas of two photogrammetric surveys

of the field site before and after the experiment on March 9th, 2015. The instrument positions described in panel (a) are shown in panels (b) and (c) as: seaward, grey circle; middle, dark grey diamond; landward, black star. The elevation change depicted is representative of the change in bed level across a single tidal cycle. In this figure, the average error in bed level is approximately 8 mm (see text for details). Areas with no data are colored in white. Panel (c) bed level after the experiment on March 9th, 2015. 127

Figure 4.11: Keulegan-Carpenter (KC) number versus the normalized scour depth (S/D). The black curve is Eq. 9 from Sumer et al. (1992). The experiments with the largest and smallest S/D are labeled (Table 4.1). 128

Figure 4.12: The distribution of the net elevation change over a single event for all flood (panel a) and ebb (panel b) tides. See text for definition of event. 129

Figure 4.13: Boxplots depicting the net elevation change for individual events during flood and ebb tides. The top row depicts events that resulted in bed accretion and the bottom row depicts events that resulted in bed erosion. 130

Figure 5.1: A comparison of mangrove environments. (a) From left to right: Daniel Culling, Aaron Fricke, and Ben Norris taking vibracore samples of the substrate under the cover of *Sonneratia caseolaris* mangroves on Cù Lao Dung. For reference, Ben is ~1.6 m tall above ground. (b) Erik Horstman (~1.85 m above ground) setting up instruments in the Firth of Thames, New Zealand. Photos provided by Julia Mullarney. 144

Figure 5.2: A solitary Vectrino Profiler deployed offshore of the mangrove fringe on the mudflat. Many juvenile *Sonneratia caseolaris* mangroves are visible in the distance. 146

Figure 5.3: Waves breaking within the trees of the mangrove fringe 147

List of Tables

Table 1.1: The mechanisms, temporal and spatial scales of active abiotic and biotic processes within mangrove forests. The solid boxes indicate the scope of this thesis. Based on: McIvor et al. (2012); McIvor et al. (2013); Bullock et al. (2017); Cowell & Thom (1994).....	7
Table 2.1: The locations of quadrat surveys and hydrodynamic measurements collected. Quadrats are organized by their cross-shore location. Each vegetation survey was accompanied by hydrodynamic measurements collected by the listed instruments deployed. ADCP refers to a Nortek Aquadopp, Vectrino refers to the Nortek Vectrino Profiler, and ADV refers to a Nortek Vector. Quadrats with the designation ‘a’, ‘b’ and ‘c’ were deployed in the same location and multiple vegetation surveys were collected at this site. Synoptic ‘tidal flats-to-forest’ experiments were conducted in three locations on the same days. Measurement heights were measured prior to conducting the experiment and are relative to the initial bed levels of the experiments. Deployment durations are rounded to the nearest half hour.	37
Table 2.2: Pneumatophore survey statistics. All values reported (excluding n and h_c) are from the height of the corresponding velocity measurement, h_v . Unless explicitly stated in the column header, values are reported for the 1 m ² quadrats. Values of minimum and maximum a (a_{min} and a_{max} , respectively) are given for the 20 cm ² quadrats.	47
Table 3.1: Summary of instrument deployment settings. The Nortek Vector and Aquadopp are referred to in the text as ‘ADV’ and ‘ADCP’, respectively.	72
Table 3.2: Vegetation statistics for each experimental site. Whole quadrat statistics are denoted by an asterisk (*).	73
Table 3.3: Flow properties measured within the HTA and VTA. Highlighted peak frequencies from the power spectra (Figure 3.10) are listed as f_d . $S_t = f_d d / U_w$, and $l = U_w / 2\pi f_d$	88
Table 4.1: Locations of hydrodynamic and sediment measurements (ref. Figure 4.1 for locations), deployment durations and general conditions during the experiments. All experiments were conducted in 2015. Column headers are as follows: T_p = peak wave period, H_s = significant wave height, n = number of pneumatophores per square meter, aD = normalized root density, z = Vectrino probe height above bed, d_{50} = median grain size, Sand = percent sand in sediment sample, Mud = percent mud in sediment sample.	111
Table 4.2: Statistics for wave and infragravity-length events across the mudflat, fringe and forest sites.	132
Table 4.3: Multiple linear regression model results for the mudflat, fringe and forest sites. Symbols correspond to included model parameters: h , the	

water depth, τ_b , the bed shear stress, ε , the TKE dissipation rate, and \bar{u} , the mean current velocity. 133

List of Symbols

ADCP	Acoustic Doppler Current Profiler.	HTA	Horizontal Turbulence Array
ADV	Acoustic Doppler Velocimeter (see also VEC).	H_s	significant wave height.
a	canopy frontal area density.	h	water depth.
A_δ	wave orbital excursion.	h_v	height of velocity measurement.
COI	Cone Of Influence.	h_c	canopy height.
C_D	drag coefficient.	KC	Keulegan-Carpenter number.
C_v^2	dissipation empirical constant.	k	wave number.
D	(vegetation) patch width.	k_0	roll-off wavenumber.
d	stem (root) diameter.	k_c	cutoff wavenumber.
d_{50}	median grain size diameter.	k_N	Nikurade roughness length.
f	frequency.	k_w	hydraulic roughness length.
f_d	shedding frequency.	LL	Low tide stage.
F_D	drag force.	l	eddy length scale.
f_w	wave friction factor.	l_t	length scale of the largest turbulent eddies.
f_{wc}	wave cutoff frequency.	ML	Medium-Low tide stage.
f_{hc}	high-frequency cutoff.	MH	Medium-High tide stage.
g	gravitational constant.	NE	North East.
HH	High tide stage.	n	number of stems per square meter.

r	along-beam Vectrino velocity bin separation distance.	v	north/south or across-current velocity.
Re	Reynolds number.	v'	turbulent fluctuations in the along-current direction.
SSC	Suspended Sediment Concentration.	WBBL	Wave Bottom Boundary Layer.
ΔS	average stem spacing.	w	vertical velocity.
S_t	Strouhal number.	w'	turbulent fluctuations in the vertical direction.
s_v	Vectrino sampling volume width.	XWT	cross-wavelet analysis.
SW	South West.	x	lateral position of measurement location.
TKE	Turbulent Kinetic Energy.	z	height above bed.
T_w	wave period.	z_0	bed roughness amplitude.
u	east/west or along-current velocity.	β	normalization factor.
u'	turbulent fluctuations in the along-current direction.	γ	wave breaking parameter (Thornton & Guza, 1983).
u^*	friction velocity.	ε	turbulent kinetic energy dissipation rate.
U	wave-and-current flow velocity.	κ	Von Kármán's constant.
U_d	mean drift velocity	ρ	water density.
U_δ	peak bottom wave orbital velocity.	Λ	Ratio of the wave period to the time scale for dissipation (Henderson et al. 2017).
VTA	Vertical Turbulence Array.		
VEC	Nortek Vector.		

λ_0	length scale of stress-carrying eddies.	ϕ	volume fraction occupied by vegetation.
λ	canopy roughness factor (Belcher et al. 2003).	ω_r	wave radian frequency.
ν	kinematic viscosity of seawater.	ω_y	lateral vorticity.
ν_t	eddy viscosity.	Subscripts	
δ_R	wave boundary layer thickness.	c	parameter associated with current.
σ_B	uncertainty estimate of ε .	max	maximum value of.
σ_n	standard deviation.	min	minimum value of.
σ_w	wave orbital velocity.	rms	root mean squared velocity.
τ_c	bed shear stress due to currents.	w	parameter associated with oscillatory flow.
τ_m	time-averaged and cycle-mean bed shear stress (Soulsby, 1997).	Other	
τ_{max}	maximum bed shear stress.	—	time average.
τ_w	bed shear stress due to waves.	$\langle \rangle$	spatial average operator.
		$\hat{}$	dimensionless variable.
		$ $	absolute value.

Chapter 1

Background and Introduction

1.1 The Value of Mangroves

Mangrove forests thrive at the interface between land and sea and offer a multitude of ecosystem services: mangroves form the habitat for many fish and animal species (particularly juveniles), and hence contribute to the world's biodiversity. For humans, mangroves provide raw building materials, sources of medicine, fuel and food for local communities (Saenger, 2002). Forming a buffer zone along coastlines, mangroves protect communities from coastal hazards (Mazda et al., 2005, 2006), stabilize sediments to prevent erosion (Temmerman et al., 2013), and act as filters to terrestrial runoff by decreasing the amount of physical and chemical waste that would otherwise end up in the coastal ocean (Lin & Dushoff, 2004; Tam & Wong, 1996). Despite only covering 0.1% of the Earth's continental surface, mangroves account for 11% of the total terrestrial carbon storage, and 10% of total terrestrial dissolved organic carbon exported to the ocean (Dittmar et al., 2006; Jennerjahn & Ittekkot, 2002). Estimates of the monetary value of these ecosystem services vary widely, e.g., between \$3000 – 40000 USD per hectare per year (Salem & Mercer, 2012).

Mangrove forests are generally in decline worldwide, due largely to human pressures (Alongi, 2002; Spalding et al., 1997). It is estimated that one-half of global mangrove coverage has been lost since pre-industrial times (Giri et al., 2011), about 35% of which was lost between 1980 and 2000 (Valiela et al., 2001). Among the most threatened areas are large tropical deltas in Asia, such as the Mekong Delta in Vietnam, the Ganges Delta in India and Bangladesh, the Ayeyarwady Delta in Myanmar, and the Indus Delta in Pakistan (Allison et al., 2017). The decline of mangrove forests is predominantly caused by conversion of coastal areas to agriculture, aquaculture, and urban development (Alongi, 2002; Giri et al., 2008). Mangrove forest expansion may also be limited by local sea level rise and accelerated coastal subsidence, caused by sand mining and the construction of dams and sea dykes within major deltaic systems (Anthony et al., 2015). In such cases, mangroves would typically retreat landward as ground is lost; however, the

presence of human settlements often precludes this shoreward migration, leading to the so-called “coastal mangrove squeeze” (Phan et al. 2015).

Calls for mangrove conservation gained traction following the 2004 Indian Ocean tsunami (e.g., Walton et al., 2006), after several studies reported that mangrove-lined coastlines saved lives and property (Danielsen et al., 2005; Kathiresan & Rajendran, 2005). While many attempts have been made, efforts to rehabilitate or restore critically affected mangrove ecosystems have often had mixed results, with the main reasons for failure being improper site or species selection, and planting techniques (Ellison, 2000). Recent studies suggest that the success rate of seedling establishment is based on a narrow window of hydrodynamic conditions in which propagules can take root (Balke et al., 2011). To improve the chances of propagule recruitment, some rehabilitation efforts have taken to designing offshore structures such as breakwaters to simulate the low-energy conditions found within undisturbed forests (Schmitt et al., 2013; Temmerman et al., 2013). A report from the International Union for Conservation of Nature (IUCN) states that a successful restoration effort, in addition to other factors, will “...have a thorough understanding of the hydrological processes at each planting location” (IUCN, 2011, pg. 12). Hence, a better understanding of the physical forces that shape mangrove environments will contribute to more comprehensive vulnerability assessments and improve conservation and restoration efforts (Friess et al., 2012). The focus of this thesis is to understand how mangrove roots modify their physical environment by studying the hydro- and morphodynamic feedbacks within established coastal mangroves.

1.2 An Overview of Mangrove Characteristics

“Mangrove” is an ecological term referring to a taxonomically diverse assemblage of trees and shrubs that form the dominant communities in tidal, saline wetlands along tropical and subtropical coasts. Mangroves typically occur in low-gradient intertidal zones with an abundant supply of fine-grained sediment and fresh water input through rainfall, run-off, or river discharge (Walsh, 1974). Mangroves are classified as halophytes: species that can tolerate salinities from brackish to seawater (0.5 – 35 ppt). The vertical extent of mangroves is limited to mean sea level (MSL) and the highest spring tidal depth (Alongi, 2009). Below MSL,

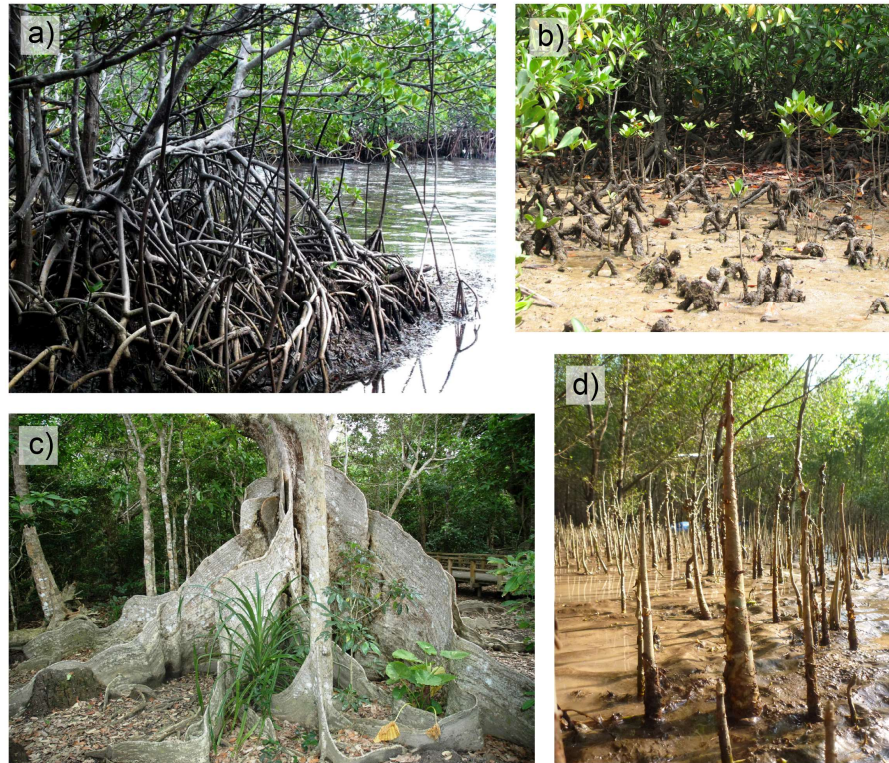


Figure 1.1: Mangrove roots, (a) prop roots of *Rhizophora* spp., (b) knee roots of *Bruguiera* spp., (c) buttress roots of *Xylocarpus* spp., and (d) pneumatophores of *Sonneratia* spp. Photo source for panels (a – c): http://www.mangrove.at/mangrove_roots.html

mangroves seedlings cannot settle, and in low-saline environments mangroves are outcompeted by other plants (Schiereck & Booij, 1995). Apart from their salt water tolerance, mangroves are also distinguished by their characteristic above-ground root structures. These aerial roots enable mangroves to exchange oxygen with their exterior environment, as the substrates of mangrove forests are often anoxic. Large assemblages of roots are referred to as “canopies” for the dense permeable layer they form above the bed surface. Of the many species of mangroves, only four distinct root types are observed (Spalding et al., 2010; Tomlinson, 1986):

- **Prop roots:** Common to the *Rhizophora* spp., ‘stilt’ or prop roots form a complex network of limbs that descend downwards from the main trunk and lower branches of the tree (Figure 1.1a). A single tree can produce hundreds of roots, with radial diameters up to 10 meters near the bed surface.

- **Knee roots:** Knee roots are the above-ground knob-like protrusions of the underground lateral root systems common to *Bruguiera* and *Ceriops* mangroves (Figure 1.1b).
- **Plank roots:** Plank or ‘buttress’ roots grow along the vertical axis of mangrove tree trunks and extend laterally outward from the trunk base in a sinuous pattern (Figure 1.1c). Plank roots are common to *Xylocarpus* and *Heritiera* spp.
- **Pneumatophores:** Also called ‘pencil’ roots for their conical shape, pneumatophores are the above-ground extensions of the underground root system of *Avicennia* and *Sonneratia* mangroves (Figure 1.1d). In *Avicennia* spp., pneumatophores are often shorter, only growing up to 30 cm tall. In contrast, the pneumatophores of *Sonneratia* spp. grow slowly to become woodier, which enables them to reach heights of 40 to 60 cm on average.

1.2.1 Global Distribution

The global distribution of mangroves is limited by the 20° C isotherm of seawater in winter (Duke, 1992), which corresponds to the latitude band spanning 30° N and 40° S. Worldwide, the roughly 70 species of mangroves cover approximately 138,000 km² of land area (Giri et al., 2011; Spalding et al., 1997), with the equatorial regions of Indonesia, Australia, Brazil and Nigeria account for roughly 43% of the world’s mangrove forests (Alongi, 2002). The Indo-West Pacific region (highlighted in Figure 1.2) contains the greatest mangrove biodiversity worldwide.



Figure 1.2: Global distribution of mangroves (Giri et al. 2011), with the Indo-West Pacific region highlighted as a red circle.

1.2.2 Mangrove Environments

Following Cintron & Novelli, (1984), mangrove-dominated environments can be classified into three types based on their topographic features: riverine forest, basin forest, and fringe forest (Figure 1.3). Woodroffe, (1992) modified these classifications to describe the physical processes responsible for sediment transport and deposition within each environment. The following descriptions were adapted from Mazda & Wolanski, (2007):

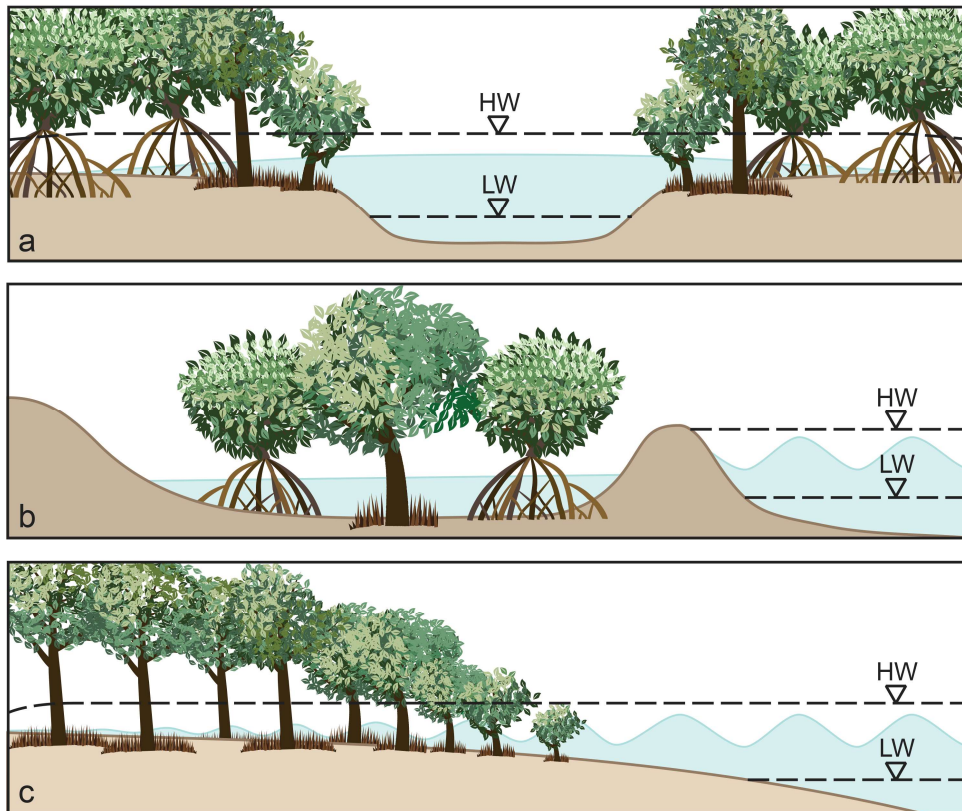


Figure 1.3: Three main types of mangrove landforms: a) riverine, b) basin, and c) fringe. After Mazda & Wolanski, (2007).

- **Riverine forests:** (R-Type, Figure 1.3a) occur on the floodplains alongside river channels or tidal creeks. Water levels within riverine forests are modulated by tidal oscillations; forests are dry at low tide and inundated at high tide. Sediment is supplied to the forest predominantly from the adjacent river. Waves are uncommon in such forests because of wave dissipation along the tidal channels. Water flow through the forest is controlled by flow routing through adjacent tidal creeks, and in-forest flow is roughly perpendicular to the flow in the creeks (Horstman et al., 2015; Kobashi & Mazda, 2005; Mazda et al., 2005).

- **Basin forests:** (B-Type, Figure 1.3b) develop in shallow depressions that are rarely inundated except for the highest tides. Water cycling of these systems is dominated by groundwater flows (Woodroffe, 1992).
- **Fringe forests:** (F-Type, Figure 1.3c) are the most dynamic mangrove landform of the abovementioned classes. In this class, mangroves grow in the confluence between river distributaries and the coastal ocean. Tidal oscillation exposes the substrate during low tide and inundates the forest during high tide. Wind and swell waves may pass directly into the forest from offshore, dominating the hydrodynamic environment. The mangrove forest in which the research for this thesis was conducted is classified by this latter category.

1.2.3 Physical Processes in Mangroves

Mangroves are sometimes referred to as ‘ecosystem engineers’, organisms that modify their abiotic environment to improve their chances of survival (Jones et al., 1994, 1997; Walles et al., 2015). Mangrove forests dissipate tidal currents and waves through drag forces generated within the dense mass of aerial roots, trunks and leaf canopies. Through this mechanism, wide swaths of mangrove forests can be effective buffers against storm surge and coastal flooding associated with storms and tsunamis (Alongi, 2008; Krauss et al., 2009; Möller et al., 2014; Montgomery et al., 2018; Montgomery et al., 2019; Temmerman et al., 2013; Wolanski, 2007; Zhang et al., 2012). The slowing of flows within mangrove forests gradually reduces erosive forces, thereby limiting sediment resuspension and promoting sedimentation (Bouma et al., 2005; Duarte et al., 2013; Furukawa & Wolanski, 1996). Over time, the feedback between energy dissipation and sedimentation may lead to net accretion in mangrove-dominated reaches through the accumulation of allocthonous sediment and autochthonous organic and inorganic material (Allison & Lee, 2004; Cahoon et al., 2006; Ellison, 2009; McKee, 2011; Woodroffe & Davies, 2009). Under some circumstances, mangrove soil surfaces may be able to keep pace with local sea level rise (Krauss et al., 2010; Lovelock et al., 2011; McKee, 2011; McKee et al., 2007). Hence, mangroves ‘engineer’ their environment by creating a sheltered intertidal area in which they can proliferate.

Table 1.1: The mechanisms, temporal and spatial scales of active abiotic and biotic processes within mangrove forests. The solid boxes indicate the scope of this thesis. Based on: McIvor et al. (2012); McIvor et al. (2013); Bullock et al. (2017); Cowell & Thom (1994).

Category	Process	Physical Mechanism	Time Scale	Spatial Scale
Hydrodynamic (abiotic)	Turbulence	Interaction of tides and currents with vegetation; wave breaking	Seconds	mm - cm
	Wind waves	Wind shear, gravity	Seconds	cm - m
	Swell Waves	Wind waves	Seconds	cm - m
	Infragravity	Wind and swell waves	Minutes	m - 100 m
	Tides	Gravitational action of the moon and sun, Earth's rotation	Hours	m - km
	Storm surge	Wind stress, atmospheric pressure variation in combination with local bathymetry and geomorphology	Days	km - 100 km
	Changes in sea level	Eustatic sea level variation	Years - Decades	km - 1000 km
Morphodynamic (abiotic)	Sediment Transport	Tidal and wave action, enabling the preferential scouring and deposition of sediment depending on the intensity of conditions	Seconds - Hours	mm - m
	Surface elevation change	Sedimentation, accumulation of organic material	Hours - Months	cm - m
	Sub-surface elevation changes	Mangrove root growth or decomposition, compaction	Months - Years	m - km
	Change in land level	Isostatic adjustments, removal of oil or water, urban development	Years - Decades	km - 1000 km
Mangrove (biotic)	Seedling establishment	Quiescent conditions suitable for root growth and establishment of pioneer species	Hours - Months	cm - m
	Tree Growth	Root and tree growth increasing forest density	Months - Decades	m - km
	Species Zonation	Establishment of secondary species	Decades - Centuries	km

Mangroves form a dynamic ecosystem, where ecological processes are intermixed with hydrodynamic and morphodynamic processes of differing temporal and spatial scales (Table 1.1). Understanding the role of mangroves in coastal protection, stabilization, and mitigation of sea level rise requires knowledge of the underlying short-term, small-scale (fast, local) processes that underlie these long-term, large-scale (slow, regional) processes. For example, the interactions between tides, waves and mangrove roots affect other morphodynamic and biological processes such as sediment transport and seedling establishment (Balke et al., 2011; Furukawa et al., 1997). Over time, the interaction between surface and sub-surface processes results in net surface elevation change, which in turn affects mangrove forest growth and zonation (Bullock et al., 2017; Fagherazzi et al., 2017). These long-term processes feed back into the short-term processes by altering the biogeomorphic landscape that affects the mangroves' inundation time, sediment supply, and sediment transport capacity (McIvor et al., 2013). As discussed in the next section, much of the previous work in mangrove systems has focused on the aforementioned long-term and large-scale processes, while less work has focused on the underlying short-term and small-scale processes, such as turbulence and sediment transport. Hence, this thesis focuses on these short-term and small-scale processes in order to develop a process-based understanding of how the feedbacks between mangrove vegetation and hydrodynamics shape mangrove environments.

1.3 Mangrove Hydrodynamics and Morphodynamics

Much of the early work in mangroves focused on describing mangrove ecology, their geographical characteristics, and their physiology (Lugo & Snedaker, 1974; Watson, 1928). Initial studies inferred that mangroves are 'land builders'; species that colonize intertidal mudflats thereby promoting a higher rate of vertical accretion of the bed (Davis, 1940). Latter studies instead suggested that mangroves merely follow accretion and enhance the retention and deposition of sediments once established (Bird, 1971; Thom, 1982; 1967; Woodroffe, 1992). Others recognized the role of mangrove roots in sedimentary processes by observing the depositional patterns within grids of canes used to simulate *Avicennia* pneumatophores (Bird, 1971; Spenceley, 1977). Spenceley (1977) suggested two roles for the root structures: "Under low-energy conditions velocities are further reduced, causing deposition of material to take place. When medium to high-energy conditions are

prevalent, the obstructions cause eddy currents to develop which initiate localized scour and erosion in their immediate vicinity”.

Until the 1980's, the majority of literature focused on mangrove ecology, while most studies of the physical processes in mangroves remained qualitative (Mazda & Wolanski, 2007). Early pioneers recognized this knowledge gap, stating: “...it is necessary to obtain a quantitative understanding of the physical processes and hydrodynamic mechanisms that take place in these intertidal areas... [to understand] the condition for the existence of mangroves” (Mazda & Wolanski, 2007). Today, the feedback between mangrove forest hydrodynamics and morphodynamics is still an active area of research. The following sections provide an overview of the present understanding of the large spatial and temporal scale hydrodynamic (e.g., tidal flow, wave dissipation) and morphodynamic processes (e.g., sedimentation), and the small spatial and temporal scale processes (e.g., turbulence) in mangroves.

1.3.1 Tidal-scale Flow

The pioneering work in mangrove systems focused on describing tidal flow routing and sediment transport mechanisms between mangrove forests and creeks (Furukawa et al., 1997; Mazda et al., 1995; Wolanski, 1995; Wolanski et al., 1980; Woodroffe, 1985). According to early model simulations, ebb tides last longer than flood tides in mangrove forests, and peak flood velocities exceed peak ebb velocities (Mazda et al., 1995). Friction in mangrove forests delays the discharge of ebb tidal waters and enhances channel flow through creeks that incise the forest (Mazda et al., 1995; Wolanski et al., 1980). These asymmetries result in a net import of sediment into mangrove forests (Wolanski et al. 1990; Furukawa et al. 1997; Van Santen et al. 2007). In contrast, flow within dissecting creeks is often ebb-dominant due to the delayed discharge of water from the hydraulically rough areas (Mazda et al., 1995; Wolanski et al., 1980; Wolanski, 2007). Mangrove creeks are maintained through self-scour and enable material exchange between the forest and the ocean (Wolanski et al., 1980).

Flow routing in mangrove systems was first explored through depth-averaged, simplified numerical models, where both the mangrove vegetation and topography were highly idealized (Aucan & Ridd, 2000; Furukawa et al., 1997; Mazda et al.,

1995; Wolanski et al., 1980). In these early models, vegetation density was parameterized from a small number of field measurements using an adjusted Manning roughness coefficient that was based on approximations of atmospheric flow around common crops (Petryk & Bosmajian, 1975). Furukawa et al., (1997) estimated a Manning coefficient of $n = 0.1$, a value four times larger than that of adjacent tidal creeks. Water flow through the dense vegetation resulted in the formation of “jets, eddies and stagnation zones”; evidence of vegetation-induced friction.

More detailed mechanistic insights of creek-forest flow were later developed through flume experiments that employed arrays of dowels representing a scaled mangrove forest incised by a creek (Struve et al., 2003; Wu et al., 2001). From their experiments, Wu et al., (2001) developed a numerical model to account for the drag force and flow blockage of the model trees. These flume experiments corroborated the findings of the earlier field observations: enhanced drag within vegetated areas increases flow velocities in adjacent creeks.

Tidal flow routing through mangroves is thought to be controlled by the balance of four factors: drag forces from the submerged vegetation, turbulence generated by vegetative drag, bottom friction, and wind stress (Mazda & Wolanski, 2007). However in vegetated areas, bottom friction is negligible compared to vegetative drag forces (Nepf, 1999), and wind stress can often be neglected as mangrove trees inhibit wind within forests (Mazda et al., 2005). Hence, flow routing in mangroves depends only on a balance between the drag force and vegetation density (Mazda et al., 2005). To account for vertical differences in vegetation cover, Mazda et al., (2005) derived analytical models for water flows through vegetation based off of the vegetation frontal area, volume, and an effective vegetation length scale. This latter parameterization suggests that both the drag force and eddy viscosity decrease with respective increases in vegetation density. From point velocity measurements, Mazda et al., (2005) demonstrated that currents within vegetated areas rotate away from the mean current direction in creeks due to differing magnitudes of drag forces and turbulence. Similar patterns of flow rotation have recently been observed in both exposed coastal mangroves (Mullarney et al., 2017a), and in sheltered, channelized mangrove forests (Chen et al., 2016; Horstman et al., 2013). Finally, the differential between the low-friction unvegetated areas (creeks, mudflats) and

high-friction vegetated areas (forests) results in two distinct flow regimes (Horstman et al., 2013). One regime, designated ‘creek flow’, occurs during low water levels and is identified by strong currents in the creeks and minimal exchange across the forest. The other regime, designated ‘sheet flow’, describes direct water exchange across the forest and occurs only after the water level exceeds a threshold depth.

1.3.2 Wave Dissipation

It is well-established that mangroves play a role in the dissipation of wind and swell waves (Brinkman et al., 1997; Horstman et al., 2012; Massel et al., 1999; Mazda et al., 2006; Mazda et al., 1997; Quartel et al., 2007; Vo-Luong & Massel, 2008) and in defending coasts against storm surges (Krauss et al., 2009; Zhang et al., 2012). Factors known to affect wave attenuation in mangroves includes the water depth, which is a function of topography/bathymetry and tidal stage, the incident wave height, and specific vegetation characteristics such as density, size and spatial distribution of mangrove trees (McIvor et al., 2012). Multiple studies have shown that wave dissipation is greatest at water depths below the lower root or above the upper leaf canopies of mangrove trees (Brinkman et al., 1997; Horstman et al., 2012; Mazda et al., 2006). For intermediate water depths, dissipation decreases as there are fewer obstacles to induce drag. In a recent study, Henderson et al. (2017) demonstrated that wave dissipation is maximum at order-one values of the dimensionless ratio, $A = T_w/(2\pi T_f)$ where T_w is the wave period and T_f is time scale for dissipation by canopy friction. The parameter A increases with vegetation density, and depends on both wave parameters (wave period, amplitude) and canopy geometry (Mullarney et al., 2017b). Henderson et al. (2017) suggested that mangroves might maintain ratio of $A \sim 1$ as an adaptation to prevent high sediment accumulation that could result poor health or even death (Moffett et al., 2015; Nardin, et al., 2016b).

To provide adequate coastal protection against wave inundation and erosion, a mangrove forest must be of sufficient width and density to dissipate a range of incident wave heights. According to Bao, (2011) the minimum width of forest required to effectively dissipate incident wave energy to a safe level decays exponentially with increasing forest complexity- a function of the average tree

height, density and canopy closure (a measure of close packing). From field experiments, between 60 – 90% of incident short-period ($T_w = 1 - 30$ s) wind and swell waves were dissipated over 50 – 300 m of mangrove forest (Brinkman, 2006; Henderson et al., 2017; Horstman et al., 2012; Mazda et al., 2006; Quartel et al., 2007), with greater dissipation rates corresponding to greater forest density. These field observations have also been corroborated by a recent numerical study that simulated short-wave dissipation over a range of tree densities from 0.5 – 1.7 trees m^{-2} (Phan et al., 2015). Unlike short-period waves, long-period infragravity waves ($T_w > 30$ s) may propagate distances greater than 1 km onshore before being dissipated, even in dense forests (Phan et al., 2015). From scaling arguments of the shallow water mass conversion equation and the diffusion wave equation, Mullarney & Henderson, (2018) suggest that long-period waves can propagate inland across a flat-bed wetland a distance of order

$$L = \left(\frac{2gT_w^2\eta_0}{a} \right)^{1/3}, \quad (1.1)$$

where η_0 and T are wave height and duration, respectively. From this scaling argument, a mangrove forest with $a = 0.035$ m^{-1} , significant attenuation of infragravity waves with $\eta_0 = 0.5$ m and $T_w = 8$ min would require on the order of 525 m of forest. Although this estimate is highly simplified, it is in fair agreement with the scale over which long-wave heights are halved in the simulations of Phan et al., (2015). Hence, it has been hypothesized that short-period waves do not play a major role in determining the health of a mangrove forest. Instead, the large-scale patterns in seedling dispersal and sedimentation may be controlled by infragravity energy (Phan et al., 2015). While the role of short-period waves in sediment transport and resuspension in coastal mangroves has been qualitatively described (Van Santen et al., 2007; Winterwerp et al., 2005), the role of long-period waves has not yet been explored.

1.3.3 Sedimentation

A substantial amount of work has focused on understanding accretion rates within mangrove forests in response to fluctuations in eustatic sea level rise throughout the Holocene (e.g., Ellison, 2009; Fujimoto, 1998; McKee et al., 2007; Walsh & Nittrouer, 2004; Woodroffe, 1990). However, as this thesis is concerned with

present-day mechanisms of vegetated morphodynamics, the following discussion will instead focus on surficial sedimentary processes in coastal mangroves.

Mangrove forests are generally regarded as net sinks of sediment due to tidal current asymmetries set up by vegetative drag forces. Suspended terrigenous material is transported through the combined action of tides and waves into mangrove forests (e.g., Woodroffe & Davies, 2009; Van Santen et al. 2007), or through storm or tsunami events (Ellison, 2009). Sediment trapping by mangroves is thought to be facilitated through flocculation/deflocculation processes and by turbulence generation in the wake of mangrove roots (Furukawa et al., 1997; Wolanski, 1992; 1995b). In sufficiently dense vegetation, wake turbulence may create eddies and stagnation zones that help to trap suspended sediments. Deposition is thought to occur at slack tide when current velocities decline (Furukawa et al., 1997). The sediment is not re-entrained into the water at ebb tide so long as drag forces prevent currents from reaching critical shear thresholds.

Accretion within mangrove forests occurs if the rate of deposition exceeds the rate of erosion over time. Factors influencing accretion are those that stabilize the substrate, such as: the prevalence of benthic algal mats, aerial root and tree density, leaf litter (Krauss et al., 2003; Kumara et al., 2010; McKee, 2011), and those that supply sediment, such as: the inundation regime and tidal range of the forest (Rogers et al., 2006; Rogers et al., 2005). Erosion occurs if the shear stress of the substrate is exceeded by the hydrodynamic forces of tidal currents and waves. Although mangroves typically inhabit sheltered intertidal areas that are only exposed to weak currents and small waves, the high-energy conditions prevalent during storm events can cause large-scale erosion of the mangrove platform (Van Santen et al., 2007). As formerly discussed, mangrove roots dissipate tidal and wave currents and hence provide protection against erosion (e.g., Massel et al., 1999; Mazda et al., 1997a; Quartel et al., 2007). However, mangrove roots up to a critical density will enhance energy dissipation, thereby creating the conditions for erosion (Furukawa et al., 1997; Henderson et al., 2017). These two seemingly contradictory roles for mangrove vegetation reflect the balance between the competing processes of turbulence production and energy dissipation, which is governed by the spatial distribution and density of vegetation. However, as of yet, no field studies in mangroves have quantitatively connected vegetation density and hydrodynamics to

depositional patterns. Such patterns have only been qualitatively described for mangroves (e.g., Krauss et al., 2003; Kumara et al., 2010; Mullarney et al., 2017b; Spenceley, 1977).

1.3.4 Turbulence

The ability of mangroves to hydrologically engineer their environment arises from the turbulence generated within their root and leaf canopies (Krauss et al., 2003; Mullarney et al., 2017a; Spenceley, 1977). Recent studies have suggested that circulation patterns at the forest-scale are dominated by drag forces generated within the mangrove root canopies when the water depth is of the order of the root height (Mullarney et al., 2017a). However, relatively few studies have investigated turbulent wake production within mangroves at the root scale (e.g., Furukawa et al., 1997; Furukawa & Wolanski, 1996; Mazda et al., 1997b; 2005). In the field, Furukawa & Wolanski, (1996) observed “jets, eddies and stagnation zones” forming in the wake of *Rhizophora* prop roots. The flow rate through the root structures was later quantified in Furukawa et al., 1997 using the VORTEX model to simulate the complex flow structure forming in the wake of the obstructions. As of yet, no studies have quantified turbulence in mangrove roots in situ. Meanwhile, much work has been completed in other marine ecosystems such as salt marshes and seagrasses at the spatial resolution of the vegetation stems (e.g., Lacy & Wyllie-Echeverria, 2011; Leonard & Croft, 2006; Widdows et al., 2008). Given the horizontal and vertical heterogeneity of mangrove root canopies (Liénard et al., 2016), simplified models (e.g., Furukawa et al., 1997; Mazda et al., 2005; Struve et al., 2003; Wu et al., 2001) may not accurately represent the complex 3D root-scale flow structure. Similarly, lessons from saltmarsh or seagrass vegetation cannot be simply applied to mangroves due to the striking differences in vegetation structure, flexibility, height and density between the relatively uniform saltmarsh vegetation and the much more heterogeneous mangrove vegetation. Recent studies suggest that high near-bed turbulence has been shown to correlate with the formation of scour pits and other depositional features (Yager & Schmeckle, 2013). Understanding the impact of vegetation on sediment transport is important because vegetation is ubiquitous in water environments. Hence, recent work has focused on examining the role of near-bed turbulence and bed shear stress in sediment transport within model vegetation (Etminan et al., 2018; Yang et al., 2015; Yang & Nepf, 2018).

While these studies are highly instructive, there needs to be direct measurements to understand the link between root-scale hydrodynamics and sediment transport in nature.

1.4 Research Objectives

Previous sections have shown that while there is an abundance of information on the large-scale processes in mangroves (tidal flow, wave dissipation, and sedimentary patterns), the underlying small-scale processes (turbulence, sediment transport) are relatively understudied. While there are few studies that have that examined the modification of the flow-field by mangrove root structures (e.g., Furukawa et al., 1997; Horstman et al., 2018; Maza et al., 2017; Mazda et al., 1997b), none of these studies did so in situ. The lack of such data limits our understanding of the fundamental processes that shape mangrove ecosystems.

The present work aims to improve our understanding of these short-term and small-scale interactions in coastal mangroves, through (i) the collection and analyzation of field data from instruments placed within mangrove roots, under (ii) a variety of environmental conditions and over (iii) a range of root densities to quantify the effect that the horizontal and vertical distribution of mangrove vegetation has on local hydrodynamics and morphodynamics.

1.5 Research Questions

The work encompassed in this thesis attempts to answer the following research questions:

1. How does the spatial distribution of mangrove pneumatophore roots affect the temporal and spatial distribution of turbulence within the mangrove forest? Specifically, how is turbulent energy dissipation affected by wave breaking and the water depth (tidal stage)?
2. How does the heterogeneous vertical distribution of mangrove pneumatophores modify the flow field?
3. How does the bed level respond to variations in hydrodynamic forcing conditions (e.g., currents, turbulence, and water depth) throughout a tidal cycle? How does bed level movement inside the mangrove forest differ from the unvegetated mudflat?

4. How do the spatial patterns in hydrodynamics (e.g., tides, waves, and turbulence) affect the distribution of sediment within the mangrove forest?

1.6 Regional Setting: Field Site and Data Collection

The Mekong River is one of eight large river systems that flow out of the Himalayan Plateau and flows through six countries. In Vietnam, the Mekong River Delta (MRD) is home to roughly 20 million people, and is heavily utilized for agriculture, aquaculture, oil and gas production, and sand mining (Allison et al., 2017; Anthony et al., 2015). These development pressures, in addition to the widespread defoliation that occurred during the Vietnam-American War, have affected mangrove coverage in the delta. Mangrove extent reached a minimum of 157 thousand hectares in 1999, and since has rebounded to 270 thousand hectares in 2015 due to planting efforts by the Vietnamese government (Allison et al., 2017).

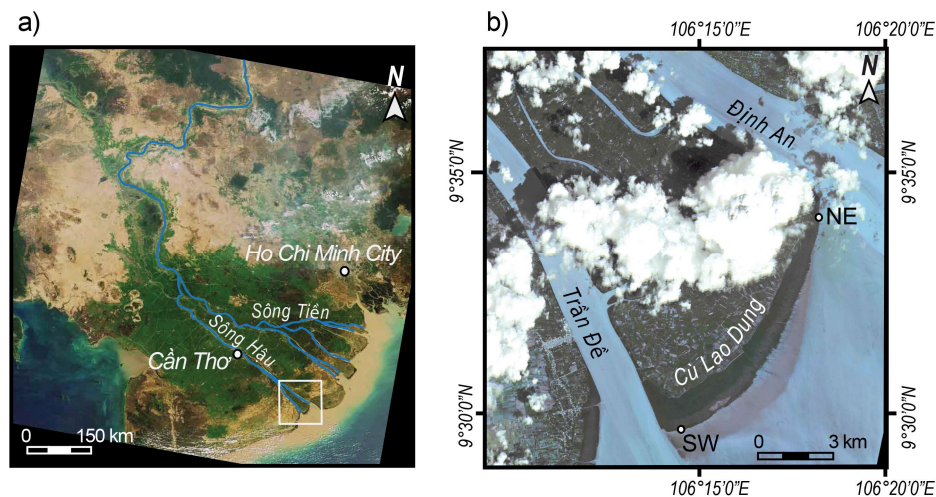


Figure 1.4: Regional context of experiments: a) Mekong River Delta with the Sông Tiền and Sông Hậu distributaries identified. The white square shows approximately the extent of Cù Lao Dung in the Sông Hậu distributary channel (panel b). Photo sources are: Envistat (panel a) and Rapideye (panel b).

Data were collected during two seasons between September – October 2014 and in March 2015 as part of the collaborative Mekong Tropical Delta Study (MTDS). The primary objective of this overarching study was to understand the sediment transport pathways that shaped the evolution of the MRD during the Holocene and will continue to shape the delta into the future (Allison et al., 2017; Nitrouer et al., 2017). Field studies were focused on the Bassac River or Sông Hậu, spanning the section between Cần Thơ and the coast (Figure 1.4a). The Sông Hậu is bisected at

its terminus by the mid-channel island Cù Lao Dung (Figure 1.4b). Experiments for the present work were conducted in the coastal mangrove forest that lines the southern seaward edge of the island.

The Mekong River discharges 470 billion cubic meters of sediment out of its delta into the East Sea (South China Sea) per annum on average (Milliman & Syvitski, 1992). River discharge is modulated by seasonal monsoons. The high-flow period is associated with a southwesterly monsoon during the months of July – December (Wolanski et al., 1998). This season is categorized by consistent rainfall in the delta, light winds, and relatively quiescent marine conditions (wave heights and currents). During this period sediment is discharged from the Sông Hậu distributary into the East Sea (Fricke et al., 2017; McLachlan et al., 2017). In contrast, the low-flow period occurs during the northeast monsoon (January – July) which is characterized by drier conditions, higher wind speeds and larger swell waves. During this period, energetic marine conditions mobilize sediment from the continental shelf, moving it towards Cù Lao Dung through the combined action of river flow, tides and waves (Eidam et al., 2017). As is evident from satellite imagery, Cù Lao Dung is prograding in an asymmetric manner. The southwest corner of the island has expanded since the mid 1970's through a combination of sediment delivery, physical mixing by wave action in the Trần Đề sub-distributary (Figure 1.4b), and the biophysical processes in mangroves. In contrast, the progradation of the northeastern corner of the island has been limited due to a reduced sediment supply caused by stratified and less turbid conditions in the Định An sub-distributary (Fricke et al., 2017).

The southern edge of Cù Lao Dung is covered in a mangrove forest that occupies approximately 12.2 km² between farmland, the river channels, and the East Sea. Seaward of the forest, a shallowly sloping interlaminated sand and mudflat extends offshore for several kilometers into the estuary (Fricke et al., 2017). Early in the 1980's, mangrove areas that had been converted to shrimp ponds and sugar cane fields experienced greater erosion rates, prompting the government to plant *Sonneratia caseolaris* mangroves to manage land loss (Fagherazzi et al., 2017). Over time, sediment accumulation on the island has favored mangrove expansion, predominantly in the southwest. Presently, the southern edge of the island is colonized by *Sonneratia caseolaris*, with a mix of *Avicennia marina*, *Aegiceras*

corniculatum mangroves, and *Nypa fruticans* palms that inhabit the higher inshore areas (Bullock et al., 2017). Despite human assistance in plant establishment, this species distribution currently provides similar ecological functions as a natural forest (Wölcke et al., 2016).

Experiments were conducted in the southwestern (SW) and northeastern (NE) corners of the island (Figure 1.4b) using a combination of fixed and independent movable instrument arrays arranged along a across-shore transect spanning the mudflat to the forest interior. Instruments (velocimeters and pressure sensors) were configured to record changes in the local hydrodynamic conditions over the varying substrates and regions of mangrove density. Fixed instruments were left in place for the duration of the field experiments, while the moveable instrument packages were used to record several tides before being redeployed in a new configuration. Such experiments had one of two configurations: either ‘flats to forest’ (Figure 1.5a – c), where instruments were deployed simultaneously in the mudflat, mangrove forest fringe, and forest environments, or ‘fine scale’ (Figure 1.5d), where instruments were deployed in close proximity to dense canopies of pneumatophore roots and to each other. These two instrument configurations were used to address the primary questions of this thesis (Section 1.5). Large-scale trends in the turbulence production across the gradient of mangrove vegetation between fringe and forest (Questions 1 and 3) were assessed with the ‘flats to forest’ instrument configurations, and the small-scale flow patterns around the root structures (Question 2) were assessed with the ‘fine scale’ configurations. The linkages between hydrodynamics and sediment transport (Question 4) were also assessed with the ‘flats to forest’ configurations, in addition to sediment sampling in the vicinity of the instrument deployment locations (discussed below).

Specific information on instrument deployment configurations, data logging parameters, quality control, and analysis are given in the methods sections of each subsequent chapter for the individual experiments. In brief, flow speeds and directions were measured using a variety of acoustic current meters, either Nortek Aquadopps or Nortek Vectors (generically, an ADCP and ADV, respectively). Fixed instrument deployments typically consisted of either an ADCP or an ADV mounted to the bed, and recorded pressure and 3D velocity measurements at high-frequency (8 Hz or 32 Hz, respectively) to resolve waves. In some experiments,

either an ADCP or ADV was deployed within a fine-scale array to record conditions above the pneumatophore canopy. A weather station was deployed in the SW approximately 130 m offshore of the mangrove forest fringe 3.6 m above the mudflat to record local atmospheric conditions (Figure 1.5f).

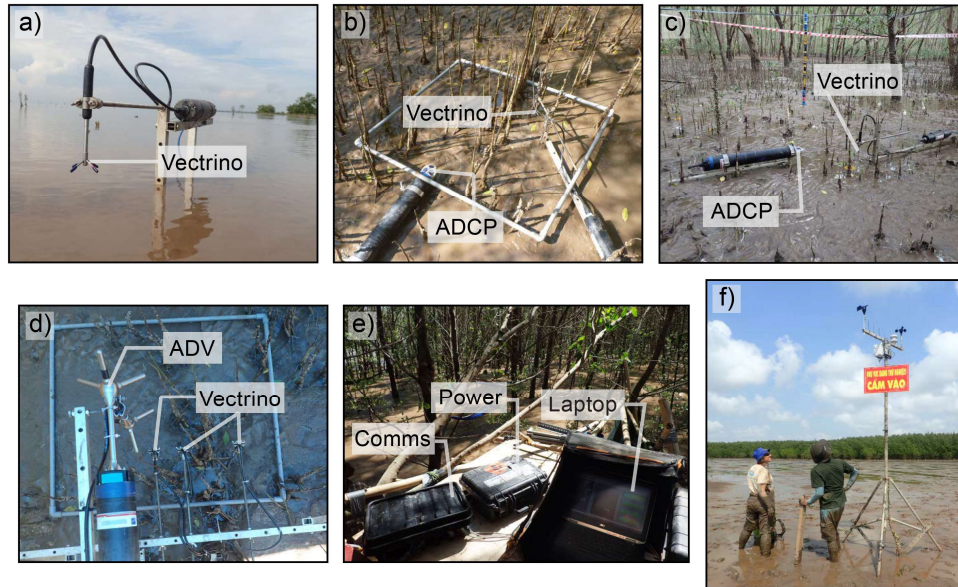


Figure 1.5: (a) to (c): example ‘flats to forest’ instrument configurations. (d): a ‘fine scale’ configuration. Three Vectrinos were deployed in a horizontal row amongst a cluster of pneumatophore roots. (e): Vectrino data logging station with the communications and power boxes, and a field laptop in a special water-resistant housing. (f): a HOBOT U30 weather station deployed offshore on the mudflat in front of the mangrove forest in the SW. Scientists for scale (approximately 1.6 m with 0.2 m in the mud).

A novel feature of these experiments was the use of the Nortek Vectrino Profiler (or ‘Vectrino’ for short) in the field. The Vectrino is an instrument designed to resolve flows over very fine spatial resolutions (1 mm) at very high frequencies (up to 100 Hz), making these instruments ideal for resolving turbulence. However, these instruments were designed for laboratory use only as they require a power supply and do not internally log data on their own. Experiments were designed around the deployment of three Vectrinos, either in separate environments (as per the ‘flats to forest’ configuration), or the same environment (as per the ‘fine scale’ configuration). Each Vectrino was connected via 100 m cables to a laptop that synced measurements between instruments and logged current data (Figure 1.5e). Power was supplied to the instruments and laptop using two 12 V batteries that were connected through an in-house designed communications box (see: Mullarney et

al., 2017b for details). Each instrument was mounted to an aluminum frame that was driven into the substrate at each measurement location, typically tens of centimeters above the bed. Prior to data collection, the Vectrinos were aligned to the vertical using a bubble level.

As many of the primary questions addressed in this thesis depend on assessments of vegetation density, high-quality measurements of vegetation geometry were required. Traditionally, assessments of vegetation characteristics are made by hand-counts and caliper measurements of feature diameters within small cordoned off areas delineated by a quadrat. However, recent advances in photogrammetric techniques for recreating complex 3D geometries have enabled better and more efficient surveying methods (e.g., Gatzliolis et al. 2015). During the data collection periods in the Mekong Delta, a new sampling method for resolving pneumatophore geometries was developed. At each instrument deployment location, vegetation characteristics (where applicable) were surveyed within a 1 m² PVC quadrat by photographing the quadrat from ground-parallel to an overhead oblique view in 360°, totaling between approximately 50 – 300 photos per quadrat (Figure 1.6a). After returning from the field, these photo data sets were fed into the freeware VisualSFM (Wu, 2011) that reconstructs the relative camera position for each photo and produces a sparse 3D model of the scene. Point clouds were then edited in the freeware CloudCompare to remove features that were not of interest, such as any instruments within the quadrat boundary, features outside of the quadrat, and the quadrat itself (Figure 1.6b). Pneumatophore geometries were then reconstructed from the point clouds using an algorithm developed by Liénard et al., (2016). Their ‘sector-slice’ algorithm identifies individual root structures and classifies their diameters over height ‘slices’ extending from 1 cm of the bed every 5 mm to the top of the canopy (Figure 1.6c).

Sediment characteristics were quantified from hand samples and sediment cores collected in the near vicinity of the instrument deployment locations. Sediment grain size was determined by separating mud and sand fractions of each sample by wet sieving through a 64 µm sieve, then grain size distributions were determined in the laboratory with a particle sizer instrument. In addition to sediment samples, optical backscatter sensors (OBS) were co-deployed with some of the ADCPs. OBS measurements were made for 6 to 8 minutes every 10 minutes

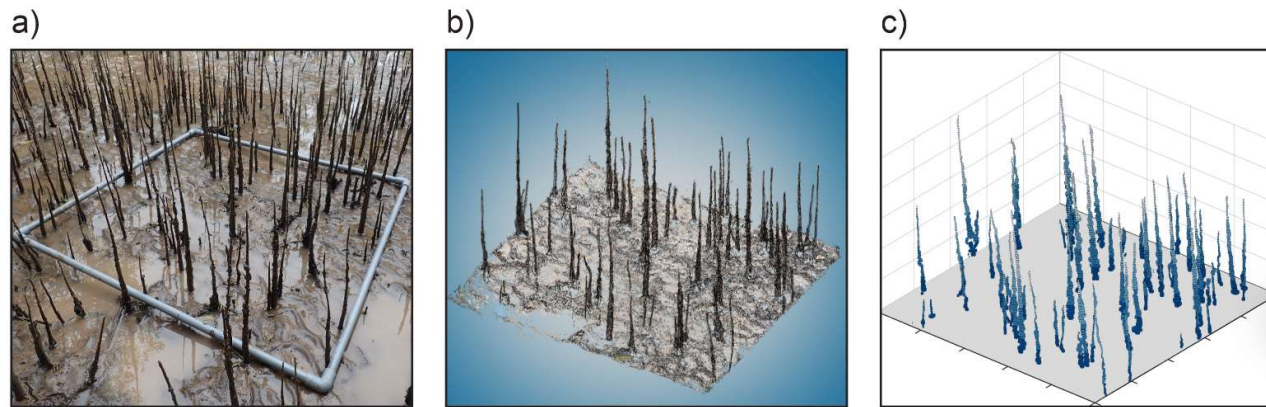


Figure 1.6: Illustration of the photogrammetric reconstruction method used to obtain high-resolution estimates of pneumatophore geometries. (a): a sample photo from one of the photo sets used to reconstruct vegetation geometry. In this image a 1 m² quadrat delineates features of interest. (b): The point cloud created from inputting the photo set into VisualSFM. Note that the quadrat has been removed from this reconstruction. (c): Pneumatophores represented as three-dimensional shapes from near the bed level (dark colors) to the top of the canopy (light colors). Each height ‘slice’ is represented here as a cylinder, where the cylinder diameter is the twice the mean of the radius of each slice as generated by the sector-slice algorithm (Liénard et al. 2016).

at either 2 or 6 Hz. Turbidity levels were determined by calibrating instrument voltages with in situ water samples. The sediment sample analysis and calibrated OBS data were provided by Aaron Fricke from the University of Washington.

1.7 Thesis Outline

Each of the following three chapters was intended as a stand-alone document for submission to an international, peer-reviewed journal.

- Chapter 2 focuses on the large-scale patterns (100 m) of the turbulent kinetic energy dissipation measured within clusters of mangrove pneumatophore roots across the mudflat to the forest interior. Spatial patterns in sediment grain size distributions were correlated to the hydrodynamic measurements to infer morphodynamics. This study was the first to quantify the spatial distribution of turbulent energy dissipation in relation to environmental conditions (i.e., variance in water depth, wave height) and mangrove root density. This work was published in *Continental Shelf Research* in August, 2017 for a special issue on the MTDS, with myself as first author. Additionally, some of the findings from this study were also published in a special issue of *Oceanography* magazine in September, 2017 with myself as third author.
- The objective of Chapter 3 is to link the vertical (heterogeneous) distribution of mangrove pneumatophore roots with zones of turbulence generation, as the root structures can often occupy a large fraction of the water depth in shallow (~3 m) intertidal environments. Turbulence statistics were calculated from high-resolution velocity measurements collected by instrument arrays that were designed to quantify the horizontal and vertical evolution of flows around the root structures. Although numerical modeling studies often require parameterizations of turbulence in vegetated areas, measurements of this detail have not been made in mangroves before. This work has been submitted to the *Journal of Geophysical Research: Oceans*.
- Chapter 4 explores the physical linkages between turbulence generated within mangrove roots and sediment transport. Oscillations in the near-bed velocity were correlated using a cross-wavelet transform with oscillations in the temporally variable bed level at each measurement location. Net bed level changes during highly coherent ‘movement events’ were also statistically correlated with variables commonly associated with sediment transport (i.e., the

bed shear stress, turbulent energy dissipation, mean current velocity, wave orbital velocity and water depth) to reveal how temporal and spatial changes in these variables affect the sediment transport capacity of the forest. Further, to understand the effect of mangrove roots on morphodynamics, the small-scale (< 1 m) spatial distributions of pneumatophores are correlated with bed level change over a single tidal cycle. This work will be submitted to *Geomorphology*.

The three research chapters are followed by a concluding discussion in Chapter 5, which summarizes the main findings of this thesis and ends with overall conclusions and suggestions for further research.

Chapter 2

The Effect of Pneumatophore Density on Turbulence: A Field Study in a *Sonneratia*-dominated Mangrove Forest, Vietnam



Measuring the flood tide waters entering the mangrove forest fringe in the southwest of Cù Lao Dung, Vietnam.

Contribution of Authors

Chapter 2 presents the article entitled “The Effect of Pneumatophore Density on Turbulence: A Field Study in a *Sonneratia*-dominated Mangrove Forest, Vietnam”, which was published in *Continental Shelf Research* in 2017. Data were collected for this study during two field seasons (Section 1.6) in Vietnam by myself, Dean Sandwell, Julia C. Mullarney, and Stephen M. Henderson. I wrote scripts to load, quality control, and analyze all of the hydrodynamic data. I also prepared all of the figures and wrote the initial and subsequent drafts of this manuscript. My co-authors, Julia C. Mullarney, Karin R. Bryan and Stephen M. Henderson edited my drafts and provided helpful comments, direction, and editorial help responding to reviewers’ comments.

Abstract

This chapter examines the role of mangrove pneumatophore roots as a spatial control over the turbulent kinetic energy (TKE) dissipation rate within a natural mangrove forest. Measurements of turbulence at millimeter scales were compared with vegetation geometries reconstructed using a novel photogrammetric technique. These small-scale relationships were then averaged to show larger-scale patterns in turbulence across the mudflat and mangrove fringe-forest transition. Although turbulence estimates varied with across-shore position, TKE dissipation was always elevated in the fringe relative to mudflat and forest interior sample sites. The largest dissipation rates ($4.5 \times 10^{-3} \text{ W kg}^{-1}$) were measured as breaking waves propagated over canopies in very shallow water. Dissipation was reduced, but often remained intense ($10^{-5} - 10^{-4} \text{ W kg}^{-1}$) under non-breaking waves at the fringe, likely indicating turbulent generation in pneumatophore wakes. Pneumatophore density was positively correlated with the spatial distribution of TKE dissipation. Turbulence was also correlated positively with wave height and negatively with water depth. Fringe sediments were sandier and less muddy than sediments onshore and offshore, suggesting that the intense turbulence may lead to winnowing of fine-grained sediments at the fringe.

2.1 Introduction

Mangrove forests are characterized by high biological productivity and are known to provide a variety of valuable ecosystem services. Growing in intertidal regions, mangroves' aerial root structures dissipate the energy of waves and currents, fostering an environment that is suitable for their proliferation (Furukawa et al., 1997; Thampanya et al., 2002). In coastal and riverine zones, mangroves can lead to substrate stabilization (McKee & McGinnis, 2002), wave attenuation (Horstman et al., 2012; 2013; Mazda et al., 2006), and the aggradation of sediments to form new landmass (Krauss et al., 2003). Although limited in their global extent, mangrove forests are also regions of rapid carbon burial (Duarte et al., 2005). Today, many mangrove stands are in decline, with total worldwide coverage reduced from 18.8×10^6 ha in 1980 (Wolanski, 2007) to about 13.8×10^6 ha in 2010 (Giri et al., 2011). In many regions, rehabilitation efforts are being undertaken to restore critically affected mangrove forests (Alongi, 2002). Informed planning of

such projects requires an understanding of the hydrodynamics that influence forest growth.

Over large spatial scales (tens to hundreds of meters), flow patterns have been examined around mangrove creeks, rivers and in the nearshore (see: Aucan & Ridd, 2000; Furukawa et al., 1997; Horstman et al., 2013; Wolanski et al., 1980). Several studies have quantified the spatially averaged drag force within mangroves, and bulk parameterizations for drag have been developed (Mazda et al., 1997b, 2005; Vo-Luong & Massel, 2008; Wolanski et al., 1980). At smaller scales, Furukawa & Wolanski, (1996) observed large turbulent fluctuations in water velocity near the prop roots of *Rhizophora* mangroves, but did not quantify the dissipation of turbulence. Instead, simplified numerical models were used (Furukawa et al., 1997) to simulate flow around the roots to explain their observed sedimentation patterns. Much of the present process-based understanding of the small-scale hydrodynamics of vegetated regions comes from flume and numerical studies. However, the extension of this understanding is complicated by the challenge of effectively recreating the geometry and spatial distribution of natural vegetation in the laboratory. The geometric properties and distribution of vegetation are an important factor controlling the development of vegetation-induced turbulent features (Bouma et al., 2007; Nepf, 2012b). These turbulent features, in turn, influence the larger-scale flow patterns that have been observed by previous authors. Although formulations to parameterize vegetated flow and wave interaction have been developed, these have not yet been tested in natural mangrove vegetation.

Many published field studies on the hydrodynamic effects of vegetation density focus on saltmarsh species such as *Spartina* spp. Generally, these experiments demonstrated a negative correlation between vegetation density and canopy flow, and hence turbulence (e.g., Leonard & Croft, 2006; Leonard & Luther, 1995). Stands of cordgrass may vary in stem density (n) from 150 stems m^{-2} to >1800 stems m^{-2} (ϕ) (Leonard & Luther, 1995; Lightbody et al., 2008; Widdows et al., 2008). The frontal area blocking the flow (a) varies from 1 to 7 m^{-1} (this parameter is discussed further in Section 2.2 below) and the fraction of canopy volume occupied by solid stems varies from 10^{-3} to 10^{-2} . Mangrove root morphologies vary between species, resulting in a wide range of recorded root densities. For *Sonneratia* mangrove pneumatophores, n ranges from zero to 150 stems m^{-2} , with basal

diameters often between one and two centimeters. Corresponding a and ϕ values often reach 1 m^{-1} and 0.01 respectively, with higher values observed in particularly dense patches (Krauss et al., 2003; Liénard et al., 2016; Mazda et al., 1997b). While past studies focusing on mangrove vegetation have shown that the increase in mangrove root densities enhances canopy drag and modulates reach-scale flow routing (Horstman et al., 2015; Mazda et al., 1997b), these studies did not focus on small-scale flow variability and turbulence. However, similar studies have been undertaken within canopies of *Spartina* (e.g., Leonard & Croft, 2006; Widdows et al., 2008). We cannot necessarily extrapolate the canopy effects of flexible species such as *Spartina* spp.; mangrove roots are morphologically distinct from other leafy estuarine vegetation and are also relatively rigid. Stem rigidity greatly modifies turbulent dissipation rates, with flexible stems dissipating less energy than equivalent rigid stems (Luhar & Nepf, 2016; Mullarney & Henderson, 2010). Similarly, while flume and modeling experiments have yielded many valuable insights into the nature of vegetated hydrodynamics (e.g., Bouma et al., 2005), field observations are required to examine turbulence under natural conditions, with energetic, directionally spread waves and currents in complex, heterogeneous natural canopies. The need for such work is motivated by the connection between spatially variable turbulent intensity and sediment transport, which ultimately affects marsh morphodynamics (Yager & Schmeckle, 2013; Yang et al., 2015).

It is well established that the addition of vegetation greatly modifies flow fields and turbulence (e.g., Mullarney & Henderson, 2018; Nepf, 1999; Tanino & Nepf, 2008b), which ultimately affects the distribution of sediment within vegetated reaches. Using artificial canopies and flume models to represent *Spartina* tussocks, Bouma et al., (2007) observed that patches of higher density canes promoted sedimentation in their interior while erosion occurred around the edges. These patterns were associated with high turbulence around patch edges, and lower turbulence in their interior. In field studies of *Spartina* marshes, increasing stem densities decreases turbulence and hence sediment transport for flows transitioning between the channel/marsh interface and 20 m inside the vegetation (Leonard & Croft, 2006). However, erosion around the edges of *Spartina* tussocks is pronounced, particularly during higher-energy conditions (Widdows et al., 2008). Ultimately whether or not mangrove roots can provide a similar sheltering effect as saltmarsh plants such as *Spartina* will be determined by local conditions and species

morphology. Mangrove forests have previously been shown to be sinks of allochthonous sediment (Van Santen et al., 2007; Walsh & Nittrouer, 2004; Wolanski, 1992). Specifically, Van Santen et al., (2007) observed variable sedimentation rates in an *Aegiceras corniculatum*-dominated mangrove forest in the Red River Delta (Vietnam). Across a transect of ~100 m, episodic wave events resulted in variable sedimentation and erosion in the fringe, while the forest interior experienced consistent deposition. Data and observations presented in this chapter suggest a similar pattern of sedimentation within a *Sonneratia*-dominated mangrove forest.

Using field observations from a natural mangrove fringe-forest system, the present study examines the broad-scale spatial variability of turbulent energy dissipation. We quantify the relationship between turbulence, the spatial distribution of mangrove pneumatophore vegetation, and other environmental factors such as wave height and water depth. The aim of this study is to link these patterns to understand how mangroves might exert a morphodynamic control over their environment. Measurements were taken from a fringing mangrove forest in the southern Mekong Delta, Vietnam during two different seasons and sixteen individual locations to encompass a wide range of vegetation densities and hydrodynamic conditions. Both the vegetation and velocimetry data presented herein exhibit pronounced spatial variability. We examine the contributions to turbulence from the presence of vegetation and derive patterns in these data through averaging. High turbulent dissipation rates are associated with correspondingly high vegetation density. Based on these measurements and observations of sediment properties, we discuss possible effects on regional morphodynamics.

2.2 Background

Drag forces and turbulent intensity depend on properties of the flow (e.g., the flow velocity, and level of submergence) as well as the vegetation characteristics: the number, size, shape and flexibility of stems (Ghisalberti & Nepf, 2006; Leonard & Croft, 2006; Mullarney & Henderson, 2010; Nepf, 1999; Nepf & Vivoni, 2000). Flows encountering vegetation will form turbulent wakes once the Reynolds number ($Re = Ud/\nu$, where U = water velocity, d = stem diameter, and ν = kinematic viscosity) is greater than about 50 for a single stem and is within the range of 150 – 200 for multiple stems (Kiya et al., 1980; Nepf et al., 1997). Within these wakes,

the energy of waves and currents is converted into turbulent energy. At high Reynolds numbers, the rate of energy conversion is the rate at which work is done by the flow against the canopy drag (Raupach & Shaw, 1982). As defined in many numerical models of steady flows in rigid vegetation (e.g., Nepf, 2012a; Temmerman et al., 2005), the canopy drag force per cubic meter, denoted as F_D , is a function of both the vegetation geometry and the properties of the flow:

$$F_D = a(C_D/2)\rho U^2, \quad (2.1)$$

where C_D is the drag coefficient, $a = nd$ is the frontal area of the canopy per cubic meter (units m^{-1}), and n is the number of stems per square meter of the bed (Nepf, 2004). For complex stems in heterogeneous natural canopies, a varies widely with both elevation above the bed and with horizontal location (Li nard et al., 2016). The drag coefficient is a function of the canopy density and the Reynolds number, and can be accurately predicted by the cross-sectional velocity between stems in a dense array (Etminan et al., 2017). This interaction between stems depends on the solid volume fraction occupied by the vegetation, ϕ , with modifications in the effective drag coefficient found in laboratory experiments for ϕ exceeding about 0.05 – 0.2 (Raupach, 1992; Tanino & Nepf, 2008a). For regular, cylindrical stems, a and ϕ are related by $\phi = (\pi/4)nd^2 = (\pi/4)(ad)$. Although values of ϕ may range from 0 (bare bed) to 1 (solid body), in many natural canopies, $\phi < 0.05$, in which case interactions between stems are typically neglected, when estimating drag (Tanino and Nepf, 2008b). For rigid canopies with high Re and small ϕ , multiplying the drag (Equation 2.1) by the velocity U gives the rate of work done on the flow, which often equals the turbulent dissipation rate. Then dividing by density ρ yields a turbulent energy dissipation rate per kilogram of water $\varepsilon = (C_D/2)aU^3$. Under waves, an additional force proportional to the acceleration must be added to Equation (2.1) (Sumer & Freds e, 1997). However, this additional force is in quadrature with the velocity and therefore does no mean work, so the formula for the dissipation rate is unmodified if averaged over many wave periods.

Finally, the within-canopy velocity U that appears in Equation (2.1) is itself dependent on vegetative drag. In submerged horizontally-uniform canopies, steady mean flows are greatly reduced, relative to velocities above the canopy, for large values of $\lambda = ah_c$, where h_c is the canopy height and λ is the canopy roughness,

defined as the frontal area of canopy elements per unit floor area (Belcher et al., 2003; Nepf, 2012b). In such cases the reduction of intra-canopy flow and turbulence helps to prevent sediment suspension and hence erosion (Nepf, 2004). Conversely, sparse canopies with λ below about 0.1 are characterized by stem-scale turbulent wakes that may locally enhance erosional processes and diminish sediment settling (Nepf, 2012b). These results for steady flows are modified under waves, where within-canopy flows are often forced by fluctuating pressure gradients, in contrast to the shear stresses that force steady flows (Lowe et al., 2005). For waves, the potential sheltering effect of canopies is often controlled not by λ but instead by $\Lambda = aC_D U_w T_w / (4\pi)$, where T_w = wave period and U_w is a typical amplitude of wave-induced velocity fluctuations. For waves with $\Lambda < 1$, as for steady flows with small λ , stems are expected to enhance dissipation and erosional processes (Henderson et al., 2017).

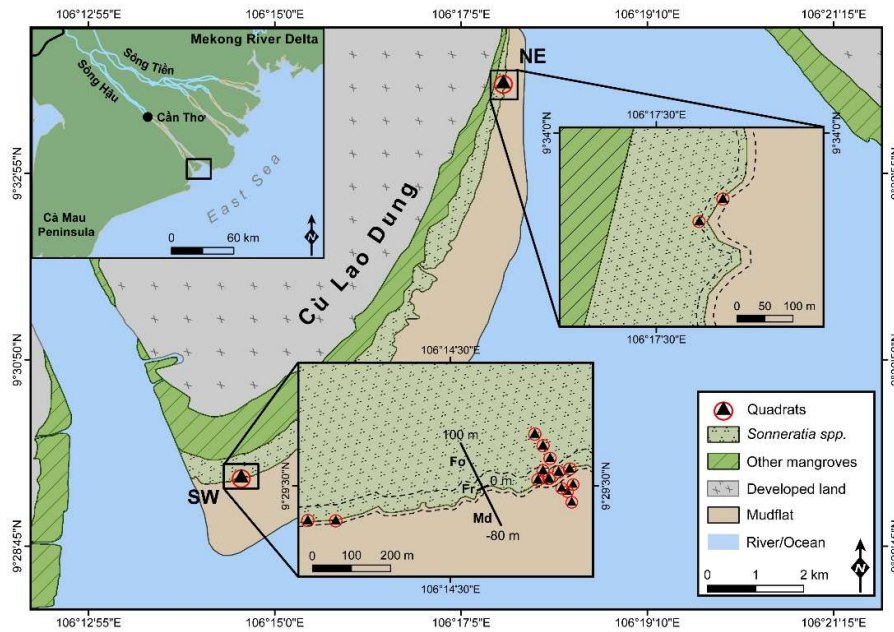


Figure 2.1: Overview map of Cù Lao Dung, located in the Sông Hậu distributary channel of the Lower Mekong Delta. Two main field sites are highlighted, the southwest and northeast (SW and NE), with insets depicting the locations of individual measurement and vegetation survey sites within the mudflat, mangrove fringe and forest. In SW inset, ‘Md’ stands for ‘mudflat’, ‘Fr’ for ‘fringe’ and ‘Fo’ for ‘forest’. Dotted lines in both insets denote the fringe zone of the forest. Vegetation type was digitized to differentiate between *Sonneratia* and other mangroves by comparing maps provided by Bullock et al., (2017), and Google Earth images.

2.3 Field Measurements

2.3.1 Field Site

The study area is located along the southern edge of Cù Lao Dung (approximately 9°30'53.38"N, 106°16'6.4"E) in the southern reach of the Mekong Delta in Vietnam (Figure 2.1). This mid-channel island bisects the Sông Hậu distributary channel of the Mekong Delta as it meets the East Sea (South China Sea). The discharge of the Mekong River is modulated by seasonal monsoons. High-flow is associated with a southwesterly monsoon season during the months of July – December (Wolanski et al., 1998). This season is categorized by consistent rainfall in the delta, relatively calm marine conditions (wave heights and currents) and lighter winds. During this season, sediment discharged from both channels of the Sông Hậu is transported offshore (McLachlan et al., 2017, Fricke et al., 2017). The northeast monsoon season (January – July) is characterized by drier conditions, higher winds and larger waves. During this period, the energetic marine conditions may mobilize offshore sediment, moving it toward Cù Lao Dung through the interaction of river flow, waves and tides (Eidam et al., 2017). Though a combination of sediment supply and physical forcing, the island is prograding in an asymmetric manner. The relatively rapidly prograding southwest corner of the island is characterized by an extensive mudflat and wide mangrove forest that tapers to a shorter mudflat and forest in the northeast. This asymmetry produces differences in the wave climate and the bed slope at each site. Recorded wave heights in the southwest exceeded those of the northeast, while the northeast floods more quickly due to a steeper bed slope (Fricke et al., 2017). At the mouth of the river, the tidal range is ~3 m (Wolanski et al., 1996)

Although much of Cù Lao Dung has been developed for agriculture, an artificial levee separates farmland from a sea-fringing and dense mangrove forest. The higher elevations of the forest interior near the levee are predominantly composed of *Avicennia* spp., and *Aegiceras corniculatum* mangroves and *Nypa fruticans* palms (Hong & San, 1993). The seaward fringe along the southern tip of the island is dominated by the pioneering *Sonneratia* spp., both *Sonneratia alba* and *Sonneratia caseolaris* mangroves (Nardin et al., 2016a). The two main study sites were located within the southwestern (SW) and northeastern (NE) corners of the island (Figure 2.1). All experiments were conducted either on the un-vegetated mudflat, or under

the cover of *S. caseolaris* mangrove trees. Tree density is highest in the seaward fringe region ($x = -10$ m to $x = 20$ m onshore) along the southwest transect (Bullock et al., 2017), and declines with distance inside the forest. Within the seaward fringe, groups of mangrove trees produced a dense and patchy ‘canopy’ of pneumatophore (pencil) roots with diameters on the order of 1 cm. In contrast, the northeast mangrove fringe is predominately sparse, established *Sonneratia* mangroves with substantially larger diameter ($\sim 1.5 - 2$ cm) pneumatophore roots. Particularly dense clusters of these aerial roots were observed adjacent to the mangrove tree trunks. Tree density at this location increased with onshore distance from the fringe (Bullock et al., 2017). Experimental sites were chosen to encompass a range of vegetation and hydrodynamic conditions within areas of the fringe ($x = -10 - 20$ m of the forest edge) and deeper into the forest interior ($x = 20 - 100$ m inside the forest).

2.3.2 Vegetation Sampling

Field measurements were obtained between September – October of 2014 and in March 2015 within the mangrove forest of Cù Lao Dung during a spring-neap transition. Sites were selected by locating clusters of pneumatophores to sample regions within both the seaward mangrove fringe and the forest interior (Figure 2.1). Instruments were deployed in clusters of pneumatophores and were located away from tree trunks to avoid upstream wake effects. Pneumatophores surrounding instruments were then delineated using a 1 m² quadrat. In the SW, eight deployment locations were chosen in the fringe to span the range of observed root densities. Note that a single quadrat was collected in the vegetated fringe seaward of the digitized location of the fringe line, $x = 0$ (see Figure 2.1, SW inset), owing to the ambiguity in the exact location of the ‘fringe’. Due to logistical constraints, fewer deployments were conducted in the forest interior of the SW. Two deployments were also conducted in the seaward mangrove fringe on the NE side of the island.

Vegetation geometry was estimated using the photogrammetric reconstruction method developed by Liénard et al., (2016), which is summarized briefly here. Each quadrat was photographed 55 – 390 times in 360° around the site while varying the pitch angle from ground-parallel to oblique-overhead. Image sets were then processed using the open source structure-from-motion software package Visual

SFM (see: Wu, 2011) to generate a dense 3D point cloud. In addition to resolving pneumatophores, these point clouds allowed for the precise positioning of the Vectrino current meters used to measure turbulence (Figure 2.2b, Section 2.3.3). After editing point clouds in the open-source software CloudCompare to remove features such as the instruments and the quadrat, three-dimensional pneumatophore geometries were reconstructed (Figure 2.2c), using the sector-slice algorithm developed by Liénard et al., (2016). The resultant datasets contained the center point and diameter for every pneumatophore, evaluated every 5 mm along a vertical profile extending from about 2 cm above the bed to the top of the root canopy. To generate vegetation statistics that are representative of drag on the predominantly horizontal (on-site measurements confirm horizontal dominance) near-bed flows, a and ϕ were estimated at the sampling heights (h_v) of the velocity measurements (Table 2.1, Section 2.3.3). To evaluate a within a quadrat, the number of stems that reached h_v were multiplied by the mean root diameter and divided by the quadrat area. Relative errors in a values obtained by this method are usually $< 10\%$ (Liénard et al., 2016). The volume fraction of the vegetation, ϕ , was estimated by summing the enclosed areas of all pneumatophores at h_v , and then dividing by the quadrat area.

2.3.3 Hydrodynamic Observations

After surveying the vegetation, we deployed up to three Nortek Vectrino Profilers (hereafter, Vectrinos) inside each quadrat area as well as a single additional current meter (either a 2 MHz Nortek Aquadopp or a Nortek Vector) near the quadrat (Figure 2.2a). Vectrinos are acoustic instruments that are typically used in laboratory settings to resolve velocity profiles at millimeter resolution (for example, see: Tinoco & Coco, 2014). Field deployments of these laboratory instruments are not common (for an exception, see: Lanckriet & Puleo, 2013). Instrument deployments were arranged at low tide in either ‘fine-scale’ or ‘flats-to-forest’ configurations. For fine-scale deployments, the three Vectrinos were deployed in a single quadrat to resolve the small-scale flow variability. For flats-to-forest deployments, the three Vectrinos were split between three separate quadrats to record conditions synoptically in the mudflat, fringe and forest. For these cases, instrument deployments were typically separated by >40 m (Table 2.1). Each configuration was used for one to two days before instruments were moved and

arranged in a new configuration. Prior to each experiment, instruments were deployed during low tide. Vectrinos were mounted to fixed frames and were deployed within the pneumatophore canopy. Synchronized data from the three Vectrinos were recorded by a single laptop, connected to the instruments by 50 m cables. Data were recorded continuously at 50 Hz. For flood tide cases, Vectrino data collection began just after all three instruments were submerged by the rising tide and continued until just before slack tide. For ebb tide cases, data collection began at high tide and continued until instruments emerged from the water. The co-located Nortek Aquadopps or Vectors were set to record nearly continuously at 8 Hz or 32 Hz, respectively, for the duration of each experiment. Aquadopps sampled at 25 mm vertical resolution over short profile lengths of 0.45 m (SW side) and 0.22 m (NE side). These instruments provided ancillary data such as wave height, current direction and velocity, measured above the pneumatophore canopy. Prior to analysis, Vector and Aquadopp time series were cropped to the length of the corresponding Vectrino deployments. Instrument deployment configurations and the Vectrino record durations are listed in Table 2.1, ordered by their across-shore distance from the mangrove fringe.

Table 2.1: The locations of quadrat surveys and hydrodynamic measurements collected. Quadrats are organized by their cross-shore location. Each vegetation survey was accompanied by hydrodynamic measurements collected by the listed instruments deployed. ADCP refers to a Nortek Aquadopp, Vectrino refers to the Nortek Vectrino Profiler, and ADV refers to a Nortek Vector. Quadrats with the designation ‘a’, ‘b’ and ‘c’ were deployed in the same location and multiple vegetation surveys were collected at this site. Synoptic ‘tidal flats-to-forest’ experiments were conducted in three locations on the same days. Measurement heights were measured prior to conducting the experiment and are relative to the initial bed levels of the experiments. Deployment durations are rounded to the nearest half hour.

Location	Date	Start time (HH:MM)	Deployment Duration	Quadrat Name	Across-Shore Distance (m)	Instruments Deployed	h_v (m)
SW	29/09/2014, 30/09/2014	15:23, 06:20	3 hours, 3.5 hours	Mudflat	-60.96	ADCP, 1 Vectrino	0.11
SW	05/03/2015, 06/03/2015	13:00, 13:40	3 hours, 3 hours	Mudflat	-50.54	ADCP, 1 Vectrino	0.09
SW	11/03/2015, 12/03/2015	15:20, 07:00	3 hours, 3 hours	Mudflat	-50.35	ADCP, 1 Vectrino	0.02
SW	27-09-14	14:00	3 hours	Mudflat	-37.17	ADV, 3 Vectrinos	0.06
SW	28-09-14	14:40	3 hours	Q1	-11.48	ADCP, 3 Vectrinos	0.04
SW	29/09/2014, 30/09/2014	15:23, 06:20	3 hours, 3.5 hours	Q2	0	ADCP, Vectrino	0.04
SW	07/03/2015	14:00	4 hours	Q3a	0	ADV, 3 Vectrinos	0.02
SW	08/03/2015	14:20	5 hours	Q3b	0	ADV, 3 Vectrinos	0.21
SW	10/03/2015	14:50	3 hours	Q3c	0	ADV, 3 Vectrinos	0.51
SW	05/03/2015, 06/03/2015	13:00, 13:40	3 hours, 3 hours	Q4	0.54	ADCP, 1 Vectrino	0.09
SW	11/03/2015, 12/03/2015	15:20, 07:00	3 hours, 3 hours	Q5	1.37	ADCP, 1 Vectrino	0.02
SW	24-09-14	12:13	1 hours	Q6	4.95	ADCP, 3 Vectrinos	0.10
SW	25-09-14	12:45	2.5 hours	Q7	5.92	ADCP, 3 Vectrinos	0.04
SW	26-09-14	13:30	3 hours	Q8	6.16	ADCP, 3 Vectrinos	0.04
NE	03/10/2014	6:30	6 hours	Q9	11.70	ADCP, 3 Vectrinos	0.07
NE	13/03/2015, 14/03/2015	18:50, 07:00	5 hours, 6 hours	Q10	24.52	ADCP, 3 Vectrinos	0.03
SW	29/09/2014, 30/09/2014	15:23, 06:20	3 hours, 3.5 hours	Q11	49.39	ADCP, 1 Vectrino	0.11
SW	11/03/2015, 12/03/2015	15:20, 07:00	3 hours, 3 hours	Q12	72.64	ADCP, 1 Vectrino	0.02
SW	05/03/2015, 06/03/2015	13:00, 13:40	3 hours, 3 hours	Q13	93.76	ADCP, 1 Vectrino	0.04

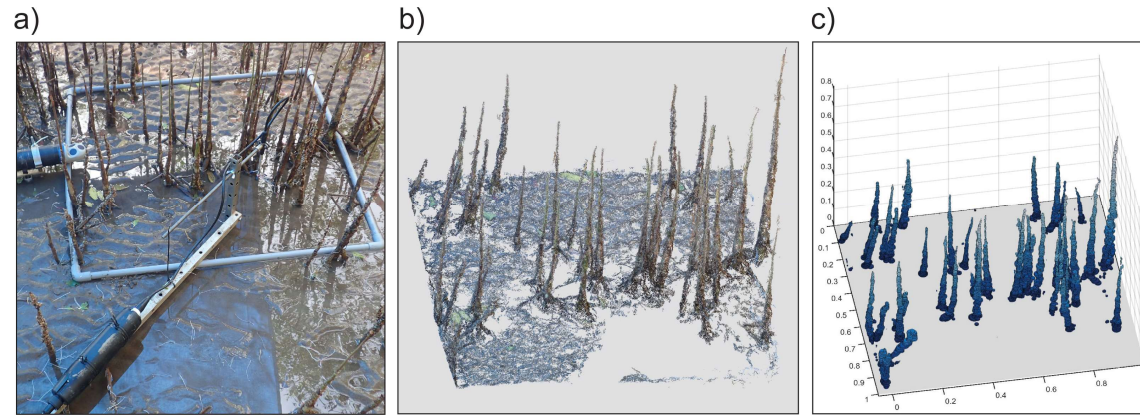


Figure 2.2: (Panel a) a typical instrument deployment around one of the vegetation survey sites on the SW transect within the mangrove fringe. (Panel b) 3D point cloud generated by the structure-from-motion software created from approximately 200 photographs of the quadrat scene. (Panel c) Pneumatophores represented as 3D shapes with circular horizontal cross-section, and with elevation-dependent diameter and location, fitted to the 3D point cloud.

2.4 Data Analysis

Aquadopp velocity data were post-processed by first removing data with low correlation coefficients. Bins that exhibited phase-wrapped velocities (see Lohrmann & Nylund, 2008) were removed and gap filled using data with the same spectral characteristics. Vector and Vectrino velocities were similarly filtered to remove data with low correlations and signal-to-noise ratios, then outlier velocity spikes were identified, removed, and gap filled by interpolation following the routine outlined in Goring & Nikora, (2002). For each Aquadopp and Vector pressure record, significant wave heights, H_s and peak periods T_p , were estimated every 10 minutes, calculated from measured 0.05 – 1 Hz pressure fluctuations, using linear wave theory to account for frequency-dependent depth attenuation ($T_p = 1/f_p$ where f_p is the frequency band with the greatest energy; H_s estimated as 4 times the standard deviation of the surface elevation). For details see: Wiberg and Sherwood, (2008). From the Vectrino data, time averaged velocities were produced for every depth bin using the following method. Vectrino velocity records were first split into segments containing $n = 1500$ samples (30 seconds) using a 30% overlap between segments. Velocities were rotated into across-shore (u), along-shore (v) and vertical (w) components. Finally, mean horizontal velocities were computed. To account for the variation in current direction with cross-shore position, horizontal velocity magnitudes were calculated, $U = \sqrt{u^2 + v^2}$, and then were time-averaged, to produce one velocity magnitude per segment, per depth bin. Additionally, turbulence statistics (the dissipation rates) were calculated from the same original Vectrino velocity profiles using the method outlined in Section 2.4.1, below.

2.4.1 Dissipation rate of turbulent kinetic energy

The Turbulent Kinetic Energy (TKE) dissipation rate was calculated from vertical velocity profiles recorded at each Vectrino deployment location using the structure function method of Wiles et al., (2006). The structure function has previously been employed to calculate dissipation rates using Vectrino Profiler measurements (Lanckriet & Puleo, 2013). Using this method, turbulence estimates can be readily derived from differences between velocities measured at several closely spaced locations (“bins”) along the sampled profile. This differencing technique filters out

large-scale variability in the velocity field, such as wave oscillations, permitting the ability to focus on small-scale turbulent eddies.

First, Vectrino velocity records were split into segments containing $n = 1500$ samples (30 seconds). At every elevation z along the measured profile, 30-second time series of the vertical velocities were linearly detrended to yield a 50 Hz time series, $w(z)$. The second-order longitudinal structure function $D(z,r)$ is then:

$$D(z,r) = \overline{[w(z) - w(z+r)]^2} \quad (2.2)$$

where the overbar denotes a time average. Therefore, $D(z,r)$ is the variance of the difference between two velocities separated by a distance r , with the first velocity at the along-beam position z . This structure function represents the intensity of small-scale velocity variability, which is dominated by turbulence. From Kolmogorov's theory, for scales of r within the inertial subrange,

$$D(z,r) = C_v^2 \varepsilon^{2/3} r^{2/3}, \quad (2.3)$$

where $C_v^2 = 2.0$, is an empirical constant (Pope, 2000). Therefore, whereas D is a function of separation distance r , the turbulent dissipation rate ε is a single scalar characterizing the intensity of small-scale turbulence. To estimate ε , the measured $D(z,r)$ is fitted by linear regression to the equation

$$D(z,r) = 2\sigma_B^2 + Ar^{2/3} \quad (2.4)$$

where the fitted slope A is related to dissipation by $A = C_v^2 \varepsilon^{2/3}$, and the fitted offset $2\sigma_B^2$ accounts for instrument noise, and is otherwise assumed to be independent of r (Wiles et al., 2006). This fitting of Equation (2.4) was performed for $r = 1 - 5$ mm, yielding ε estimates every 1 mm along a profile length of 30 mm (which is the length of the Vectrino profile minus r_{max}). The maximum lag of 5 mm was chosen as a compromise between the aim of eliminating wave motions (best achieved using small r_{max}) and the goal of obtaining stable estimates of slope (provided by larger r_{max}). To examine the sensitivity of the structure function to r_{max} , a range of maximum lags from 4 to 10 mm were tested. Results show small increases in ε up to a lag distance of 6 mm, while larger lags produce smaller estimates of ε and poor fits to Equation (2.4). The TKE dissipation rate estimates derived from these two

vertical velocity estimates were averaged together to create one estimate per 30-second interval for the entire duration of the Vectrino deployment.

When Vectrinos were deployed very near the bed (≤ 0.06 m, 21% of deployments) velocity bins whose elevation was less than 10% of the range from the transducer to the bed were excluded to eliminate measurements contaminated by sidelobe reflections from the bed. Furthermore, any bins whose height was less than that of the wave boundary layer were also excluded from the analysis. Since the structure function employs a ‘center differenced’ approach, bins +2 mm (towards the bed) from any center bin near the boundary layer was also excluded. Following Fredsøe & Deigaard, (1992), the wave boundary layer thickness was estimated as,

$$\frac{\delta_R}{k_N} = 0.09 \left(\frac{A_\delta}{k_N} \right)^{0.82}, \quad (2.5)$$

where the wave orbital excursion $A_\delta = U_w/\omega_r$, the wave velocity amplitude is U_w (Appendix A) the wave radian frequency is ω_r , and the Nikuradse roughness length k_N was estimated as the median grain diameter of sediments collected from near the instrument (Fricke et al., 2017). Of the experiments where the Vectrinos were within 0.06 m of the bed, velocity samples removed for being within the wave boundary layer account for no more than 10% of all samples.

Where possible, turbulence estimates were extracted from the middle bin in the profile (where the signal-to-noise ratio was maximum). When Vectrinos were near the bed, and the middle bin was too close to the bed to provide useful data, turbulence estimates were selected from either bin 5, or the lowest bin above the wave boundary layer. Measurement heights h_v at which turbulence estimates were obtained are listed in Table 2.1. Turbulence estimates and time-averaged velocity magnitudes were compared with the root densities estimated at the same height h_v .

2.4.2 Tide Intervals and Quadrat Subsampling

Although the 1 m² quadrats provide representative samples of the seaward fringe and forest root densities, they do not resolve the sub-meter variability within the quadrats themselves. In most cases, the Vectrinos were placed inside the quadrat adjacent to a cluster of roots a few tens of centimeters across. Under mean currents, patches on the order of this diameter are expected to generate stem-wakes

downstream at a distance of 2 – 3 times the patch diameter (Nicolle & Eames, 2011; Zong & Nepf, 2012). Additionally, wave orbital displacements are expected to advect turbulence a few tens of centimeters from the pneumatophores. Since hydrodynamic conditions such as the water velocity and wave height depend on the level of tidal inundation, different stem clusters around the Vectrino may have been responsible for generating wake turbulence throughout the tide. To improve estimates of the effective densities that generate turbulence within the quadrat boundary, a subsampling method was used to focus on the clusters of roots most likely to have generated stem-wake turbulence. Vegetation density was measured within small 20-by-20 cm ‘quadrats’ upstream of the instruments.

To examine the dependence of turbulence on the level of tidal inundation, the pressure time series from the co-located velocimeters (Aquadopps or Vectrinos) were divided into four sections of equal length (Figure 2.3), referred to as: LL, ML, MH and HH for low tide, medium-low, medium-high and high tide, respectively. For fine-scale deployments, the start of the LL subsection was defined as approximately the same tidal depth (0.42 m on average) between the individual experiments. For the tidal flats-to-forest experiments, the LL stage began as soon as all three Vectrinos were submerged. Typically, these requirements meant the LL stage began

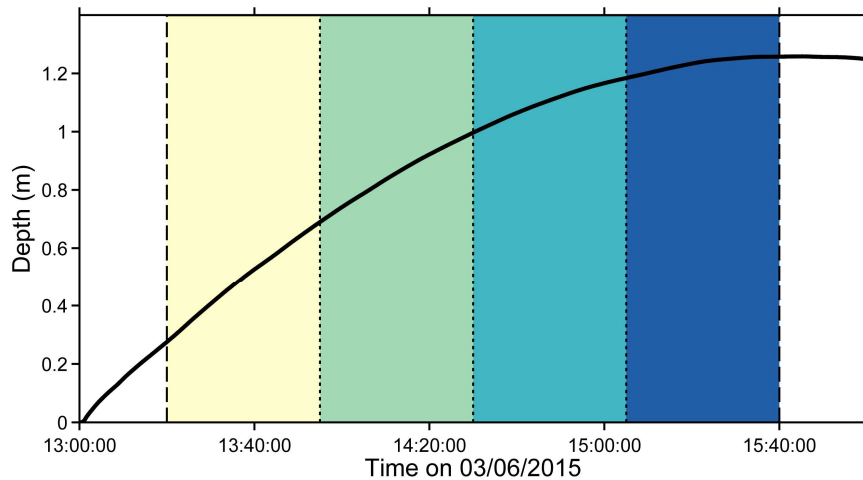


Figure 2.3: Example tidal divisions for low (LL), medium-low (ML), medium high (MH) and high (HH). Tidal sections are of equal length, beginning after the instruments are submerged then finishing at slack tide. Colors correspond to the same tidal stages in the subsequent figures.

approximately 20 – 30 minutes after the arrival of the incoming flood tide. Averaged across all experiments, tidal subsections correspond to water depths of 0.54, 0.82, 1.0, and 1.14 m for LL, ML, MH and HH, respectively.

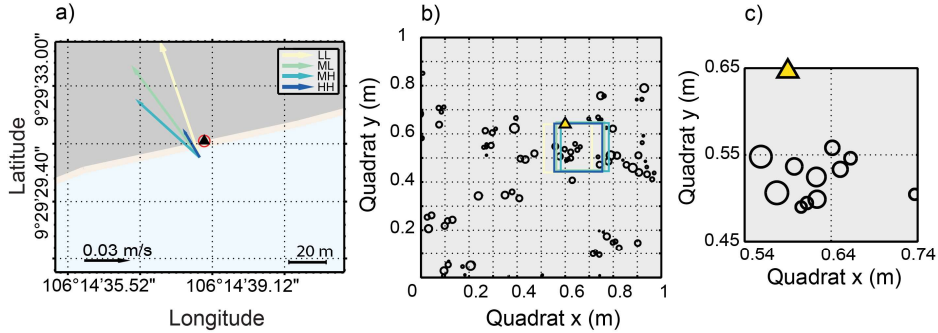


Figure 2.4: (Panel a) Current vector map showing both the location of the collocated instrument and the quadrat deployment (circle and triangle). (Panel b) Quadrat reconstruction of pneumatophore diameters at the height slice of the velocity measurements. The triangle represents the location of the Vectrino Profiler. Squares denote the subsampling process according to the arrows in panel a. (Panel c) a single 20 cm² subsample of the vegetation proximal to the Vectrino Profiler. This particular example is the dark blue box (HH) in panel b.

For every subsection of every tide, the “upstream” direction was defined by averaging Vector or Aquadopp velocities over the subsection (Figure 2.4a). Quadrat reconstructions were rectified so the upstream side was parallel to the coastline. Then, 20 cm quadrats were centered over a point directly upstream of the Vectrino (Figure 2.4b). Vegetation statistics (n , d and a and ϕ) were calculated for roots within the 20-cm quadrats (Figure 2.4c) as outlined in Section (2.3.2). For fine-scale experiments where the three Vectrinos were deployed in the same 1 m² quadrat (not shown), three separate 20-cm quadrats were used, one upstream of each instrument.

Finally, a dataset of vegetation characteristics (n , d , a and ϕ) at the height of each Vectrino was generated from all 20-cm quadrats for each tidal stage. Similar datasets were created for the environmental factors (tidal depth, and H_s) and the fine-scale measurements (TKE dissipation rate, velocity magnitude) by averaging the measurements that corresponded to times within each tidal stage. For cases where the ebb tide was recorded, averaged hydrodynamic values were taken at the same tidal depths of the flood tide values. The result was four datasets for each tidal stage, each containing a single value of vegetation characteristics or hydrodynamic conditions for every subsample. This averaging by tidal stage will be used to

summarize trends across the range of conditions encountered between sites and across seasons.

2.5 Results

2.5.1 Hydrodynamic and vegetation observations

During the September 2014 experiment, water depths measured at high tide in the southwest ranged from 1.3 m on the mudflat to 0.7 m inside the forest (location Q13). Measured peak wave periods varied from 2 to 3 seconds, and significant wave heights ranged up to 0.4 m. Wave-averaged velocities just above the wave boundary layer (3 – 11 mm above the bed) on the mudflat, fringe, and forest interior respectively reached 0.16 ms^{-1} , 0.14 ms^{-1} and 0.13 ms^{-1} . Turbulent dissipation rates ranged from 3.1×10^{-6} to $3.2 \times 10^{-5} \text{ W kg}^{-1}$ on the mudflat, 3.7×10^{-6} to $8.9 \times 10^{-4} \text{ W kg}^{-1}$ at the fringe, and 2.8×10^{-6} to $2.6 \times 10^{-5} \text{ W kg}^{-1}$ in the forest. In March 2015, water depths were similar to those in September, but waves were more energetic, with periods ranging between 3 and 6 seconds, and significant wave heights ranging up to 0.72 m. Wave-averaged velocities just above the boundary layer reached 0.17 m s^{-1} on the mudflat, 0.16 m s^{-1} at the fringe, and 0.12 m s^{-1} in the forest. Spatial variability of turbulence resembled that seen during September, with the fringe sites producing the largest dissipation rates of $3.7 \times 10^{-4} \text{ W kg}^{-1}$ during one of the synoptic flats-to-forest experiments (Q4), and $4.5 \times 10^{-3} \text{ W kg}^{-1}$ during one of the fine-scale experiments (Q3a). Oblique shoreward wave-averaged currents were observed during the rising tide. Large-scale flow patterns are summarized by Mullarney et al., (2017a), Bryan et al., (2017), and Fricke et al., (2017). The particular example highlighted in Figure 2.5 is the experiment conducted during the flood tide of March 6th, Mudflat ($x = -50.54 \text{ m}$), Q4 and Q13 (Table 2.1). Although current velocities and turbulence between the three regions varied in intensity with wave height, the patterns shown in this figure were consistent for all the other flats-to-forest experiments. Onshore velocities over the mudflat (Figure 2.5a) declined, and even reversed, as flood tide proceeded (beginning around 14:45). In the vegetated regions (Figures 2.5b – c), velocities were directed onshore throughout the flood tide. Turbulence (Figure 2.5d – f) was most intense at the fringe, where dissipation exceeded $3.0 \times 10^{-4} \text{ W kg}^{-1}$ (Figure 2.5d). Dissipation over the mudflat was less intense than in the fringe, although short ‘hotspots’ of intense turbulence were still observed (Figure 2.5e). Within the forest, turbulence measurements between the

synoptic experiments were variable in intensity. In this particular example, dissipation rates did not exceed $2.5 \times 10^{-4} \text{ W kg}^{-1}$ and importantly, also depict lower-intensity turbulence compared to the other two sites. Figures 2.5f and 2.5i were of the furthest experiment inshore of the fringe, Q13. Shortened time series of dissipation (Figures 2.5g – i) show distinct hotspots of turbulence generated by the remnants of passing breakers (Figure 2.5g) and turbulent wake structures (Figures 2.5h and 2.5i) generated within mangrove root canopies.

In the northeast, seasonal patterns in the hydrodynamic measurements resembled those observed in the southwest. Water depths in the fringe were similar between seasons (up to 1.6 m and 1.75 m at high tide for September and March respectively). Larger peak periods (2 – 5 seconds compared with 1.5 – 3 seconds) and waves (up to 1.2 m compared with 0.4 m) were recorded in March compared to September.

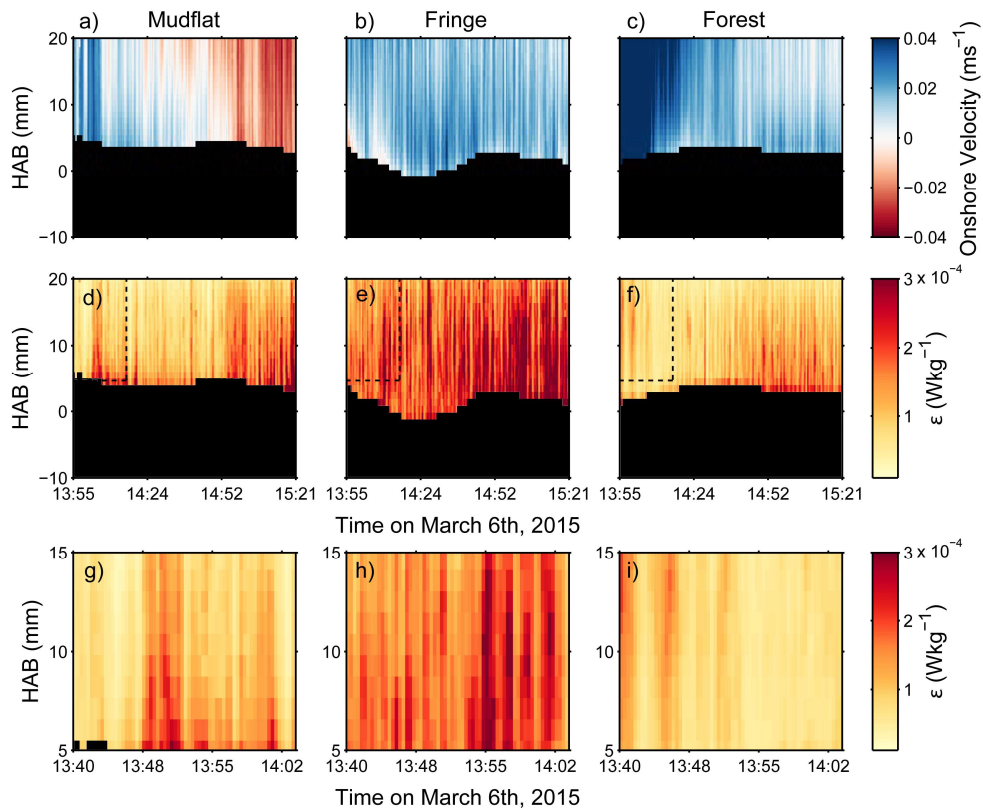


Figure 2.5: Vertical profiles of currents and turbulent dissipation during 30 minutes on March 6th (HAB = ‘Height Above Bed’). Panels (a–c): Onshore current velocities measured at mudflat (a), fringe (b) and forest (c) locations. Raw velocities were averaged using a 30 second window and a 30% overlap, removing wave-frequency flows. Below-bed values and values corresponding to the wave boundary layer, have been removed (in black). (Panels d–f) TKE dissipation rates for the mudflat (d), fringe (e) and forest (f). Dissipation rates were calculated using a 30 second window of vertical velocities, per depth bin. Similarly to (a–c) below-bed and wave boundary layer values have been excluded (in black). Panels (g–i) show detailed view of times and elevations bounded by dashed boxes in (d–f).

Table 2.2: Pneumatophore survey statistics. All values reported (excluding n and h_c) are from the height of the corresponding velocity measurement, h_v . Unless explicitly stated in the column header, values are reported for the 1 m² quadrats. Values of minimum and maximum a (a_{min} and a_{max} , respectively) are given for the 20 cm² quadrats.

Location	Quadrat Name	n	h_c (m)	d (cm)	a (m ⁻¹)	λ	ϕ	20 cm ² , a_{min}	20 cm ² , a_{max}
SW	Mudflat	0	0	0	0	0	0	0	0
SW	Mudflat	0	0	0	0	0	0	0	0
SW	Mudflat	0	0	0	0	0	0	0	0
SW	Mudflat	0	0	0	0	0	0	0	0
SW	Q1	81	0.49	1.1	0.77	0.38	8.0E-03	1.45	1.50
SW	Q2	166	0.36	1.2	1.06	0.38	1.3E-02	1.38	2.32
SW	Q3a	66	0.64	2.0	1.17	0.75	2.4E-02	1.97	6.24
SW	Q3b	62	0.54	1.6	0.47	0.25	6.2E-03	0	2.71
SW	Q3c	61	0.57	0.6	0.04	0.02	2.7E-04	0	0.76
SW	Q4	102	0.82	2.0	1.06	0.87	1.8E-02	1.70	4.15
SW	Q5	45	0.56	1.2	0.49	0.27	5.0E-03	0.45	1.28
SW	Q6	139	0.55	1.1	0.76	0.42	7.5E-03	0	2.31
SW	Q7	110	0.37	0.7	0.65	0.24	4.3E-03	0	0.51
SW	Q8	116	0.41	1.1	0.96	0.39	1.0E-02	2.01	2.01
NE	Q9	95	0.49	1.4	0.97	0.47	1.3E-02	0.17	0.54
NE	Q10	77	0.55	1.5	0.84	0.46	1.2E-02	0.22	1.99
SW	Q11	87	0.35	1.0	0.23	0.08	1.9E-03	0	0.30
SW	Q12	84	0.27	1.4	0.93	0.25	1.3E-02	0.47	1.33
SW	Q13	37	0.21	0.6	0.10	0.06	8.5E-04	0.12	0.98

As there were no flats-to-forest experiments conducted in the northeast, we cannot compare mudflat, fringe and forest environments. Averaged near-bed velocities in the fringe reached $1.1 \times 10^{-2} \text{ m s}^{-1}$ and 0.1 m s^{-1} , and turbulent dissipation ranged from $3.7 \times 10^{-7} - 1.3 \times 10^{-4} \text{ W kg}^{-1}$ and $1.6 \times 10^{-6} - 3.0 \times 10^{-4} \text{ W kg}^{-1}$, in September and March, respectively. These values of dissipation are comparable to moderate dissipation values recorded in the fringe at the southwestern site.

Vegetation surveys showed high spatial variability in pneumatophore root densities between the quadrat sample sites (Table 2.2). High-density patches of pneumatophores occur when the lateral runner roots of two (or more) nearby mangroves intersect, creating root clusters near the point of intersection. Pneumatophore canopies are less dense between these clusters, leading to a heterogeneous patchwork of mangrove vegetation. In the southwest, higher tree densities within a roughly 20-meter-wide band along the seaward forest fringe produced a dense but patchy canopy of pneumatophore roots (often $n > 100$ pneumatophores per m^2). Here, average root diameters varied between 1 and 2 cm.

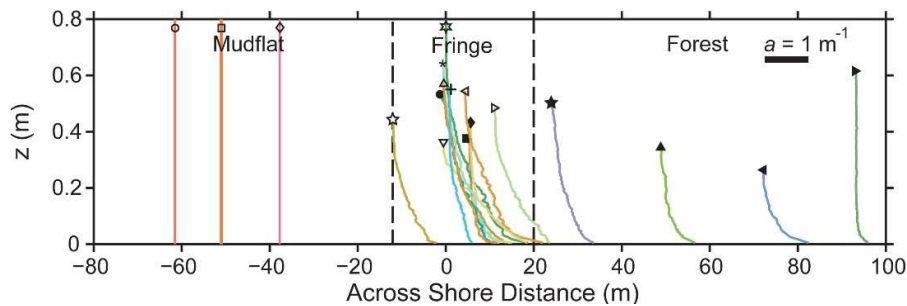


Figure 2.6: Profiles of the frontal area density as a function of height above the bed, $a(z)$. Symbols on the un-vegetated mudflat represent surveys without pneumatophores ($a = 0 \text{ m}^{-1}$). The black bar shows a unit of 1 m^{-1} for reference. Quadrat locations (Tables 2.1 and 2.2) are denoted by symbols: open circle, square and diamond: mudflat deployments; open five-pointed star: Q1; cross: Q2; triangle: Q3a; asterisk: Q3b; closed circle: Q3c; closed square: Q4; downward-facing triangle: Q5; six-pointed star: Q6; closed diamond: Q7; left-pointing triangle: Q8; right-pointing triangle: Q9; closed five-pointed star: Q10; closed triangle: Q11; closed left-pointing triangle: Q12; closed right-pointing triangle: Q13.

Canopy heights generally decreased with distance inside the forest, with taller roots measured at the forest fringe (up to 0.82 m) compared to the forest interior (up to 0.61 m, a special case discussed below). In relatively limited sampling of northeast vegetation, a wider range of diameters (1 – 4 cm) was observed but with fewer ($n < 100 \text{ m}^{-2}$) pneumatophores (Table 2.2, Q9, Q10). Vertical profiles of the frontal area density $a(z)$, which plays a key role in drag parameterizations (Equation 2.1), are summarized in Figure 2.6. In general, the frontal area density decreased with increasing z . An anomalous survey at $x = -93.76 \text{ m}$ (Q13) shows a low-density, short canopy near the bed, with a single tall member that brought the max canopy height to around 0.6 m. Excluding this peculiar pneumatophore, both canopy density and canopy height decreased with distance landward in our survey sites.

One possible explanation for the pattern of decreasing canopy height with landward distance could be the level of sediment accumulation between the fringe and forest. The across-shore profile of the southwest increased linearly in elevation from mudflat to mangrove forest (Bryan et al., 2017). We observed signs of erosion near the bases of pneumatophores in the fringe during March (Figure 2.7a). In contrast scour was not observed around the pneumatophores of the forest interior (Figure 2.7b). Moreover, fringe sediments contained more sand, and less mud, than the forest interior sediments. Evidence provided in the following section suggests that elevated turbulence within the fringe may influence the scour around pneumatophores and account for these observations.

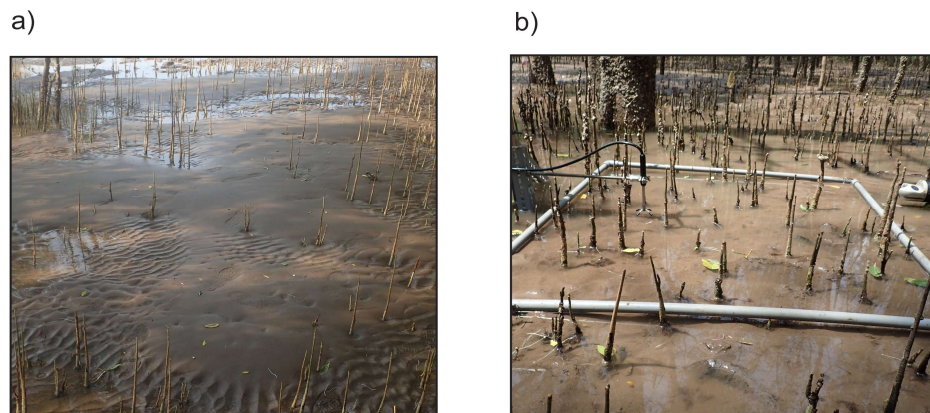


Figure 2.7: (Panel a) Fringe location showing pronounced erosion near pneumatophores (e.g. scour pits around small clusters of stems in the middle of the photo). (Panel b) Forest location, 94 m landward of the fringe, with no clear scour around pneumatophores.

2.5.2 Spatial Trends

Figure 2.8 summarizes the across-shore variability of TKE dissipation, pneumatophore frontal area density, and wave height. To create this figure, all data from all Vectrino deployments were combined and then binned by the across-shore location. The data presented in this figure are from different across-shore locations that were often not contemporaneous. Locations of high dissipation also tended to be locations of high vegetation density (compare Figures 2.8a and 2.8b). The highest turbulent dissipation rate ($4.5 \times 10^{-3} \text{ W kg}^{-1}$) occurred during the low-tide stage (LL) at the fringe (yellow triangle at 0 m across-shore, Figure 2.8a), coincident with the peak of vegetation density (Figure 2.8b). Turbulence was also elevated at other positions in the fringe. The highest dissipation rates measured on

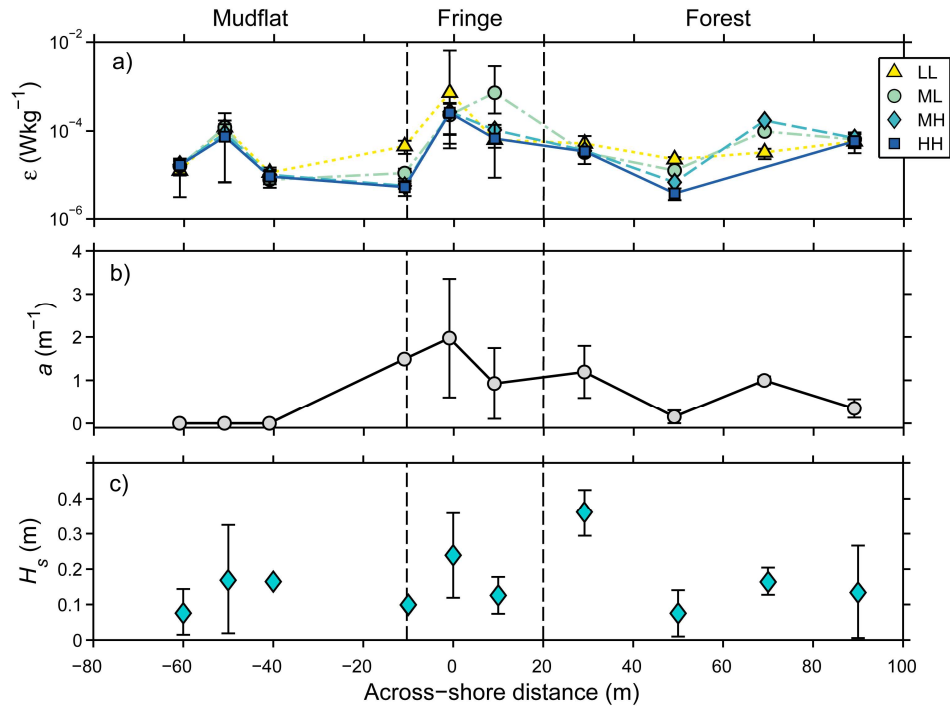


Figure 2.8: Turbulent dissipation rates (Panel a), vegetation frontal area density (Panel b) and significant wave height (Panel c), with observations from all deployments binned at 10 m cross-shore intervals to emphasize spatial variability. Symbols and error bars respectively represent the mean and standard deviation of all observations within a 10-m bin. Panel (a): TKE dissipation, shown separately for each tidal stage. Panel (b): vegetation frontal area profiles surveyed at low tide, with values corresponding to current meter elevations presented. Panel (c): Significant wave heights, with all tidal stages combined. Error bars depict the range of H_s over the four tidal stages.

the mudflat, at the $x = -50$ m across-shore position, exceeded the dissipation measured at several of the forest interior sites (this case is discussed in Section 2.6.1). The highest dissipation rates in the forest interior were measured at the $x = 70$ m, where the pneumatophore canopy was relatively dense. At most vegetated locations, dissipation was maximum early in the rising tide (LL or ML). The exception was the dissipation hotspot at the $x = 70$ m, where dissipation was maximum at MH. In general, dissipation rates were diminished inside the forest relative to the fringe.

In addition to the dependence on vegetation density discussed above, dissipation was also correlated with other environmental factors such as the significant wave height (Figure 2.8c). Comparison between Figure 2.8a and 2.8c shows inconsistent correlation between wave heights and dissipation rates. Linear regression between values of H_s in each tidal stage and the corresponding dissipation rates confirms a significant but weak correlation between these measurements at each deployment position (r-squared: 0.29, p-value < 0.01). Since measurements were not synoptic, this weak correlation may have resulted from a timing (i.e., tidal stage) dependency in the variables. To conduct a more systematic examination of the dependence of TKE dissipation on vegetation density, other vegetation parameters (h_c , n , d and a), significant wave height, and the other environmental variables (velocity magnitude and tide depth), a stepwise multiple linear regression model for all quadrats was used. Each quadrat was relatively representative of the hydrodynamic climate and canopy density at each location, as care was taken to space the synoptic measurements >40 m apart. For the other experiments, quadrats (and instruments) were deployed in different regions of the fringe and forest on different days to capture the variability of these conditions at each position. Model results suggest a significant tidal variability in the dependence of turbulence on vegetation density and other environmental factors. At the lowest tide stage (LL), the significant wave height (H_s), water depth (h), normalized instrument height to water depth (h_i/h) and a collectively explain 50% of the variance in the TKE dissipation rate ($F = 11.8$; p-value < 0.01), with H_s as the most important predictor of the response in turbulence (p-value < 0.01). Similarly, at mid-low tide (ML), both H_s and a combined explain 31% of the variance in turbulence ($F = 7.59$; p-value < 0.01). Unlike the lowest tide stage, the mid-low tide (Figure 2.3) model shows the vegetation density a as being the most significant predictor of the response in turbulence (p-value < 0.01). For

both the mid-high (MH) and high (HH) tide models, a was the only variable significantly correlated with turbulence, explaining 24% and 13% of the variance ($F = 16.2$; p -value < 0.01 and $F = 7.32$; p -value = 0.01), respectively. In summary, dissipation rates decreased with increasing water depth, and increased with increasing significant wave height and vegetation density. From Equation (2.1), the drag force and therefore the turbulent dissipation will increase with both flow speed and vegetation density, so these trends are not unexpected. The particular importance of significant wave height during the low tidal stages is also as expected, because larger waves in shallow waters generate higher flow speeds. Many of the r^2 values quoted above are not especially high, likely because turbulence by its nature is intermittent, varies over many orders of magnitude, and is highly spatially and temporally variable. Averaging data was necessary to derive any patterns in turbulence, particularly over the spatial scales (up to 100 m) and limited temporal scales (over half a tidal cycle) considered here.

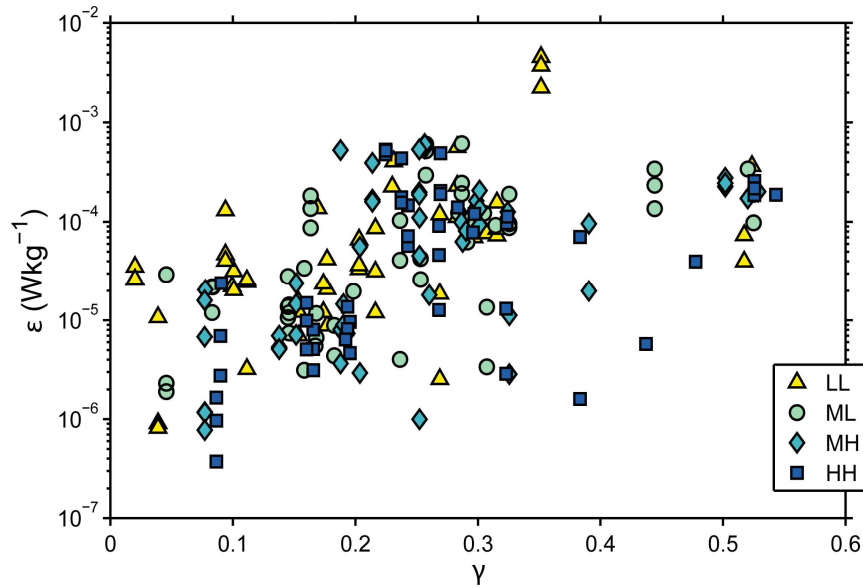


Figure 2.9: Dissipation rate (ϵ) versus wave breaking parameter ($\gamma = \text{wave height/water depth}$) for all four tidal stages. Each point represents ϵ and γ for a single measurement location, averaged from the start to the end of a single tidal stage. Most points fall below $\gamma < 0.3$ indicating minimal breaking, so that wake-induced turbulence provides the most likely source for high turbulent dissipation rates. For $\gamma > 0.3$, wave breaking likely contributes turbulence.

During more quiescent periods (September), minimal wave breaking was observed except for occasional wind-generated whitecapping over the tidal flats. The more energetic conditions of March brought breakers inside the fringe, and occasionally

into the forest. Depending on the frequency of breaking over the instrument sites, breaker-injected turbulence may have contributed significantly to the measured dissipation rates. The wave breaking parameter, γ , defined by $\gamma = H_s/h$, is often used to determine the probability of shallow water breaking. Breaking is common for γ exceeding 0.5, but rare for $\gamma < 0.3$ (e.g., Equation (20) of Thornton & Guza, (1983), with their fitted power law, suggests 50% of waves break for $\gamma = 0.5$, but only 6.5% break for $\gamma = 0.3$). To assess the importance of breaking to turbulence observations, γ and ε are compared in Figure 2.9. Consistent with visual observations of breaking, cases with $\gamma > 0.3$ were observed. For example, the largest dissipation rates ($4.5 \times 10^{-3} \text{ W kg}^{-1}$, Figure 2.8a) were recorded during the LL tidal stage when $\gamma = 0.36$, suggesting a possible role for wave-injected turbulence within the dense canopy at this position (Figures 2.6 and 2.8b). High dissipation was also measured during the subsequent tidal stages under breaking conditions ($\gamma > 0.5$) as expected. Nevertheless, high dissipation rates were also observed in the numerous cases with minimal breaking ($\gamma < 0.3$). For example, breaking was minimal ($\gamma < 0.3$) for most cases with dissipation in the range 10^{-5} to $10^{-3} \text{ W kg}^{-1}$. Therefore, many cases of intense turbulence cannot be explained by wave breaking. We attribute these high turbulence levels in non-breaking cases to canopy drag.

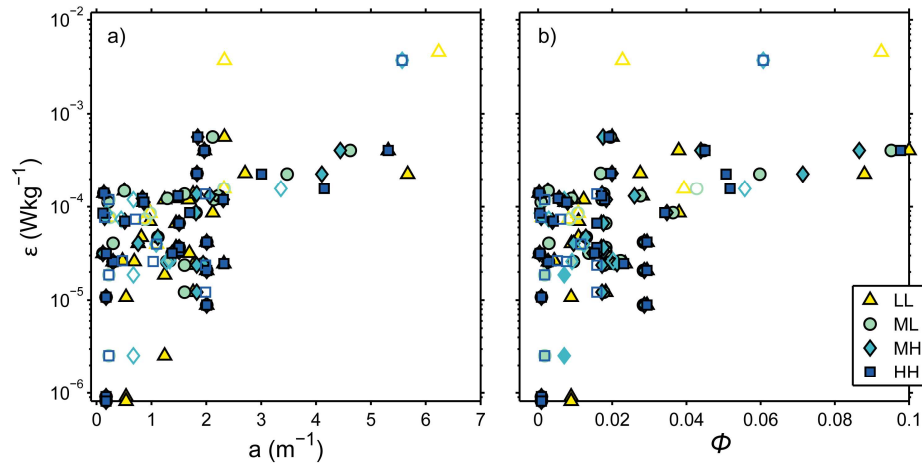


Figure 2.10: TKE dissipation rate (ε) versus vegetation frontal area (a) (Panel a) or solid volume fraction ϕ (Panel b) for 20 cm^2 quadrat subsamples. Open symbols correspond to values of $\gamma > 0.3$, closed symbols correspond to cases with $\gamma < 0.3$ (i.e. cases with minimal breaking).

Finally, as expected for turbulence produced by canopy drag, the turbulent dissipation was correlated with vegetation density (Figure 2.10), with all stages of the tide depicting a similar positive trend. Cases with likely breaking ($\gamma > 0.3$, unfilled symbols in Figure 2.10) displayed a similar dependence on vegetation density to cases with minimal breaking ($\gamma < 0.3$, filled symbols). In the measurements collected in this study, wave velocities (U_w) often exceeded current velocities (U_c) above the wave-boundary layer (Appendix A). Defining wave-dominated cases as those for which $U_w > 2U_c$, we find for the data displayed in Figure 2.10, waves were dominant in most cases with some exceptions early in the tide ($U_w > 2U_c$ for 77% of LL cases, and 95% of HH cases, not shown).

2.6 Discussion

2.6.1 Dissipation rate magnitude

Dissipation rates across all sampling sites ranged from 3.7×10^{-7} to 4.5×10^{-3} W kg⁻¹, with a mean dissipation rate of 1.0×10^{-4} W kg⁻¹ averaged over all tide stages. Peak turbulence occurred at the fringe soon after the arrival of the flood tide. Although hotspots of turbulence were observed at other locations during later tide stages, turbulence in the fringe was usually elevated relative to the other sites. For comparison, estimates of turbulent energy dissipation in other coastal environments are typically highest in the surf and swash zones of beaches, while lower turbulence is typically found in intertidal areas and tidal rivers. In swash zones ($h < 0.25$ m), measured dissipation rates from 6×10^{-5} to 1×10^{-1} W kg⁻¹ have been reported (Lanckriet & Puleo, 2013; Raubenheimer et al., 2004), whereas in surf zones, measured dissipation rates have ranged between 3×10^{-7} to 3×10^{-3} W kg⁻¹ (although wave energy balances imply more rapid dissipation very near the surface, where turbulence has not been directly measured, Bryan et al., 2003; Feddersen, 2012; Trowbridge & Elgar, 2001). In more quiescent intertidal flats and tidal channels, measured dissipation rates from $O(10^{-7})$ to $O(10^{-4})$ W kg⁻¹ (Jones & Monismith, 2008; Mullarney & Henderson, 2012) and $O(10^{-7})$ to $O(10^{-3.4})$ W kg⁻¹ (MacDonald & Mullarney, 2015), respectively, have been reported. In this study, the maximum values measured in the fringe were comparable to those measured in highly turbulent swash and surf zones. It was expected that the mudflat sites produced lower turbulence than the vegetated sites overall, as vegetated regions generate higher turbulence intensities (Nepf, 1999).

While turbulence was most intense at the seaward fringe, estimates were variable on the mudflat and inside the forest. Dissipation rates along the transect corresponding to the breaking condition $\gamma > 0.3$ (Figure 2.11) shows that the high turbulence on the mudflat at $x = -50$ m, and further inside the forest ($x = 70$ and 90 m), were likely due to wave breaking. Lower dissipation on the mudflat $O(10^{-5})$ might be balanced by turbulence production in the bottom boundary layer while moderately high dissipation (10^{-4} W kg $^{-1}$) might be balanced by injection of turbulence from breaking waves above (e.g., Feddersen, 2012). Mudflat estimates of the dissipation rate in the present study were sometimes higher and sometimes lower than dissipation inside the forest. For example, sparse vegetation and small waves resulted in relatively weak dissipation at $x = 50$ m, whereas more dense vegetation and larger, possibly breaking waves resulted in larger dissipation rates at $x = 70$ m across-shore (Figures 2.8 and 2.11).

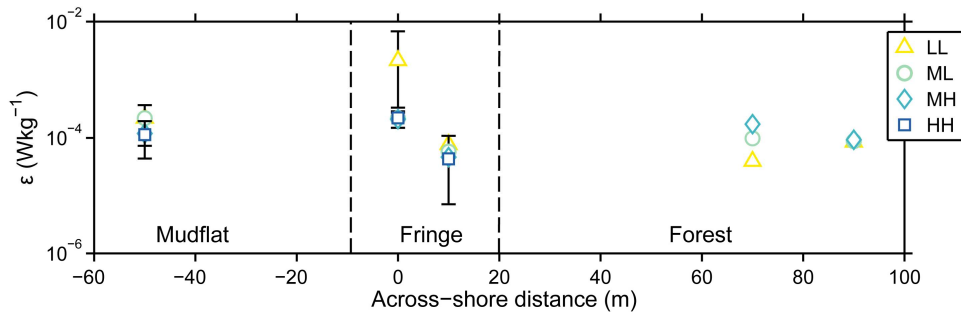


Figure 2.11: All measured TKE dissipation rates corresponding to the breaking condition, $\gamma > 0.3$ by across-shore position. Points are binned with horizontal distance at intervals of 10 m.

The high intensity of turbulence in the fringe was likely generated locally and cannot be explained by onshore advection of turbulence generated on the flats. This conclusion is supported by the observation that the turbulent dissipation at the fringe was one to two orders of magnitude larger than over the mudflat. Furthermore, turbulence was advected only a few meters before most energy was dissipated. To establish this, note that the length scale over which turbulence can be advected before substantial dissipation is of order $\bar{u}(L^2/\epsilon)^{1/3}$, where the length scale L of turbulent eddies is set to the water depth (likely an overestimate) and \bar{u} is the mean advection velocity. For typical depths (0.2 - 1.75 m), currents (0.17 ms $^{-1}$) and dissipation rates $O(10^{-4})$ W kg $^{-1}$, turbulence could be advected only about

5 m (weaker currents, smaller depths, and higher dissipation rates would yield smaller advection scales).

Over muddy seabeds, very high density suspensions sometimes develop very near the seabed. Such “fluids muds” can be associated with rapid wave dissipation (McAnally et al., 2007). However, fluid muds were unlikely to be responsible for the rapid turbulent dissipation we observed at the fringe, partly because fringe sediments were relatively coarse (Fricke et al., 2017), and partly because the high viscosity of fluid muds would be expected to damp small-scale motions, whereas our high ε values correspond to intense small-scale motions.

2.6.2 Canopy density effects on turbulence

While waves and wave breaking were a significant contributor, the observed patterns in turbulence were also strongly influenced by the patterns in canopy density. Estimated pneumatophore densities ranged from $\phi = 2.7 \times 10^{-4}$ to 0.024 for 1 m² quadrats, and from $\phi = 0$ to 0.1 in the 20 cm² subsamples, which tended to focus on the denser clusters of pneumatophore roots (see Table 2.2 for corresponding values of a). These values are lower than other comparable measurements of *Sonneratia* and *Avicennia* pneumatophore densities, which ranged from $\phi = 0.02$ to 0.045 for 1 m² quadrats (Horstman et al., 2012; Krauss et al., 2003). These values are also much smaller than values reported for the knee roots of *Bruguiera* and the characteristic stilt-roots of *Rhizophora* mangroves (at least within close proximity to tree trunks), with densities ranging between $0.19 < \phi < 0.45$ (Furukawa et al., 1997; Horstman et al., 2012; Mazda et al., 1997b). Turbulence estimates in the present study suggest that high turbulence is generated within small clusters of pneumatophores. Linear fits between the logarithm of a and the dissipation rate for the 20 cm² quadrats were significant below a 90% confidence level (p-value < 0.1) for all tidal stages, while fits of the 1 m² quadrats were not significant (p-value > 0.1) with the exception of the lowest tide stage. Therefore in terms of stem-wake turbulence, the 1 m² quadrats may not provide a representative scale for approximating the drag-generating features that produce turbulence. The correlation between the high density canopies and correspondingly high turbulent dissipation rates resulted in the relationship depicted in Figure 2.10. Previous experiments (Tanino & Nepf, 2008a) suggest interference between stem wakes has minimal effect on total dissipation, given the pneumatophore densities we observed

in most cases, although a small (about 20%) damping effect is expected at the highest pneumatophore densities ($\phi \sim 0.1$). Since turbulence in the wake of mangrove tree trunks was not measured, their contribution to the overall wave and current dissipation of the forest cannot be quantitatively extrapolated. However, dissipation is proportional to $a(z)$ (Section 2.2), so the relative importance of pneumatophores and tree trunks to horizontally averaged dissipation can be estimated by comparing their respective values of $a(z)$. For pneumatophores, $a(z)$ is order 1 m^{-1} near the bed, whereas for tree trunks $a(z)$ is of order 0.004 m^{-1} (here, we have used a typical observed tree density of $n = 0.005$ trunks per square meter (Bullock et al. 2017), and a trunk diameter of 0.8 m). Since near-bed $a(z)$ values were hundreds of times larger for pneumatophores than for tree trunks, near-bed dissipation was likely dominated by pneumatophores. For depth-integrated dissipation, calculations are complicated by the depth-dependence of velocity and trunk geometry. Neglecting such depth-dependence, an order-of-magnitude estimate of pneumatophore and trunk contributions to depth-integrated dissipation is obtained by comparing their respective contributions to the depth-integral of $a(z)$. For pneumatophores, the depth-integral of $a(z)$ is about 0.1, whereas for tree trunks it reaches about 0.006 at high tide (taking trunks with $a = 0.004 \text{ m}^{-1}$ extending over the water depth of 1.5 m). This rough calculation suggests that pneumatophores dominate depth-integrated dissipation, although detailed measurements of depth-dependent velocity and trunk geometry would be required to draw firm conclusions. Other studies have measured variable rates of wave and current dissipation with increasing tidal depth, specifically observing that dissipation is highest when the tidal depth is below the height of the root structures (suggesting a large role for pneumatophores) and again when the tide reaches the height of the tree canopies (suggesting an important role for branching, neglected in above calculations; Mazda et al., 2006, Horstman et al., 2012).

2.6.3 Geomorphological implications

In the present study, root densities were too sparse to shelter the bed from turbulence at the fringe; instead, turbulence increased with stem density. However, over larger scales ($\sim 100 \text{ m}$), turbulence did decrease with distance landward. These patterns suggest that turbulence is enhanced in the fringe, then due to wave dissipation and vegetative drag, eventually decreases creating a relatively sheltered

forest interior. Since *Sonneratia* pneumatophores are often shorter and are less dense than many marsh plants such as *Spartina* spp. (Leonard & Croft, 2006; Neumeier, 2007; Widdows et al., 2008) waves are expected to propagate relatively large distances into forests, leading to a relatively wide fringe region of enhanced dissipation.

Since turbulence is in turn is a primary component in the initiation of sediment motion (Yager and Schmeckle, 2013), it is interesting to compare the intensified turbulence near the forest edge with observations by Fricke et al., (2017) of relatively coarse-grained sediments at the forest fringe that fine with distance landward. Possible geomorphological implications are sketched in Figure 2.12: sediment is carried shoreward by the rising tide. Energetic turbulence during the lower stages of the flood tide may preferentially remove fines from the fringe, a suggestion supported by observations of relatively coarse sediments and scour around the pneumatophores in this fringing region (Figure 2.7a). Sediment may then be advected farther into the marsh and deposited as turbulence levels decline, particularly as flows grow weaker approaching slack tide (e.g., Furukawa et al., 1997). The lack of scour around the forest pneumatophores (Figure 2.7b), and the fining of sediment grain sizes in the forest supports this theory. Furthermore, these proposed zones of preferential suspension (fringe) and deposition (forest) may influence the across-shore bed elevation profile reported in Bryan et al., (2017).

This preferential distribution of fines inside the mangrove forest is consistent with observations by Wolanski et al., (1998) in the Fly River Delta (Papua New Guinea), Furukawa et al., (1997) who described the capture of fines as current velocities dropped near slack tide, and Van Santen et al., (2007), who quantified sedimentation rates. While these studies did not specifically measure turbulence in situ, the latter two inferred that the observed patterns in sedimentation were a result of the reduction of current velocities with distance inside the mangroves. The results of the present study suggest the connection between spatially variable turbulence, generated in root canopies by currents and waves, may be a control on the morphodynamics of mangrove forests. The patterns in sedimentation, particularly the preferential suspension of sediment at the fringe, is consistent with the observations of Van Santen et al., (2007) in mangroves, and experiments utilizing vegetation analogues (Bouma et al., 2007; Spenceley, 1977).

Over longer time scales, these bio-geomorphic feedbacks may influence the progradation and succession of mangrove forests. Species such as *Sonneratia* that are more resistant to salt water inundation and wave energy may initially comprise coastal mangrove forest fringes. Through mangrove-influenced land progradation, mangroves that were once in the fringe may be replaced by other species that prefer higher elevations (Nardin et al., 2016b; Bullock et al., 2017). The fringe moves seaward, continuing to be occupied by pioneering species. This feedback mechanism should function as long as there is ample sediment supply to the mangrove forest (Anthony et al., 2010).

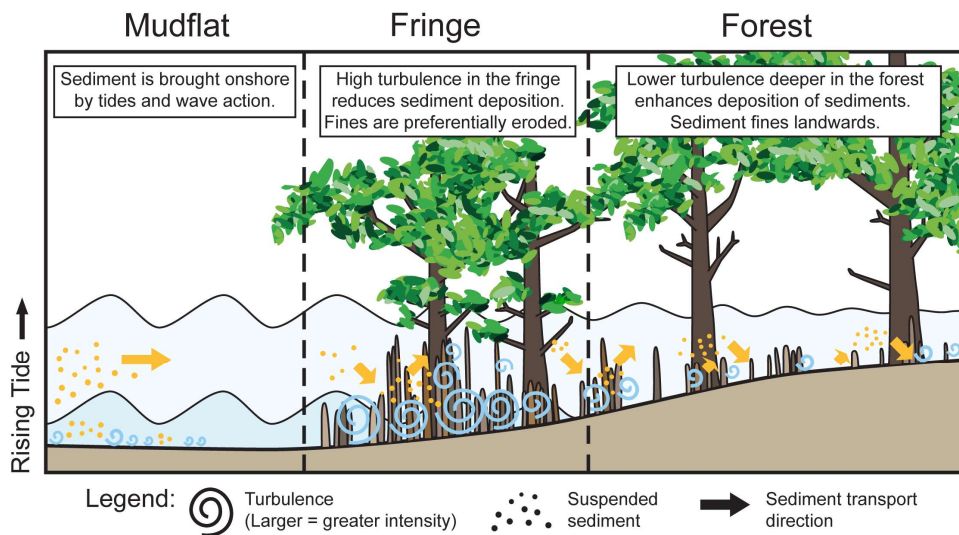


Figure 2.12: A conceptual diagram of the mangrove bio-geomorphic feedback mechanism presented in this chapter. Larger spirals mean higher intensity turbulence. Note: the two illustrated water levels show the tide rising.

2.7 Conclusions

This chapter examines the role of pneumatophores as a spatial control on the dissipation of turbulent kinetic energy. Turbulence, measured at millimeter scales, was compared with complex canopy geometry measured using a three-dimensional photogrammetric reconstruction technique. Turbulent dissipation was maximum at the forest fringe, where pneumatophore densities were highest. Dissipation was highly variable inside the forest throughout the flood tide, with intense turbulence corresponding to regions of particularly dense vegetation. Across a range of sites, TKE dissipation was positively correlated with vegetation density. Dissipation also depended on wave heights and water depths, with the most intense dissipation

observed for relatively large waves in shallow water. High turbulent energy at the forest fringe may suspend fine sediments that can then be redistributed elsewhere in the forest. This theory is supported by observations of coarse fringe sediments, scouring around fringe pneumatophores, and an absence of scouring farther inside the forest. Such observations suggest a mangrove-influenced geomorphic feedback, in which coastal mangrove shorelines accrete landmass from their interior outwards. This control may facilitate mangrove succession, whereby stress-tolerant mangrove species are replaced by less tolerant species as the seaward fringe expands outwards.

Chapter 3

Turbulence within Natural Mangrove Pneumatophore Canopies



Billows of sediment reveal turbulent wakes forming behind pneumatophore roots in the forest fringe.

Contribution of Authors

Chapter 3 presents the article entitled “Turbulence within Natural Mangrove Pneumatophore Canopies”, which was submitted to the *Journal of Geophysical Research: Oceans* for review in 2018. Data were collected for this study during two field seasons (Section 1.6) in Vietnam by myself, Dean Sandwell, Julia C. Mullarney, and Stephen M. Henderson. I wrote scripts to load, quality control, and analyze all of the hydrodynamic data. I also prepared all of the figures and wrote the initial and subsequent drafts of this manuscript. My co-authors, Julia C. Mullarney, Karin R. Bryan and Stephen M. Henderson edited my drafts and provided helpful comments and direction, and editorial help responding to reviewers’ comments.

Abstract

High-resolution velocity measurements were collected within and above two dense canopies of mangrove pneumatophore roots in a wave-exposed mangrove forest. In both canopies, root density decreased steadily with height above bed owing to the variability in root heights and the tapered shape of the roots. Within the canopies, we consider turbulence within three zones: near the bed above the wave boundary layer, around the mean canopy height, and above the canopy. The near-bed turbulence was particularly intense (up to $6.5 \times 10^{-4} \text{ W kg}^{-1}$), likely owing to oscillatory wave-driven currents flowing past dense vegetation. Near the bed and around the mean canopy height, peaks in horizontal velocity power spectra at frequencies corresponding to Strouhal numbers of ~ 0.2 may indicate Von Kármán wake shedding in the lee of the pneumatophores. Furthermore, a recirculation zone was observed immediately behind a cluster of pneumatophores at intermediate heights. These coherent flow structures were associated with zones of enhanced Reynolds stresses (up to $5.3 \times 10^{-3} \text{ m}^2 \text{ s}^{-2}$), and eddy viscosities (up to $1.9 \times 10^{-3} \text{ m}^2 \text{ s}^{-1}$). Large near-bed stresses were associated with near-bed drag coefficients (a parameterization of the bed shear stress) that are up to an order of magnitude larger than those expected in the absence of vegetation. Observed eddy viscosities are consistent with theoretical expectations, derived from scaling arguments using a standard mixing-length model. These results suggest that pneumatophore roots can contribute greatly to turbulent mixing (e.g., eddy viscosities were on average $O(10^{-4} - 10^{-3} \text{ m}^2 \text{ s}^{-1})$), and therefore may enhance the sediment entrainment occurring in mangrove forest fringes.

3.1 Introduction

Mangroves are a diverse family of salt-tolerant trees and shrubs that often form the dominant plant communities along tropical and subtropical coasts. Mangroves are characterized by their complex aerial root systems that effectively dissipate wave and tidal currents (Mazda et al., 1997a; McIvor et al., 2012), and hence provide protection against wave inundation (Massel et al., 1999; Mazda et al., 2006; Vo-Luong & Massel, 2008) and tropical storms (Alongi 2008; Wolanski 2007) in places that often lack hard coastal defense structures. Through the damping of waves and currents, mangroves can also facilitate the deposition of sediment. Provided there exists an ample sediment supply, the accumulation rate of sediment and organic material in mangrove-dominated reaches may be comparable to the rate of eustatic sea level rise (Krauss et al., 2010; Lovelock et al., 2015; McKee, 2011; McKee et al., 2007). Despite these valuable services, mangrove forests are generally in decline worldwide due largely to human pressures (Alongi, 2002). Former efforts to rehabilitate or restore mangrove ecosystems have been met with mixed results, with some failures attributed to improper site or species selection, and planting techniques (Ellison, 2000). Recent studies suggest that the success rate of seedling establishment is based on a narrow window of hydrodynamic conditions in which propagules can take root (Balke et al., 2011). Hence, a thorough understanding of the physical forces that shape mangrove ecosystems may improve future conservation and restoration efforts.

The hydrodynamics of mangrove environments have been previously explored through multiple field studies which focused on forest-scale flow routing (Furukawa et al., 1997; Horstman et al., 2013; Mazda et al., 1997; Wolanski et al., 1980), wave dissipation (Horstman et al., 2012; Massel et al., 1999; Vo-Luong & Massel, 2008) and sedimentation (Van Santen et al. 2007; Walsh & Nittrouer, 2004; Wolanski, 1995). Contemporary research has suggested that the forest-scale patterns are largely dominated by the drag force induced by mangrove roots, particularly when the water depth is on the order of the root canopy height (Mullarney et al., 2017a; Norris et al. 2017). However, studies focused on the flows within the mangrove root structures (Henderson et al. 2017, Furukawa et al., 1997; Furukawa & Wolanski, 1996; Mazda et al., 2005; Mazda et al., 1997) are less numerous than comparable studies of other marine ecosystems such as saltmarshes

and seagrasses (e.g., Lacy & Wyllie-Echeverria, 2011; Leonard & Croft, 2006; Widdows et al., 2008). For example, Henderson et al (2017) considered only wave (rather than turbulent) flows, and Furukawa & Wolanski, (1996) only qualitatively described root-scale turbulent structures in the field. Flow velocities were later quantified by Furukawa et al., 1997) through the VORTEX model to simulate the complex flow structure forming in the wake of the roots. Given the horizontal and vertical heterogeneity of mangrove root canopies (Liénard et al., 2016), simplified models (e.g., Lowe et al. 2005; Henderson et al. 2017; Furukawa et al., 1997; Mazda et al., 2005; Struve et al., 2003) may not represent the complex 3D flow structures that are critical to predicting sedimentation in vegetated areas (Yager & Schmeeckle, 2013). Direct, turbulence-resolving measurements are therefore crucial for understanding the link between root-scale hydrodynamics and forest-scale morphodynamics.

The field of vegetated flow dynamics has been widely studied through laboratory flume and numerical modeling experiments (see reviews by: Nepf, 2012a; 2012b; Mullarney and Henderson 2018). Experiments are typically conducted on artificial canopies with structures of uniform-height, where canopy geometry is described by the height, h_c , the element diameter, d , the canopy frontal area density a (units of m^{-1} , $a = nd$ where n is the number of elements per square meter) and the average element spacing ΔS . Wake shedding is initiated at Reynolds numbers ($Re = Ud/\nu$, where U is the velocity of the flow and ν is the kinematic viscosity) greater than 50 for a solitary element perpendicular to a current, and between 150 – 200 for patches of elements (Kiya et al., 1980; Nepf et al., 1997). Once initiated, vortex shedding from array elements will generate narrow peaks in the downstream velocity power spectrum that are equivalent in frequency f to a Strouhal number, $St = fd/U$ of about 0.2 (Schewe, 1983).

When Reynolds numbers are sufficiently high that wake-shedding is initiated, within-canopy flows often become turbulent, resulting in the standard quadratic dependence of drag on water velocity (e.g., Batchelor, 2000). Expressed per unit water mass and summed over all stems, the canopy drag force is then

$$F_D = (C_D/2)aU^2, \quad (3.1)$$

where C_D is the canopy drag coefficient, which is typically $O(1)$. Canopy drag generates turbulence, hence Equation (3.1) relates to the dissipation rate of turbulent kinetic energy by $\varepsilon = F_D U / \rho$. For steady flows through submerged, uniform canopies, in-canopy velocities tend to be constant with depth, provided the canopy density is sufficiently large enough to create drag forces that exceed the bed stress, which occurs at the threshold $C_D a h_c \geq 0.23$ (Nepf et al., 2007; Nepf, 2012b). In sparse canopies where $C_D a h_c \leq 0.23$, turbulent eddies penetrate to the bed, and near-bed wake shedding can be observed behind individual elements (Nepf, 2012b; Stoesser et al., 2009). In cases where the mean stem diameter is less than the stem spacing, i.e., $d \leq \Delta S$, the length scale of turbulent stem wakes l is controlled by d . At greater canopy densities, wake interference becomes measurable when $\Delta S < 5d$ (Zhang & Zhou, 2001), and in very dense cases, the turbulent length scale, $l = \Delta S$ if $d > \Delta S$ (Tanino & Nepf, 2008b). The above results for steady flows were based on laboratory experiments using depth-uniform canopies, but recent studies have shown that these uniform canopies do not necessarily represent the dynamics of natural (heterogeneous) pneumatophore canopies (Horstman et al., 2018). In general, velocity profiles, and hence turbulence, are strongly dependent both on the submergence depth and the non-uniformity of the canopy (Horstman et al., 2018; Liu et al., 2010). Recently, two laboratory studies investigated turbulence within modeled mangrove forests (Maza et al., 2017; Zhang et al., 2015). Both studies focused on *Rhizophora* mangroves with dense prop root structures, whose geometry differs substantially from the pneumatophores of the predominant *Sonneratia* mangroves considered in this chapter. Maza et al., (2017) and Zhang et al., (2015) observed two distinct zones of enhanced turbulent kinetic energy: one near-bed zone generated by stem and trunk wakes, and another zone formed by velocity shear that was generated by the sharp decrease in vegetation density at the top of the prop roots.

Under oscillatory (wave) forcing, in-canopy flow velocities are forced by fluctuating pressure gradients in addition to the shear stresses that force steady flows (Lowe et al., 2005). When pressure gradients dominate over shear stresses, the drag-induced reduction of within-canopy flows scales with $\Lambda = C_D a A_\delta / 2$, where A_δ is the wave orbital excursion. Wave dissipation is greatest between low and high canopy density regimes, which occurs at values of $\Lambda = 1.4$ (Henderson et al., 2017).

Relative to above-canopy flows, unsteady flow is greatly reduced within a canopy if and only if Λ is sufficiently large. For the cases presented in the present study, Λ values were sufficiently low (0.17 – 0.38) that in-canopy wave velocities were only slightly reduced by canopy friction (Henderson et al., 2017). For steady currents, the parameter $\lambda = \int a(z)dz$ plays a role similar to that of Λ in unsteady flow. Specifically, for $\lambda > 0.2$, canopy drag greatly reduces near-bed velocity and bed stress (Belcher et al., 2003; Heidi M Nepf, 2012).

These previous studies provide an overview of key principals governing the hydrodynamics within idealized mimic and real pneumatophore canopies. However, the detailed flow structure around natural mangrove roots has not yet

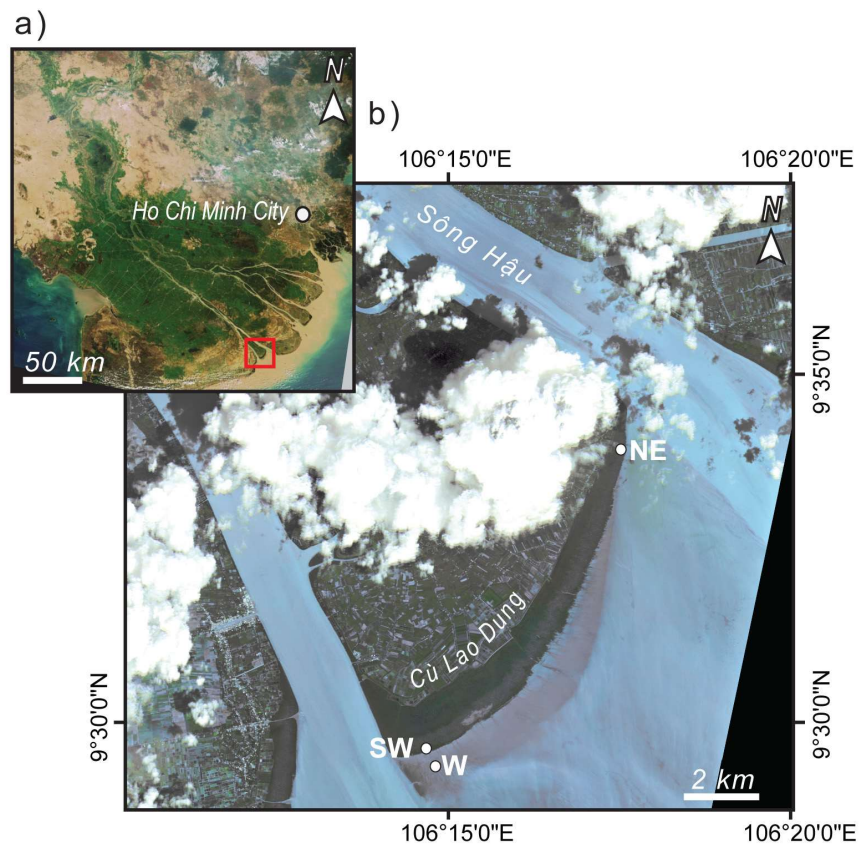


Figure 3.1: Overview map of Cù Lao Dung, located in the Sông Hậu distributary channel in the lower Mekong Delta. (Panel a) Regional context of deployment region (red square). (Panel b) Deployment locations on the seaward edge of Cù Lao Dung; the horizontal turbulence array (HTA) experiment was deployed in the southwest, and the vertical turbulence array (VTA) in the northeast within 10 m of the mudflat/mangrove forest fringe boundary. The symbol ‘W’ denotes the location of the weather station in the southwest. Data sources are, Envistat (panel a) and Rapideye (panel b).

been described in the field. The present study provides a dataset of high-resolution velocity measurements collected in situ within and above dense canopies of natural roots in a wave-exposed mangrove forest. From these data, we derive turbulence statistics: the turbulent kinetic energy dissipation rate, frequency spectra, Reynolds stress and eddy viscosity, as well as several positions of turbulent wake shedding, to understand how mangrove pneumatophore roots modify the flow field under natural conditions.

3.2 Field Experiments and Methods

3.2.1 Experimental Setup

Field experiments were carried out between 3 – 15 March, 2015 in the mangrove forest on Cù Lao Dung, within in the southern Mekong River Delta, Vietnam (Figure 3.1). The island is located at the terminus of the Sông Hậu distributary channel of the river where it discharges into the East Sea (South China Sea). The southeastern, seaward edge of the island is covered by a mangrove forest that grades from dominantly *Sonneratia caseolaris* mangroves at the shoreward edge to a mixture of *Sonneratia spp.*, *Avicennia spp.*, and *Aegiceras corniculatum* mangroves and *Nypa fruticans* palms in the forest interior (Bullock et al., 2017). Seaward of the mangrove forest, a shallow interlaminated mud and sand flat extends for several kilometers (Fricke et al., 2017). Experiments were conducted in the mangrove fringe (< 10 m from the unvegetated mudflat) at the seaward edge of the island within the pneumatophore root canopies of the dominant *Sonneratia caseolaris* mangroves. Two sites of dense pneumatophore were selected using a 1 m² quadrat on each side of the island (located at the SW and NE sites, Figure 3.1). Care was taken to select sites containing dense root clusters that were situated far away from trees in order to focus on turbulence generated by the pneumatophores alone. Distances were determined from scaling arguments for turbulent dissipation produced by roots versus tree trunks in Norris et al., (2017).

Three 10 MHz Nortek Vectrino Profilers (‘Vectrinos’) were deployed in the 1 m² quadrat areas within and above the mangrove pneumatophore root canopies (Figure 3.2). In the SW, a horizontal array of Vectrinos was constructed to observe the evolution of flows as they encountered a dense cluster of pneumatophore roots (Figure 3.2a – b). The Vectrinos were situated with one instrument seaward of a

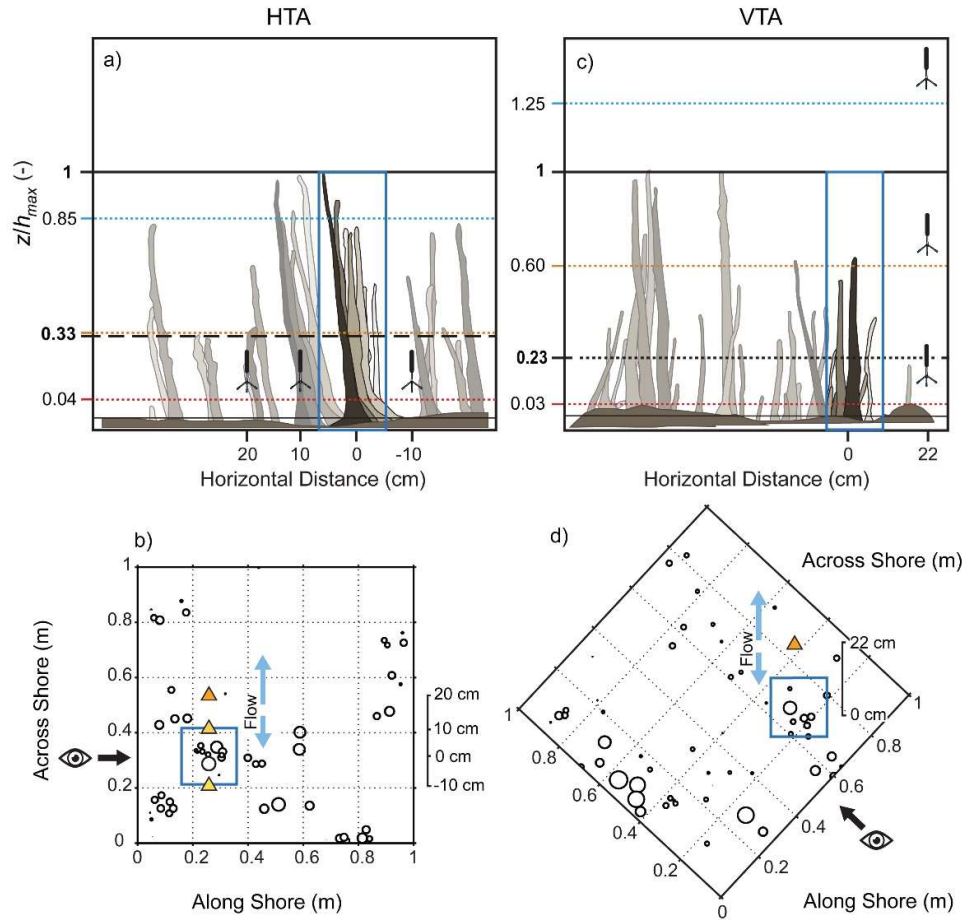


Figure 3.2: Experimental setup for the HTA experiment (panels a – b) and the VTA (panels c – d). Canopies in panel (a) and panel (c) were created by tracing the 3D SFM reconstructions of the canopies in profile-view, and depict the height of canopy elements relative to the measurement positions. Thick dashed and solid lines respectively show the mean canopy height $\langle h_c \rangle$ and max canopy height h_{max} . Colored dotted lines are the normalized measurement height of the three Vectrinos. Canopy elements in blue boxes in panels (a) and (c) correspond to the subsampled elements depicted in the blue boxes in panels (b) and (d). Eye symbols show the viewing angle of the plan-view panels (a, c) relative to the profile view panels (b, d). In panels (b) and (d), triangles show the Vectrino positions. Light blue arrows show the mean current flow direction through the canopies. Pneumatophore basal diameters are represented by black circles. The x-axis scales of panels (a) and (c) are shown for reference in panels (b) and (d).

row of pneumatophores at the $x = -10$ cm position (where $x = 0$ marks the row of pneumatophores), and two instruments landward of the row at the $x = 10$ cm and $x = 20$ cm positions (hereafter, we use HTA to represent ‘Horizontal Turbulence Array’). For brevity, these instrument positions will sometimes be referred to in the text as ‘seaward’, for the $x = -10$ cm position, and ‘landward’, for the $x = 10$ and 20 cm positions. Over the course of three days, this array of three sensors was moved

from a height near the bed ($z/h_{max} = 0.04$), then to a position near the mean canopy height ($z/h_{max} = 0.33$) and finally to below the top of the tallest elements within the canopy, but above the mean canopy height ($z/h_{max} = 0.85$) where z is the measurement height and h_{max} is the maximum canopy height (Figure 3.2a). Hereafter, references to HTA1 – 3 in the text refer to each of these three experiments. In the NE, a vertical array of the three Vectrinos was installed to measure flows within and above the canopy synoptically (hereafter, VTA for ‘Vertical Turbulence Array’) at positions $z/h_{max} = 0.03, 0.60$ and 1.25 (Figure 3.2c – d). Vectrinos recorded velocity profiles over 35 vertical bins at a resolution of 1 mm continuously at a rate of 50 Hz for 10-minute bursts. Prior to data collection, all Vectrinos were leveled with a bubble level to minimize instrument tilt errors (see: Mullarney et al., 2017b for details).

A single Nortek Vector (ADV) was deployed above the third Vectrino ($x = 20$ cm) of each HTA experiment above the canopy at a height of $z/h_{max} = 1.6$, and recorded pressure and velocities continuously at 32 Hz (Figure 3.3a). For the VTA experiment, above-canopy velocities were captured by the third Vectrino, and pressure was measured by an RBR Duet deployed at the same height as the second Vectrino, which sampled continuously at 16 Hz. In addition, a single downward-looking 2 MHz Nortek Aquadopp (ADCP) was deployed 2 m south of the VTA at a height of $z/h_{max} = 1.3$ (Figure 3.3b). This instrument logged nearly continuous velocities and pressure at 8 Hz (burst lengths of 512 s with a 3-s separation between bursts) over a 0.22 m profile at a bin resolution of 0.025 m and was used to estimate the mean wave and current directions above the canopy near the instrument array. See Table 3.1 for a complete overview of the instrument deployment settings.

Hydrodynamic measurements were conducted during the rising tides on March 7th, 8th and 10th in the SW (HTA experiments) and on March 14th in the NE (VTA experiment). All self-contained instruments (ADCP, ADV, Duet) were set to record for the duration of the experiments. Vectrino data were collected from the time at which all of the instruments were submerged by the rising tide until just before high tide. In one instance (HTA2, March 8th), the ebb tide was also recorded. Owing to the variability in height of the individual canopy elements, some of the taller pneumatophores were exposed initially during HTA1 (Figure 3.2a) and became

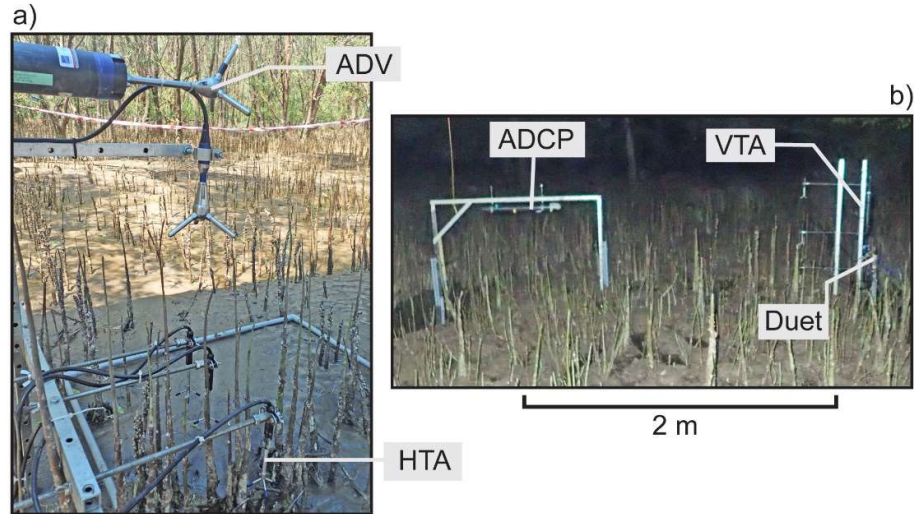


Figure 3.3: Photographs of the experimental set-up showing the locations of collocated sensors to the HTA (panel a) and VTA (panel b). The unlabeled downward-looking ADV in panel (a) was not used here, and the quadrat was removed prior to the experiment.

fully submerged 40 minutes after the beginning of the experiment. The canopy was submerged during all other experiments, with water depth to canopy height ratios (h/h_{max}) ranging from 1.1 to 2.4. The root canopy at each site was surveyed using the Structure-From-Motion (SFM) photogrammetric method described in Liénard et al., (2016). The frontal area density of the canopy as a function of height above the bed was calculated as the number of stems per square meter of the bed times the mean stem diameter. The volume fraction occupied by the vegetation, $\phi = n\pi d^2/4$, was estimated from the total enclosed pneumatophore area divided by the total area at height intervals of 5 mm from 5 cm above the bed to the top of the canopy. The spatial-mean canopy height $\langle h_c \rangle$, where h_c is the height of an individual pneumatophore, was estimated by averaging the number of pneumatophores reaching a given height interval across all height intervals. To examine causes of spatial variations in turbulent dissipation within the canopy, the vegetation directly upstream of the Vectrino arrays was also subsampled (cf. Figure 2.4, Chapter 2). A bounding box with a length of 20 centimeters was used to isolate the pneumatophores that were likely to be responsible for creating wakes (blue boxes, Figure 3.2b, d). From the pneumatophores selected within these boxes, vegetation geometries were computed at the measurement height for each experiment and are given in Table 3.2.

3.2.2 Data Processing

ADCP data were processed to remove low quality data corresponding to correlations below 70% and phase-wrapped velocities (e.g., Lohrmann et al., 1990). ADV and Vectrino velocities were similarly processed to remove data with low correlations and low signal-to-noise ratios, and then were despiked following the method of Goring & Nikora, (2002). Data gaps were filled using a linear or cubic interpolation for gaps of less or greater than 100 points, respectively. Finally, ADCP and ADV velocities were rotated into an east (E), north (N) and up (U) coordinate system, and Vectrino velocities were rotated to the direction of the mean current, where u is along-current, v is across-current, and w is vertical.

Table 3.1: Summary of instrument deployment settings. The Nortek Vector and Aquadopp are referred to in the text as ‘ADV’ and ‘ADCP’, respectively.

Site	Instrument (Figure 3)	Profiling Range (m)	Bin Size (m)	Sampling Frequency (Hz)	Sampling Mode
HTA	Nortek Vectrino Profiler (x3)	0.035	0.001	50	Continuous
HTA	Nortek Vector	-	-	32	Continuous
VTA	Nortek Vectrino Profiler (x3)	0.035	0.001	50	Continuous
VTA	Nortek Aquadopp	0.22	0.025	8	512-s burst, 3-s between bursts
VTA	RBR Duet	-	-	16	Continuous

Table 3.2: Vegetation statistics for each experimental site. Whole quadrat statistics are denoted by an asterisk (**). The subsampled area statistics are given below.

Site	Date	Duration (min)	Area (m ²)	h_{max} (m)	$\langle h_c \rangle$ (m)	z/h_{max} (m)	n (m ⁻²)	d (m)	ΔS (m)	a (m ⁻¹)	ϕ (-)
HTA*			1.0	0.60	0.2 ± 0.18		66	0.02 ± 0.011	0.15	1.31	0.03
HTA1	3/7/15	210	0.04	0.54	0.33 ± 0.17	0.04	11	0.02 ± 0.014	0.03	3.8	0.08
HTA2	3/8/15	290				0.33	7	0.019 ± 0.002	0.04	1.74	0.02
HTA3	3/10/15	114				0.85	2	0.002 ± 0.001	0.06	0.1	1.6×10^{-4}
VTA*			1.0	0.60	0.14 ± 0.13		84	0.02 ± 0.011	0.26	1.49	0.03
VTA	3/14/15	210	0.04	0.37	0.23 ± 0.15	0.03	8	0.014 ± 0.007	0.04	3.1	0.04
VTA	3/14/15	210				0.60	1	0.004 ± 0	0.13	0.09	2.8×10^{-3}
VTA	3/14/15	210				1.25	0	0	0	0	0

In cases when the Vectrinos were mounted close to the bed (the HTA1 experiment and the lowest instrument of the VTA experiment), all measurements below the depth with the strongest acoustic backscatter, defined as the bed level (e.g., Craig et al., 2011) were removed. Additionally, measurements within the Wave Bottom Boundary Layer (WBBL) were rejected prior to analysis. Fredsøe & Deigaard, (1992) estimated the WBBL thickness as

$$\delta_R/k_N = (A_\delta/k_N)^{0.82}, \quad (3.2)$$

where A_δ is the orbital excursion and k_N is the Nikuradse roughness length, which was estimated here as the d_{50} of sediment (123 μm and 3.62 μm for the southwest and northeast sites, respectively) collected nearby the instrument arrays (Fricke et al., 2017). WBBL thickness estimates varied between 2 mm to 6 mm, with greater values corresponding to periods with larger wave heights. For the near-bottom Vectrinos, the top five profile bins (1 – 5) were always above the bed and the WBBL for the duration of the data record. In all other cases, analysis was conducted using the five middle profile bins (13 – 17), or the ‘sweet spot’ of the instrument, where the signal-to-noise ratio was maximum (Brand et al., 2016). Further analysis was conducted using 10-minute windows for all datasets (Vectrinos, ADCP, ADV, Duet), chosen to capture turbulent time scales while maintaining quasi-stationary statistics within each window (Soulsby, 1980).

3.2.3 *Turbulent Dissipation Rate*

The Turbulent Kinetic Energy (hereafter, TKE) dissipation rate was estimated from velocity data using the structure function method (Wiles et al., 2006). The structure function has been employed to study turbulence in the ocean (Mohrholz et al., 2008; Thomson, 2012), in estuaries (MacDonald & Mullarney, 2015; Mullarney & Henderson, 2012), in surf zones (Lanckriet & Puleo, 2013), and recently, in mangrove forests (Norris et al., 2017). The structure function uses differenced adjacent along-beam locations (“bins”) up to a number of lags (bin distances) within a velocity profile to estimate dissipation rates. This differencing technique is effective at filtering out large-scale variability, such as wave oscillations, that are not associated with inertial subrange turbulence. The structure function is an alternative to estimating dissipation rates from velocity spectra (e.g., McMillan and Hay, 2017). Both methods require the measurement of velocity fluctuations in the

inertial subrange, where the assumption of local isotropy holds. See Appendix B for a comparison of the structure function and spectral methods. For a profile of vertical velocities w , the second-order longitudinal structure function D is defined as,

$$D(z, r) = \overline{[w(z) - w(z + r)]^2} \quad (3.3)$$

where z is the vertical position and r the separation distance between adjacent velocity measurements (Wiles et al., 2006). The overbar denotes a time average. From Kolmogorov's inertial subrange theory, the structure function is expected to take the form,

$$D(z, r) = C_v^2 \varepsilon^{2/3} r^{2/3} \quad (3.4)$$

in the inertial subrange, where $C_v^2 = 2.0$ is an empirical constant (Pope, 2000). To solve for ε , the TKE dissipation rate, the second-order structure function $D(z, r)$ is fitted to the linear equation,

$$D(z, r) = 2\sigma_B^2 + Ar^{2/3}, \quad (3.5)$$

where the least-squares slope, A , is related to the dissipation rate by $A = C_v^2 \varepsilon^{2/3}$, and $2\sigma_B^2$ is an offset that represents the uncertainty in the velocity measurements due to Doppler noise. This offset is assumed independent of r (Wiles et al., 2006). TKE dissipation rates were calculated from 10-minute Vectrino velocity segments ($n = 30000$) using Equations (3.3 – 3.5) with a 50% overlap between segments. Velocities were linearly detrended, then $D(z, r)$ velocity differences were computed at steps of 1 mm up to a maximum distance of $r_{max} = 5$ (mm) to produce a profile of TKE dissipation rates 30 mm in length (profile range minus r_{max}).

3.2.4 Spectral Calculations

To estimate wave statistics, power spectra of the ADV and ADCP pressure measurements were calculated using Welch's method (MATLAB, Mathworks Inc.) over 10-minute windows. Each 10-minute window ($n = 19200$ and 4800 , respectively) was linearly detrended and was split into smaller Hamming-windowed segments (1280 and 320 measurements, respectively) with 50% overlap to yield spectra with 30 degrees of freedom. Power spectra were converted to sea

surface elevations using linear wave theory, and were transformed into significant wave heights, H_s , by integrating the surface pressure spectra over the range of 0.05 – 1.2 Hz, with

$$H_s = 4 \left[\int S(f) df \right]^{0.5}, \quad (3.6)$$

where $S(f)$ is the spectral density of the surface displacement and f is the frequency in Hz (Laing et al., 1998). The peak wave period T_p ($= 1/f_p$) was estimated from each spectrum at the frequency band with the greatest energy, f_p . Root-mean-squared wave velocities were evaluated with Equation (A.2), and wave directions from directional spectra computed using PUV analysis (Gordon & Lohrmann, 2002) using measurements collected by the ADV and ADCP collocated with the Vectrino arrays. Similarly, current speed and direction were estimated using a principal components analysis on the horizontal velocity components measured by each velocimeter.

In order to calculate turbulence statistics such as Reynolds stresses, it is necessary to first remove the effect of surface waves (i.e., wave-turbulence decomposition). In previous studies, this decomposition has been achieved by differencing measurements from two vertically separated instruments (Feddersen & Williams, 2007; Shaw & Trowbridge, 2001; Trowbridge, 1998). Unfortunately, this method is less reliable in the presence of directionally spread surface waves (e.g., Gerbi et al., 2008) or in measurements conducted near the bed (MacVean & Lacy, 2014). Hence, to separate waves and turbulence, we employed the spectral phase decomposition technique of Bricker & Monismith, (2007) that has been successfully applied in field studies within shallow (up to 3 m depth) estuarine locations (e.g., Hansen & Reidenbach, 2012; MacVean & Lacy, 2014). Spectral coherence was calculated from 10-minute windowed ADV or ADCP velocity and pressure measurements ($n = 19200$ or 4800 , respectively) using Hamming-windowed segments with 50% overlap corresponding to 30 equivalent degrees of freedom. The cut-off frequency f_{wc} was then defined as the largest frequency where coherence was significant (>0.19 , above the 95% confidence level) between vertical velocity and pressure signals (Figure 3.4a). This method yielded cutoff frequencies, marking the upper limit of the wave band, of 1.40, 1.35, 1.04 and 1.09 Hz for HTA1 – 3 and the VTA experiments, respectively (Figure 3.4b). Spectral slopes (Section

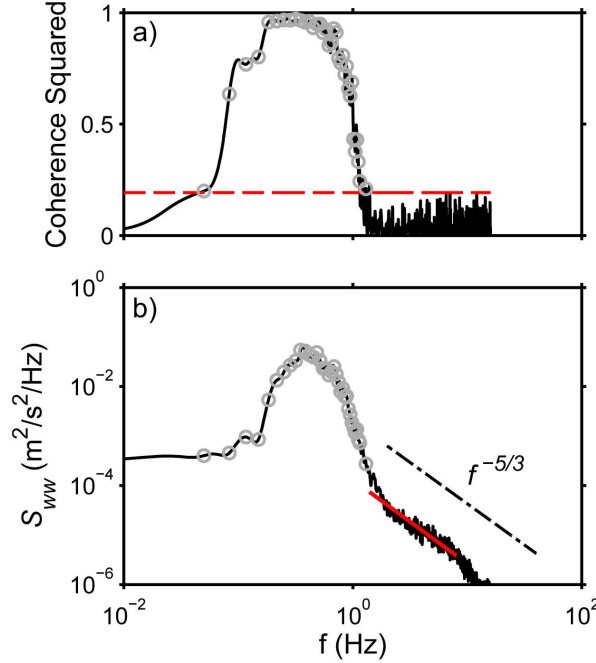


Figure 3.4: Example wave-turbulence decomposition for a 10-minute data time series from the ADV deployed above the HTA on March 7th, 2015. Coherence squared between the vertical velocity component and the pressure signal (black line), and the 95% confidence level at 30 D.O.F., 0.19 (dashed red line). Grey circles show the wave band, or frequency components that are significantly coherent. (b) Power spectral density (PSD) of the vertical velocity component (S_{ww} , solid black line). Grey circles denote frequencies in the wave band. The solid red line represents the linear fit between f_{wc} and f_{hc} used for extracting the slope of the turbulent band (Section 3.3.4.2). The dotted line is $f^{-5/3}$, as indicated.

3.3.4.2) were estimated by fitting a line to the log of the power spectrum versus log f over the frequency band defined by $f_{wc} < f < f_{hc}$ Hz (Figure 3.4b). The upper high-frequency cutoff f_{hc} corresponded to the smallest eddies well resolved by the Vectrino's finite sampling volume. Specifically, f_{hc} was estimated as $(0.25U_w)/s_v$ where $s_v = 0.006$ m is the width of the sampling volume of a Vectrino profiler. Here, U_w is the root-mean-squared velocity of the horizontal velocity components times $\sqrt{2}$. Given $U_w \sim 0.1 - 0.2$ ms^{-1} during the HTA1, HTA2 and VTA experiments (Table 3.3), f_{hc} was estimated as 8.3, 8.3 and 5 Hz, respectively. In addition to estimating spectral slopes, the cutoff frequencies were used in the estimation of Reynolds stresses (discussed below).

3.2.5 Reynolds Stress Calculation

To assess the bulk momentum transfer of water within the canopies, the along and across-current Reynolds stresses $-\overline{u'w'}$ and $-\overline{v'w'}$ were evaluated from the

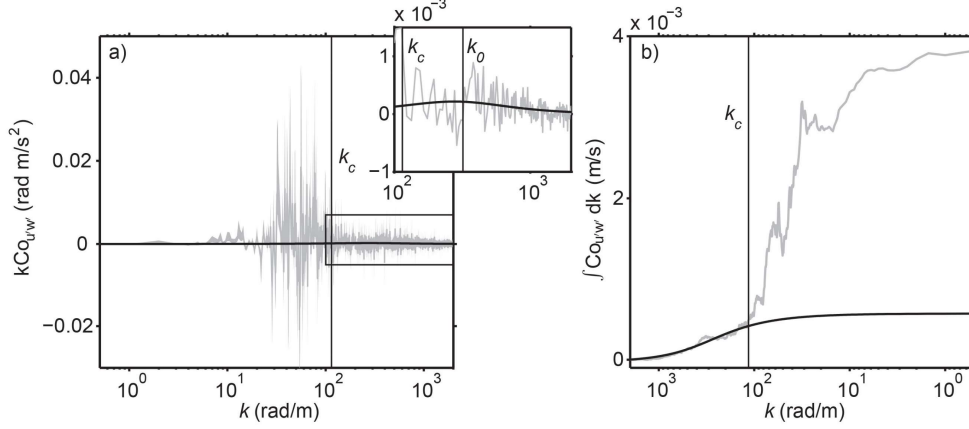


Figure 3.5: Grey curves are the variance-preserving cospectra (panel a) and integrated cospectra (ogive curves; panel b) of turbulent velocity components u' and w' from the HTA1 experiment at $x = 20$ cm, 0.018 m above the bed at 13:41 local time. The grey regions in (a) show the measurements with 95% confidence intervals for the cospectral estimates. Black curves in (a) and (b) show the model cospectra, the Kaimal curve, and thin vertical black lines show the cutoff wavenumber, k_c and the roll-off wavenumber, k_0 . The high-frequency end of the cospectra are blown up in the inset of panel (a) to aid comparison of the model and observations. Although raw cospectra were used in the model fit, spectra shown in the inset of panel (a) have been smoothed with a 10-point running mean to reduce noise for display. To compute the ogive curves, the cospectra were integrated from the Nyquist wavenumber πk to 0 to exclude wave frequencies.

cospectrum of the horizontal and vertical velocity components from each Vectrino profile depth bin above the bed and the WBBL (Section 3.2.3). In both atmospheric and oceanic boundary layers, the shape of the stress-carrying cospectrum is appropriately described by a semi-empirical model (Kaimal et al., 1972) where the spatial structure of turbulence is inferred from the time series using a frozen turbulence approximation for advection by a steady mean flow (Taylor, 1938). This model cospectrum of the Reynolds stress as described in Gerbi et al., (2008) is,

$$\frac{Co_{u'w'}(k)}{-\overline{u'w'}} = \beta \frac{1/k_0}{1+(k/k_0)^{7/3}}, \quad (3.7)$$

where

$$\beta = \frac{7}{3\pi} \sin\left(\frac{3\pi}{7}\right), \quad (3.8)$$

k_0 is the roll-off wavenumber, and β is a normalization factor to ensure the integral of Equation (3.7) is 1. The roll-off wavenumber describes the length scale λ_0 of the dominant stress-carrying eddies by $\lambda_0 = 2\pi/k_0$ and is related to the frequency

spectrum by $k_0 = \omega/U_d$ with U_d the mean drift velocity. The model cospectrum described in Equation (3.7) rolls off with $k^{-7/3}$ at wavenumbers above k_0 . k_0 also defines the peak of the variance-preserving model cospectrum (cf. Figure 4, Kirincich et al., 2010),

$$k \frac{Co_{u'w'}(k)}{u'w'} = \beta k \frac{1/k_0}{1+(k/k_0)^{7/3}}. \quad (3.9)$$

In the coastal ocean, surface wave oscillations can extend over most, if not all of the water column (Feddersen & Williams, 2007; Jones & Monismith, 2008), and are often orders of magnitude larger than the oscillations of turbulent eddies (Kirincich et al., 2010). Therefore, filtering is necessary to prevent wave contamination of the estimated turbulent stresses. However, even if wave velocities were perfectly filtered from point measurements of velocity, advection of the turbulence by wave orbital velocities distorts the frequency cospectrum computed from the filtered velocities (Lumley & Terray, 1983; Trowbridge et al., 2018). Secondly, imprecise knowledge of the sensor orientation or the presence of sloping bottoms can create large uncertainties in stress estimates (Grant & Madsen, 1986). To address the first concern, we limited Reynolds stress estimation to cases dominated by mean currents. Specifically, we excluded cases where the wave orbital velocity exceeded half the mean flow speed, i.e., $\sigma_w/U_d < 2$ (Gerbi et al., 2008). The second concern was addressed using the fact that the near-bed mean velocity flows were nearly parallel to the bed. Therefore, velocity measurements from the near bed instruments (HTA1 and the lowermost instrument of the VTA) were additionally rotated so that the mean flow direction was treated as horizontal. Such rotations were small, typically $< 4^\circ$ from horizontal. Brand & Noss, (2017) suggested that rotating the horizontal velocities to the mean current direction reduces bias induced by small but unavoidable misalignments in instrument orientation during deployment.

To estimate wave-filtered stresses and roll-off wavenumbers, the cut-off frequencies (Section 3.2.4) were converted to cut-off wavenumbers k_c , via Taylor's approximation. Similarly, the observed frequency cospectrum of u (or v) and w , $Co_{uw}(\omega)$, was converted to a wavenumber cospectrum $Co_{uw}(k)$ to match the model cospectrum (Equation 3.7). Then, the cumulative integrals- the ogive curves- of the observed and model cospectra were fit from the Nyquist wavenumber nk , to the

cutoff wavenumber k_c (Figure 3.5b) using a simple least-squares regression to estimate high-frequency wave-free stresses.

Screening criteria were then applied to ensure quality model fits to the data. Fits where k_0 was outside the observed wavenumber range (e.g., Kirincich et al., 2010), and fits where the correlation between the model and observations were less than 70% (e.g., Davis & Monismith, 2011) were rejected. Applying both the wave-drift criterion $\sigma_w/U_d < 2$ and these other quality control measures reduced the number of useable bursts from the HTA1 – 3 and the VTA experiments to 72%, 86%, 61% and 85%, for each experiment averaged over the three instruments, respectively. The uncertainty in the Reynolds stress estimates was assessed by recalculating stresses after applying an additional $\pm 1.5^\circ$ rotation to the pitch then roll axis of the velocities. Uncertainties at the 95% confidence level were estimated as $1.95\sqrt{(\sigma_n/n)}$, where σ_n is the standard deviation and n is the number of samples for each dataset. The maximum uncertainty based on a small pitch or roll adjustment was no greater than 44% of the total estimated stresses for any of the experiments. These quality control measures suggest that the estimates of $-\overline{u'w'}$ and $-\overline{v'w'}$ are accurate measures of the above-wave band part of the cospectra.

3.3 Results

3.3.1 Vegetation Geometry

The two surveyed canopies had a maximum height of 0.6 m, with 66 – 84 stems/m² (Table 3.2). Corresponding values of a and ϕ ranged from 0 – 1.51 m⁻¹ and from 0 – 0.028, respectively. Although the number of stems and mean stem diameters varied between surveyed sites, both $a(z)$ and $\phi(z)$ were comparable between sites (Figure 3.6). In the subsampled regions, the HTA canopy was both taller and denser on average than the VTA canopy, with a and ϕ reaching 3.8 and 0.08 near the bed, respectively. Although the root density of the VTA canopy was comparable to the HTA canopy near the bed ($a = 3.8$), it had fewer tall canopy elements and so had a lower spatial-mean canopy height $\langle h_c \rangle = 0.23 \pm 0.12$ m compared to 0.33 ± 0.17 m for the HTA canopy. In both cases, stem density decreased with elevation for the 1 m² quadrats and the subsampled regions (Figure 3.6c – d). Hence, the lowest measurement positions were situated within the densest region of the canopies,

while the middle and upper positions were at moderate and sparsest densities, respectively.

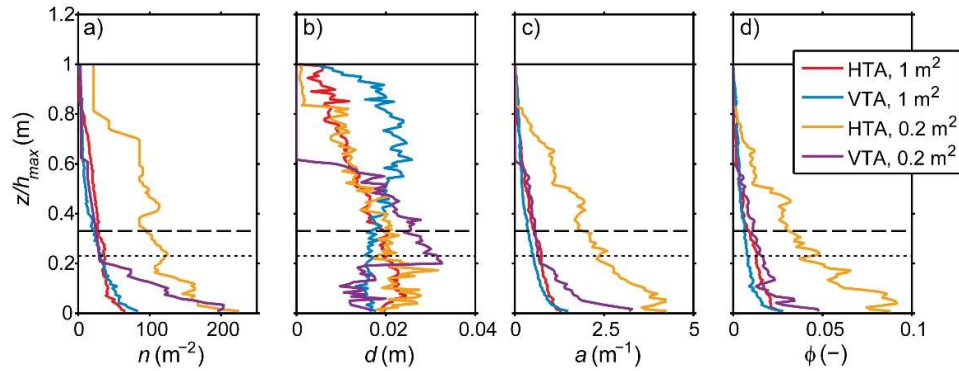


Figure 3.6: Vertical profiles of vegetation statistics. (a) Number of stems per square meter, n ; (b), the mean stem diameter, d ; (c) the frontal area of the canopy, a ; and (d), the volume fraction occupied by the vegetation, ϕ . The red line is the total canopy (1 m^2) measured at the HTA site; blue line, the total canopy (1 m^2) measured at the VTA site. The yellow and purple lines are the subsampled regions of the two canopies (Figure 3.2). Horizontal lines denote the maximum (solid line) and mean canopy heights for the HTA and VTA, dashed and dotted lines, respectively.

3.3.2 Offshore Conditions

Hydrodynamic forcing conditions are shown in Figure 3.7b – g. High-tide water depths were 1.3 m in the southwest, with wave periods ranging from 1.8 s to 4.3 s and significant wave heights up to 0.6 m during the HTA3 experiment. High tide water depths were greater in the northeast reaching 1.8 m. Peak wave periods between 2.6 and 3.1 s and significant wave heights of 0.35 m indicate lower wave energy was present during the VTA experiment than during the other experiments. Figure 3.8 depicts the mean wave and current speed and directions measured above the turbulence array canopies. In the SW, wave and current directions were generally oriented towards the northwest (the onshore direction) during the flood tide, although mean currents had a greater along-shore component than did the waves. In the NE, the mean wave direction was also generally onshore, while mean currents were oriented in the along-shore direction. Previous studies have discovered that flood tides combined with along-shore oriented winds generate strong along-shore currents (reaching up to 0.3 m s^{-1}) that flow obliquely to the coastline of Cù Lao Dung (Mullarney et al., 2017a). Although current velocities are rapidly reduced over $\sim 100 \text{ m}$ of mangrove forest, the fringe environment is subject

to the currents generated along the unvegetated mudflat. In the present study, this component dominated the mean current direction in both experimental sites.

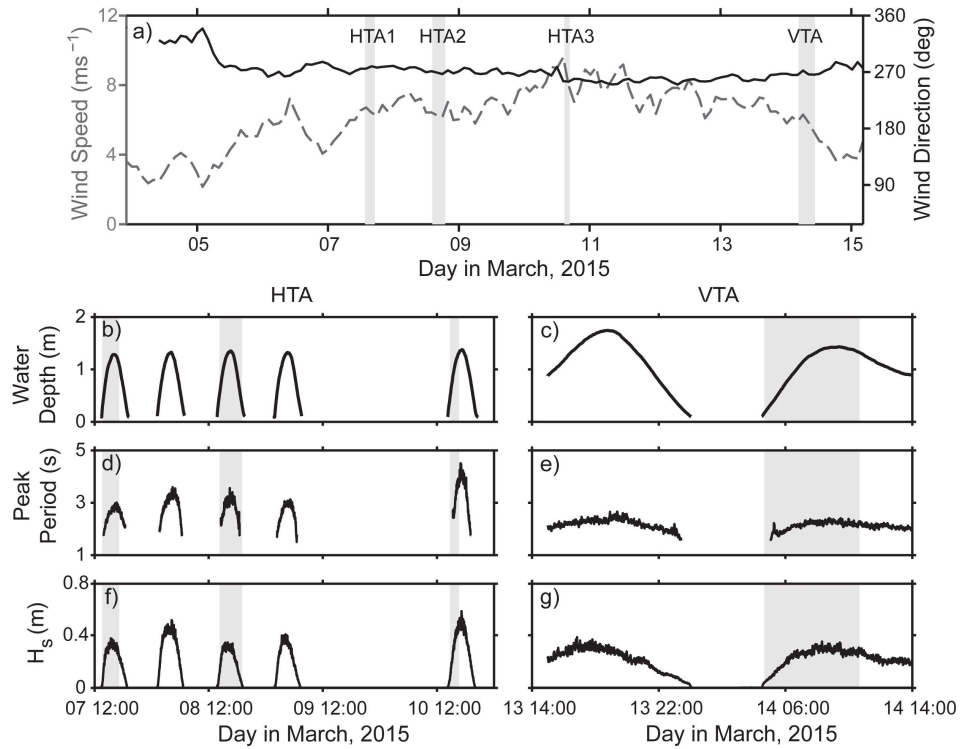


Figure 3.7: Environmental conditions measured during the experiments. Panel (a), two-hour averaged wind speeds (dashed grey line) and directions (solid black line) during the two experiments. Grey bars designate the length of each of the horizontal turbulence array (HTA) experiments and the vertical turbulence array (VTA) experiment. Panels (b – g), hydrodynamic forcing conditions: water depth (panels b, c), peak period (panels d, e) and significant wave height (panels f, g) recorded by the ADV and pressure sensor collocated with the turbulence arrays.

3.3.3 Canopy Turbulence

Time series of normalized turbulent kinetic energy dissipation rates are shown in Figure 3.9 for each instrument position for the HTA experiments (Figures 3.9a – c) and the VTA experiment (Figures 3.9d – f). Large normalized dissipation rates up to $2.3 \times 10^{-2} \text{ m}^{-1}$ ($6.5 \times 10^{-4} \text{ W kg}^{-1}$) were observed at the base of the canopies, with the greatest values occurring at the $x = 20 \text{ cm}$ measurement location of the HTA1 experiment ($z/h_{max} = 0.04$, Figure 3.8c). At the array position close to the mean canopy height ($z/h_{max} = 0.33$, Figure 3.8b), maximum normalized dissipation rates of $4.6 \times 10^{-3} \text{ m}^{-1}$ ($3.8 \times 10^{-4} \text{ W kg}^{-1}$) were found closer to the pneumatophores at the $x = 10 \text{ cm}$ position during the HTA2 experiment. Note that larger dissipation rates

occurred nearing high tide during the HTA1 experiment (~200 minutes after low tide, Figure 3.8a), and near mid tide during the HTA2 experiment (~50 minutes after low tide, Figure 3.8b). During the HTA2 experiment, turbulence decreased with the ebb tide (blue to dark blue lines). Near the top of the canopy where vegetation was relatively sparse (HTA3 experiment, Figure 3.8a), normalized turbulence was of a similar magnitude to the lowest array position around mid-tide, $2.1 \times 10^{-2} \text{ m}^{-1}$ ($1.4 \times 10^{-4} \text{ W kg}^{-1}$), and decreased with increasing water depth. For the VTA experiment, large normalized dissipation rates of $4.9 \times 10^{-2} \text{ m}^{-1}$ ($1.8 \times 10^{-4} \text{ W kg}^{-1}$) were observed near the bed (Figure 3.9f). Turbulence was less intense within the canopy at the middle array position (Figure 3.9e) and then increased at the array position above the canopy (Figure 3.9d). In the next section, the wake structure of the two canopies is quantified and connected to the positions at which the largest dissipation rates were measured.

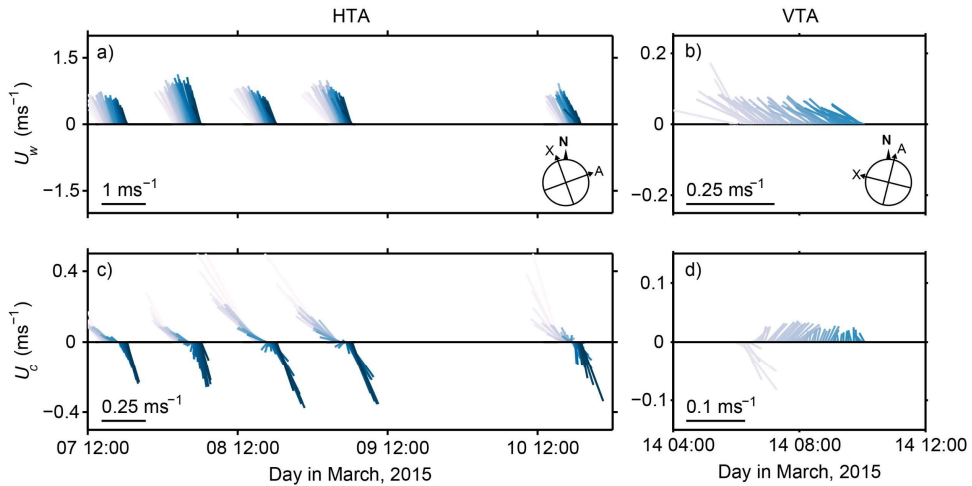


Figure 3.8: 10-minute averages of wave (a, b) and current (c, d) magnitude and directions measured above the canopies at each experimental site. The magnitudes depicted for U_w are mean orbital velocities. Color corresponds to the tidal stage, with lighter blues the flood tide and darker blues the ebb tide. The compass in the lower right-hand corner of panels (a, b) shows the orientation of the across-shore (X) and along-shore (A) directions relative to north (N).

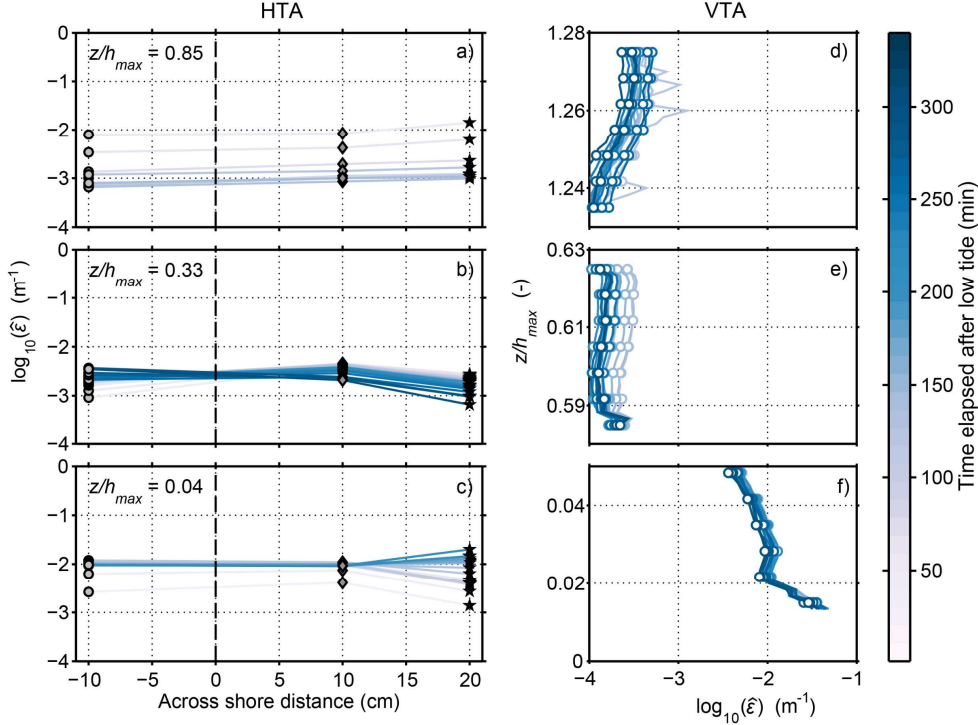


Figure 3.9: Time series of the TKE dissipation rate normalized by $|U^3|$, $(\hat{\epsilon})$, for the three positions of the HTA (panels a – c) and VTA (panels d – f). VTA dissipation rates were computed and averaged over 10-minute segments for each instrument. For the HTA, each segment is plotted against the across-shore position of the array. For the VTA, every third point in the profile is plotted as a marker w.r.t. the normalized height above bed, z/h_{max} . Colors correspond to time elapsed after low tide and are consistent between subplots.

3.3.4 Turbulence Characteristics

3.3.4.1 Wake Shedding

To visualize canopy wake shedding, power spectral densities of the velocities in the mean current direction were computed for each Vectrino over 10-minute bursts ($n = 30000$) using Welch’s method. Individual bursts were Hamming-windowed with 50% overlap to yield spectra with 30 equivalent degrees of freedom. Power spectra from the array positions HTA corresponding to the locations of high turbulence: $x = 20$ cm, $x = 10$ cm and $z/h_{max} = 0.03$ (Figure 3.9c, 3.9b and 3.9f, respectively) are shown in Figures 3.10a – c. These spectra are truncated at 10 Hz to focus on the details within the turbulent band. A large peak between 0.1 – 1 Hz corresponding to the wave band is present in all spectra. Assuming frozen turbulence, a frequency f may be converted to a wavelength (eddy length scale) roughly by $l = U_w/2\pi f$. Oscillations at the cutoff frequency between the wave and turbulence bands (1 – 1.4 Hz) are

therefore $O(0.01 - 0.1)$ m, given a the range of in-canopy rms wave velocities of $U_w = 0.2 - 0.7 \text{ ms}^{-1}$ (Table 3.3). The frequencies associated with smaller peaks are highlighted with arrows and correspond to eddy scales that are of $O(0.01)$ m. As explained below, these peaks correspond to wake shedding frequencies of Von Kármán vortices generated in the direction of the mean current. In the case of HTA1, the average stem diameter of the 11 upstream objects was $d = 0.022$ m, giving a stem Reynolds number between $\sim 3700 - 5000$, and an average Strouhal number $S_t = f_d d / U_w$ of 0.23 for frequencies f_d located at 2.1 and 2.6 Hz (Figure 3.10a; Table 3.3). Higher in the canopy, during HTA2 at $x = 10$ cm, three shedding peaks were observed in the power spectrum between $f_d = 2.0 - 2.6$ Hz (Figure 3.10b). Stem Reynolds numbers were $O(10^3)$, and associated Strouhal numbers ranged between 0.11 - 0.23. For the bottom instrument of the VTA (Figure 3.10c), the shedding peak was located at $f_d = 2.1$ Hz corresponds to an average Strouhal number of 0.23, suggesting wake shedding was also measured at this position near the bed. Vortex shedding frequency peaks in power spectra have previously been observed both in Large Eddy Simulations (LES) of turbulence, and in flume experiments behind patches of simulated vegetation, within arrays of similar stem density as the experiments in the present study ($\phi = 0.06$, Stoesser et al., (2010); $\phi = 0.03$, Zong & Nepf, (2012); $\phi = 0.02 - 0.08$, *present study*). The presence of multiple peaks in the power spectrum may indicate interference between the wakes of upstream roots, as is expected in cases with small the average spacing between roots (i.e. when $\Delta S < 5d$, Table 3.2; see also Tanino & Nepf, (2008b) and references therein). Given that the mean stem diameter d was less than the mean stem spacing ΔS in all cases, the length scale of turbulence generated within the stem wakes, l was expected to be of the order of d (Nepf, 2012a). Indeed, for all three array positions, $l \sim d$ (Table 3.2).

For comparison, power spectra from the other Vectrinos used in the HTA and VTA experiments (i.e., the array positions other than those where high turbulence was measured) are shown in Figures 3.10d – f. Here, black and grey lines differentiate between instruments. As in Figures 3.10a – c), waves are represented by the peak between 0.1 – 1 Hz. Unlike Figures 3.10a – c), no higher-frequency peaks were observed. Additionally, these spectra highlight the differences between the seaward and landward array positions of the HTA, and in- and above-canopy positions of the VTA. In Figure 3.10e, the spectrum from the $x = 20$ cm position (black line) is similar in power in the wave band as the $x = -10$ cm position (grey line) but deviates around 1 Hz. A flatter spectral slope between 1 – 5 Hz possibly indicates energy input by stem wakes at these scales (i.e., wakes observed as shedding frequencies in Figure 3.10b at $x = 10$ cm). In the VTA, the spectral power from the instrument at $z/h_{max} = 1.25$ (Figure 9f, black line) is larger across all frequencies, compared to

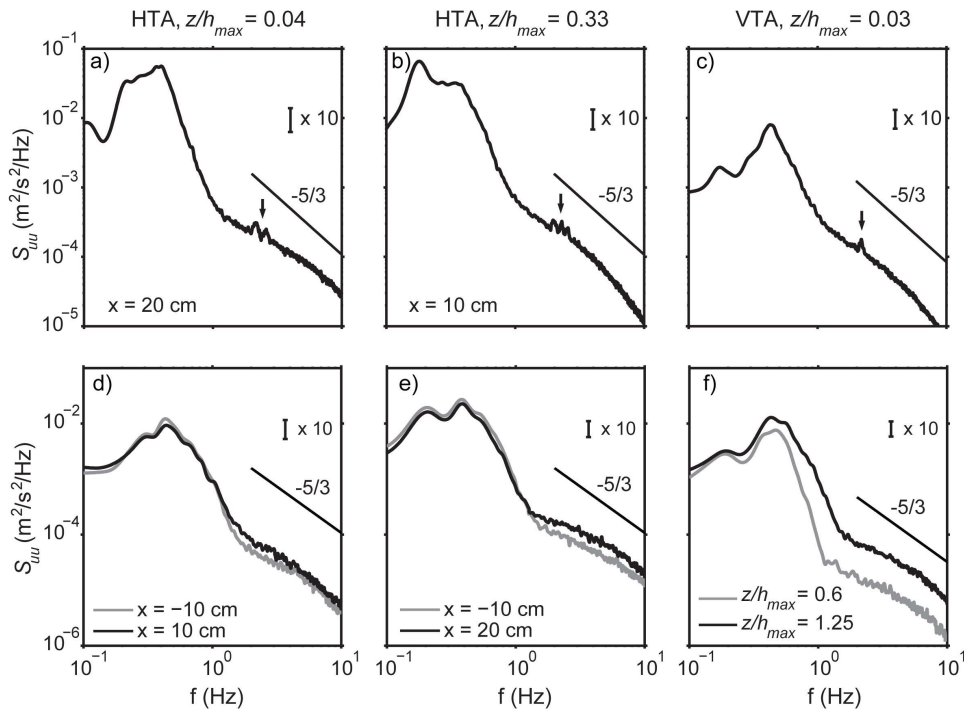


Figure 3.10: Power spectral densities of along-current velocity (S_{uu} , black line) averaged over a 1.5-hour period during the experiments. 95% confidence intervals shown at 10x actual size. The solid black line indicates a $-5/3$ slope. Panels (a – c) show velocity spectra from the array positions where high turbulence was observed in Figure 3.9: HTA1, $x = 20$ cm, HTA2 $x = 10$ cm, and the VTA, $z/h_{max} = 0.04$. Arrows highlight shedding frequency peaks of interest. Panels (d – f) show velocity spectra from the other array positions in these experiments; note the absence of peaks in frequency bands between 1 – 4 Hz.

the array position within the canopy (grey line). Since wave energy is attenuated near the bed, much of this attenuation, particularly at wave frequencies above about 0.3 Hz, is predicted by linear wave theory (cf. Figure 9, Henderson et al., 2017). At higher (turbulent) frequencies > 5 Hz, spectra show a slope near $-5/3$, as expected for turbulent spectra in the inertial subrange. Although not shown in Figure 3.10d – f, spectral slopes above 3 – 4 Hz are approximately $-5/3$ until they flatten out to the noise floor around 20 Hz before reaching the Nyquist frequency.

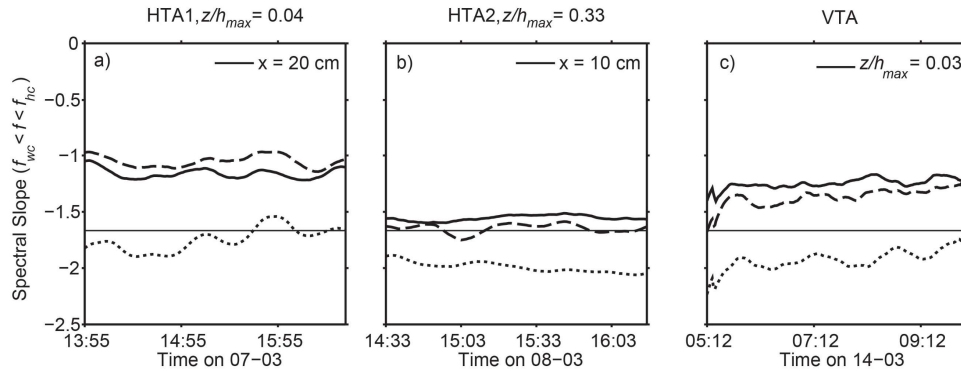


Figure 3.11: Time series of slopes of fits to auto-spectra of along-current (S_{uu} , solid lines), across-current (S_{vv} , dashed lines) and vertical (S_{wv} , dotted lines) from the array positions where high turbulence was observed in Figure 3.9. Slopes were calculated by a linear fit over the frequency range $f_{wc} < f < f_{hc}$ Hz over 10-minute windows with >30 degrees of freedom. The thin horizontal black line indicates a $-5/3$ slope.

3.3.4.2 Spectral Slopes and Anisotropy

From theory, the strain rate of large eddies is comparable to the strain rate of the mean flow velocity of unidirectional currents (Tennekes & Lumley, 1972). Analyzing the slope of the velocity power spectrum above the wave band will give some indication of the directionality of the strain rate, and hence, the direction of deformation of turbulence at these scales. As turbulence is three-dimensional, larger mean flow in one of the velocity components may drive anisotropy (deviance from a $-5/3$ slope) in that component direction. At frequencies much greater than the scale of large eddies, an inertial subrange is often observed, with all velocity components having roughly equal variance, and power spectral density scaling with $f^{5/3}$. However, wake generation could cause departures from inertial subrange

Table 3.3: Flow properties measured within the HTA and VTA. Highlighted peak frequencies from the power spectra (Figure 3.10) are listed as f_d .

$S_t = f_d d / U_w$, and $l = U_w / 2\pi f_d$.

Site	Array position	(Min) Mean (Max) U_w (m/s)	(Min) Mean (Max) U_c (m/s)	d (m)	f_d (Hz)	(Min) Mean (Max) S_t	(Min) Mean (Max) Re	(Min) Mean (Max) l (m)
HTA1	x = -10 cm	(0.17), 0.20, (0.23)	(0.01), 0.03, (0.04)	0.022	-	-	(3740), 4400, (5060)	-
HTA1	x = 10 cm	(0.18), 0.21, (0.23)	(2 x 10 ⁻⁴), 0.02, (0.04)	0.022	-	-	(3960), 4620, (5060)	-
HTA1	x = 20 cm	(0.17), 0.24, (0.28)	(7 x 10 ⁻⁵), 0.01, (0.03)	0.022	2.3 - 2.5	(0.18), 0.21, (0.32)	(3740), 5280, (6160)	(0.011), 0.015, (0.020)
HTA2	x = -10 cm	(0.18), 0.24, (0.30)	(4 x 10 ⁻⁵), 0.01, (0.06)	0.016	-	-	(2880), 3840, (4800)	-
HTA2	x = 10 cm	(0.18), 0.24, (0.29)	(9 x 10 ⁻⁴), 0.01, (0.04)	0.016	2.03 - 2.4	(0.15), 0.21, (0.29)	(2880), 3840, (4640)	(0.012), 0.017, (0.23)
HTA2	x = 20 cm	(0.19), 0.26, (0.31)	(2 x 10 ⁻⁴), 8 x 10 ⁻³ , (0.03)	0.016	-	-	(3040), 4160, (4960)	-
HTA3	x = -10 cm	(0.30), 0.43, (0.65)	(1 x 10 ⁻³), 0.05, (0.12)	0.002	-	-	(600), 860, (1300)	-
HTA3	x = 10 cm	(0.29), 0.43, (0.73)	(2 x 10 ⁻³), 0.04, (0.11)	0.002	-	-	(580), 860, (1460)	-
HTA3	x = 20 cm	(0.28), 0.43, (0.66)	(2 x 10 ⁻³), 0.04, (0.18)	0.002	-	-	(560), 860, (1320)	-
VTA	$z/h_{max} = 0.03$	(0.08), 0.10, (0.11)	(3 x 10 ⁻⁴), 3 x 10 ⁻³ , (7 x 10 ⁻³)	0.013	1.85	(0.21), 0.24, (0.29)	(1004), 1222, (1390)	(0.006), 0.008, (0.010)
VTA	$z/h_{max} = 0.6$	(0.05), 0.10, (0.12)	(7 x 10 ⁻⁴), 8 x 10 ⁻³ , (0.02)	0.004	-	-	(177), 394, (446)	-
VTA	$z/h_{max} = 1.25$	(0.10), 0.12, (0.13)	(8 x 10 ⁻³), 0.02, (0.07)	0	-	-	(0), 0, (0)	-

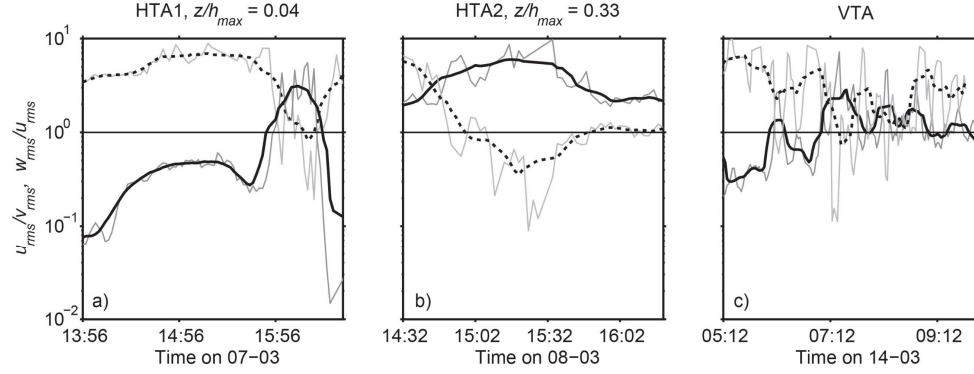


Figure 3.12: Time series of velocity ratios, u_{rms}/v_{rms} (light grey) and w_{rms}/u_{rms} (dark grey) for the array positions where high turbulence was observed in Figure 3.9. Dotted and solid black lines are 10-point moving averages of the two ratios, respectively. The solid horizontal line corresponds to ratios of one.

predictions even at the relatively small scales comparable to the stem diameter. To visualize eddy deformation in the canopy wake, the slopes of power spectra above the wave band (i.e., between $f_{wc} < f < f_{hc}$; Section 3.2.4) were computed for the flood tides at the same HTA and VTA positions where high turbulence was measured (e.g., Figure 3.9). Time series of spectral slopes derived from the three velocity components (u , v , w) are shown in Figure 3.11 for the locations with measured high turbulence. Near the bed during HTA1 and VTA experiments, spectral slopes of the horizontal velocity components ranged from -1 to -1.45, and slopes of the vertical velocities ranged from -1.6 (-5/3) to -2. During HTA2, the slopes of the horizontal velocity components were nearly -5/3 for the duration of the experiment, while slopes of vertical velocities were considerably steeper (i.e., more negative).

Large-scale anisotropy can be characterized by the ratio of the vertical to horizontal root mean squared velocity components assessed over the full spectrum, w_{rms}/u_{rms} (Godeferd & Staquet, 2003), where values smaller than 1 indicate the dominance of horizontal motion. During the near-bottom HTA1 and VTA experiments, the ratio of the horizontal velocity components u_{rms}/v_{rms} was often >1 (Figure 3.12a, 3.12c). In contrast, the vertical to horizontal ratio w_{rms}/u_{rms} was usually <1 , as vertical velocities are strongly limited by the presence of the bed in these near-bottom cases. During the HTA2 experiment, w_{rms}/u_{rms} was >1 , and was also often greater than u_{rms}/v_{rms} , indicating the presence of strong vertical velocities (Figure 3.12b; discussed in greater detail in Section 3.4, below). In contrast, the ratio of the vertical to horizontal rms velocity components assessed over the inertial subrange

(i.e., between $f_{wc} < f < f_{hc}$) was always < 1 in all cases, and the ratio of the horizontal rms velocity components was always > 1 in all cases. Former studies of turbulence in the wake of porous patches suggest the ratio of horizontal rms velocities is strongly dependent on the measurement position, with increasing v_{rms} velocities further from the patch in the patch wake (Zong and Nepf, 2012). Hence, the relatively flat spectral slopes during HTA1 and the VTA experiment (Figure 3.12a, 3.12c) suggest turbulence was anisotropic due to shear in the direction of u .

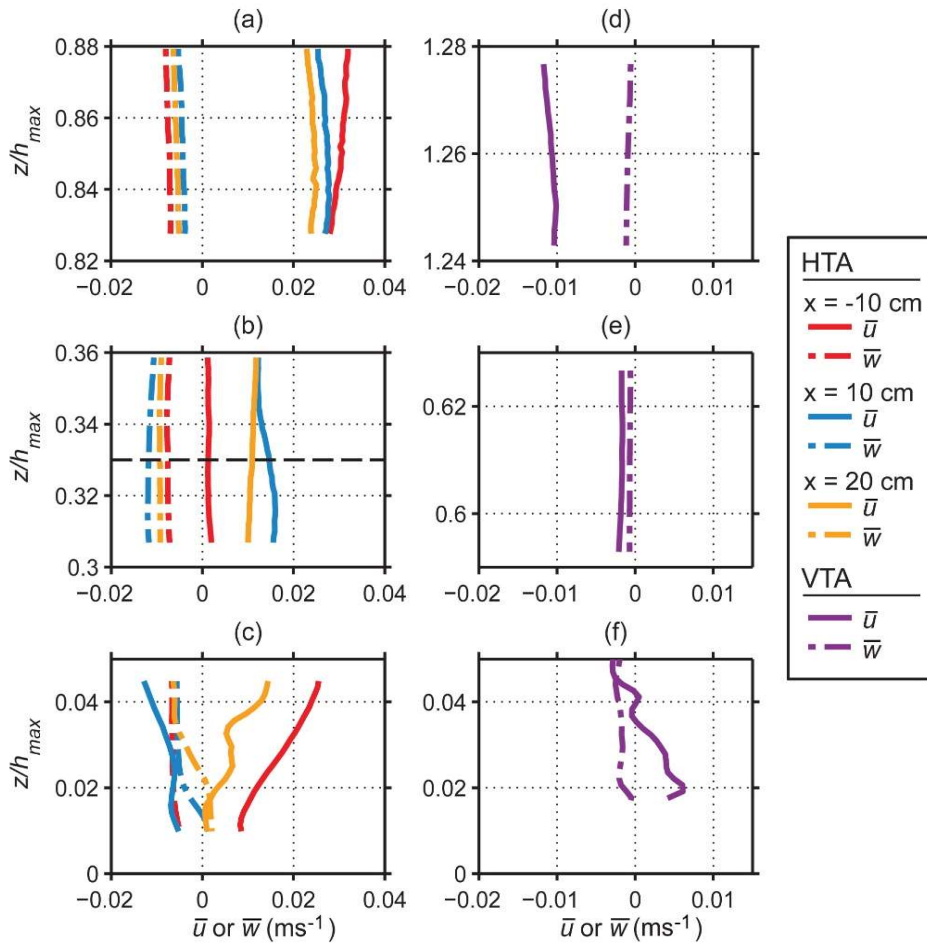


Figure 3.13: Time-averaged profiles of along-current and vertical velocities for the HTA experiments (a – c) and the VTA experiment (d – f). Note that the HTA experiments were not synoptic, and therefore panels a – c show mean velocities under different environmental conditions.

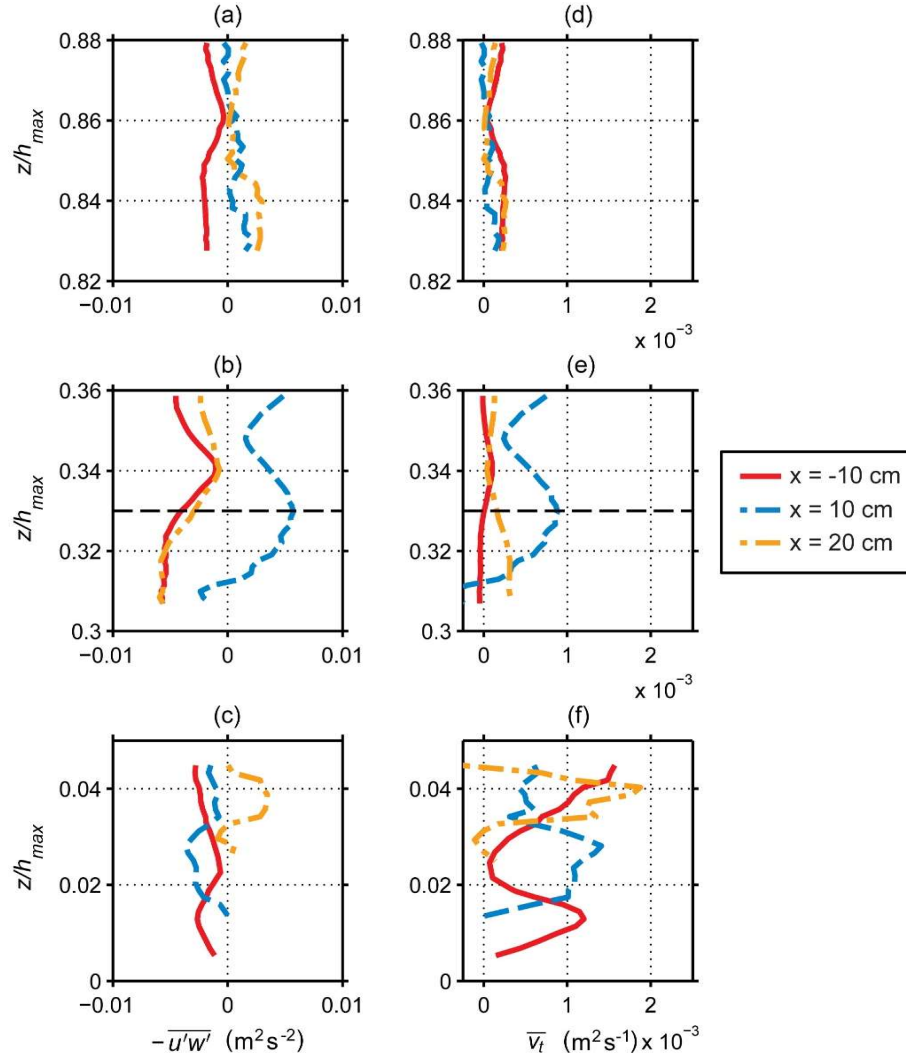


Figure 3.14: Time-averaged profiles of turbulence statistics for the HTA experiments: the vertical Reynolds stress $-\overline{u'w'}$, (panels a – c), and the eddy viscosity \overline{v}_t , (panels d – f). In panels (b, e), the dashed horizontal line denotes the mean canopy height $\langle h_c \rangle$. Note that the HTA experiments were not synoptic, and therefore each row of the figure shows turbulence statistics under different environmental conditions.

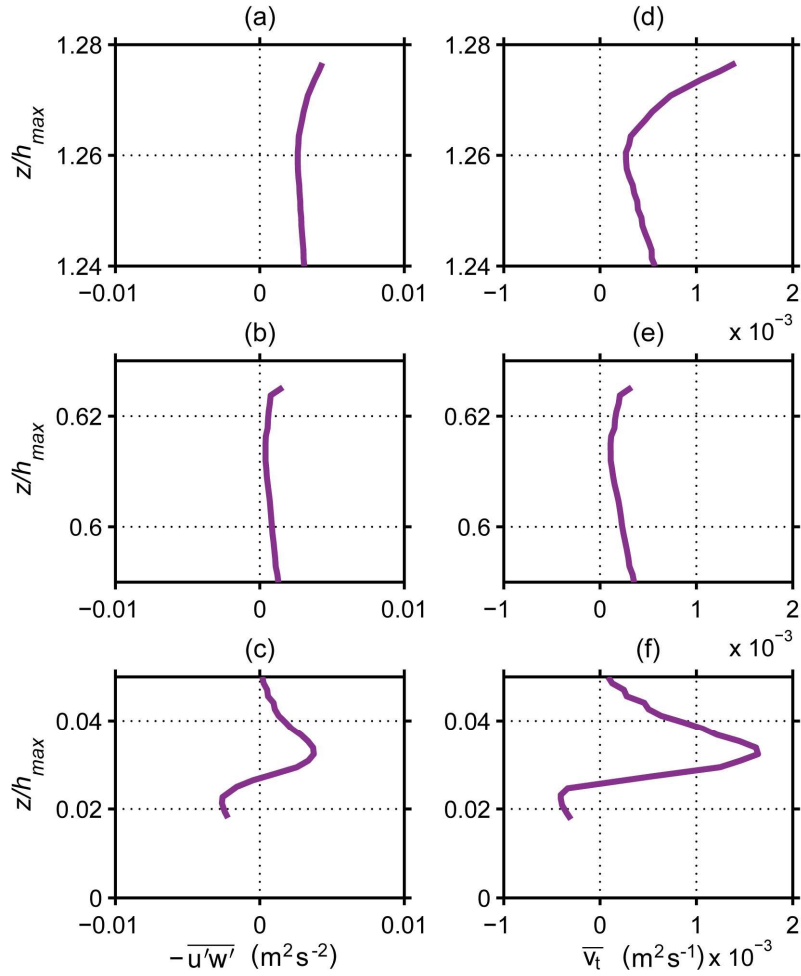


Figure 3.15: Time-averaged profiles of turbulence statistics for the VTA experiment: the vertical Reynolds stress $-\overline{u'w'}$, (panels a – c) and the time-averaged eddy viscosity $\overline{v_t}$, (panels d – f).

3.3.5 Canopy-Scale Currents

Time-averaged profiles of the u and w velocities are shown in Figure 3.13 for all experiments. From the synoptic VTA experiment, near-bed velocities were generally smaller in magnitude than those recorded above the pneumatophore canopy (compare Figures 3.13d – f). A zone of weak positive mean along-current velocities was observed in the location downstream of the dense region of the VTA canopy near the bed (Figure 3.13f). Similarly, during the HTA1 experiment, mean along current velocities were positive at the $x = 20$ cm and at the $x = -10$ cm array positions near the bed (Figure 3.13c). Around the mean canopy height during the HTA2 experiment (recalling $\langle h_c \rangle = 0.33$), strong flow was observed at the $x = 10$ cm array position, with weakening flow at the $x = 20$ cm and $x = -10$ cm positions (Figure 3.13b). Vertical velocities recorded at all three of these positions were negative. Just below the top of the HTA canopy (Figure 3.13a), horizontal velocities were strongly positive, and net vertical velocities were weakly negative at all three instrument positions.

Figures 3.14 and 3.15 depict time-averaged profiles of turbulence statistics for the HTA and VTA experiments, respectively. The first column of these figures shows depth profiles of the time-averaged Reynolds stress. Reynolds stresses were noisy and hence mean values are shown. Enhanced, positive Reynolds stresses were observed at the same positions of enhanced turbulence and wake shedding (Figures 3.14c, 3.14b, 3.15c), with the greatest stress (up to $5.3 \times 10^{-3} \text{ m}^2 \text{ s}^{-2}$) observed near the mean canopy height of the HTA2 experiment (Figure 3.13b). Reynolds stresses, in general, were diminished in the upper canopy array positions (Figures 3.14a and 3.15b), relative to the lower canopy array positions, but were enhanced in the area above the VTA canopy (Figure 14a). The second column of Figures 3.14 and 3.15 shows the eddy viscosity, $\nu_t = -\overline{u'w'} \cdot (\partial\overline{u}/\partial z)^{-1}$ (Trowbridge & Madsen, 1984), which is a measure of the effectiveness of vertical turbulent mixing of momentum, and is a fundamental parameter used in modeling the mean flow. Furthermore, the turbulent diffusivity, which can be used to model sediment suspension and mixing of ecologically significant chemicals, is expected to be comparable to the eddy viscosity (Lees, 1981). During the experiments, a few negative eddy viscosities were observed. Although localized regions of negative eddy viscosity are possible in spatially varying flows, these negative values likely result from the difficulty

obtaining accurate mean Reynolds stress estimates in statistically variable turbulent flows. Nevertheless, most eddy viscosities were positive, and in the range $0 - 1.9 \times 10^{-3} \text{ m}^2 \text{ s}^{-1}$. For comparison, adopting a standard mixing-length model (Lowe et al., 2005; Weitzman et al., 2015) and using the scaling in Appendix A.1 of Henderson et al., (2017) suggests a theoretical eddy viscosity of $\Lambda C_f u_0 \ell$, where ℓ is a mixing length, u_0 is a typical velocity magnitude (here taken to be the rms velocity), $C_f = 0.1$, $\Lambda = (4\pi)^{-1} a u_0 T_w$, and T_w is a typical wave period. The mixing length is expected to be somewhat less than the canopy height and the elevation above the bed. Taking typical values $\Lambda = 0.1$ (Henderson et al., 2017), $u_0 = 0.2 \text{ m s}^{-1}$, and $\ell = 0.1 \text{ m}$ gives a predicted eddy viscosity of $2 \times 10^{-4} \text{ m}^2 \text{ s}^{-1}$, consistent with direct observations. Therefore, the observed eddy viscosity is consistent with theoretical expectations, if the effects of the canopy on near-bed turbulence are accounted for.

The bed shear stress is often parameterized using a near-bottom drag coefficient $C_b = u_*^2 / U_d^2$. Such drag coefficients are often used to model bottom drag, and play a key role in many sediment transport formulations, for both unvegetated (e.g., Nielsen, 1992) and vegetated (Etminan et al., 2018; Yang and Nepf, 2018) cases. We do not measure shear stress at the elevation of the bed, but the shear stress at the elevation of a near-bed instrument is expected to have a similar magnitude. Therefore, the shear stress measured at the height of a near-bed instrument (denoted

$\sqrt{\overline{u'w'^2} + \overline{v'w'^2}}$) is quantified using a near-bed drag coefficient of the form

$$C_b = -\sqrt{\overline{u'w'^2} + \overline{v'w'^2}} / \overline{U_d^2}, \quad (3.10)$$

where the overbar represents a ten-minute-average. To summarize results, we vertically-average Reynolds stress and velocities along each individual Vectrino profile before evaluating (3.10). Due to rotating the horizontal components of velocity to the mean current direction, $-\overline{u'w'}$ was consistently 1 to 2 orders of magnitude larger than $-\overline{v'w'}$ making the term $\overline{v'w'^2}$ negligible in Equation (3.10). For all Vectrino observations, evaluating U_d^2 at the instrument elevation yields C_b between 4.5×10^{-2} and 4.8×10^{-1} , with a mean value of 2.6×10^{-1} and standard deviation 1.5×10^{-1} . These within-canopy estimates are one-to-two orders of magnitude higher than the values $1 - 3 \times 10^{-3}$ typically observed for bottom drag coefficients in the absence of vegetation (e.g., Feddersen et al., 2000; Geyer et al.,

2000). In many applications, near-bed stresses are parameterized in terms of overlying flow. Therefore, we re-evaluated the drag coefficient using shear stresses measured at near-bed instruments and U_d^2 evaluated above the canopy. Resulting drag coefficients remained very high (between 8.3×10^{-3} and 2.9×10^{-1} , with a mean of 6.7×10^{-2} and standard deviation 7.8×10^{-2}). Although bed stresses will differ from the near-bed stresses measured here, these elevated drag coefficients highlight the important role played by pneumatophores in greatly increasing the near-bed stress for a given overlying velocity. Generally, the near-bed wake-shedding regions of the canopies were associated with moderately large normalized friction velocities of $O(10^{-1})$ (Figure 3.16). Large values were also observed in the canopy regions where moderate to high stresses were observed, at $x = 10$ cm during the HTA2 experiment (e.g., Figure 3.14b) and above the VTA canopy at $z/h_{max} = 1.25$ (e.g., Figure 3.15a).

3.4 Discussion

The results presented in Section 3.3 suggest a complex pattern of flow, turbulence and coherent structures formed in the wake of the vertically heterogeneous canopies of pneumatophores. In both experimental sites, positive near-bed mean flows (Figures 3.13c, 3.13f) were associated with Von Kármán wake shedding (Figures 3.10a, 3.10c) that produced high turbulent energy dissipation (Figure 3.9c, 3.9f) behind canopy elements. The explanation for the weak reversal in the near-bed mean along-current velocity profile (Figure 3.13f) is unclear, although secondary circulation associated with pneumatophore patchiness (e.g., Sumer & Fredsøe, 1997) may have played a role. Wake shedding was also observed close to the canopy elements around the mean canopy height during the HTA2 experiment (Figure 3.10b). The alternation of positive and negative stresses (Figure 3.14b), large w_{rms}/u_{rms} ratios (Figure 3.12b), and high turbulent energy dissipation (Figure 3.9b) suggest a vertical recirculation zone formed in the canopy wake, similar to those observed in studies of atmospheric flows behind tree canopies (Detto et al., 2008) or in shallowly submerged coral reef environments (Hench and Rosman, 2013). Turbulence was lower in the middle position of the VTA relative to the HTA likely because the instruments were deployed adjacent to a sparser cluster of pneumatophores (Figure 3.6c) and hence there were fewer nearby upstream objects to generate wakes or other coherent turbulent structures. Throughout the VTA

experiment, normalized submergence depths h/h_{max} varied between 1.6 and 2.4. Enhanced turbulent dissipation (Figure 3.9d) and eddy viscosity (Figure 3.15d) in the region above the VTA canopy indicates that the upper array position ($z/h_{max} = 1.25$) was located within the canopy shear layer, or “vertical exchange zone” of elevated turbulence, as reported in Nepf & Vivoni, (2000). Although dissipation was also high in the upper part of the canopy during the HTA3 experiment (Figure 3.9a), measurements between experiments were not synoptic, and so we cannot confirm that high turbulence was created by the formation of a canopy shear layer. During the HTA3 experiment, normalized submergence depths h/h_{max} varied between 1.1 and 2.3, and so high turbulence early in the experiment could have been caused by wave breaking while the canopy was shallowly submerged.

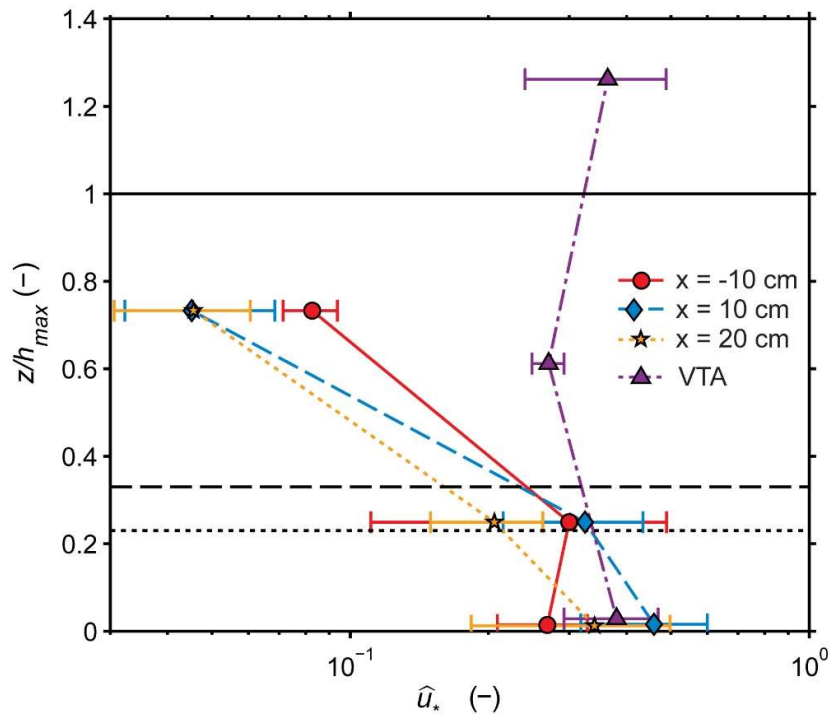


Figure 3.16: The depth and time-averaged squared friction velocity (u_*^2) scaled by the squared mean drift velocity $\langle U_d^2 \rangle$ for all experiments. Points shown are the mean value, with error bars of one standard deviation. Horizontal solid, dotted and dashed lines are the maximum and mean canopy heights of the HTA and VTA canopies, respectively.

In the synoptic vertical experiment (VTA), Reynolds stresses decreased from the maximum value above the canopy to much lower stress at the measurement position just above the bed (Figures 3.15a – c). Similar patterns have been observed previously in seagrass canopies (Hansen and Reidenbach, 2012; Lacy and Wyllie-

Echeverria, 2011) and in both rigid and flexible model canopies (Luhar et al., 2010; Pujol et al., 2013). Despite the observed dependence of stress on elevation, even near-bed stresses remained well above zero, and some high stresses were observed during both experiments (Figure 3.14, 3.15). Although this discussion has focused on the mean stress, additional fluctuating stress and turbulent dissipation is expected owing to the presence of waves, and it has been shown that these same pneumatophore canopies provided little shelter from wave-frequency motions (Henderson et al. 2017), consistent with low observed λ values (Section 3.1). Indeed, near bed stresses were significantly enhanced by the wave climate, as indicated by large values of the normalized friction velocity (a parameterization of near-bed stresses; Figure 3.16), and the drag coefficient relating near-bed stress to above-canopy velocity (Section 3.3.5). Hence, it is likely that these dense canopies, given the wave climate, could locally inhibit the deposition of fine sediment, which contradicts the expectation that dense vegetation promotes sediment retention.

The present study provides a unique dataset of the fine-scale flow features present in mangrove pneumatophore canopies. While the flow structure in and above canopies has been described for uniform-height vegetation analogues forced both by unidirectional currents (Ghisalberti & Nepf, 2006; Nepf, 1999; Nepf & Vivoni, 2000), and waves (Lowe et al., 2005; Pujol et al., 2013), flume studies employing variable-height canopies (Liu et al., 2010) that approximate the fine-scale flow dynamics around mangrove roots (Horstman et al., 2018) are less common. Furthermore, many experiments describing turbulent statistics in aquatic vegetation (e.g., turbulent dissipation, Reynolds stress, and eddy viscosity) have often been conducted in the flume (Dunn, 1996; Siniscalchi et al., 2012; and former references) or by using simplified numerical models (Bouma et al., 2007; Cui & Neary, 2008; Furukawa et al., 1997; Li & Yan, 2007; López et al., 2001; Mazda et al., 2005), which are both typically forced by unidirectional currents. Most analogous field studies were conducted in seagrass or cordgrass environments (e.g., Lacy & Wyllie-Echeverria, 2011; Leonard & Croft, 2006; Luhar et al., 2013; Neumeier, 2007), while those focusing specifically on mangrove roots are rare (with few exceptions, e.g., Furukawa & Wolanski, 1996; and recently Henderson et al., 2017; and Norris et al., 2017). Moreover, the spatially variable eddy viscosity has not been described within mangrove roots in situ before, despite often being a fundamental parameter

of numerical simulations of vegetated dynamics (Deltares, 2014; King et al., 2012; López et al., 2001).

Measured eddy viscosities ranged from $O(10^{-5} - 10^{-3}) \text{ m}^2 \text{ s}^{-1}$, with the maximum values reaching $1.9 \times 10^{-3} \text{ m}^2 \text{ s}^{-1}$. These eddy viscosities were consistent with simple models (Lowe et al., 2005; Weitzman et al., 2015, Henderson et al. 2017), and were also comparable to eddy viscosities of $O(10^{-5})$ to $O(10^{-4}) \text{ m}^2 \text{ s}^{-1}$ measured in situ within seagrass (*Zostera marina*) by Ackerman & Okubo (1993). In numerical models, vegetation effects are simulated through user-prescribed background eddy viscosities that differ between vegetated and non-vegetated areas. In two or three-dimensional models, horizontal (and vertical) time-dependent eddy viscosities are then resolved through a turbulence closure scheme (Deltares, 2014). Based on the results of the present study, the background eddy viscosities from a number of modeling experiments (Bouma et al., 2007; Bryan et al., 2017; Horstman et al., 2015; Temmerman et al., 2005) were within the expected range for natural vegetation (their values ranged from $O(10^{-4} - 10^{-3}) \text{ m}^2 \text{ s}^{-1}$ within vegetated areas).

3.5 Summary and Conclusions

Natural canopies of mangrove roots are spatially heterogeneous, with substantial variability in both height and diameter (Liénard et al., 2016). The presence of vegetation modifies the flow field by producing coherent structures that generate turbulence and induce mixing. When flows are influenced by waves, these effects are amplified by wave-driven currents, particularly in the dense region of the root canopies close to the bed (Section 3.3.5, Figure 3.16). Such patterns were observed in the present study: intense turbulence (up to $6.5 \times 10^{-4} \text{ W kg}^{-1}$) was found in the lower canopy regions and in the near-wake of canopy elements. Weaker turbulence was also associated with the decrease in canopy density with height within the vegetated region of the water column. Estimates of the eddy viscosity reached $1.9 \times 10^{-3} \text{ m}^2 \text{ s}^{-1}$, while values between $O(10^{-4} - 10^{-3} \text{ m}^2 \text{ s}^{-1})$ were also common. These observed viscosities are consistent with theoretical expectations, based on scaling arguments using a standard mixing-length model. Additionally, high near-bed Reynolds stresses correspond to drag coefficients up to one order of magnitude larger than expected for unvegetated areas. Hence, spatially variable vegetation affects both the vertical and horizontal distributions of turbulence, which in turn modifies the downstream drag on other roots (Nepf, 2004) and the sediment

transport capacity of the vegetation (Furukawa et al., 1997; Furukawa & Wolanski, 1996). This study emphasizes the need for future modeling or numerical studies to consider the horizontal and vertical variability found in natural vegetation to correctly represent turbulence or predict depositional patterns.

Chapter 4

Hydrodynamically Driven Changes in the Bed Elevation within a Coastal Mangrove Forest



Ripples and other depositional features are created by waves as they pass through the mangrove fringe.

Contribution of Authors

Chapter 4 presents the article entitled “The Response in Bed Elevation to Small-scale Hydrodynamic Forcing within Coastal Mangroves”, which will be submitted to *Geomorphology* for review. Data were collected for this study during two field seasons (Section 1.6) in Vietnam by myself, Dean Sandwell, Julia C. Mullarney, and Stephen M. Henderson. I wrote scripts to load, quality control, and analyze all of the hydrodynamic data. I also prepared all of the figures and wrote the initial and subsequent drafts of this manuscript. My co-authors, Julia C. Mullarney, Karin R. Bryan and Stephen M. Henderson edited my drafts and provided helpful comments and direction.

Abstract:

Field experiments were carried out within a wave-exposed coastal mangrove forest to quantify the change in bed level throughout a tidal cycle using high-resolution velocity and bed level measurements collected in situ. Experiments spanned the unvegetated mudflat, mangrove forest fringe and forest, where data were collected during single tidal cycles (flood-ebb) during a two-week period. Cross-wavelet transforms of the velocity and bed level measurements were often highly correlated ($\geq 90\%$ squared coherence) over a range of frequencies, spanning those corresponding to short-period wind and swell waves to long-period infragravity waves. Bed level change events associated with short-period waves were more frequent in the mudflat and fringe, while those associated with long-period waves were much more frequent in the forest. Net bed level changes over single events were nearly normally distributed, indicating similar numbers of events resulting in accretion and erosion, regardless of the across-shore position. Still, bed level change events exceeding the observed net tidal elevation change occurred infrequently. This pattern suggests that the net tidal elevation change within the mangrove forest must be related to the frequency of these infrequent events. Large bed level changes were often associated with high bed shear stresses ($0.3 - 1.5 \text{ N m}^{-2}$) and turbulence of $O(10^{-3} \text{ W kg}^{-1})$, particularly on the mudflat and in the forest fringe. Across all experiments, the mudflat and forest site experienced net accretion (4.5 and 6.8 mm, respectively) while the fringe experienced net erosion (-9.5 mm). This work suggests a dynamic role for waves in mangroves: short-period waves stir sediment on the mudflat and forest fringe, while infragravity waves help advect entrained sediment inside the forest.

4.1 Introduction

Mangroves are salt-tolerant shrubs and trees that thrive in the intertidal areas of tropical and subtropical coastlines. Mangroves are characterized by their massive above-ground root systems that actively dissipate incident wave energy (Massel et al., 1999; Mazda et al., 2006), reduce current velocities (Furukawa et al., 1997; Mazda et al., 1997a; Wolanski et al., 1980), and facilitate the deposition of fine-grain sediments through the stagnation of sediment-laden water (Furukawa & Wolanski, 1996; Wolanski, 1995a; Wolanski et al., 1996). Over time, the accumulation of terrigenous sediment and organic material in mangroves can lead to the aggradation of mangrove shorelines. Given these bio-physical feedbacks, a substantial amount of work has focused on whether mangrove forests have kept pace with fluctuations in eustatic sea level throughout the Holocene (Ellison, 2009; Fujimoto, 1998; Krauss et al., 2010; Lovelock et al., 2011; McKee, 2011; 2007; Walsh & Nittrouer, 2004; Woodroffe, 1990). However, to understand whether mangrove surface elevation can track local sea level rise into the future, there needs to be a thorough understanding of the physical processes controlling bed elevation change in mangrove systems. In general, these processes can be divided into surficial (i.e., sedimentation, accretion and erosion), as well as sub-surface processes (i.e., the growth or decomposition of roots, and changes to soil properties such as compaction or expansion) (McIvor et al., 2013). The former is the focus of this study, specifically the impact of mangrove vegetation on accretion and erosion. Key variables that determine the depositional patterns in mangroves are thought to be the sediment supply to the forest, hydrodynamic setting, and vegetation density (Krauss et al., 2003; Kumara et al., 2010; Rogers et al., 2006; Woodroffe, 1992).

Suspended sediment is transported into mangrove swamps through the combined action of tides and waves (Van Santen et al., 2007; Woodroffe & Davies, 2009) or through high-magnitude storm or tsunami events (Ellison, 2009). Sediment trapping by mangroves is thought to be facilitated by the generation of turbulence in the wake of mangrove roots, which breaks up flocs and creates stagnation zones in which sediment can be deposited (Furukawa et al., 1997; Wolanski, 1992; 1995). Elevated turbulence levels maintain suspended sediment concentrations until current velocities drop close to slack tide (Furukawa & Wolanski, 1996). Deposited sediment is not re-entrained during the ebb tide so long as currents remain lower

than critical shear thresholds. The resulting asymmetry between flood and ebb tidal currents results in a net import of sediment into mangrove forests (Furukawa et al., 1997; Horstman et al., 2015; Van Santen et al., 2007; Wolanski et al., 1990).

In general, vegetated regions tend to reduce wave orbital velocities relative to waves above a plain bed (Hansen & Reidenbach, 2012). Previous studies have shown that aquatic vegetation acts as a low-pass filter of wave energy, with longer-period waves penetrating greater distances within vegetated regions (Bradley & Houser, 2009; Hansen & Reidenbach, 2012; Horstman et al., 2012; Riffe et al., 2011; Vo-Luong & Massel, 2008). While the role of short-period waves in sediment transport and resuspension in coastal mangroves has been qualitatively described (e.g., Van Santen et al., 2007; Winterwerp et al., 2005), the role of long-period infragravity waves has yet to be explored. Short period wind and swell waves can easily erode the soft mud of mangrove coastlines (Winterwerp et al., 2005). Although mangroves typically inhabit sheltered intertidal areas that are only exposed to weak currents and small waves, the high-energy conditions typical of storm events can cause large-scale erosion of the mangrove platform (Van Santen et al., 2007). While short-period waves may be readily attenuated over hundreds of meters within mangrove forests (Henderson et al., 2017; Horstman et al., 2012; Vo-Luong & Massel, 2008), long-period infragravity waves require substantially larger widths (up to 10x) of forest to be effectively attenuated (Phan et al., 2015). Hence, it has been hypothesized that short-period waves do not play a major role in determining the sedimentation regimes within a mangrove forest (Phan et al., 2015). Instead, forest-scale patterns in sedimentation may be controlled by the propagation of infragravity waves.

Depositional patterns are also affected by the spatial variability in vegetation density across vegetated regions. The abrupt change in roughness from mudflat to vegetation cover can induce turbulence (Nepf, 1999) which reduces the settling of fine particles and can cause the resuspension of deposited material around the edges of the mudflat (Neumeier, 2007; Widdows et al., 2008). Further inside the forest, turbulence may also encourage the deposition of fine-sediments in stagnation zones created in the wake of mangrove roots (Furukawa et al., 1997). Actual depositional patterns are highly dependent on the vegetation properties, sediment supply and characteristics, and local hydrodynamic conditions. For example, while some

authors have observed a positive correlation between sediment accretion and mangrove root densities (Kumara et al., 2010; Young and Harvey, 1996), others have observed the opposite effect (Krauss et al., 2003; Mullarney et al., 2017b; Spenceley, 1977). These accretionary trends likely reflect the balance of drag forces and turbulent dissipation, which is governed by the spatial distribution and density of the vegetation. Enhanced turbulence at the fringe of the forest stirs up sediments and decreases incident wave energy, eventually creating a relatively sheltered forest interior that is favorable to sedimentation (Norris et al., 2017).

While sediment transport is generally considered to be driven by the near-bottom shear stress, this stress is difficult to quantify in vegetated areas (Le Bouteiller and Venditti, 2015). Over denuded beds, the bed shear stress can be estimated from the near-bed friction velocity derived from a simple law-of-the-wall relationship. However, in regions of submerged dense vegetation, skimming flow precludes the formation of a logarithmic boundary layer as flow is severely reduced within the canopy (Ghisalberti & Nepf, 2006; Nepf & Vivoni, 2000). Rough-wall boundary layers may still form in sparse vegetation (Poggi et al., 2004) as observed in field experiments by Sukhodolov & Sukhodolova, (2006) and Lacy & Wyllie-Echeverria, (2011). Recently, several studies have developed methods for estimating bed shear stresses in vegetated systems (Etminan et al., 2018; Yang et al., 2016; Yang and Nepf, 2018), the latter method we have employed for the vegetated cases presented here. Evidence suggests that high near-bed turbulence levels are correlated with high bed load fluxes, and the formation of scour holes and other sedimentary structures (Yager and Schmeckle, 2013). Such depositional patterns have been observed in mangroves before (Mullarney et al., 2017b; Norris et al., 2017); however, these patterns have not yet been quantitatively linked to the hydrodynamic climate.

The purpose of this chapter is to investigate the causes of bed level variability throughout a tidal cycle within varying densities of mangrove pneumatophore roots across a transect of mangrove vegetation. The goals of this study are to quantify: (i) the spatial and temporal variation in the bed level within patches of roots, (ii) the hydrodynamic forcing conditions expected to correlate with bed movement (i.e., the bed shear stress, turbulence, and mean current velocity), and (iii) the effect of hydrodynamic burst (or event) length on bed level change throughout the tidal

cycle. Results for mangrove vegetation are compared to the unvegetated mudflat as a control.

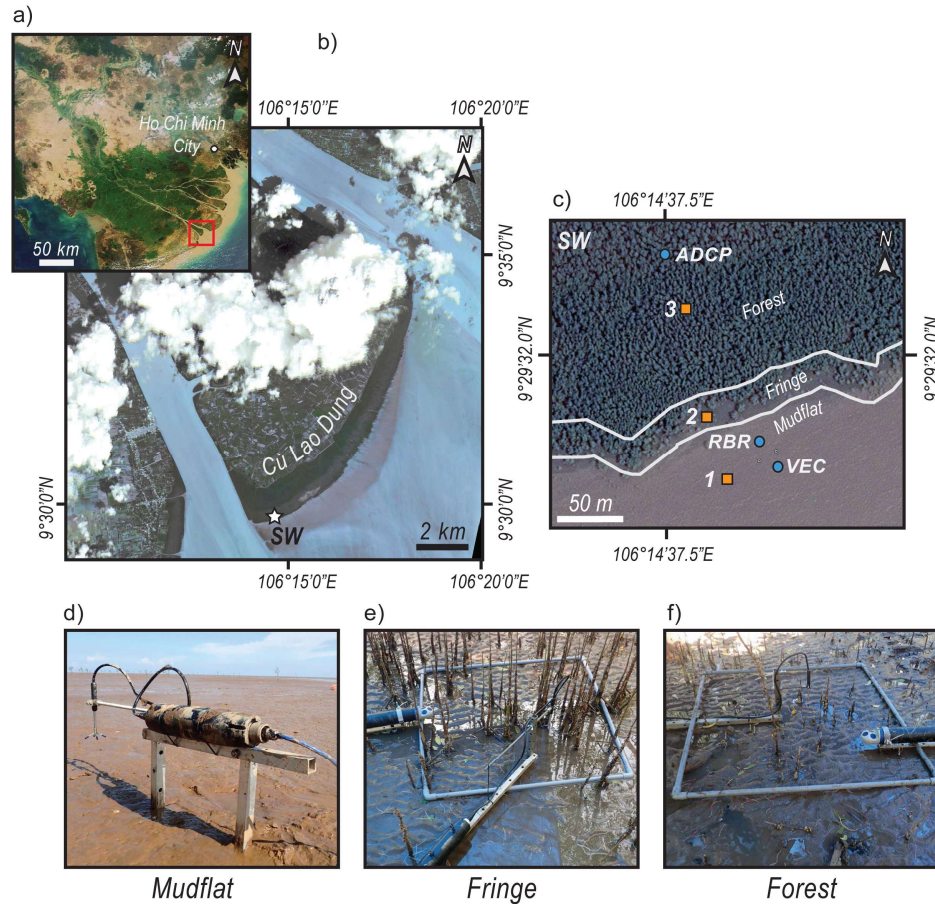


Figure 4.1: Deployment location. Panel (a) Regional context of deployment region (red square) situated within the lower Mekong Delta. (b) Deployment locations (SW) on the seaward edge of Cù Lao Dung, shown in detail in panel (c), where white lines denote the relative position of the boundaries between the mudflat, fringe and forest. Fixed instruments are denoted with blue circles, and moveable array sites 1–3 with orange squares. Panels (d, e, f) photos of deployment configurations in each of the three environments, 1 m² quadrats for scale. Note, the mudflat ADCP is not shown in panel (d). Data sources are respectively, Envisat (a), Rapideye (b), Google Earth (c).

4.2 Methods

4.2.1 Field Site

Field observations were conducted in the mangrove forest fringe that lines the seaward shore of Cù Lao Dung in the southern Mekong River Delta, Vietnam (Figure 4.1a – b). The lower southwestern corner of the island is prograding rapidly, with a sandy substrate and a shallow slope of approximately 1 in 800 (Bryan et al.,

2017). Here, a wide belt of young *Sonneratia caseolaris* mangroves inhabit the shoreward 150 m of forest, with the highest tree density in the forest fringe (Bullock et al., 2017). The island is fronted by a shallow interlaminated mud and sand flat that stretches seaward several kilometers in the southwest (Fricke et al., 2017). Waves generated offshore in the East Sea (South China Sea) propagate directly across the mudflat and into the forest. Experiments were conducted over a neap-spring transition during a two-week period in March 2015 under northeast monsoonal conditions. This period was characterized by moderately high wind speeds (~10 m/s) close to the along-shore direction, and significant wave heights up to 0.7 m offshore of the mangrove forest (Chapter 3).

4.2.2 Measurements

Instrumented frames were placed on the mudflat, mangrove fringe and forest to characterize the hydrodynamics and sediment dynamics of each area. Deployments consisted of fixed-location sensors that recorded nearly continuous measurements for the two-week period, and a series of ‘moveable array’ sensor packages that were relocated after approximately 24 – 48 hours of data collection (Figure 4.1, Sites 1 – 3). A total of 19 individual moveable array deployments were conducted in different locations within the mudflat, forest fringe and forest for a total of 29 flood and/or ebb tidal experiments (see: Norris et al., 2017 for details). This chapter focuses on six typical experiments from the 2015 field season (for a total of 14 measurement locations; Table 4.1). In addition to the hydrodynamic measurements, surface sediment samples were collected daily by hand near the moveable arrays.

The fixed-location instruments consisted of a Nortek Vector (VEC) deployed on the mudflat, an RBR Duo deployed near the mudflat/mangrove forest boundary, and a 2MHz Nortek Aquadopp (ADCP) deployed approximately 150 m inside the forest (Figure 4.1c). The RBR logged temperature, pressure and optical backscatter at 6 Hz and the Vector logged wave and current velocities, temperature and pressure continuously at 32 Hz. The Aquadopp was collocated with two vertically separated Campbell Scientific OBS 3+ optical backscatter sensors set at 0.15 and 0.40 m above the bed, and logged current velocities, pressure, temperature, and backscatter over 10-minute bursts at a sampling frequency of 2 Hz. Optical backscatter sensors were calibrated using in situ water samples collected nearby to obtain suspended

sediment concentrations (see: Fricke et al., 2017 for details). All fixed instruments were deployed near the bed on low-profile mounts to allow near-bed measurements while minimizing flow interference.

Moveable array sensor packages each consisted of a single 10 MHz Nortek Vectrino Profiler ('Vectrino') to measure near-bed flow velocities, and a single ADCP to measure the water depth and wave climate at each deployment location. With one exception, each deployment consisted of a single moveable array package deployed at three locations along an across-shore transect line in the mudflat, fringe and forest (Figure 4.1d – f). The exception was the experiment conducted on March 9th, 2015 (Table 4.1), when all three Vectrinos were deployed in the fringe to study the heterogeneity of flow patterns across a small area. The moveable-array ADCPs were set to record nearly-continuous measurements at 8 Hz in pulse-coherent mode over a profile ranging from 0.22 – 0.45 m above the bed surface at a bin resolution of 0.025 m. The three Vectrinos were connected to a laptop and logged near-bed velocity profiles 0.035 m in length at a bin resolution of 0.001 m almost continuously at 50Hz. In addition to velocity measurements, the Vectrinos also provide an estimate of the bed level from a downward-looking center transducer that records acoustic returns over a short range. The approximate bed level position is returned as the point of maximum near-bed backscatter at a sample rate of 10 Hz (Section 4.2.4.4). Hydrodynamic measurements were collected with the movable arrays during the rising flood tide and falling ebb tides of the dates listed in Table 4.1. The ADCPs were set to record for the duration of each experiment. Vectrino data were collected from the time at which all of the instruments were submerged by the rising tide (approximately 20 – 40 minutes after low tide) until just before high tide.

The root canopy at each site (where applicable) was surveyed using the photogrammetric method of Liénard et al., (2016). Datasets consisting of 50 – 300 photos taken of each quadrat from all angles were input into an open-source photogrammetric reconstruction software to generate a 3D point cloud of overlapping feature matches. Vegetation geometry was then reconstructed from each point cloud using a 'sector-slice' algorithm (Liénard et al., 2016). The frontal area density a [m^{-1}] of the canopy as a function of height above the bed was calculated as the number of stems per square meter (n) times the mean stem

diameter (d). Root clusters upstream of the Vectrinos were determined by manually comparing each of the reconstructed root canopies with the dominant 10-minute averaged current and wave directions at each measurement site (Figure 4.2). Wave directional spectra were computed from pressure and velocity measurements recorded by the ADCPs in each moveable array following the method outlined in Gordon and Lohrmann, (2002). Current and wave directions (Figures 4.2a and c) were compared to quadrat surveys rectified into the across and along-shore direction (Figures 4.2b and d) to determine which roots nearby the Vectrinos would likely have generated measureable flow disturbance. Past research has shown that the wake produced by dense clusters of cylinders with mean diameter d resembles that of a larger solid body with diameter D (e.g., Chen et al., 2012; Nicolle and Eames, 2011). It is also expected that enhanced turbulence can be measured by near-bed instruments up to (if not greater than) 20 cm from dense patches of pneumatophore roots (Norris et al., 2019). Hence, clusters of roots nearby the Vectrinos were assigned a width of D if more than four roots were within 20 cm upstream of the instrument (Figure 4.2c and d). For cases with individual isolated roots nearby the instruments (e.g., Figure 4.2a and b), $D = d$. The dimensionless population density aD [-] is reported in Table 4.1 for each experiment as an estimate of the root density in each location.

In one case, two photo surveys were collected of the same experiment location during low tide before and after the experiment on March 9th, 2015 to examine the spatial changes in the bed level across a single tidal cycle. The point clouds were aligned in the freeware CloudCompare using the basal center points of the pneumatophore roots in each cloud for reference. The mean uncertainty in the alignment was 8 mm, which was assessed by measuring the distance between the center points of 40 pneumatophore roots after aligning the point clouds. These point clouds were interpolated into rasters using a GIS (ESRI ArcMap 10.2) and then were differenced to produce a map of bed level change (Section 4.3.2).

Table 4.1: Locations of hydrodynamic and sediment measurements (ref. Figure 4.1 for locations), deployment durations and general conditions during the experiments. All experiments were conducted in 2015. Column headers are as follows: T_p = peak wave period, H_s = significant wave height, n = number of pneumatophores per square meter, aD = normalized root density, z = Vectrino probe height above bed, d_{50} = median grain size, Sand = percent sand in sediment sample, Mud = percent mud in sediment sample.

Tidal stage	Date	Area	Site	Start Time	Duration (min)	T_p (s)	H_s (m)	n (m ⁻²)	aD (-)	z (m)	d_{50} (μm)	Sand (%)	Mud (%)	
Flood Tide	03/06	Mudflat	1	13:37:46	204	2.40	0.26	0	0	0.06	58.2	85	15	
		Fringe	2			2.40	0.26	102	0.07	0.06	123.2	94	6	
		Forest	3			2.32	0.13	37	0.02	0.06	35.8	5	95	
	03/09	Fringe	2	2:10:00	140	4.34	0.20	66	0.42	0.24	123.2	94	6	
	03/11	Mudflat	1			3.31	0.39	0	0	0.06	58.2	85	15	
		Fringe	2			3.07	0.33	45	0.06	0.06	123.2	94	6	
		Forest	3			3.03	0.17	84	0.03	0.06	50.1	37	63	
	Ebb Tide	03/05	Mudflat	1	15:32:10	80	2.44	0.22	0	0	0.13	153.6	85	15
			Fringe	2			2.42	0.22	102	0.22	0.13	199.4	94	6
Forest			3	2.25			0.12	37	0.02	0.08	77.2	5	95	
03/09		Fringe	2	4:30:00	140	4.34	0.20	66	0.42	0.24	123.2	94	6	
03/12		Mudflat	1	7:01:55	131	3.01	0.29	0	0	0.06	153.6	85	15	
		Fringe	2			2.63	0.20	45	0.06	0.06	199.4	94	6	
		Forest	3			2.50	0.10	84	0.03	0.06	81.0	37	63	

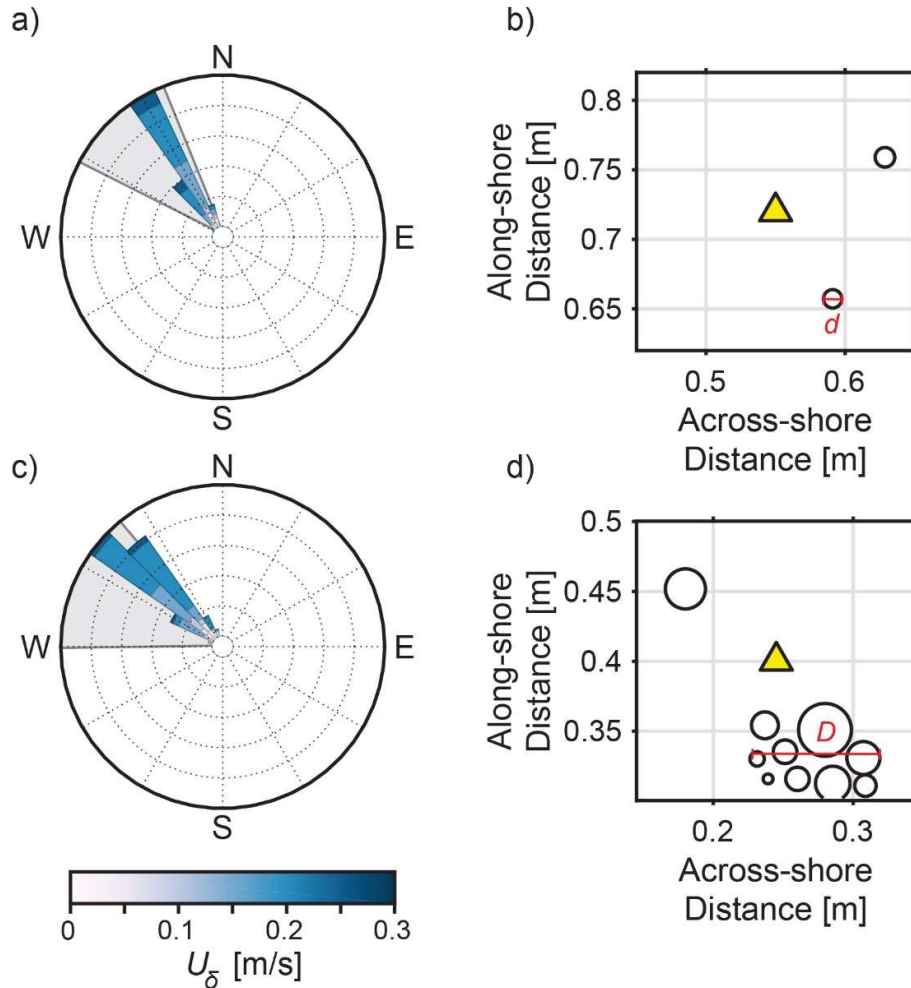


Figure 4.2: Method for estimating patches of pneumatophore roots from two of the flood tide experiments, March 11th, 2015 (panels a and b), and March 9th, 2015 (panels c and d). Panels (a, c) show the 10-minute averaged current direction measured by the ADCPs collocated with the Vectrinos as a grey sector. Current velocity magnitudes averaged 0.1 m/s during the March 11th, 2015 experiment, and 0.08 m/s during the March 9th, 2015 experiment. Panels (a, c) also show the dominant wave direction (to) colored by the wave orbital velocity. Panels (b, d) show a 20 cm² subsampled region of each quadrat survey around the Vectrino (yellow triangle). Pneumatophore basal diameters are depicted as black circles. The patch width D or individual root diameter d is shown in red for roots upstream of the Vectrinos.

4.2.3 Sample Analysis and Data Quality Control

In the laboratory, surface sediment samples were homogenized, mixed with a 0.05% sodium hexametaphosphate solution to deflocculate the samples, and then were sonicated for 15 minutes to disperse the grains. Grain size analysis was carried out on a Beckman-Coulter LS13320 Laser Diffraction Particle Size Analyzer (A. Fricke, *pers. comm.*, 2018). The classification for particle sizes follows Folk & Ward, (1957): sand ($2 - 0.063\text{mm}$), silt ($0.063 - 0.004\text{ mm}$), and clay ($<0.004\text{ mm}$). Median grain sizes for the experimental sites are reported in Table 4.1.

ADCP data were processed to remove low quality data corresponding to correlations below 70% and phase-wrapped velocities (e.g., Lohrmann et al., 1990). Vectrino and ADV data were similarly processed to remove data corresponding to low correlations and signal-to-noise ratios, and then were despiked following the routine outlined by Goring & Nikora, (2002). For experiments when the Vectrinos were mounted close to the bed (where $z \leq 0.06\text{ m}$, 63% of experiments; Table 4.1), the wave bottom boundary layer (WBBL) thickness was computed for each instrument (see: Norris et al., 2017 for details). All measurements within the WBBL and below the bed level were removed prior to analysis. Data gaps were filled either using a linear or cubic fit for gaps less or greater than 100 points, respectively. Finally, all velocity data were rotated into an across-shore (u), along-shore (v), and vertical (w) coordinate system.

4.2.4 Data Analysis

4.2.4.1 Mean Velocity and the Dissipation Rate of Turbulence

Both the mean velocity and turbulent kinetic energy (TKE) dissipation rate estimates were calculated from the Vectrino velocity records for the duration of each experiment. Velocity records sampled at 50 Hz were segmented into 3-minute bursts each containing $n = 9000$ samples and windowed time series were computed at 1 Hz. The mean velocity was computed for each burst. The dissipation rate was calculated for each Vectrino depth bin using the structure function method of Wiles et al., (2006). This method, described in greater detail in Chapter 2, uses differenced adjacent along-beam locations ('bins') up to a number of lags ('bin distances') along a profile of vertical velocities. This differencing technique has proven to be

effective at filtering out large-scale vertical variability, such as wave oscillations, that are not associated with inertial turbulence (Wiles et al., 2006). With four beams, the Vectrino provides two independent estimates of the vertical velocity, w_1 and w_2 . Velocity differences of each vertical velocity profile were computed at steps of 1 mm to a maximum lag of 5 mm, producing a profile of TKE dissipation rate estimates up 30 mm in length (or shorter, depending on the location of the bed and height of the WBBL). Finally, the two dissipation rate estimates were averaged together to produce one estimate per second, per depth bin.

4.2.4.2 Bed Shear Stress under combined Waves and Currents (τ_{cw})

Over submerged, un-vegetated surfaces, the velocity profile follows the law of the wall, where the logarithmic velocity for a rough bottom is described by the Kármán-Prandtl equation,

$$\frac{u(z)}{u_*} = \frac{1}{\kappa} \ln \left(\frac{z}{z_0} \right) \quad (4.1)$$

where $\kappa = 0.4$ is Von Kármán's constant, z_0 is the bed roughness amplitude [m], and u_* [m/s] is the friction velocity (Soulsby & Dyer, 1981; Whitehouse et al., 2000). The bed shear stress due to currents is given by, $\tau_c = \rho u_*^2$, where ρ is the density of sea water [= 1025 kg/m³]. For vegetated surfaces, τ_c can be estimated using the bed shear stress model developed by Yang et al., (2015):

$$\tau_c = \begin{cases} \frac{4\rho v \bar{u}}{d}, & Re_d = \frac{\bar{u}d}{\nu} < \frac{4}{C_f} \\ \rho C_f \bar{u}^2, & Re_d \geq \frac{4}{C_f}. \end{cases} \quad (4.2)$$

Here ν is the kinematic viscosity of seawater [= 1.05 x 10⁻⁶ m²/s], \bar{u} is the near-bottom mean current velocity, and C_f is the bed drag coefficient, estimated using a semiempirical equation containing the water depth h and the median sediment grain size d_{50} (e.g., Yang and Nepf, 2018),

$$C_f = \frac{1}{[5.75 \log(2h/d_{50})]^2}. \quad (4.3)$$

The wave-induced bed shear stress (τ_w) is obtained from the peak bottom orbital velocity U_δ and the wave friction factor, f_w (Van Rijn, 1993),

$$\tau_w = \frac{1}{4} \rho f_w U_\delta^2. \quad (4.4)$$

The peak wave orbital velocity is calculated from the near-bottom velocity spectra, S_{uu} and S_{vv} , for the u and v components of velocity using Welch's method (e.g., Wiberg and Sherwood, 2008),

$$U_{\delta} = \sqrt{2 \sum S_{uv,i} \Delta f_i}, \quad (4.5)$$

where $S_{uv} = S_{uu} + S_{vv}$ is the combined horizontal spectrum, with individual frequency band i . Following the approach in Madsen, (1994), the representative wave frequency, ω_r [s^{-1}] corresponding to U_{δ} is,

$$\omega_r = \frac{\sum_i \omega S_{uv,i} \Delta f_i}{\sum_i S_{uv,i} \Delta f_i}, \quad (4.6)$$

where $\omega = 2\pi f$ is the radian frequency, and the representative bottom wave period $T_r = 1/\omega_r$. We use Nielsen, (1992) to predict wave friction factors as a function of a physical bottom roughness. Madsen, (1994) described the wave friction factor as,

$$f_w = \exp \left[a_1 \left(\frac{U_{\delta}}{k_w \omega_r} \right)^{a_2} \right] + a_3; \quad (4.7)$$

where a_1 , a_2 and a_3 are provided by Nielsen, (1992) as 5.5, -0.2 and -6.3, respectively. The relation between the hydraulic roughness length k_w and z_0 from Equation (4.1) is $k_w = 30z_0$ for fully rough turbulent flow (Jonsson, 1966). From Soulsby, (1997), the time-averaged and cycle-mean bed shear stress due to currents and waves (τ_m , [N/m^2]) is,

$$\tau_m = \tau_c \left[1 + 1.2 \left(\frac{\tau_w}{\tau_c + \tau_w} \right)^{3.2} \right]. \quad (4.8)$$

Finally, the maximum shear stress (τ_b) during a wave cycle is,

$$\tau_b = [(\tau_m + \tau_w |\cos \phi|)^2 + (\tau_w |\sin \phi|)^2]^{0.5} \quad (4.9)$$

where ϕ is the angle between the mean currents and the direction of wave travel (Soulsby, 1997). Here, we compare τ_b against the critical shear stress τ_{cr} to determine the occurrence of sediment motion.

In the present experiment, shear stress estimates were calculated using a 3-minute window ($n = 9000$) and a 1-second step to produce a 1 Hz time series to compare with the other hydrodynamic parameters. The bed roughness length z_0 was computed by fitting Equation (4.1) using near-bottom across-shore mean velocity profiles measured by Vectrinos. Bursts that produced unrealistic roughness ($z_0 > 0.1$ m) were discarded, although most (83% of) z_0 estimates fell within the realistic range of $O(10^{-4} - 10^{-2})$ m. For the mudflat sites, τ_c was only calculated for bursts

exhibiting a logarithmic profile, determined by $r^2 > 0.7$ from the least squares regression of $u(z)$ and $\ln(z)$ (Figure 4.3). In all other cases, τ_c was estimated from near-bottom velocities, water depths and local sediment and vegetation properties using Equations (4.2 – 4.3). Estimates of τ_w were computed from ADCP measurements and the estimates of z_0 with Equations (4.4 – 4.7). Finally, the maximum combined current-wave shear stress τ_b was computed with Equations (4.8 – 4.9).

4.2.4.3 Critical Shear Stress (τ_{cr})

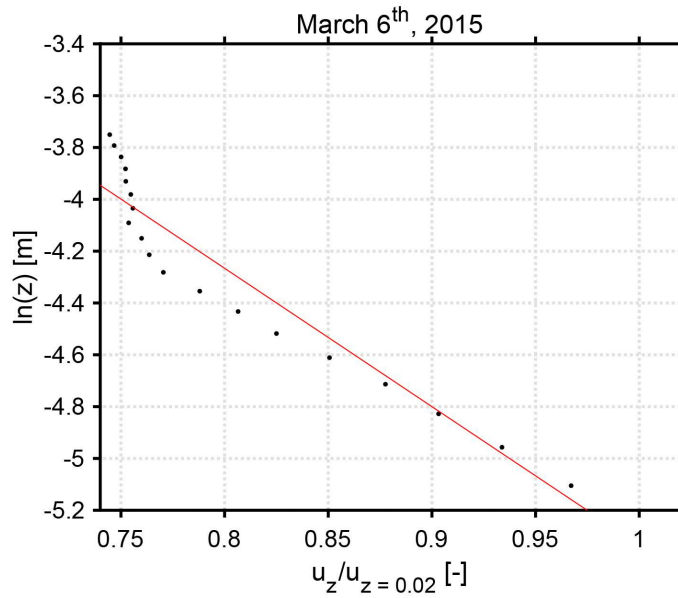


Figure 4.3: An example logarithmic fit (red line) to 10 min time-averaged velocity profiles (Equation 4.1). Data are from the mudflat site. The velocity measurements are normalized by the measurement closest to the bed. The r^2 of this example is 0.94 with $p\text{-val} < 0.05$.

As the substrates of the experimental sites ranged from dominantly sandy to dominantly muddy (Table 4.1), critical shear stresses had to be determined on a per-site basis using either a formulation for cohesive or non-cohesive sediments. Sediment samples were first grouped as cohesive or non-cohesive by the percentage of mud in each sample, where cohesive sediments were $> 15\%$ mud (Van Rijn, 1993). To compute the critical shear stress of the samples, we employed a formula developed by Wu et al., (2018) which is applicable across a range of sand and mud mixtures (between 0 – 100% mud content). This formula was developed using experimental data from several laboratory experiments where the sediment mixture ratios and grain sizes were known. To apply the formula, a user needs only to know

the percentages of sand and mud in each sample, the median diameters (d_{50}) of the sand and mud fractions (Table 4.1), and the dry density of the sample, which can be computed from the mixture d_{50} and Eqns. (3 – 4) from Wu & Wang, (2006). All other parameters required by the formula are given in Wu et al., (2017), which were derived from the other laboratory experiments. For the cohesive samples, shear stresses were computed from the sediment parameters in Table 4.1 and data from Smith et al., (2015), who measured the shear stresses of sand and Mississippi River mud mixtures over a range of 0 – 100% mud content. For the non-cohesive samples, shear stresses were computed from parameters in Table 4.1 and data from Panagiotopoulos et al., (1997) who estimated the shear stresses of low mud content mixtures.

4.2.4.4 Bed Level Extraction

Bed level identification was conducted by analyzing the backscatter returns from the Vectrinos. For near-bottom mounted instruments, two boundaries are distinguishable in the backscatter: the bed fluid interface, identified by the depth with the maximum change in acoustic backscatter, and the bed surface, identified by the depth of maximum backscatter (Staudt et al., 2017). As shown in Figure 4.4a, there is a band of high amplitude returns near -5 dB (where 0 dB is maximum) that signifies the bed surface. Above this depth, the backscatter in the water column varies between -15 and -10 dB, indicating a high concentration of suspended sediment. This suspended sediment and other organic detritus floating in the water (e.g., leaves, etc.) affects the instantaneous bed level reported by the instrument (Figure 4.4b). To estimate the bed level, the instantaneous bed level was despiked using a 512-point running-median (red curve, Figure 4.4b). The averaged bed level was compared to the depth of maximum amplitude in the backscatter to confirm its accuracy for each experiment (Figure 4.4a). Generally, a 512-point running median was sufficient, but in a few cases, either a shorter or longer window was used to produce accurate bed level traces.

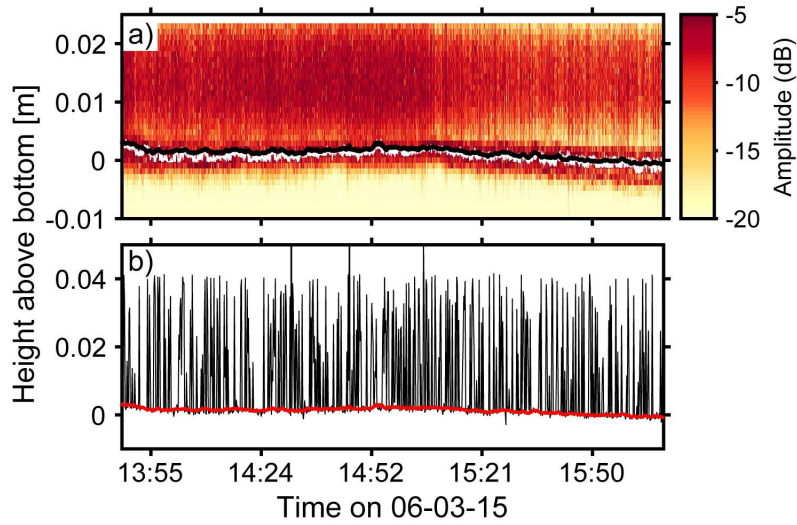


Figure 4.4: Example raw data from the experiment conducted on March 6th, 2015 at Site 3 used to identify the bed level. Panel (a) Vectrino acoustic amplitude returns, where the maximum value of the amplitude (white) is compared to the reported averaged bed level (black) from panel (b). Panel (b) Reported instantaneous (black) and running median (red; 512-point window) of the bottom track of the Vectrino.

4.2.4.5 Wavelet Analysis

For signal processing, wavelet analysis was used to examine the coherence between velocity oscillations and irregular fluctuations in the bed level beneath each Vectrino. Here, the across-shore velocity was correlated to the bed level using a cross wavelet transform (XWT), and a non-orthogonal Morlet wavelet with a non-dimensional frequency $\omega_0 = 6$ to satisfy the admissibility condition (Farge, 1992). The Morlet wavelet provides a good balance between time and frequency localization (see: Grinsted et al., 2004), and provides realistic images of the oscillations that are common to both periodic and aperiodic signals, such as those found in velocity and bed level fluctuations, respectively. The statistical significance level of the wavelet coherence was calculated using the chi-squared test for power spectra (since the wavelet spectrum is chi-squared distributed; Torrence & Compo, 1998) and 300 Monte-Carlo simulations. Software for the wavelet analysis was provided by Grinsted et al., (2004), who developed a MATLAB toolbox (<http://www.pol.ac.uk/home/research/waveletcoherence/>) to run the XWT analysis, compute phase angles, coherence levels, and significance testing on the two input signals.

The wavelet analysis was performed on the instantaneous across-shore velocity and the bed level time series for each experiment for the duration of the Vectrino data record (Table 1). Velocities were first reduced to 10 Hz to match the time step of the bed level time series. Data were linearly detrended, then histograms of each time series were plotted to ensure an approximately normal distribution (e.g., Grinsted et al., 2004). The detrended time series were then input into the XWT toolbox to produce an $M \times N$ matrix of wavelet coherences, where M is the frequency of the signals and N is time. Contour plots of squared wavelet coherence spectra (Figure 4.5) show time series of frequencies of significant spectral power. The shaded areas around the edges of the plot represent the cone of influence (COI) outside of which frequencies of high coherence were disregarded (see: Torrence & Compo, 1998). Moments of high coherence $\geq 90\%$ squared coherence) are outlined with black contours.

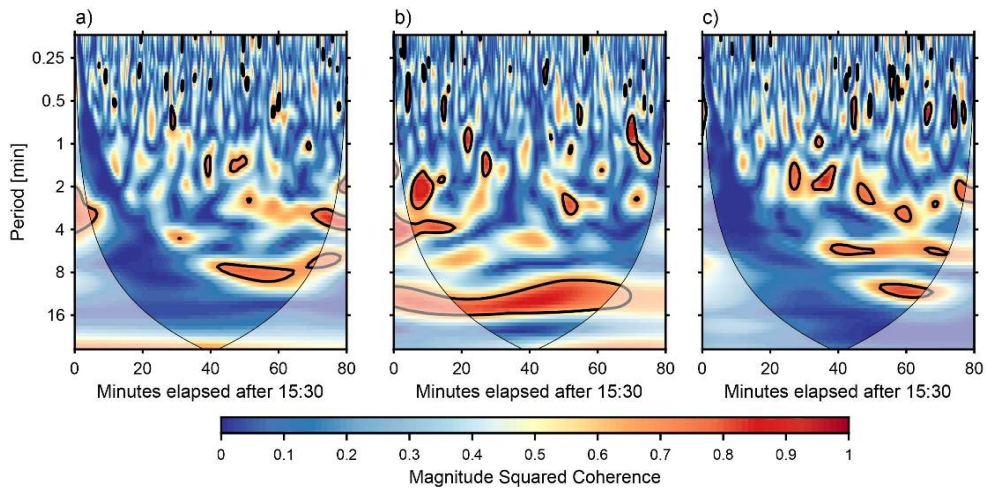


Figure 4.5: Example cross wavelet transform of the across-shore velocity (u) and the bed level for three across-shore positions: the mudflat (a), fringe (b) and forest (c) during the experiment on 6th of March, 2015. The shaded areas denote the cone of influence, where edge effects become important.

4.2.4.6 Event Identification

The example wavelet contour plots in Figure 4.5 demonstrate that changes in the bed level were often highly correlated to oscillations in velocity over a range of periods and times during both the rising (in this case) or falling tide. In this study, a movement event (also referred to hereafter as simply an ‘event’) is defined as the length of time wherein these two signals are correlated at or above a 90% coherence level (e.g., the moments defined by dark contours in Figure 4.5). From the wavelet analysis, the event period ranges from that of ~10 seconds- a lower limit defined by the averaging interval of the bed level time series- to tens of minutes. This range spans the gamut of bed level response to short period wave forcing ($10 \text{ s} < 1/\omega < 30 \text{ s}$), and long-period infragravity forcing ($1/\omega > 30 \text{ s}$). To determine event durations, all wavelet coherence datasets were subjected to the following procedure: first, values outside the COI were excluded, and then the periods of high coherence (≥ 0.9) were identified to determine individual events across all frequencies. The event duration was determined as the longest length of each coherent moment multiplied by the time step. Then, a mean value of the other hydrodynamic parameters (the water depth, significant wave height, dissipation rate, bed shear stress, and the mean across-shore velocity) was calculated using the start and stop indices for each event. Similarly, the net bed level change over a single event was calculated by subtracting the bed elevation at the end of the event from the elevation at its beginning.

4.3 Results

4.3.1 General Conditions during the Experiments

Time series of depth, mean current velocity, significant wave height and SSC clearly show differences between neap and spring conditions (Figure 4.6). Mean depth-averaged currents reached 0.62 m/s on the mudflat during spring tidal conditions. In the forest, tidal currents were much weaker, with a maximum speed of 0.23 m/s. The variation in suspended sediment concentration was strongly dependent on wave-driven resuspension (e.g., Fricke et al., 2017). Low SSC values during neap conditions corresponded to the period of lower incident wave energy (March 3 – 6th). Greater SSC values in the fringe and forest corresponded to spring conditions and much larger incident wave energy (significant wave heights up to

0.7 m; March 8th – 12th). Fringe and forest SSC levels were similar. In general, SSC levels tended to peak early in the flood tide then decreased throughout the ebb tide. Although the direction of the instantaneous sediment flux varied over the course of the tide, the fortnightly averaged sediment flux was directed into the mangrove forest throughout the experiments (cf. Figure 11, Fricke et al., 2017).

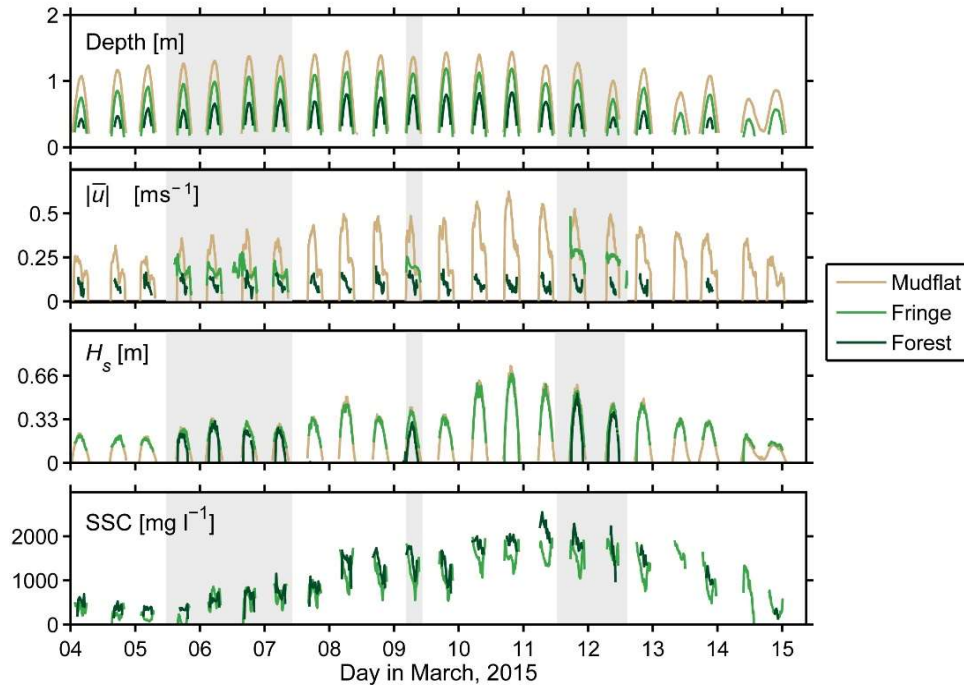


Figure 4.6: Time series of water depth, the across-shore, depth-averaged velocity ($|\bar{u}|$), significant wave height (H_s), and suspended-sediment concentration (SSC). Note some instruments were part of the moveable arrays and so records from a single location do not cover the full two-week period. The length of each experiment (Table 4.1) is represented by the shaded areas in each panel.

In general, the mean near-bottom across-shore velocity decreased with distance inside the forest during both flood and ebb tide experiments (Figure 4.7a – b). Flow velocities on the mudflat were of similar magnitude between flood and ebb tides, while maximum flow velocities in the vegetated regions decreased between the flood and ebb tides. Similarly, bed shear stresses also decreased with distance inside the forest (Figure 4.7c – d). Maximum bed shear stresses during the flood (ebb) tides were 1.7 (1.7) N/m², 1.4 (1.6) N/m², and 0.7 (0.6) N/m² for the mudflat, fringe and forest sites, respectively. Critical erosion thresholds were estimated from sediment samples to be 0.18 N/m², 0.26 N/m² and 0.40 N/m² for the mudflat, fringe and forest sites, respectively, reflecting the increase in cohesives with distance

onshore (Table 4.1). In the mudflat and fringe sites, measured shear stresses exceeded their respective critical shear stress estimates 31% and 86% of the time during the flood tide, and 89% and 75% of the time during the ebb tide. In the forest, shear stress measurements exceeded the critical value 27% and 71% of the time during flood and ebb tides, respectively. Unlike the former two parameters, the TKE dissipation rate estimates were largest in the fringe and smallest inside the forest (Figure 4.7e – f). The peak of turbulence in the fringe was directly related to the greater pneumatophore root density (Table 4.1) within this narrow band of dense trees along the boundary of the mudflat and mangrove forest (Norris et al., 2017).

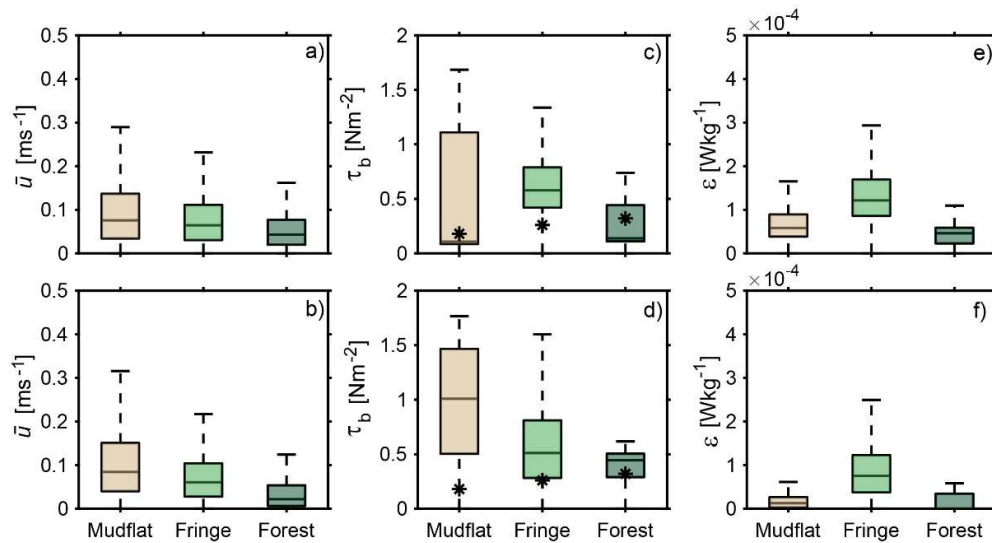


Figure 4.7: Boxplots depicting trends in the mean near-bed across-shore velocity (\bar{u}), bed shear stress (τ_b) and turbulent kinetic energy dissipation rate (ϵ) for the mudflat, fringe and forest sites. Panels (a, c, e) are of the flood tide experiments, while panels (b, d, f) are of the ebb tide experiments. In panels (c, d), the asterisk ‘*’ denotes the average critical shear stress (τ_{cr}) required to entrain the characteristic sediment type for each area.

Across all experiments, an average of $7.9 \pm 2.2\%$, $8.7 \pm 0.7\%$ $12.1 \pm 2.7\%$ of velocity and bed level measurements were significantly coherent in the mudflat, fringe and forest wavelet analyses, respectively. Wave ripples were observed at all positions along the across-shore transect line at some point during the experiments. Wave ripples migrate on a different time scale from the ones considered in the wavelet analysis, so their presence may have contributed to the generally low coherence between the instantaneous near-bottom velocity and the bed elevation. To establish this claim, ripple geometries can be modeled from wave parameters

(U_δ) and sediment characteristics (d_{50} and the sediment density) using the empirical model outlined in Wikramanayake and Madsen (1994) (Appendix C). During the experiments, wave orbital velocities ranged from $U_\delta = 7 - 29$ cm/s on the mudflat, $U_\delta = 5 - 30$ cm/s in the fringe, and $U_\delta = 1 - 19$ cm/s in the forest. Sediment d_{50} generally decreased with distance landward, ranging from a maximum of 199.4 μm in the fringe to a minimum of 35.8 μm in the forest (Table 4.1). Evaluating Equations C.1 – C.3 for these conditions, modeled ripple wavelengths were 0.5 – 0.12 cm with heights $\eta = 0.08 - 1.8$ cm, with the largest ripples in the fringe (where it was sandier) and smallest ripples in the forest (where it was siltier). The ripple migration speed U_m can then be estimated using the model in Bagnold (1941) with the formulation of van Rijn (1998), the former parameters, f_w and τ_c (Equations C.4 – C.7). Across all three sites, U_m varied between 2.2 – 29 cm/hr, demonstrating that ripples likely migrated at speeds that were significantly slower than the wave orbital velocity. Hence, bed level changes associated with ripple migration were unlikely to be coherent with instantaneous velocities.

Across all experiments, short events occupied between 16 – 116 min total time during the flood tide, and between 16 – 49 min total time during the ebb tide, corresponding to 2.3 – 8.5% and 2.3 – 4.6% of total experiment time, respectively. In contrast, infragravity-length events occupied between 4.2 – 6.2 hours during flood tide experiments, and between 4 – 4.5 hours during ebb tide experiments, corresponding to 36 – 47% and 35 – 43% of total experiment time, respectively. In general, movement events corresponding to short-period gravity waves were more common on the mudflat and fringe sites, while events corresponding to long-period infragravity waves were more frequent in the forest (see column Wave/IG events, Table 4.2). To exemplify these trends, Figure 4.8 shows three synoptic power spectral densities of pressure data from the mudflat, fringe and forest. Spectra were calculated using 2048 s de-trended Hamming-tapered segments with 50% overlap and band-averaged over 2 adjacent frequency bins (degrees of freedom > 20; 95% confidence intervals shown). In this example, spectral energy in the waveband ($0.1 < f < 1$ Hz) decreased 76% between the mudflat and forest sites (separated by 130 m), while only 23% of the energy in the infragravity band ($0.001 < f < 0.1$ Hz) was reduced over the same distance.

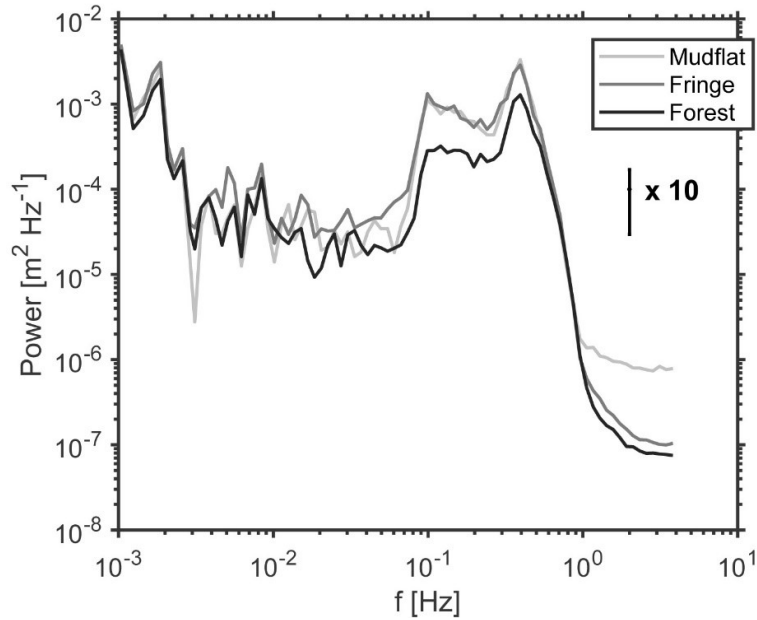


Figure 4.8: Example spectral density of the water depth from the 6th of March, 2015, computed for the mudflat, fringe and forest (light grey to dark grey lines).

4.3.2 Bed Level Variability

Figure 4.9 shows the bed level relative to the initial measured position below the Vectrino transducer at the start of the tide. These six time series show increases in the bed level variability over time, presumably related to the increase in wave heights over the two week measurement period (Figure 4.6; also discussed below). In general, the bed level tended to erode relative to the initial position during the flood tide experiments, and tended to accrete during the ebb tide experiments. High frequency oscillations were observed in all time series with fluctuations on the order of 2 mm commonly occurring. Large bed level changes greater than 10 mm also occurred but over longer time-periods (up to tens of minutes). Across all experiments, the largest bed level changes occurred in the fringe sites, while the smallest changes occurred in the forest.

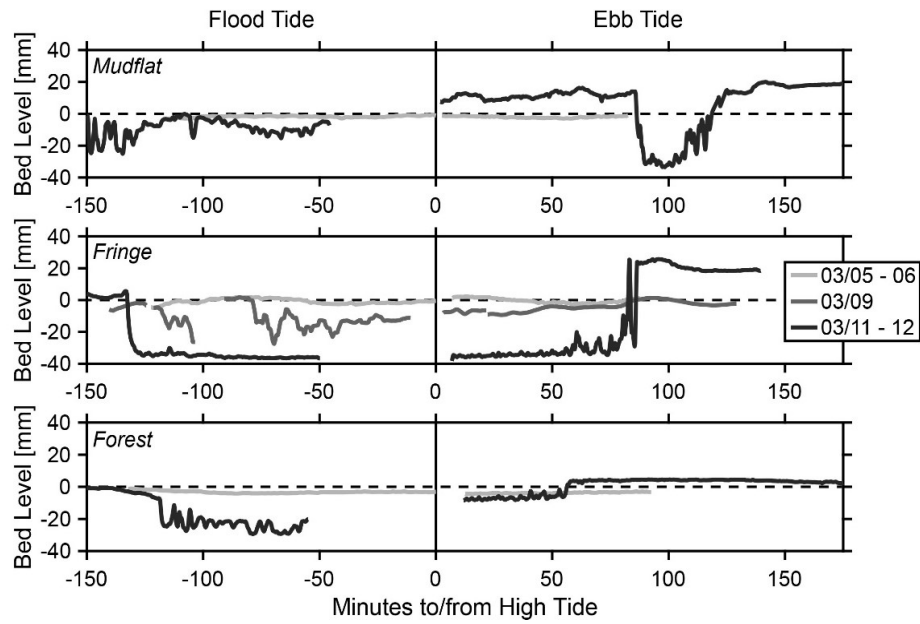


Figure 4.9: Bed level time series for each experiment. Note, only the March 9th, 2015 experiment was contiguous across high tide (Table 4.1). For the March 9th experiment, only the bed level trace from the ‘middle’ Vectrino profiler is shown (see Figure 4.10 for details).

Bed level variances recorded by three closely-spaced Vectrinos placed within a dense root canopy in the fringe is shown in Figure 4.10a. In this figure, the ‘Seaward’ and ‘Middle’ instruments were situated on either side of a row of roots, (black circles in Figures 4.10b and 4.10c) with the third ‘Landward’ instrument furthest away from the obstacles (refer to Figure 3.2) These instruments were deployed high above the bed surface (0.24 m, Table 1) to reduce the likelihood of self-scour by the Vectrino probes. Despite a small total horizontal separation of 30 cm, the bed level traces for each instrument are remarkably different. During the flood tide, all three positions show substantial variability in the bed elevation. The greatest variance occurred under the middle instrument, where the bed quickly eroded around 7 cm from baseline, then infilled as slack tide approached (Figure 4.10a). Other positions showed moderate erosion, up to 2 cm for the landward instrument, and close to zero net erosion for the seaward instrument. Relative to the flood tide, the variance of the bed level during the ebb tide decreased for all three instrument positions, although the variance was highest again at the middle instrument position, closest to the pneumatophores.

The bed level change map from this experiment (Figure 4.10b) highlights some of the spatial variability in the bed level within a 1 m² area across a single tidal cycle.

During this experiment, the maximum absolute bed level change was $30 \text{ mm} \pm 8 \text{ mm}$. Depositional patterns are clearly affected by the position of the roots, as the greatest erosion occurred in the intervening areas around clusters of pneumatophores (Figure 4.10b). In some areas, pooled water meant the photogrammetric technique was unable to resolve bed levels (white areas in Figures 4.10b and 4.10c). However, it is important to note that these areas generally corresponded local depressions in the bed surface immediately adjacent to the pneumatophores. Accretion occurred mainly in the area seaward of the instrument array, and the landward position furthest away from pneumatophore roots in the upper left quadrant of the survey area (Figure 4.10c). Hence, depositional patterns in mangrove roots in the forest fringe are highly variable and are spatially dependent on the heterogeneous distribution of roots within a given area.

To collate depositional patterns across all experiments, the relative scour depth S/D is well-represented by the established relationship with the Keulegan-Carpenter (KC) number from Sumer et al., (1992): $S/D = 1.3[1 - \exp(-0.03(KC - 6))]$ (Figure 4.11). Within engineering literature, the KC number has been established as a reliable predictor of wave-induced scour (e.g., Silinski et al., 2016). In the present study, the scour depth (S) was estimated by finding the 500 minimum bed levels for each time series, representing a range of the minimum bed states during each experiment, and D was determined as in Figure 4.2 (Section 4.2.2). As $KC = U_{\delta}T_r/D$, the greatest relative scour depths correspond to large values of KC and hence to intermediate values of aD , because KC and D are inversely proportional. Indeed, the largest relative scour depths occurred in the fringe during the March 11th and 12th experiments when waves were large (Figure 4.6) in a canopy of moderate density ($aD = 0.06$). The smallest relative scour depth occurred during the March 9th experiment, due to the large size of the patch relative to the scour depth.

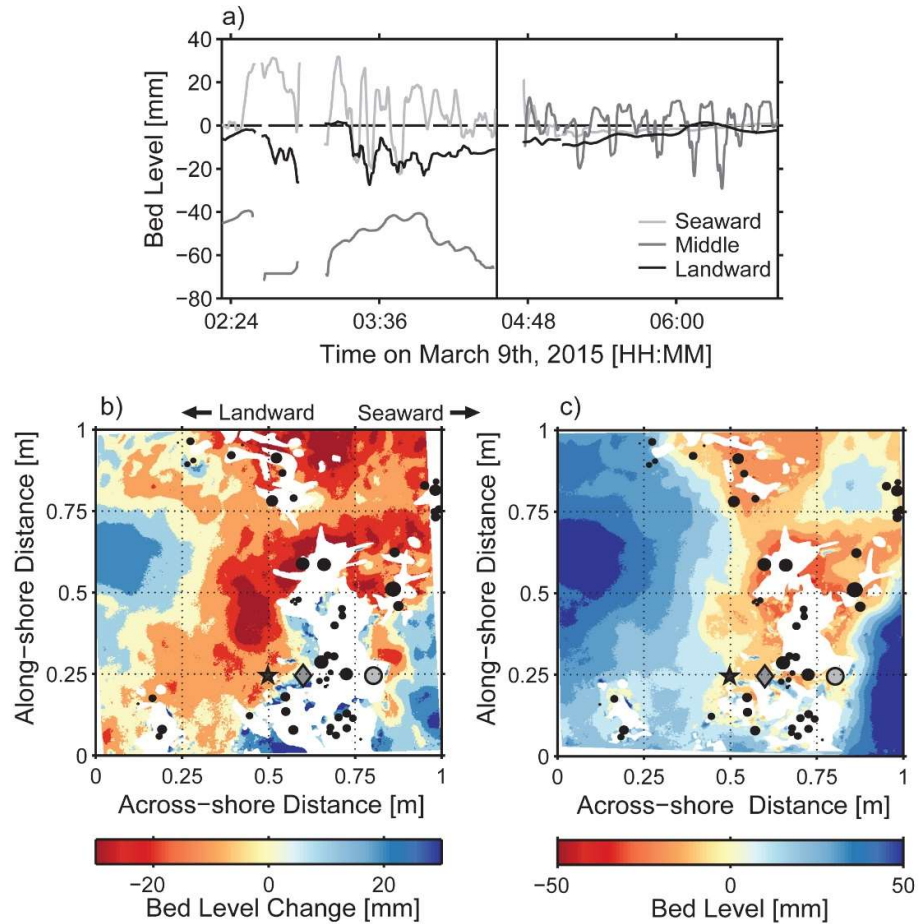


Figure 4.10: Bed level during the experiment on March 9th, 2015. Panel (a) time series of the bed level across a single flood-ebb tide transition, with high tide indicated as the vertical black line. The initial bed level, surveyed prior to the experiment, is shown by the horizontal black line. Breaks in each curve are gaps in the data record. The bed level traces have been smoothed using a 50-point running mean for display purposes. Panel (b) a map of the bed elevation change computed by differencing the bed elevation areas of two photogrammetric surveys of the field site before and after the experiment on March 9th, 2015. The instrument positions described in panel (a) are shown in panels (b) and (c) as: seaward, grey circle; middle, dark grey diamond; landward, black star. The elevation change depicted is representative of the change in bed level across a single tidal cycle. In this figure, the average error in bed level is approximately 8 mm (see text for details). Areas with no data are colored in white. Panel (c) bed level after the experiment on March 9th, 2015.

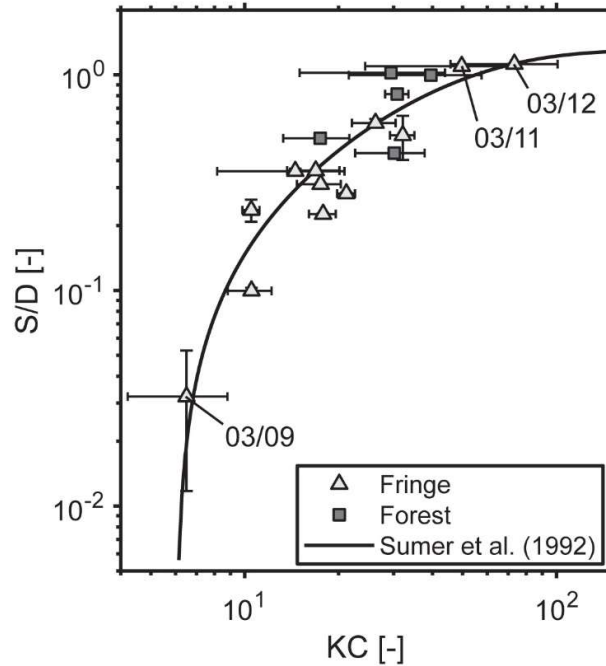


Figure 4.11: Keulegan-Carpenter (KC) number versus the normalized scour depth (S/D). The black curve is Eq. 9 from Sumer et al. (1992). The experiments with the largest and smallest S/D are labeled (Table 4.1).

4.3.2.1 Elevation Change over Events and Tidal Cycles

Probability distributions of the net elevation change over individual events (Section 4.2.4.6) are similar for all three areas (Figure 4.12). The number of events retained was 238, 938, and 236 for the flood tide experiments, and 139, 478 and 133 for the ebb tide experiments; mudflat, fringe and forest, respectively. These event bed level distributions are nearly normally-distributed (with a goodness-of-fit values significant at the 95% level based on a chi-square test statistic with >40 degrees of freedom), and hence show a similar number of events resulting in net erosion or accretion. In general, most net elevation changes within single events (i.e., ~55% of events for flood tides, and ~58% of events for ebb tides) were between ± 16 mm. Still, large bed changes exceeding ± 40 mm occurred but only in small percentages (< 5%). The event bed level distributions are also skewed, for example the forest sites tended towards negative elevations during the flood tide, and tended towards positive elevations during the ebb tide. In contrast, the mudflat and forest

distributions were similar in that they slightly tended towards positive elevations during the flood tide and towards negative elevations during the ebb tide.

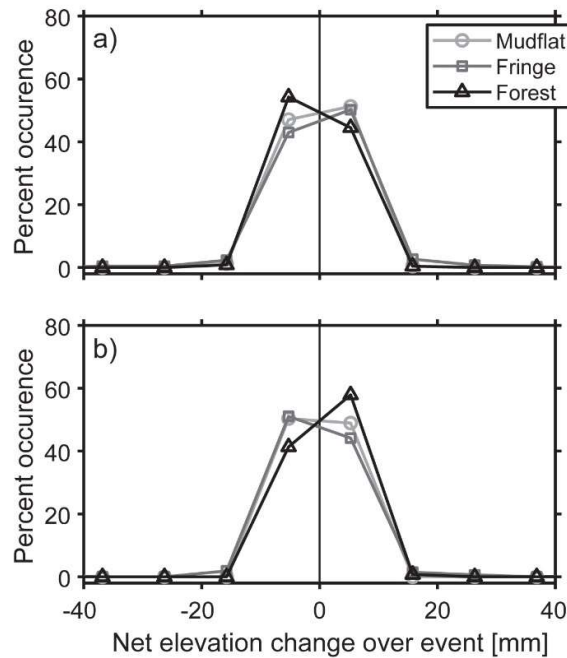


Figure 4.12: The distribution of the net elevation change over a single event for all flood (panel a) and ebb (panel b) tides. See text for definition of event.

For the majority of events (e.g., 69 – 86% of all events regardless of experiment location or tidal stage), the net bed level change was nearly zero ($\leq \pm 1 \times 10^{-3}$ m). As previously noted, bed level changes greater than ± 40 mm occurred with some regularity, predominantly in the fringe sites during both flood and ebb tide experiments (Figure 4.13). As the event bed level distributions are skewed, these data were grouped according to events resulting in accretion (change in bed level > 0) and erosion (change in bed level < 0). In this figure, the red and blue dots show the extreme outliers ($>1.5 \times \text{IQR}$) for the minority of the flood and ebb data, respectively. As evident in the figure, the uncommon events were responsible for the greatest net change in bed level across all locations. Across all locations, the largest bed level changes were associated with infragravity-length events as these longer events capture a greater amount of bed level variation. Still, significant bed level changes up to ± 20 mm were observed during short events- particularly in the fringe- reflecting the importance of incident frequency waves as a driver for scour

around pneumatophore roots (e.g., Figure 4.11). In the forest, the largest bed level changes were mainly associated with long events regardless of the tidal stage (Figure 4.13e – f). These patterns are not unexpected given the observed reduction in short-period wave energy with distance inside the forest (Figure 4.8). In general, net bed level changes were not dependent on event length: there was only weak correlation between the bed level and event duration for the forest sites ($r^2 = 0.22$, and $r^2 = 0.33$; flood and ebb tides, respectively), and poor correlation for the mudflat and fringe sites ($r^2 < 0.1$ in all cases).

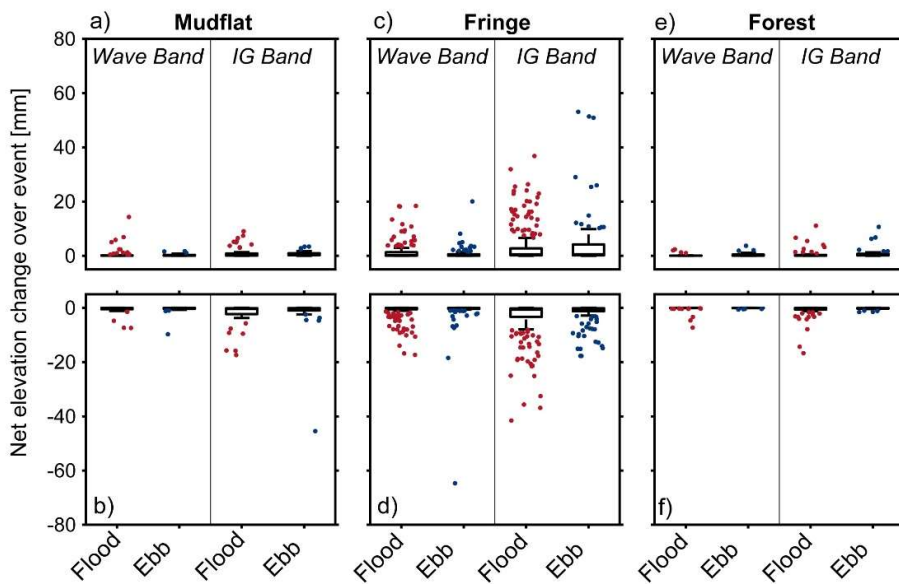


Figure 4.13: Boxplots depicting the net elevation change for individual events during flood and ebb tides. The top row depicts events that resulted in bed accretion and the bottom row depicts events that resulted in bed erosion.

The statistics presented in Table 4.2 reiterate the different roles for short-period and infragravity waves in the morphodynamics of each across-shore location. Forest sites experienced a lower ratio of short events to long events than the other two sites. During the flood tide experiments, short events were more commonly associated with greater positive bed level change (accretion) over individual events on the mudflat and fringe, while long events were more commonly associated with greater negative bed level change (erosion) in the forest. During the ebb tide experiments, short events contributed greater erosion than accretion in all three areas. However, long events resulted in positive bed level changes in the forest that were 6.8 times greater than negative bed level changes under the same event period.

Across all events during the flood tide experiments, net positive bed elevations occurred in the mudflat and forest sites, while the fringe tended towards negative bed elevations. During ebb tide experiments, all areas tended towards negative bed elevations. However, the net change between flood and ebb tides in the mudflat and forest was positive (4.55 and 6.82 mm, respectively) while the forest was negative (-9.46 mm).

4.3.2.2 Relationship to Forcing Conditions over the Tidal Cycle

To conduct a systematic examination of the dependence of the net change in bed level during single events on the forcing conditions (e.g., h , H_s , \bar{u} , τ_b , and ε), a stepwise multiple linear regression model was constructed for each sampling location (Table 4.3). Model results suggest that the net change in bed level positively scaled with increasing water depth, and negatively scaled with the other environmental variables across all sites. On the mudflat, the significant wave height was the most important predictor (largest absolute value of the standardized model coefficients) of the bed level. At this location, only h , H_s , τ_b , and ε were included model predictors, collectively explaining between 74 – 87% of the variance in bed level ($F = 164$, and $F = 224$ for flood and ebb tides, respectively; $p\text{-val} < 0.01$). Inclusion of all the parameters in the mudflat models resulted in decreased F-statistics, indicating overfitting. In the fringe, the inclusion of up to four environmental variables could collectively only explain between 21 – 47% of the variance in bed level for either flood or ebb tides ($F = 285$, and $F = 62.5$, respectively; $p\text{-val} < 0.01$). In contrast, the inclusion of four environmental variables in the forest site models collectively explained between 87 – 93% of the variance in bed level ($F = 236$, and $F = 212$, respectively; $p\text{-val} < 0.01$). The low r^2 values quoted above reflect the dynamics of the forest fringe, suggesting vegetated sites exposed to a strong short-period wave climate produce a non-linear response of the bed level to the forcing conditions.

Table 4.2: Statistics for wave and infragravity-length events across the mudflat, fringe and forest sites.

Tidal Stage	Area	# Wave/IG events (-)	# Accretion/Erosion Events (-)		Max Accretion/Erosion (-)		Net change in bed level across all events (mm)			
			Wave	IG	Wave	IG	Min	Median	Max	Net
Flood Tide	Mudflat	1.1	1.1	1	1.9	0.5	6.08	10.1	14.5	10.3
	Fringe	1.2	1.1	1.1	1.1	0.9	-42.6	-5.37	39.4	-2.5
	Forest	0.7	0.7	0.9	0.3	0.7	0.49	9.95	19.4	10.0
Ebb Tide	Mudflat	1.2	1.0	0.9	0.2	0.1	-11.2	-5.75	-0.22	-5.75
	Fringe	1.1	0.8	1.1	0.3	3.0	-56.6	-0.83	65.7	-6.96
	Forest	0.7	1.4	1.4	1.7	6.8	-11.1	-2.23	-1.27	-3.18

Table 4.3: Multiple linear regression model results for the mudflat, fringe and forest sites. Symbols correspond to included model parameters: h , the water depth, τ_b , the bed shear stress, ε , the TKE dissipation rate, and \bar{u} , the mean current velocity.

Tidal Stage	Area	Variance Explained	Significance	Standard Error (m)	Model f-statistic	Significant Predictors
Flood Tide	Mudflat	$R^2 = 0.74$	$P < 0.01$	0.01	164	$Y = 2.4E-16 + 0.25h - 0.55H_s - 0.30\tau_b - 0.48\varepsilon$
	Fringe	$R^2 = 0.47$	$P < 0.01$	0.02	285	$Y = -2.6E-16 + 0.28h - 0.42\bar{u} - 0.39\tau_b - 0.23\varepsilon$
	Forest	$R^2 = 0.93$	$P < 0.01$	0.03	236	$Y = 6.3E-16 + 0.32h - 0.81H_s - 0.06\bar{u} - 0.42\varepsilon$
Ebb Tide	Mudflat	$R^2 = 0.87$	$P < 0.01$	0.006	224	$Y = 9.0E-16 + 0.31h - 0.81H_s - 0.45\tau_b - 0.34\varepsilon$
	Fringe	$R^2 = 0.21$	$P < 0.01$	0.004	62.5	$Y = 2.5E-16 - 0.25H_s - 0.50\varepsilon$
	Forest	$R^2 = 0.87$	$P < 0.01$	0.007	212	$Y = 6.8E-16 - 0.61H_s - 0.47\bar{u} - 0.39\tau_b - 0.63\varepsilon$

4.4 Discussion

Bed levels were measured within patches of mangrove pneumatophore roots of varying densities throughout a tidal cycle. Bursts of bed level movement were often correlated with the near-bed velocities over a range of periods, spanning that of short-period wind waves ($1/\omega < 30$ s) to long-period infragravity waves ($1/\omega > 30$ s). Regardless of event duration, the majority of movement events resulted in bed level changes that were close to zero. For non-zero movement events, there were nearly equal numbers of events resulting in accretion and erosion (Figure 4.12). However, a few movement events resulted in large bed level changes that exceeded the total net bed level change over a tidal cycle (Figure 4.13 and Table 4.2). Hence, the net change in bed level across the tidal cycle was the cumulative result of opposing sediment transport signals.

In general, short events were slightly more common on the exposed mudflat and fringe areas, while long events were much more common in the forest than in the other sites (Table 4.2). These results reiterate the importance of long-period infragravity energy as a driver of morphological change in mangroves. Along the coast of southern Vietnam, longer-period northeast monsoon waves with their larger infragravity component have been identified as a likely cause of greater sediment resuspension and coastal erosion (Anthony et al., 2015; Loisel et al., 2014). The results of the present study are not inconsistent with these observations; incident wave-driven resuspension was a major driver of bed level change throughout the experiments (Figure 4.11), and infragravity energy was associated with erosion during the flood tide in the forest sites (Figure 4.13). However, across all experiments, net accretion occurred in the forest, indicating that- at least for the short window of observation- the forest is a net sink of sediment. Further, as the landward boundary of the mangrove forest is above high tide, the landward-dominant flux of sediment strongly implies that deposition occurred inside the mangrove forest (Fricke et al., 2017). A recent study of the long-term (decadal) trends in sedimentation on Cù Lao Dung suggests these patterns we observed over a short, two-week period are likely representative of the dominant processes acting over longer timescales (Fricke et al., 2017). Sediment may be mobilized by the greater incidence of short-period wave energy on the mudflat and fringe (Figures 4.8, 4.9 and 4.11), and then may be transported into the forest through a

combination of long-period infragravity waves and tidal currents. During flood tides, turbulence and bed shear stress either scours the bed or keeps sediment in suspension inside the mangrove forest (Figure 4.6). This sediment may be deposited around slack tide (e.g., Furukawa & Wolanski, 1996) and is only re-entrained if turbulence and bed shear stresses reach critical values (Figure 4.7).

The bed shear stress was often one of the most important predictors in the multiple linear regression models, regardless of the across-shore location and tidal stage (Table 4.3). Overall, measured bed shear stresses were greatest on the mudflat and declined with distance landward (Figure 4.7), consistent with the concept that shear stress is reduced in the presence of vegetation (e.g., Bennett et al., 2008; Tsujimoto, 1999). Conversely, estimates of the critical shear stress increased in accordance with the decrease in grain size (and increase in the fraction of cohesives) with distance landward. Although the estimated critical shear stress values neglect contributions from biotic factors, such as sediment stabilization due to microphytobenthos (e.g., by diatom mats (Paterson, 1989)), or destabilization due to bioturbating macrofauna (Harris et al., 2016), bed movement at all three locations indicates the critical shear stress was often exceeded throughout the experiments. The greatest bed mobility was observed on the mudflat and fringe (Figure 4.9), the locations that experienced large shear stresses and the highest turbulence (Figure 4.7). Erosional patterns in the fringe were highly spatially variable but were related to the spatial distribution of root structures over short distances (Figures 4.10 and 4.11). These findings emphasize that turbulence generated within mangrove roots plays an important role in sediment transport. Indeed, Norris et al., (2019) found that mangrove roots, if exposed to a strong wave climate, generate intense near-bed turbulence that could cause local scouring from around the base of the roots.

These results are important for future modeling studies that aim to recreate sedimentary processes in mangroves because: (i) The estimated critical shear stress values were larger than values that are often prescribed to vegetated platforms in numerical models (Horstman et al., 2015; Widdows et al., 2007). (ii) Models utilizing patches of regular, idealized vegetation analogues (López & García, 1998; Wu et al., 2001) cannot effectively recreate the depositional patterns that arise from the spatial distribution of mangrove roots (however, some recent studies such as

Horstman et al., (2015) have taken this effect into consideration). (iii) Many modeling studies of the sediment dynamics of salt marshes (Fagherazzi et al., 2012 and references therein) and some of mangroves (Li et al., 2014) assume surface erosion is negligible over vegetated surfaces, implying these areas are net sinks of sediment with zero resuspension. This approach has two shortcomings, one that erosion around the edges of vegetated platforms (as observed here and by Bouma et al., 2007) is often poorly reconstructed, and two, the sediment entrained by resuspension can be advected by larger-scale flow patterns, such as riverine circulation and seasonal variation in wind and wave direction (McIvor et al., 2013; Wolanski et al., 1980), which affects the long-term morphodynamics of vegetated systems (Eidam et al., 2017b; Fricke et al., 2017).

The depositional patterns observed in the present study are likely a result of the moderately low root densities of the mangroves of Cù Lao Dung (compared to other mangrove species and localities, e.g., Krauss et al., 2003). Denser mangrove forests, such as the *Avicennia marina* forests described in Young & Harvey, (1996) and the mixed *Avicennia*, *Sonneratia*, *Rhizophora* and *Bruguiera* mangrove forests described in Horstman et al., (2012) are more effective at inhibiting wave propagation, and hence may effectively stabilize the shoreline over shorter distances. The decline of root densities from the mangrove fringe inwards on Cù Lao Dung sets up a gradient of turbulent energy and wave dissipation (Norris et al., 2017; Henderson et al., 2017). Enhanced dissipation at the fringe reduces the transmission of waves landward, eventually creating a sheltered forest interior where deposition can occur. Under storm conditions, enhanced turbulence would increase dissipation within the fringe and forest region (Henderson et al., 2017) and would likely erode the deeper forested areas. Unfortunately, the intensity of severe storms is predicted to increase in southeast Asia (Goodess, 2013), and sea levels are predicted to rise up to 1 m by 2100 in southern Vietnam (Nguyen, 2009) due to climate change. Rising sea levels, combined with a typhoon recurrence frequency of ~1.9 years (Imamura & To, 1997), could create greater inundation of coastal areas which could affect the sediment dynamics of coastal mangrove forests. As mangrove health is tied to a delicate balance between erosion and deposition (Fagherazzi et al., 2017), these changes could have profound effects for

communities that rely on mangroves for coastal defense, food and building materials.

Finally, recent studies by Balke et al., (2013; 2011) have shown that there are narrow ‘windows of opportunity’ wherein hydrodynamic conditions are suitable for *Avicennia* or *Sonneratia* spp. mangrove propagules to establish on frontal mudflats or in mangrove fringes. The observations from the present study suggest that both the bed shear stresses and short-lived bed level changes occasionally exceeded the failure thresholds for young mangrove seedlings (e.g., Balke et al., 2013). Climate change processes, such as increases in severe weather, could alter the external forcings to mangroves and other disturbance-driven ecosystems such as salt marshes. Quantifying the biophysical interactions is therefore key to better management and protection of these valuable ecosystems, now and in the future.

4.5 Conclusions

Field experiments were conducted within a wave-exposed coastal mangrove forest to quantify the forces responsible for bed level changes over a tidal cycle. These observations have yielded the following key insights of sedimentary processes within this and other coastal mangrove forests.

- (1) Time series of the bed level were often correlated to oscillations in velocity over a range of frequencies, from short-period wind and swell wave to long-period infragravity frequencies.
- (2) Although short-period wave energy decreased with distance inside the forest, infragravity wave energy was less reduced, consistent with the simulations of Phan, et al. (2015).
- (3) Of the bed level changes that were coherent with hydrodynamics, the bed movement on the exposed mudflat and fringe was dominated by short-period wave energy, while bed movement in the sheltered forest was largely associated with long-period infragravity energy.
- (4) Net bed level changes under both wave and infragravity events were normally distributed, with similar numbers of accretionary and erosive events. The largest bed level changes (up to ± 65 mm over a single event) were infrequent. Net bed level change over a tidal cycle is therefore determined by the balance of these larger events.

- (5) Inside the forest, changes in the bed level were correlated with changes in the water depth, significant wave height, bed shear stress, mean across-shore velocity, and the turbulent dissipation rate. In multiple linear regression, the same (or fewer) forcing variables produced substantially weaker relationships with the change in bed level on the mudflat and fringe.
- (6) Over short distances (< 1 m), depositional patterns were associated with the spatial distribution of pneumatophore roots. These patterns are likely tied to intense near-bed turbulence generated by waves in the near vicinity of the roots.

Chapter 5

General Conclusions

5.1 Review of Major Concepts

The research presented in this thesis aimed to enhance our understanding of the hydrodynamic and biogeomorphic feedbacks between mangroves and their environment that actively shape coastal mangrove forests. Four questions were identified, focusing on: (i) understanding how the heterogeneous distribution of mangrove pneumatophore roots affects turbulent dissipation within a *Sonneratia* mangrove forest; (ii) how the roots modify their flow field with respect to turbulence, (iii) how these spatial and temporal variations in turbulence affect sediment transport within mangrove roots and (iv) how these patterns indicative of the morphodynamic control by mangroves on their environment. Conclusions regarding each of the research questions are reiterated below:

1. How does the spatial distribution of mangrove pneumatophore roots affect the temporal and spatial distribution of turbulence within the mangrove forest? Specifically, how is turbulent energy dissipation affected by wave breaking and the water depth (tidal stage)?

By measuring both the geometry of pneumatophores and the hydrodynamic conditions therein, Chapter 2 related the spatial patterns of root density with turbulence. Surveys of root geometries within 1 m² quadrats spanning the mudflat to the forest interior revealed that root density was greatest within a narrow ~20 m wide band of trees at the mangrove forest fringe. Although turbulence was variable with the across-shore position and tidal depth, synoptic measurements showed that turbulence was elevated in the fringe relative to the other measurement locations (mudflat, forest). Within the fringe, averaged turbulent dissipation rates often exceeded 10⁻⁴ to 10⁻³ W kg⁻¹ over ten-minute bursts, which are much larger than in typical estuarine systems (Jones & Monismith, 2008; Mullarney & Henderson, 2012), and are comparable to dissipation rates measured in highly energetic swash and surf-zones (Bryan et al., 2003; Feddersen, 2012; Lanckriet & Puleo, 2013). Indeed, turbulence was strongly influenced by the wave climate, with the largest recorded dissipation rates corresponding to breaking waves in shallow water.

Nevertheless, high dissipation rates were also observed in numerous cases with minimal wave breaking, suggesting that turbulence also was generated within the root structures themselves.

Given that turbulence was greatest inside the dense vegetation of the forest fringe, dissipation rates were positively correlated with vegetation density at the 90% confidence level (p -value < 0.1). However, this relationship between dissipation and density was only revealed by subsampling the quadrat vegetation surveys to identify the group of pneumatophores directly responsible for inducing wakes that were measured by the instruments. In contrast, fits of the dissipation rates with the root densities averaged over the 1 m² quadrat surveys were non-significant at the 90% confidence level (p -value < 0.1). This result suggests that turbulence is highly variable within pneumatophore canopies over short, submeter distances.

2. How does the heterogeneous vertical distribution of mangrove pneumatophores modify the flow field?

Chapter 3 presented the first attempt to quantitatively characterize the flow field around mangrove roots under natural conditions in the field. Two experiments were carried out to measure the evolution of currents around dense clusters of pneumatophore roots inside the mangrove fringe. The first experiment implemented a horizontal array of high-resolution current profilers situated such that one instrument was upstream of a root cluster, and two instruments were downstream. Measurements were made at three heights within the root canopy over the course of three days. The second experiment implemented a vertical array of current profilers to simultaneously study currents within and above the root canopy. Turbulent statistics (dissipation rates, Reynolds stresses and eddy viscosities) were calculated from velocity measurements collected at each array position.

Between the two experiments, three zones of enhanced turbulence were identified: near the bed, around the mean canopy height, and above the canopy. These hotspots of turbulence were associated with the formation of coherent flow structures in the lee of the pneumatophores. Turbulence in the lower canopy was generated by Von Kármán vortices shedding behind the roots in the direction of the mean current. Vortex shedding was identified by small, narrow peaks in velocity power spectra that were equivalent in frequency to a Strouhal number of ~ 0.2 (Schewe, 1983).

Alternating positive and negative Reynolds stresses behind the pneumatophores in the first experiment indicated the presence of a recirculation zone, similar to those observed behind dense tree canopies in atmospheric flows (e.g., Detto et al., 2008). Above the root canopy of the second experiment, enhanced turbulence was associated with velocity shear that formed between the reduced in-canopy velocities and accelerated above-canopy velocities.

This work indicates that, in wave-dominated climates, wave currents in mangrove roots produce strong turbulence, particularly in the dense region of the root canopies near the bed. These patterns are unlike those observed in former laboratory experiments when mangrove roots were subjected to unidirectional currents (Horstman et al., 2018). In this former case, turbulence was found to be negatively correlated with canopy density due to reduced flow velocities within the relatively dense canopy region near the bed. Hence in natural settings, mangrove root canopies affect both the horizontal and vertical distributions of turbulence, which can influence the drag forces of adjacent roots (Nepf, 2004) and the sediment transport capacity of the mangrove forest (Furukawa et al., 1997) by concentrating intense turbulence near the bed. Maintaining enhanced near-bed turbulence levels may be an adaptation by mangroves to prevent sediment accumulation that could otherwise lead to poor health or even death (e.g., Henderson et al., 2017).

3. How does the bed level respond to variations in hydrodynamic forcing conditions (e.g., currents, turbulence, and water depth) throughout a tidal cycle? How does bed level movement inside the mangrove forest differ from the unvegetated mudflat?

Chapter 4 focused on the pathways of sediment transport within the mangrove forest. In Chapters 2 and 3, the heterogeneous distribution of mangrove pneumatophore roots was found to be a principal control over the horizontal and vertical distribution of turbulence, even over small, submeter scales. In Chapter 4, an experiment was designed to concurrently measure near-bottom velocities and the bed level at three locations on the unvegetated mudflat, the forest fringe, and forest interior. Based on lessons from the former two chapters, it was expected that enhanced turbulence generated within the mangrove roots would be a control over the depositional patterns within the forest.

Cross-wavelet transforms of velocity and bed level time series were highly correlated ($\geq 90\%$ squared coherence) over a range of frequencies, spanning those corresponding to short-period wind and swell waves ($T = 1 - 30$ s) to long-period infragravity waves ($T > 30$ s). Bed level movement events associated with short-period (high-frequency) waves decreased with increasing distance inside the forest, while movement events associated with long-period (low-frequency) waves increased inside the forest. These patterns suggest that short-period waves are more rapidly attenuated in mangroves than are long-period infragravity waves, supporting recent work (Phan et al., 2015). The net bed level change was normally distributed for both short-period and long-period events, regardless of the across-shore position, suggesting that neither short nor long-period events create greater accretion or erosion. Nevertheless, several infrequent events resulted in high-magnitude bed level changes up to $\pm O(0.01)$ m over a single event, suggesting the total bed level change observed over a tidal cycle is due in large part to these infrequent events.

As expected, the near-bottom bed shear stress was often the most important predictor of the variance in the bed level, based on a stepwise linear regression model constructed from time series of the net bed level change, the water depth, the mean current velocity, the bed shear stress, and the TKE dissipation rate. The greatest bed mobility was observed on the mudflat and in the fringe which experienced large shear stresses and the highest turbulence. Erosional patterns in the fringe were spatially variable, yet were related to the spatial distribution of the pneumatophore roots over short (< 1 m) distances. In support of this claim, the scour depth measured at each location scaled positively with the Keulegan-Carpenter (KC) number, or put simply, greater turbulence resulted in greater scour depths. Finally, over the short time periods covered in this study (one to two tidal cycles), net erosion (positive total bed level change) took place during the flood tide, and net accretion (negative total bed level change) took place during the ebb tide, with the greatest positive bed level change observed inside the forest. These observations are consistent with decadal trends in sedimentation on Cù Lao Dung observed by Fricke et al., (2017), and in general, support the concept that mangroves inhibit ebb tidal currents enabling the retention of entrained sediments (Furukawa et al., 1997; Wolanski, 1995a).

4. How do the spatial patterns in hydrodynamics (e.g., tides, waves, and turbulence) affect the distribution of sediment within the mangrove forest?

This final question ties in observations from Chapters 2 – 4, suggesting the depositional patterns across the mangrove forest were related to the spatially variable patterns in turbulence. Chapter 2 suggested that the concentration of intense turbulence within the dense roots of the fringe region preferentially winnowed fine grained sediment inside the forest. This conjecture was supported by observations of relatively course-grained sediments at the forest fringe that fined with distance landward (Fricke et al., 2017). When subjected to an energetic wave climate, pneumatophore roots in the fringe create intense near-bed turbulence (Chapter 3) that causes the preferential removal of fines. This conclusion is supported by observations of local scour around the pneumatophores of the fringe after a large wave event (Chapter 2). Furthermore, a map of bed level change over a 1 m² quadrat (Chapter 4) clearly demonstrates that erosion was concentrated within 0.2 – 0.4 m diameter clusters of pneumatophores, again reiterating the spatial control of pneumatophore roots over turbulence and hence sedimentary patterns at submeter scales. These patterns in sedimentation, particularly the preferential suspension of sediment in the fringe, are consistent with observations from Van Santen et al., (2007) in mangroves, and other experiments utilizing vegetation analogues (Bouma et al., 2007; Spenceley, 1977).

5.2 Recommendations for Future Work

5.2.1 *Species-dependent energy dissipation*

As evidenced throughout the work presented in this thesis, small clusters of mangrove pneumatophore roots exhibit a spatial control over the flow field that extends a few tens of centimeters. This near-field effect is most evident in the downstream current direction immediately behind the obstructions (e.g., Chapter 3), but may also be multi-directional due to variable, directionally spread wave currents (e.g., the erosional patterns in Chapter 4 suggest variability in turbulence over submeter scales). Hence, there is a need to resolve the submeter-scale variability when comparing turbulence with canopy geometry. Moreover, the near-field effect of mangrove roots is likely dependent on the mangrove species morphology and the wave climate. In the present work, wavier days were associated

with greater dissipation rates measured inside the root canopies of the forested areas (e.g., Chapter 2). In general, the rate of wave energy reduction in mangroves scales positively with vegetation density (cf. Figure 9, Horstman et al., 2012). Hence, mangrove species such as *Avicennia marina* that form a dense network of near-bed roots, branches and leaf canopies (e.g., in the Firth of Thames, New Zealand; Figure 5.2b) may greatly inhibit the transmission of wave energy onshore within tens of meters from the shoreline, instead of over hundreds of meters as predicted by Henderson et al., (2017) within the open-structured forest of Cù Lao Dung (Figure 5.2a). It has been suggested that swaths of mangroves could be included in some coastal management plans as a primary coastal defense (e.g., Spalding et al., 2014). Hence, future work should focus on understanding the dissipation characteristics of multiple different mangrove species to assess their efficiency in providing coastal protection.

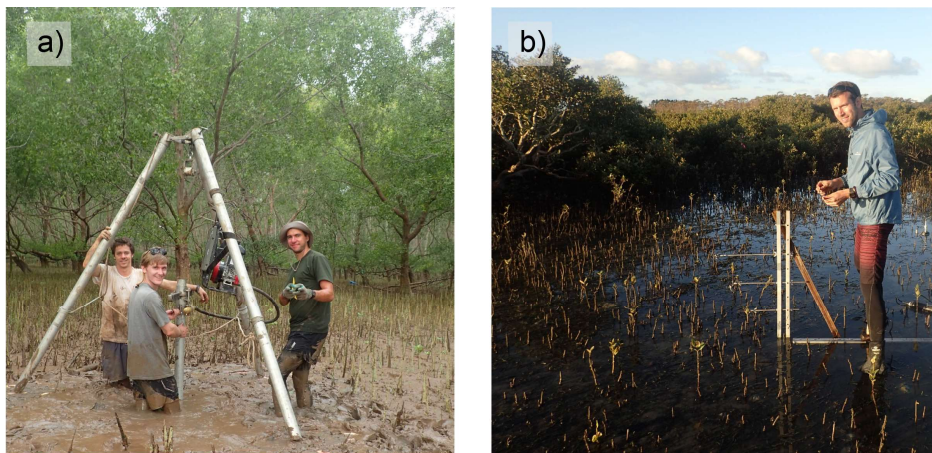


Figure 5.1: A comparison of mangrove environments. (a) From left to right: Daniel Culling, Aaron Fricke, and Ben Norris taking vibracore samples of the substrate under the cover of *Sonneratia caseolaris* mangroves on Cù Lao Dung. For reference, Ben is ~1.6 m tall above ground. (b) Erik Horstman (~1.85 m above ground) setting up instruments in the Firth of Thames, New Zealand. Photos provided by Julia Mullarney.

5.2.2 Wake length scales

The question of wake formation length scales was alluded to but was never precisely quantified in this thesis. From one of the horizontal experiments presented in Chapter 3, we observed a turbulence maximum at 20 cm from the roots near the bed that was associated with Von Kármán wake shedding. Former studies of the wake structure of porous patches (Zong & Nepf, 2012) have shown that patches

generate two distinct peaks of turbulence, one corresponding to individual stem-wakes, and another much further downstream that corresponds to the patch-scale wake. Chen et al., (2012) provides scaling arguments to estimate the patch wake formation length scale, $L_{wake} = (1.2 + (25 \pm 10)C_D a D^{(-0.9 \pm 0.2)})D$, where C_D is the drag coefficient, assumed here as $C_D \sim 2$ (Henderson et al., 2017), $a \sim 1.3 \text{ m}^{-1}$ is the frontal area density of the patch, and $D \sim 0.2 \text{ m}$ is the patch width (Chapter 2), yields estimates of L_{wake} between 5 and 15 m (greater densities and patch widths would yield smaller length scales). Although simplified, this estimate suggests that even small clusters of pneumatophores could have a substantial effect on the downstream flow conditions. From laboratory experiments, it is known that the drag from upstream objects reduces both the impact velocity and delays the point of separation on the downstream objects, resulting in a lower pressure differential and hence lower drag (Nepf, 2004). Scaling arguments for the length scale of turbulent dissipation (Chapter 2.6.1) estimated significant dissipation would occur over $\leq 5 \text{ m}$ given the conditions and root densities measured in the field. Therefore, wake shedding from dense patches of pneumatophores in mangrove fringes could generate lower-turbulence regions within < 10 meters from the fringe line. Future work may consider studying mangrove root patch-wake length scales, as these might affect the energy dissipation across swaths of vegetation and hence modify the long-term evolution of marshes (e.g., Mariotti & Fagherazzi, 2010; Temmerman et al., 2007).

5.2.3 The establishment of young mangroves

To date, mangrove restoration efforts have often proved unsuccessful due to a poor understanding of the physical thresholds and conditions necessary for mangrove propagule establishment (e.g., Lewis III, 2005). Recent studies by Balke et al., (2013; 2011) have shown that there are narrow ‘windows of opportunity’ wherein hydrodynamic conditions are suitable for *Avicennia* or *Sonneratia* spp. mangrove propagules to establish on frontal mudflats or in mangrove fringes. In their study Balke et al., (2011) determined that juvenile *Avicennia* could be dislodged from the substrate if exposed to bed shear stresses up to 0.5 Nm^{-2} shortly after rooting. In our experiments, shear stresses on the mudflat and in the forest fringe ranged between $0 - 1.7 \text{ Nm}^{-2}$ (Chapter 4) supporting observations by Balke et al., (2013) that the hydrodynamic failure thresholds for young seedlings could often be exceeded.

Moreover, erosional events were occasionally in the range of 1 – 3 cm, which is approximately the threshold at which young *Sonneratia* seedlings can be dislodged (Balke et al., 2013). Nevertheless, many juvenile *Sonneratia caseolaris* mangroves were observed on the mudflat in front of the mangrove forest on Cù Lao Dung, suggesting these ‘windows of opportunity’ occur frequently enough to enable seedling establishment (Figure 5.3). Since these windows were not observed during the present study, it would be interesting to measure hydrodynamics over the long-term (3 – 6 months) to look at the inter-seasonal variation in hydrodynamic conditions that could allow for the establishment of pioneering species.



Figure 5.2: A solitary Vectrino Profiler deployed offshore of the mangrove fringe on the mudflat. Many juvenile *Sonneratia caseolaris* mangroves are visible in the distance.

5.3 Summary

This thesis addresses the contribution of short-term bio-physical interactions in coastal mangroves to the morphodynamic processes that actively shape mangrove forests and underlie tropical deltaic evolution. Mangrove vegetation was found to play a considerable role in turbulent dissipation, and hence the baffling of tidal currents, waves, and the promotion of sediment transport within mangroves. From observational evidence presented herein, established mangrove forests withstand substantial forces at their fringes, which is indicative of their ability to weather changes in climate and rising sea levels.



Figure 5.3: Waves breaking within the trees of the mangrove fringe

Appendix A: Calculation of wave and current velocities

To calculate wave and current velocities, we followed the method presented by Luhar et al., (2013):

Starting with a Vectrino velocity time series from above the wave boundary layer, the mean (i.e., time averaged) north and east velocities, N_c and E_c , respectively, in a 30-second interval ($n = 1500$ samples) is,

$$E_c = \frac{1}{n} \sum_{i=1}^n E_i \quad (\text{A.1})$$

where E_i is an individual sample. Mean velocities were then subtracted from the record to calculate root-mean-squared oscillatory velocities, e.g.,

$$E_{w,rms} = \sqrt{\frac{1}{n} \sum_{i=1}^n (E_i - E_c)^2}. \quad (\text{A.2})$$

Total mean current and oscillatory velocities were calculated as,

$$|U_c| = \sqrt{E_c^2 + N_c^2} \quad (\text{A.3})$$

$$\text{and, } |U_{w,rms}| = \sqrt{E_{w,RMS}^2 + N_{w,RMS}^2}. \quad (\text{A.4})$$

Note that $|U_{w,rms}|$ is assumed as the oscillatory velocity, although in actuality it encompasses all other unsteady flows. Finally, the amplitude of oscillatory velocity fluctuations was calculated from the rms velocities by assuming perfect sinusoids, e.g. $U_w = \sqrt{2}U_{w,rms}$.

Ten cases were selected based on wave heights, five experiments with the lowest mean H_s , and five with the largest mean H_s , for each of the four tidal stages. Total mean current (U_c) and oscillatory velocities (U_w) were calculated for a single bin above the respective wave boundary layers for all three Vectrinos in each experiment, using samples corresponding to each tidal stage. U_w typically exceeded U_c by $O(1 - 10)$, with the closest comparative magnitudes occurring during the lowest tidal stage (LL), and the largest differences occurring during the highest tidal stage (HH).

Appendix B: Spectral and structure function estimates of the TKE dissipation rate

In general, the dissipation rate of turbulence can be estimated from the power spectrum of vertical velocities,

$$\varepsilon_{Sp} = B_w \frac{S_{ww}^{2/3}}{U_\delta} f^{5/2}, \quad (\text{B.1})$$

where $S_{ww}(f)$ is the power spectral density of w in the inertial subrange, U_δ is the wave orbital velocity, and B_w is ~ 10 (Hay, 2008). Here, the subscript ε_{Sp} refers to the spectral method. Hereafter, the subscript ε_{SF} refers to the second-order structure function (Section 3.2.3).

To compare the spectral method with the structure function, estimates of ε_{Sp} were computed with Equation B.1 from 10-minute Vectrino velocity segments ($n = 30000$) recorded during the HTA2 experiment with a 50% overlap between segments. The width of the inertial subrange was defined as $f_{wc} < f < f_{hc}$ (Section 3.2.4).

As shown in Figure B.1, the spectral method overestimates the dissipation rate compared to the structure function by approximately 10% between the three instruments ($x = -10$ cm, $x = 10$ cm and $x = 20$ cm) of the HTA2 experiment; $\varepsilon_{SF} \sim 0.9\varepsilon_{Sp}$. Former studies have also compared the structure function and spectral methods and have found the two methods produce dissipation rate estimates that agree to within 16% depending on the experimental location and flow direction (flood tide vs. ebb tide), with the tendency that $\varepsilon_{SF} < \varepsilon_{Sp}$ (McMillan and Hay, 2017). In general, the spectral method is typically employed using point measurements of velocity. As this method relies on a horizontal advection speed (U_δ in Equation B.1) to convert frequencies to wave numbers via Taylor's frozen turbulence hypothesis, i.e., $k = 2\pi f/U_\delta$, its usage can be problematic in wave-dominated environments where the unsteady advection of wave energy into the turbulence band might affect turbulence estimates (Trowbridge et al., 2018). Hence we have chosen to use the structure function approach of Wiles et al., (2006) to estimate dissipation rates as this method has been proven to be robust for use with profiling velocimeters in wave-dominated environments (e.g., Lanckriet and Puleo, 2013). Furthermore,

given that our structure function estimates of dissipation ranged between 10^{-5} and $10^{-3} \text{ W kg}^{-1}$ (Section 3.3.3), the corresponding range of the Kolmogorov microscale, $\eta_k = (\nu^3/\varepsilon)^{1/4}$ was between 0.58 and 0.18 mm given a kinematic viscosity of seawater at 25 °C equal to $1.05 \times 10^{-6} \text{ m}^2 \text{ s}^{-1}$. Hence, the microscale range was smaller than the 1 mm spacing in between the Vectrino Profiler bins; higher dissipation estimates would produce smaller estimates of η_k . Therefore, the structure function method should be sufficient to produce a first-order estimate of ε .

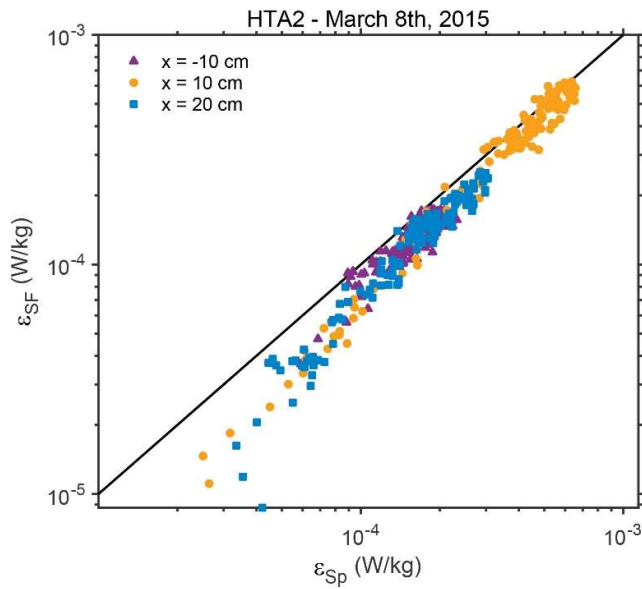


Figure B.1: Comparison of dissipation rates computed over 10-minute intervals from HTA2 velocity measurements using the spectral method (ε_{Sp}) and a second-order structure function (ε_{SF}). The solid black line is a 1:1 ratio.

Appendix C: Estimation of ripple geometry

The empirical model for wave generated ripples by Wikramanayake and Madsen (1994) and the parameterization suggested by Styles and Glenn (2002) is,

$$\frac{\eta}{A_\delta} = \begin{cases} 0.3X^{-0.39} & X \leq 2 \\ 0.45X^{-0.99} & X \geq 2 \end{cases} \quad (\text{C.1})$$

$$\frac{\lambda}{A_\delta} = \begin{cases} 1.96X^{-0.28} & X \leq 2 \\ 2.71X^{-0.75} & X \geq 2 \end{cases} \quad (\text{C.2})$$

where the parameter X for monochromatic waves is defined as,

$$X = \frac{4\nu U_\delta^2}{d_{50} \left[\left(\frac{\rho_s}{\rho} - 1 \right) g d_{50} \right]^{1.5}}, \quad (\text{C.3})$$

ρ_s is the sediment density ($= 2650 \text{ kg/m}^3$), ν is the kinematic viscosity of seawater, η is the ripple height, and λ the wavelength. The bedform migration velocity, U_m is related to the volumetric bedload transport flux per unit width, Q_b following Bagnold (1941),

$$U_m = \frac{Q_B}{\eta \left(1 - \frac{\rho_s}{\rho} \right)}, \quad (\text{C.4})$$

a model based on sand dune migration which assumes the bedform shape and migration rate are constant. The bedload flux Q_B is given by the formulation in van Rijn (1998),

$$Q_B = 9.1 \left(g \frac{\rho_s - \rho}{\rho} d_{50}^3 \right)^{0.5} (\theta - \theta_{crit})^{1.78} \frac{V_m}{|V_m|}, \quad (\text{C.5})$$

where V_m is the depth-averaged current velocity. The Shields parameter θ , and critical Shields parameter θ_{crit} , are respectively given by:

$$\theta = \frac{0.5\rho f_w U_\delta^2}{(\rho_s - \rho) g d_{50} \left(1 - \frac{\pi\eta}{\lambda} \right)^2}, \quad (\text{C.6})$$

and,

$$\theta_{crit} = \frac{\tau_c}{\rho \left(\frac{\rho_s}{\rho} - 1 \right) g d_{50}}. \quad (\text{C.7})$$

References

- Aberle, J., Järvelä, J., 2015. Hydrodynamics of vegetated channels. *GeoPlanet Earth Planet. Sci.* 50, 519–541. https://doi.org/10.1007/978-3-319-17719-9_21
- Allison, M.A., Lee, M.T., 2004. Sediment exchange between Amazon mudbanks and shore-fringing mangroves in French Guiana. *Mar. Geol.* 208, 169–190.
- Allison, M.A., Nittrouer, C.A., Ogston, A.S., Mullarney, J.C., Nguyen, T.T., Wallace, P.J., Martin, R., White, I., Hicks, B.J., Jones, M.H., 2017. Sedimentation and survival of the Mekong Delta: A case study of decreased sediment supply and accelerating rates of relative sea level rise. *Oceanography* 30, 98–109. <https://doi.org/https://doi.org/10.5670/oceanog.2017.318>
- Alongi, D.M., 2009. *The energetics of mangrove forests*, 1st ed. Springer Science & Business Media. Springer Netherlands. <https://doi.org/10.1007/978-1-4020-4271-3>
- Alongi, D.M., 2008. Mangrove forests: resilience, protection from tsunamis, and responses to global climate change. *Estuar. Coast. Shelf Sci.* 76, 1–13.
- Alongi, D.M., 2002. Present state and future of the world's mangrove forests. *Environ. Conserv.* 29, 331–349. <https://doi.org/10.1017/S0376892902000231>
- Anthony, E.J., Brunier, G., Besset, M., Goichot, M., Dussouillez, P., Nguyen, V.L., 2015. Linking rapid erosion of the Mekong River delta to human activities. *Sci. Rep.* 5, 1–12. <https://doi.org/10.1038/srep14745>
- Anthony, E.J., Gardel, A., Gratiot, N., Proisy, C., Allison, M.A., Dolique, F., Fromard, F., 2010. The Amazon-influenced muddy coast of South America: A review of mud-bank--shoreline interactions. *Earth-Science Rev.* 103, 99–121.
- Aucan, J., Ridd, P. V., 2000. Tidal asymmetry in creeks surrounded by saltflats and mangroves with small swamp slopes. *Wetl. Ecol. Manag.* 8, 223–231. <https://doi.org/10.1023/A:1008459814925>
- Bagnold, R.A., 1941. *The Physics of Blown Sand and Desert Dunes*. CRC Press, Boca Raton, Fla.
- Balke, T., Bouma, T.J., Herman, P.M.J., Horstman, E.M., Sudtongkong, C., Webb, E.L., 2013. Cross-shore gradients of physical disturbance in mangroves: Implications for seedling establishment. *Biogeosciences* 10, 5411–5419. <https://doi.org/10.5194/bg-10-5411-2013>
- Balke, T., Bouma, T.J., Horstman, E.M., Webb, E.L., Erfemeijer, P.L.A., Herman, P.M.J., 2011. Windows of opportunity: Thresholds to mangrove seedling establishment on tidal flats. *Mar. Ecol. Prog. Ser.* 440, 1–9. <https://doi.org/10.3354/meps09364>

- Bao, T.Q., 2011. Effect of mangrove forest structures on wave attenuation in coastal Vietnam. *Oceanologia* 53, 807–818. <https://doi.org/10.5697/oc.53-3.807>
- Belcher, S., Jerram, N., Hunt, J., 2003. Adjustment of a turbulent boundary layer to a “canopy” of roughness elements. *J. Fluid Mech.* 488, 369–398. <https://doi.org/10.1017/S0022112003005019>
- Bennett, S.J., Wu, W., Alonso, C. V., Wang, S.S.Y., 2008. Modeling fluvial response to in-stream woody vegetation: Implications for stream corridor restoration. *Earth Surf. Process. Landforms* 33, 890–909. <https://doi.org/10.1002/esp.1581>
- Bird, E.C.F., 1971. Mangroves as land-builders. *Vic. Nat* 88, 189–197.
- Bouma, T.J., De Vries, M.B., Low, E., Peralta, G., Tánzos, I.C., Van De Koppel, J., Herman, P.M.J., 2005. Trade-offs related to ecosystem engineering: A case study on stiffness of emerging macrophytes. *Ecology* 86, 2187–2199. <https://doi.org/10.1890/04-1588>
- Bouma, T.J., van Duren, L.A., Temmerman, S., Claverie, T., Blanco-Garcia, A., Ysebaert, T., Herman, P.M.J., 2007. Spatial flow and sedimentation patterns within patches of epibenthic structures: Combining field, flume and modelling experiments. *Cont. Shelf Res.* 27, 1020–1045. <https://doi.org/10.1016/j.csr.2005.12.019>
- Bradley, K., Houser, C., 2009. Relative velocity of seagrass blades: Implications for wave attenuation in low-energy environments. *J. Geophys. Res. Earth Surf.* 114, 1–13. <https://doi.org/10.1029/2007JF000951>
- Brand, A., Noss, C., 2017. High-resolution flow characterization close to the sediment-water interface in a run of the river reservoir. *Water Resour. Res.* 53, 4286–4302. <https://doi.org/10.1002/2016WR020203>
- Brand, A., Noss, C., Dinkel, C., Holzner, M., 2016. High-resolution measurements of turbulent flow close to the sediment-water interface using a bistatic acoustic profiler. *J. Atmos. Ocean. Technol.* 33, 769–788. <https://doi.org/10.1175/JTECH-D-15-0152.1>
- Bricker, J.D., Monismith, S.G., 2007. Spectral wave-turbulence decomposition. *J. Atmos. Ocean. Technol.* 24, 1479–1487. <https://doi.org/10.1175/JTECH2066.1>
- Brinkman, R.M., 2006. Wave attenuation in mangrove forests: an investigation through field and theoretical studies. PhD Thesis James Cook University, Townsville, Australia. (146 pp).
- Brinkman, R.M., Massel, S.R., Ridd, P. V, Furukawa, K., 1997. Surface wave attenuation in mangrove forests, in: *Pacific Coasts and Ports’ 97: Proceedings of the 13th Australasian Coastal and Ocean Engineering Conference and the 6th Australasian Port and Harbour Conference; Volume 2.* p. 909.

- Bryan, K.R., Black, K.P., Gorman, R.M., 2003. Spectral Estimates of Dissipation Rate within and near the Surf Zone. *J. Phys. Oceanogr.* 33, 979–993. [https://doi.org/10.1175/1520-0485\(2003\)033<0979:SEODRW>2.0.CO;2](https://doi.org/10.1175/1520-0485(2003)033<0979:SEODRW>2.0.CO;2)
- Bryan, K.R., Nardin, W., Mullarney, J.C., Fagherazzi, S., 2017. The role of cross-shore tidal dynamics in controlling intertidal sediment exchange in mangroves in Cù Lao Dung, Vietnam. *Cont. Shelf Res.* 147, 128–143. <https://doi.org/10.1016/j.csr.2017.06.014>
- Bullock, E.L., Fagherazzi, S., Nardin, W., Vo-Luong, P., Nguyen, P., Woodcock, C.E., 2017. Temporal patterns in species zonation in a mangrove forest in the Mekong Delta, Vietnam, using a time series of Landsat imagery. *Cont. Shelf Res.* 147, 144–154.
- Cahoon, D.R., Hensel, P.F., Spencer, T., Reed, D.J., McKee, K.L., Saintilan, N., 2006. Coastal wetland vulnerability to relative sea-level rise: wetland elevation trends and process controls, in: *Wetlands and Natural Resource Management*. Springer, Berlin, Heidelberg, 271–292.
- Chen, Y., Li, Y., Cai, T., Thompson, C., Li, Y., 2016. A comparison of biohydrodynamic interaction within mangrove and saltmarsh boundaries. *Earth Surf. Process. Landforms* 41, 1967–1979.
- Chen, Z., Ortiz, A., Zong, L., Nepf, H., 2012. The wake structure behind a porous obstruction and its implications for deposition near a finite patch of emergent vegetation. *Water Resour. Res.* 48. <https://doi.org/10.1029/2012WR012224>
- Cintron, G., Novelli, Y.S., 1984. Methods for studying mangrove structure, in: *Mangrove Ecosystem: Research Methods*. UNESCO, 91–113.
- Craig, R.G.A., Loadman, C., Clement, B., Rusello, P.J., Siegel, E., 2011. Characterization and testing of a new bistatic profiling acoustic Doppler velocimeter: The Vectrino-II, in: *Current, Waves and Turbulence Measurements (CWTM)*, 2011 IEEE/OES 10th. 246–252.
- Cui, J., Neary, V.S., 2008. LES study of turbulent flows with submerged vegetation. *J. Hydraul. Res.* 46, 307–316. <https://doi.org/10.3826/jhr.2008.3129>
- Danielsen, F., Sørensen, M.K., Olwig, M.F., Selvam, V., Parish, F., Burgess, N.D., Hiraishi, T., Karunagaran, V.M., Rasmussen, M.S., Hansen, L.B., Quarto, A., Suryadiputra, N., 2005. The Asian tsunami: A protective role for coastal vegetation. *Science* 310, 5748, 643. <https://doi.org/10.1126/science.1118387>
- Davis, J.H., 1940. *The ecology and geologic role of mangroves in Florida*, Carnegie Institution of Washington Publication. Carnegie Institution of Washington.

- Davis, K.A., Monismith, S.G., 2011. The Modification of Bottom Boundary Layer Turbulence and Mixing by Internal Waves Shoaling on a Barrier Reef. *J. Phys. Oceanogr.* 41, 2223–2241. <https://doi.org/10.1175/2011JPO4344.1>
- Deltares, 2014. Delft3D-FLOW, User Manual 1–684.
- Detto, M., Katul, G.G., Siqueira, M., Juang, J.Y., Stoy, P., 2008. The structure of turbulence near a tall forest edge: The backward facing step flow analogy. *Ecol. Appl.* 18, 1420–1435.
- Dittmar, T., Hertkorn, N., Kattner, G., Lara, R.J., 2006. Mangroves, a major source of dissolved organic carbon to the oceans. *Global Biogeochem. Cycles.* 20. <https://doi.org/https://doi.org/10.1029/2005GB002570>
- Duarte, C.M., Losada, I.J., Hendriks, I.E., Mazarrasa, I., Marbà, N., 2013. The role of coastal plant communities for climate change mitigation and adaptation. *Nat. Clim. Chang.* 3, 961–968.
- Duarte, C.M., Middelburg, J.J., Caraco, N., 2005. Major role of marine vegetation on the oceanic carbon cycle. *Biogeosciences* 2, 1–8. <https://doi.org/10.5194/bgd-1-659-2004>
- Duke, N.C., 1992. Mangrove floristics and biogeography. Chapter 4 in: *Trop. Mangrove Ecosyst.* Robertson, A.I., Alongi, D.M., (Eds). Coastal Estuarine Studies Series. American Geophysical Union, Washington DC. 41, 63–100.
- Dunn, C., F. Lopez, and M. Garcia (1996), Mean flow and turbulence structure induced by vegetation: Experiments, *Hydraul. Eng. Ser. 51*, Dep. of Civ. Eng., Univ. of Ill. at Urbana-Champaign, Urbana.
- Eidam, E.F., Nittrouer, C.A., Ogston, A.S., DeMaster, D.J., Liu, J.P., Nguyen, T.T., Nguyen, T.N., 2017. Dynamic controls on shallow clinoform geometry: Mekong Delta, Vietnam. *Cont. Shelf Res.* 147, 165–181. <https://doi.org/10.1016/j.csr.2017.06.001>
- Ellison, A.M., 2000. Mangrove restoration: Do we know enough? *Restor. Ecol.* 8, 219–229. <https://doi.org/10.1046/j.1526-100X.2000.80033.x>
- Ellison, J.C., 2009. Geomorphology and sedimentology of mangroves, in: Perillo, E., Wolanski, E., Cahoon, D.R., Brinson, M. (Eds), *Coastal Wetlands: An Integrated Ecosystem Approach*. Elsevier BV, Amsterdam, pp. 565–591.
- Etminan, V., Ghisalberti, M., Lowe, R., 2018. Predicting bed shear stresses in vegetated channels. *Water Resour. Res.* 54, 3179–3196. <https://doi.org/10.1029/2018WR022811>
- Etminan, V., Lowe, R.J., Ghisalberti, M., 2017. A new model for predicting the drag exerted by vegetation canopies. *Water Resour. Res.* 53, 3179–3196. <https://doi.org/10.1002/2016WR020090>
- Fagherazzi, S., Bryan, K., Nardin, W., 2017. Buried Alive or Washed Away: The Challenging Life of Mangroves in the Mekong Delta. *Oceanography* 30, 48–59. <https://doi.org/10.5670/oceanog.2017.313>

- Fagherazzi, S., Kirwan, M.L., Mudd, S.M., Guntenspergen, G.R., Temmerman, S., Rybczyk, J.M., Reyes, E., Craft, C., Clough, J., 2012. Numerical models of salt marsh evolution: Ecological, geomorphic, and climatic factors. *Rev. Geophys.* 50, 1–28.
<https://doi.org/10.1029/2011RG000359.1>.INTRODUCTION
- Farge, M., 1992. Wavelet Transforms And Their Applications To Turbulence. *Annu. Rev. Fluid Mech.* 24, 395–457.
<https://doi.org/10.1146/annurev.fluid.24.1.395>
- Fedderson, F., 2012. Observations of the Surf-Zone Turbulent Dissipation Rate. *J. Phys. Oceanogr.* 42, 386–399. <https://doi.org/10.1175/JPO-D-11-082.1>
- Fedderson, F., Guza, R.T., Elgar, S., Herbers, T.H.C., 2000. Velocity moments in alongshore bottom stress parameterizations. *J. Geophys. Res.* 105, 8673.
<https://doi.org/10.1029/2000JC900022>
- Fedderson, F., Williams, I.J., 2007. Direct estimation of the Reynolds stress vertical structure in the nearshore. *J. Atmos. Ocean. Technol.* 24, 102–116.
<https://doi.org/10.1175/JTECH1953.1>
- Folk, R.L., Ward, W.C., 1957. Brazos River bar [Texas]; a study in the significance of grain size parameters. *J. Sediment. Res.* 27, 3–26.
<https://doi.org/10.1306/74D70646-2B21-11D7-8648000102C1865D>
- Fredsøe, J., Deigaard, R., 1992. *Mechanics of Coastal Sediment Transport*, in: *Advanced Series on Ocean Engineering*. World Scientific, London, UK. 392.
<https://doi.org/10.1142/1546>
- Fricke, A.T., Nittrouer, C.A., Ogston, A.S., Vo-Luong, H.P., 2017. Asymmetric progradation of a coastal mangrove forest controlled by combined fluvial and marine influence, Cù Lao Dung, Vietnam. *Cont. Shelf Res.* 147, 78–90.
<https://doi.org/10.1016/j.csr.2017.07.012>
- Friess, D.A., Krauss, K.W., Horstman, E.M., Balke, T., Bouma, T.J., Galli, D., Webb, E.L., 2012. Are all intertidal wetlands naturally created equal? Bottlenecks, thresholds and knowledge gaps to mangrove and saltmarsh ecosystems. *Biol. Rev.* 87, 346–366. <https://doi.org/10.1111/j.1469-185X.2011.00198.x>
- Fujimoto, K., 1998. Mangrove habitat evolution related to Holocene sea-level changes on Pacific islands. *Oceanogr. Lit. Rev.* 9, 1532.
- Furukawa, K., Wolanski, E., 1996. Sedimentation in mangrove forests. *Mangroves Salt Marshes.* 1, 3–10. <https://doi.org/10.1023/A:1025973426404>
- Furukawa, K., Wolanski, E., Mueller, H., 1997. Currents and Sediment Transport in Mangrove Forests. *Estuar. Coast. Shelf Sci.* 44, 301–310.
<https://doi.org/10.1006/ecss.1996.0120>

- Gatziolis, D., Liénard, J. F., Vogs, A., & Strigul, N. S. 2015. 3D tree dimensionality assessment using photogrammetry and small unmanned aerial vehicles. *PloS one*, 10, 9, e0137765.
- Gerbi, G.P., Trowbridge, J.H., Edson, J.B., Plueddemann, A.J., Terray, E.A., Fredericks, J.J., 2008. Measurements of Momentum and Heat Transfer across the Air–Sea Interface. *J. Phys. Oceanogr.* 38, 1054–1072. <https://doi.org/10.1175/2007JPO3739.1>
- Geyer, W.R., Trowbridge, J.H., Bowen, M.M., 2000. The Dynamics of a Partially Mixed Estuary. *J. Phys. Oceanogr.* 30, 2035–2048. [https://doi.org/10.1175/1520-0485\(2000\)030<2035:TDOAPM>2.0.CO;2](https://doi.org/10.1175/1520-0485(2000)030<2035:TDOAPM>2.0.CO;2)
- Ghisalberti, M., Nepf, H., 2006. The structure of the shear layer in flows over rigid and flexible canopies. *Environ. Fluid Mech.* 6, 277–301. <https://doi.org/10.1007/s10652-006-0002-4>
- Giri, C., Ochieng, E., Tieszen, L.L., Zhu, Z., Singh, A., Loveland, T., Masek, J., Duke, N., 2011. Status and distribution of mangrove forests of the world using earth observation satellite data. *Glob. Ecol. Biogeogr.* 20, 154–159. <https://doi.org/10.1111/j.1466-8238.2010.00584.x>
- Giri, C., Zhu, Z., Tieszen, L.L., Singh, A., Gillette, S., Kelmelis, J.A., 2008. Mangrove forest distributions and dynamics (1975-2005) of the tsunami-affected region of Asia. *J. Biogeogr.* 35, 519–528. <https://doi.org/10.1111/j.1365-2699.2007.01806.x>
- Godefert, F.S., Staquet, C., 2003. Statistical modelling and direct numerical simulations of decaying stably stratified turbulence. Part 2. Large-scale and small-scale anisotropy. *J. Fluid Mech.* 486, 115–159. <https://doi.org/10.1017/S0022112003004531>
- Goodess, C.M., 2013. How is the frequency, location and severity of extreme events likely to change up to 2060? *Environ. Sci. Policy* 27, 4–14. <https://doi.org/10.1016/j.envsci.2012.04.001>
- Gordon, L., Lohrmann, A., 2002. Near-Shore Doppler Current Meter Wave Spectra, in: *Ocean Wave Meas. Anal. Edge*, B.L., Hemsley, M.J. (Eds). Fourth Internat. Symp. Ocean Wave Meas. Analys., San Francisco, CA, USA 33–43. [https://doi.org/10.1061/40604\(273\)4](https://doi.org/10.1061/40604(273)4)
- Goring, D.G., Nikora, V.I., 2002. Despiking Acoustic Doppler Velocimeter Data. *J. Hydraul. Eng.* 128, 117–126. [https://doi.org/10.1061/\(ASCE\)0733-9429\(2002\)128:1\(117\)](https://doi.org/10.1061/(ASCE)0733-9429(2002)128:1(117))
- Grant, W.D., Madsen, O.S., 1986. The Continental-Shelf Bottom Boundary Layer. *Annu. Rev. Fluid Mech.* 18, 265–305. <https://doi.org/10.1146/annurev.fl.18.010186.001405>
- Grinsted, A., Moore, J.C., Jevrejeva, S., 2004. Application of the cross wavelet transform and wavelet coherence to geophysical time series. *Nonlinear Process. Geophys.* 11, 561–566. <https://doi.org/10.5194/npg-11-561-2004>

- Hansen, J.C.R., Reidenbach, M.A., 2012. Wave and tidally driven flows in eelgrass beds and their effect on sediment suspension. *Mar. Ecol. Prog. Ser.* 448, 271–287. <https://doi.org/10.3354/meps09225>
- Harris, R.J., Pilditch, C.A., Greenfield, B.L., Moon, V., Kröncke, I., 2016. The Influence of Benthic Macrofauna on the Erodibility of Intertidal Sediments with Varying mud Content in Three New Zealand Estuaries. *Estuaries and Coasts* 39, 815–828. <https://doi.org/10.1007/s12237-015-0036-2>
- Hay, A.E., 2008. Near-bed turbulence and relict waveformed sand ripples: Observations from the inner shelf. *J. Geophys. Res. Ocean.* 113, 1–24. <https://doi.org/10.1029/2006JC004013>
- Hench, J.L., Rosman, J.H., 2013. Observations of spatial flow patterns at the coral colony scale on a shallow reef flat. *J. Geophys. Res. Ocean.* 118, 1142–1156. <https://doi.org/10.1002/jgrc.20105>
- Henderson, S.M., Norris, B.K., Mullarney, J.C., Bryan, K.R., 2017. Wave-frequency flows within a near-bed vegetation canopy. *Cont. Shelf Res.* 147, 91–101. <https://doi.org/10.1016/j.csr.2017.06.003>
- Hong, P.N., San, H.T., 1993. *Mangroves of Vietnam*. IUCN, Bangkok, Thailand. [https://doi.org/10.1016/0304-3770\(95\)90004-7](https://doi.org/10.1016/0304-3770(95)90004-7)
- Horstman, E., Dohmen-Janssen, M., Narra, P., Berg, N.-J. van den, Siemerink, M., Balke, T., Bouma, T., Hulscher, S., 2012. Wave attenuation in mangrove forests. Field data obtained in Trang, Thailand. *Coast. Eng. Proc.* 1, 1–15. <https://doi.org/10.9753/icce.v33.waves.40>
- Horstman, E.M., Bryan, K.R., Mullarney, J.C., Pilditch, C.A., Eager, C.A., 2018. Are flow-vegetation interactions well represented by mimics? A case study of mangrove pneumatophores. *Adv. Water Resour.* 111, 360–371. <https://doi.org/10.1016/j.advwatres.2017.11.018>
- Horstman, E.M., Dohmen-Janssen, C.M., Bouma, T.J., Hulscher, S.J.M.H., 2015. Tidal-scale flow routing and sedimentation in mangrove forests: Combining field data and numerical modelling. *Geomorphology* 228, 244–262. <https://doi.org/10.1016/j.geomorph.2014.08.011>
- Horstman, E.M., Dohmen-Janssen, C.M., Hulscher, S.J.M.H., 2013. Flow routing in mangrove forests: A field study in Trang province, Thailand. *Cont. Shelf Res.* 71, 52–67. <https://doi.org/10.1016/j.csr.2013.10.002>
- IUCN, 2011. *An Appraisal of Mangrove Management in Micro-tidal Estuaries and Lagoons in Sri Lanka*. IUCN (International Union for Conservation of Nature), Sri Lanka Office, Colombo, LK.
- Jennerjahn, T.C., Venugopal, I., 2002. Relevance of mangroves for the production and deposition of organic matter along tropical Relevance of mangroves for the production and deposition. *Sci. Nat.* 89, 23–30. <https://doi.org/10.1007/s00114-001-0283-x>

- Jones, C.G., Lawton, J.H., Shachak, M., 2014. Positive and Negative Effects of Organisms as Physical Ecosystem Engineers. *Ecology* 78, 1946–1957.
- Jones, C.G., Lawton, J.H., Shachak, M., 2009. Organisms as Ecosystem Engineers Organisms as ecosystem engineers, in: *Ecosystem Management*. Springer, 373–386.
- Jones, N.L., Monismith, S.G., 2008. The Influence of Whitecapping Waves on the Vertical Structure of Turbulence in a Shallow Estuarine Embayment. *J. Phys. Oceanogr.* 38, 1563–1580. <https://doi.org/10.1175/2007JPO3766.1>
- Jonsson, I.G., 1966. Wave Boundary Layers and Friction Factors, in: *Proceedings of the 10th International Conference on Coastal Engineering*, Tokyo 1966. 127–148.
- Kaimal, J.C., Wyngaard, J.C., Izumi, Y., Cote, O.R., 1972. Spectral characteristics of surface layer turbulence. *Quart. J. Roy. Meteorol. Soc.* 98, 563–589. <https://doi.org/10.1002/qj.49710745309>
- Kathiresan, K., Rajendran, N., 2005. Coastal Mangrove Forests Mitigated Tsunami. *Estuar. Coast. Shelf Sci.* 65, 601–606. <https://doi.org/https://doi.org/10.1016/j.ecss.2005.06.022>
- King, A.T., Tinoco, R.O., Cowen, E.A., 2012. A k - ϵ turbulence model based on the scales of vertical shear and stem wakes valid for emergent and submerged vegetated flows. *J. Fluid Mech.* 701, 1–39. <https://doi.org/10.1017/jfm.2012.113>
- Kirincich, A.R., Lentz, S.J., Gerbi, G.P., 2010. Calculating Reynolds stresses from ADCP measurements in the presence of surface gravity waves using the cospectra-fit method. *J. Atmos. Ocean. Technol.* 27, 889–907. <https://doi.org/10.1175/2009JTECHO682.1>
- Kiya, M., Tamura, H., Arie, M., 1980. Vortex Shedding from a Circular Cylinder in moderate Reynolds number shear flow. *J. Fluid Mech.* 141, 721–737. <https://doi.org/10.1017/S0022112080001899>
- Kobashi, D., Mazda, Y., 2005. Tidal flow in riverine-type mangroves. *Wetl. Ecol. Manag.* 13, 615–619. <https://doi.org/10.1007/s11273-004-3481-4>
- Krauss, K.W., Allen, J.A., Cahoon, D.R., 2003. Differential rates of vertical accretion and elevation change among aerial root types in Micronesian mangrove forests. *Estuar. Coast. Shelf Sci.* 56, 251–259. [https://doi.org/10.1016/S0272-7714\(02\)00184-1](https://doi.org/10.1016/S0272-7714(02)00184-1)
- Krauss, K.W., Cahoon, D.R., Allen, J.A., Ewel, K.C., Lynch, J.C., Cormier, N., 2010. Surface elevation change and susceptibility of different mangrove zones to sea-level rise on Pacific high islands of Micronesia. *Ecosystems* 13, 129–143. <https://doi.org/10.1007/s10021-009-9307-8>

- Krauss, K.W., Doyle, T.W., Doyle, T.J., Swarzenski, C.M., From, A.S., Day, R.H., Conner, W.H., 2009. Water level observations in mangrove swamps during two hurricanes in Florida. *Wetlands* 29, 142–149. <https://doi.org/10.1672/07-232.1>
- Kumara, M.P., Jayatissa, L.P., Krauss, K.W., Phillips, D.H., Huxham, M., 2010. High mangrove density enhances surface accretion, surface elevation change, and tree survival in coastal areas susceptible to sea-level rise. *Oecologia* 164, 545–553. <https://doi.org/10.1007/s00442-010-1705-2>
- Lacy, J.R., Wyllie-Echeverria, S., 2011. The influence of current speed and vegetation density on flow structure in two macrotidal eelgrass canopies. *Limnol. Oceanogr. Fluids Environ.* 1, 3855. <https://doi.org/10.1215/21573698-1152489>
- Laing, A.K., Gemmill, W., Magnusson, A.K., Burroughs, L., Reistad, M., Khandekar, M., Holthuijsen, L., Ewing, J.A., Carter, D.J.T., 1998. *Guide to Wave Analysis and Forecasting*, 2nd ed, WMO-No. 702. Geneva, Switzerland.
- Lanckriet, T., Puleo, J.A., 2013. Near-bed turbulence dissipation measurements in the inner surf and swash zone. *J. Geophys. Res. Ocean.* 118, 6634–6647. <https://doi.org/10.1002/2013JC009251>
- Le Bouteiller, C., Venditti, J.G., 2015. Sediment transport and shear stress partitioning in a vegetated flow. *Water Resour. Res.* 51, 2901–2922. <https://doi.org/10.1002/2014WR015825>
- Lees, B.J., 1981. Relationship between eddy viscosity of seawater and eddy diffusivity of suspended particles. *Geo-Marine Lett.* 1, 249–254. <https://doi.org/10.1007/BF02462442>
- Leonard, L.A., Luther, M.E., 1995. Flow hydrodynamics in tidal marsh canopies. *Limnol. Oceanogr.* 40, 1474–1484. <https://doi.org/10.4319/lo.1995.40.8.1474>
- Leonard, L.A., Croft, A.L., 2006. The effect of standing biomass on flow velocity and turbulence in *Spartina alterniflora* canopies. *Estuar. Coast. Shelf Sci.* 69, 325–336. <https://doi.org/10.1016/j.ecss.2006.05.004>
- Li, C.W., Yan, K., 2007. Numerical Investigation of Wave–Current–Vegetation Interaction. *J. Hydraul. Eng.* 133, 794–803. [https://doi.org/10.1061/\(ASCE\)0733-9429\(2007\)133:7\(794\)](https://doi.org/10.1061/(ASCE)0733-9429(2007)133:7(794))
- Li, L., Wang, X.H., Andutta, F., Williams, D., 2014. Effects of mangroves and tidal flats on suspended-sediment dynamics: Observational and numerical study of Darwin Harbour, Australia. *J. Geophys. Res. Ocean.* 119, 5854–5873. <https://doi.org/10.1002/2014JC009987>
- Liénard, J., Lynn, K., Strigul, N., Norris, B.K., Gatziolis, D., Mullarney, J.C., Bryan, K.R., Henderson, S.M., 2016. Efficient three-dimensional reconstruction of aquatic vegetation geometry: Estimating morphological parameters influencing hydrodynamic drag. *Estuar. Coast. Shelf Sci.* 178, 77–85. <https://doi.org/10.1016/j.ecss.2016.05.011>

- Lightbody, A.F., Avenier, M.E., Nepf, H.M., 2008. Observations of short-circuiting flow paths within a free-surface wetland in Augusta, Georgia, U.S.A. *Limnol. Oceanogr.* 53, 1040–1053. <https://doi.org/10.4319/lo.2008.53.3.1040>
- Lin, B.B., Dushoff, J., 2004. Mangrove filtration of anthropogenic nutrients in the Rio Coco Solo, Panama. *Manag. Environ. Qual. An Int. J.* 15, 131–142. <https://doi.org/10.1108/14777830410523071>
- Liu, D., Diplas, P., Hodges, C.C., Fairbanks, J.D., 2010. Hydrodynamics of flow through double layer rigid vegetation. *Geomorphology* 116, 286–296. <https://doi.org/10.1016/j.geomorph.2009.11.024>
- Lohrmann, A., Hackett, B., Røed, L.P., 1990. High Resolution Measurements of Turbulence, Velocity and Stress Using a Pulse-to-Pulse Coherent Sonar. *J. Atmos. Ocean. Technol.* 7, 19–37. [https://doi.org/10.1175/1520-0426\(1990\)007<0019:HRMOTV>2.0.CO;2](https://doi.org/10.1175/1520-0426(1990)007<0019:HRMOTV>2.0.CO;2)
- Lohrmann, A., Nylund, S., 2008. Pure coherent Doppler systems - How far can we push it?, in: *Proceedings of the IEEE Working Conference on Current Measurement Technology*. pp. 19–24. <https://doi.org/10.1109/CCM.2008.4480837>
- Loisel, H., Mangin, A., Vantrepotte, V., Dessailly, D., Ngoc, D., Garnesson, P., Ouillon, S., Lefebvre, J., Mériaux, X., Minh, T., 2014. Remote Sensing of Environment Variability of suspended particulate matter concentration in coastal waters under the Mekong's influence from ocean color (MERIS) remote sensing over the last decade. *Remote Sens. Environ.* 150, 218–230. <https://doi.org/10.1016/j.rse.2014.05.006>
- López, F., García, M.H., 2001. Mean Flow and Turbulence Structure of Open-Channel Flow through Non-Emergent Vegetation. *J. Hydraul. Eng.* 127, 392–402. [https://doi.org/10.1061/\(ASCE\)0733-9429\(2001\)127:5\(392\)](https://doi.org/10.1061/(ASCE)0733-9429(2001)127:5(392))
- López, F., García, M.H., 1998. Open-channel flow through simulated vegetation: Suspended sediment transport modeling. *Water Resour. Res.* 34, 2341–2352. <https://doi.org/10.1029/98WR01922>
- Lovelock, C.E., Bennion, V., Grinham, A., Cahoon, D.R., 2011. The role of surface and subsurface processes in keeping pace with sea level rise in intertidal wetlands of Morten Bay, Queensland, Australia. *Ecosystems* 14, 745–757. <https://doi.org/10.1007/s12192-010-0223-9>
- Lovelock, C.E., Cahoon, D.R., Friess, D.A., Guntenspergen, G.R., Krauss, K.W., Reef, R., Rogers, K., Saunders, M.L., Sidik, F., Swales, A., Saintilan, N., Thuyen, L.X., Triet, T., 2015. The vulnerability of Indo-Pacific mangrove forests to sea-level rise. *Nature* 526, 559–U217. <https://doi.org/10.1038/nature15538>
- Lowe, R.J., Koseff, J.R., Monismith, S.G., 2005. Oscillatory flow through submerged canopies: 1. Velocity structure. *J. Geophys. Res. C Ocean.* 110, 1–17. <https://doi.org/10.1029/2004JC002788>

- Lugo, A.E., Snedaker, S.C., 1974. The Ecology of Mangroves. *Annu. Rev. Ecol. Syst.* 5, 39–64. <https://doi.org/10.1146/annurev.es.05.110174.000351>
- Luhar, M., Coutu, S., Infantes, E., Fox, S., Nepf, H., 2010. Wave-induced velocities inside a model seagrass bed. *J. Geophys. Res. Ocean.* 115, 1–15. <https://doi.org/10.1029/2010JC006345>
- Luhar, M., Infantes, E., Orfila, A., Terrados, J., Nepf, H.M., 2013. Field observations of wave-induced streaming through a submerged seagrass (*Posidonia oceanica*) meadow. *J. Geophys. Res. Ocean.* 118, 1955–1968. <https://doi.org/10.1002/jgrc.20162>
- Luhar, M., Nepf, H.M., 2016. Wave-induced dynamics of flexible blades. *J. Fluids Struct.* 61, 20–41. <https://doi.org/10.1016/j.jfluidstructs.2015.11.007>
- Lumley, J.L., Terray, E.A., 1983. Kinematics of Turbulence Convected by a Random Wave Field. *J. Phys. Oceanogr.* [https://doi.org/10.1175/1520-0485\(1983\)013<2000:KOTCBA>2.0.CO;2](https://doi.org/10.1175/1520-0485(1983)013<2000:KOTCBA>2.0.CO;2)
- MacDonald, I.T., Mullarney, J.C., 2015. A novel “FlocDrifter” platform for observing flocculation and turbulence processes in a Lagrangian frame of reference. *J. Atmos. Ocean. Technol.* 32, 547–561. <https://doi.org/10.1175/JTECH-D-14-00106.1>
- MacVean, L., Lacy, J.R., 2014. Interactions between waves, sediment, and turbulence on a shallow estuarine mudflat. *J. Geophys. Res. Ocean.* 1534–1553. <https://doi.org/10.1002/2013JC009477>.Received
- Madsen, O.S., 1994. Spectral Wave-Current Bottom Boundary Layer Flows. *Coast. Eng. Proc.* 1, 384–398. <https://doi.org/10.9753/icce.v24>
- Mariotti, G., Fagherazzi, S., 2010. A numerical model for the coupled long-term evolution of salt marshes and tidal flats. *J. Geophys. Res. Earth Surf.* 115, 1–15. <https://doi.org/10.1029/2009JF001326>
- Massel, S.R., Furukawa, K., Brinkman, R., 1999. Surface wave propagation in mangrove forests. *Fluid Dyn. Res.* 24, 219–249. [https://doi.org/10.1016/S0169-5983\(98\)00024-0](https://doi.org/10.1016/S0169-5983(98)00024-0)
- Maza, M., Adler, K., Ramos, D., Garcia, A.M.P., Nepf, H.M., 2017. Velocity and drag evolution from the leading edge of a model mangrove forest. *J. Geophys. Res. Ocean.* 1–22. <https://doi.org/10.1002/2017JC012945>
- Mazda, Y., Kanazawa, N., Wolanski, E., 1995. Tidal asymmetry in mangrove creeks. *Hydrobiologia* 295, 51–58. <https://doi.org/10.1007/BF00029110>
- Mazda, Y., Kobashi, D., Okada, S., 2005. Tidal-scale hydrodynamics within mangrove swamps. *Wetl. Ecol. Manag.* 13, 647–655. <https://doi.org/10.1007/s11273-005-0613-4>
- Mazda, Y., Magi, M., Ikeda, Y., Kurokawa, T., Asano, T., 2006. Wave reduction in a mangrove forest dominated by *Sonneratia* sp. *Wetl. Ecol. Manag.* 14, 365–378. <https://doi.org/10.1007/s11273-005-5388-0>

- Mazda, Y., Magi, M., Kogo, M., Phan Nguyen Hong, 1997a. Mangroves as a coastal protection from waves in the Tong King Delta, Vietnam. *Mangroves Salt Marshes*. <https://doi.org/10.1023/A:1009928003700>
- Mazda, Y., Wolanski, E., King, B., Sase, A., Ohtsuka, D., Magi, M., 1997b. Drag force due to vegetation in mangrove swamps. *Mangroves Salt Marshes* 1, 193–199. <https://doi.org/10.1023/A:1009949411068>
- Mazda, Y., Wolanski, E., Ridd, P., 2007. Outline of the Physical Processes within Mangrove Systems. *Role Phys. Process. Mangrove Environ.* 3–64.
- McAnally, W.H., Teeter, A., Schoellhamer, D., Friedrichs, C., Hamilton, D., Hayter, E., Shrestha, P., Rodriguez, H., Sheremet, A., Kirby, R., 2007. Management of Fluid Mud in Estuaries, Bays, and Lakes. II: Measurement, Modeling, and Management. *J. Hydraul. Eng.* 133, 9–22. [https://doi.org/10.1061/\(ASCE\)0733-9429\(2007\)133:1\(9\)](https://doi.org/10.1061/(ASCE)0733-9429(2007)133:1(9))
- McIvor, A., Möller, I., Spencer, T., Spalding, M., 2013. The response of mangrove soil surface elevation to sea level rise. *Nat. Coast. Prot. Ser. Rep.* 3 1–59. <https://doi.org/ISSN 2050-7941>
- McIvor, A., Möller, I., Spencer, T., Spalding, M., 2012. Reduction of Wind and Swell Waves by Mangroves. *Nat. Coast. Prot. Ser. Rep.* 1 1–27. <https://doi.org/ISSN 2050-7941>.
- McKee, K.L., 2011. Biophysical control on accretion and elevation change in Caribbean mangrove ecosystems. *Estuar. Coast. Shelf Sci.* 91, 1–10. <https://doi.org/10.1016/j.ecss.2010.05.001>
- McKee, K.L., Cahoon, D.R., Feller, I.C., 2007. Caribbean mangroves adjust to rising sea level through biotic controls on change in soil elevation. *Glob. Ecol. Biogeogr.* 16, 545–556.
- McKee, K.L., McGinnis, T.I., 2003. Hurricane Mitch: Effects on Mangrove Soil Characteristics and Root Contributions to Soil Stabilization. *US Geol. Surv. Open File Rep.* OFR 03-178.
- McLachlan, R.L., Ogston, A.S., Allison, M.A., 2017. Implications of tidally-varying bed stress and intermittent estuarine stratification on fine-sediment dynamics through the Mekong’s tidal river to estuarine reach. *Cont. Shelf Res.* 147, 27–37. <https://doi.org/10.1016/j.csr.2017.07.014>
- McMillan, J.M., Hay, A.E., 2017. Spectral and structure function estimates of turbulence dissipation rates in a high-flow tidal channel using broadband ADCPs. *J. Atmos. Ocean. Technol.* 34, 5–20. <https://doi.org/10.1175/JTECH-D-16-0131.1>
- Milliman, J.D., Syvitski, J.P.M., 1992. Geomorphic/Tectonic Control of Sediment Discharge to the Ocean: The Importance of Small Mountainous Rivers. *J. Geol.* 100, 525–544. <https://doi.org/10.1086/629606>

- Moffett, K., Nardin, W., Silvestri, S., Wang, C., Temmerman, S., 2015. Multiple Stable States and Catastrophic Shifts in Coastal Wetlands: Progress, Challenges, and Opportunities in Validating Theory Using Remote Sensing and Other Methods. *Remote Sens.* 7, 10184–10226. <https://doi.org/10.3390/rs70810184>
- Mohrholz, V., Prandke, H., Lass, H.U., 2008. Estimation of TKE dissipation rates in dense bottom plumes using a Pulse Coherent Acoustic Doppler Profiler (PC-ADP) - Structure function approach. *J. Mar. Syst.* 70, 217–239. <https://doi.org/10.1016/j.jmarsys.2007.03.004>
- Möller, I., Kudella, M., Rupprecht, F., Spencer, T., Paul, M., Van Wesenbeeck, B.K., Wolters, G., Jensen, K., Bouma, T.J., Miranda-Lange, M., et al., 2014. Wave attenuation over coastal salt marshes under storm surge conditions. *Nat. Geosci.* 7, 727.
- Montgomery, J.M., Bryan, K.R., Mullarney, J.C., and E.M. Horstman (2019). Attenuation of storm surges by coastal mangroves, in press in *Geophys. Res. Lett.* 10.1029/2018GL081636.
- Montgomery, J.M., Bryan, K.R., Horstman, E.M., Mullarney, J.C., 2018. Attenuation of tides and surges by mangroves: Contrasting case studies from New Zealand. *Water (Switzerland)* 10. <https://doi.org/10.3390/w10091119>
- Mullarney, J.C., Henderson, S.M., Reyns, J.A.H., Norris, B.K., Bryan, K.R., 2017a. Spatially varying drag within a wave-exposed mangrove forest and on the adjacent tidal flat. *Cont. Shelf Res.* 141, 102–113. <https://doi.org/10.1016/j.csr.2017.06.019>
- Mullarney, J., Henderson, S.M., Norris, B.K., Bryan, K.R., Fricke, A.T., Sandwell, D.R., 2017b. A question of scale: How turbulence around aerial roots shapes the seabed morphology in mangrove forests of the Mekong Delta. *Oceanography*. *Oceanography* 30, 34–47. <https://doi.org/https://doi.org/10.5670/oceanog.2017.312>
- Mullarney, J.C., Henderson, S.M., 2018. Flows Within Marine Vegetation Canopies, in: Panchang, V., Kaihatu, J. (Eds.), *Advances in Coastal Hydraulics*. World Scientific Publishing Ltd., pp. 1–46. https://doi.org/10.1142/9789813231283_0001
- Mullarney, J.C., Henderson, S.M., 2012. Lagrangian Measurements of Turbulent Dissipation over a Shallow Tidal Flat from Pulse Coherent Acoustic Doppler Profilers. *Coast. Eng.* 1–12.
- Mullarney, J.C., Henderson, S.M., 2010. Wave-forced motion of submerged single-stem vegetation. *J. Geophys. Res. Ocean.* 115, C12061. <https://doi.org/10.1029/2010JC006448>
- Nardin, W., Locatelli, S., Pasquarella, V., Rulli, M.C., Woodcock, C.E., Fagherazzi, S., 2016a. Dynamics of a fringe mangrove forest detected by Landsat images in the Mekong River Delta, Vietnam. *Earth Surf. Process. Landforms* 41, 2024–2037. <https://doi.org/10.1002/esp.3968>

- Nardin, W., Woodcock, C.E., Fagherazzi, S., 2016b. Bottom sediments affect *Sonneratia* mangrove forests in the prograding Mekong delta, Vietnam. *Estuar. Coast. Shelf Sci.* 177, 60–70. <https://doi.org/10.1016/j.ecss.2016.04.019>
- Nepf, H.M., 2012. Flow and Transport in Regions with Aquatic Vegetation. *Annu. Rev. Fluid Mech.* 44, 123–142. <https://doi.org/10.1146/annurev-fluid-120710-101048>
- Nepf, H.M., 2012. Hydrodynamics of vegetated channels. *J. Hydraul. Res.* 50, 262–279.
- Nepf, H.M., 2004. Vegetated Flow Dynamics Introduction : Scales of Morphology and Flow in a Tidal Marsh. *Coast. Estuar. Stud.* 59, 137–163.
- Nepf, H.M., 1999. Drag, turbulence, and diffusion in flow through emergent vegetation. *Water Resour. Res.* 35, 479–489. <https://doi.org/10.1029/1998WR900069>
- Nepf, H.M., Ghisalberti, M., White, B., Murphy, E., 2007. Retention time and dispersion associated with submerged aquatic canopies. *Water Resour. Res.* 43, 1–10. <https://doi.org/10.1029/2006WR005362>
- Nepf, H.M., Sullivan, J.A., Zavitoski, R.A., 1997. A model for diffusion within an emergent plant canopy. *Limnol. Oceanogr.* 42(8), 85–95.
- Nepf, H.M., Vivoni, E.R., 2000. Flow structure in depth-limited, vegetated flow. *J. Geophys. Res. Ocean.* 105, 28547–28557. <https://doi.org/10.1029/2000JC900145>
- Neumeier, U., 2007. Velocity and turbulence variations at the edge of saltmarshes. *Cont. Shelf Res.* 27, 1046–1059. <https://doi.org/10.1016/j.csr.2005.07.009>
- Nguyen, P.K., 2009. Climate Change and Sea Level Rise Scenarios for Viet Nam - Summary for Policymakers, Ministry of Natural Resources and Environment. Viet Nam Ministry of Natural Resources and Environment (MONRE). Hanoi, Viet Nam.
- Nicolle, A., Eames, I., 2011. Numerical study of flow through and around a circular array of cylinders. *J. Fluid Mech.* 679, 1–31. <https://doi.org/10.1017/jfm.2011.77>
- Nielsen, P., 1992. Coastal Bottom Boundary Layers and Sediment Transport. World Scientific Publishing Company, Singapore. <https://doi.org/10.1142/1269>
- Nittrouer, C.A., Mullarney, J.C., Allison, M.A., Ogston, A.S., 2017. Sedimentary processes building a tropical delta yesterday, today, and tomorrow: The mekong system. *Oceanography* 30, 10–21. <https://doi.org/10.5670/oceanog.2017.310>

- Norris, B.K., Mullarney, J.C., Bryan, Karin, R., Henderson, S.M., 2019. Turbulence within Natural Mangrove Pneumatophore Canopies, in press in *J. Geophys. Res. Ocean.*
- Norris, B.K., Mullarney, J.C., Bryan, K.R., Henderson, S.M., 2017. The effect of pneumatophore density on turbulence: A field study in a *Sonneratia*-dominated mangrove forest, Vietnam. *Cont. Shelf Res.* 147, 114–127. <https://doi.org/10.1016/j.csr.2017.06.002>
- Panagiotopoulos, I., Voulgaris, G., Collins, M.B., 1997. The influence of clay on the threshold of movement of fine sandy beds. *Coast. Eng.* 32, 19–43. [https://doi.org/10.1016/S0378-3839\(97\)00013-6](https://doi.org/10.1016/S0378-3839(97)00013-6)
- Paterson, D.M., 1989. Short-term changes in the erodibility of intertidal cohesive sediments related to the migratory behavior of epipelagic diatoms. *Limnol. Oceanogr.* 34, 223–234. <https://doi.org/10.4319/lo.1989.34.1.0223>
- Petryk, S., Bosmajian, G., 1975. Analysis of Flow Through Vegetation. *J. Hydraul. Div.* 101, 871–884.
- Phan, L.K., van Thiel de Vries, J.S.M., Stive, M.J.F., 2015. Coastal Mangrove Squeeze in the Mekong Delta. *J. Coast. Res.* 300, 233–243. <https://doi.org/10.2112/JCOASTRES-D-14-00049.1>
- Poggi, D., Porporato, A., Ridolfi, L., Albertson, J.D., Katul, G.G., 2004. The effect of vegetation density on canopy sub-layer turbulence. *Boundary-Layer Meteorol.* 111, 565–587. <https://doi.org/10.1023/B:BOUN.0000016576.05621.73>
- Pope, S.B., 2000. *Turbulent Flows*. Cambridge University Press, Cambridge U.K.
- Pujol, D., Casamitjana, X., Serra, T., Colomer, J., 2013. Canopy-scale turbulence under oscillatory flow. *Cont. Shelf Res.* 66, 9–18. <https://doi.org/10.1016/j.csr.2013.06.012>
- Quartel, S., Kroon, A., Augustinus, P.G.E.F., Van Santen, P., Tri, N.H., 2007. Wave attenuation in coastal mangroves in the Red River Delta, Vietnam. *J. Asian Earth Sci.* 29, 576–584. <https://doi.org/10.1016/j.jseaes.2006.05.008>
- Raubenheimer, B., 2004. Observations of swash zone velocities: A note on friction coefficients. *J. Geophys. Res.* 109, C01027. <https://doi.org/10.1029/2003JC001877>
- Raupach, M., Shaw, R., 1982. Averaging procedures for flow within vegetation canopies. *Boundary-Layer Meteorol.* 22, 79–90.
- Raupach, M.R., 1992. Darg and drag partitioning on rough surfaces. *Boundary-Layer Meteorol.* 60, 375–395.
- Riffe, K.C., Henderson, S.M., Mullarney, J.C., 2011. Wave dissipation by flexible vegetation. *Geophys. Res. Lett.* 38, L18607. <https://doi.org/10.1029/2011GL048773>

- Rogers, K., Saintilan, N., Cahoon, D., 2005. Surface elevation dynamics in a regenerating mangrove forest at Homebush Bay, Australia. *Wetl. Ecol. Manag.* 13, 587–598. <https://doi.org/10.1007/s11273-004-0003-3>
- Rogers, K., Wilton, K.M., Saintilan, N., 2006. Vegetation change and surface elevation dynamics in estuarine wetlands of southeast Australia. *Estuar. Coast. Shelf Sci.* 66, 559–569. <https://doi.org/10.1016/j.ecss.2005.11.004>
- Saenger, P., 2002. Introduction: The Mangrove Environment, in: *Mangrove Ecology, Silviculture and Conservation*. Springer Netherlands, 1–10. https://doi.org/10.1007/978-94-015-9962-7_1
- Salem, M.E., Mercer, D.E., 2012. The economic value of mangroves: A meta-analysis. *Sustainability* 4, 359–383. <https://doi.org/10.3390/su4030359>
- Schewe, G., 1983. On the force fluctuations acting on a circular cylinder in crossflow from subcritical up to transcritical Reynolds numbers. *J. Fluid Mech.* 133, 265–285. <https://doi.org/10.1017/S0022112083001913>
- Schierreck, G.J., Booij, N., 1995. Wave transmission in mangrove forests.pdf. *Int. Conf. Coast. Port Eng. Dev. Ctries.* 1969–1983.
- Schmitt, K., Albers, T., Pham, T.T., Dinh, S.C., 2013. Site-specific and integrated adaptation to climate change in the coastal mangrove zone of Soc Trang Province, Viet Nam. *J. Coast. Conserv.* 17, 545–558. <https://doi.org/10.1007/s11852-013-0253-4>
- Shaw, W.J., Trowbridge, J.H., 2001. The direct estimation of near-bottom turbulent fluxes in the presence of energetic wave motions. *J. Atmos. Ocean. Technol.* 18, 1540–1557. [https://doi.org/10.1175/1520-0426\(2001\)018<1540:TDEONB>2.0.CO;2](https://doi.org/10.1175/1520-0426(2001)018<1540:TDEONB>2.0.CO;2)
- Silinski, A., Heuner, M., Troch, P., Puijalón, S., Bouma, T.J., Schoelynck, J., Schröder, U., Fuchs, E., Meire, P., Temmerman, S., 2016. Effects of contrasting wave conditions on scour and drag on pioneer tidal marsh plants. *Geomorphology* 255, 49–62. <https://doi.org/10.1016/j.geomorph.2015.11.021>
- Siniscalchi, F., Nikora, V.I., Aberle, J., 2012. Plant patch hydrodynamics in streams: Mean flow, turbulence, and drag forces. *Water Resour. Res.* 48, 1–14. <https://doi.org/10.1029/2011WR011050>
- Smith, J., Perkey, D., Priestas, A., 2015. Erosion thresholds and rates for sand-mud mixtures. Tech. Report, US Army Eng. Res. Dev. Cent.
- Soulsby, R.L., 1997. Dynamics of marine sands: a manual for practical applications, *Dynamics of marine sands: a manual for practical applications*. Thomas Telford. <https://doi.org/10.1680/doms.25844>
- Soulsby, R.L., 1980. Selecting Record Length and Digitization Rate for Near-Bed Turbulence Measurements. *J. Phys. Oceanogr.* 10, 208–219. [https://doi.org/10.1175/1520-0485\(1980\)010<0208:SRLADR>2.0.CO;2](https://doi.org/10.1175/1520-0485(1980)010<0208:SRLADR>2.0.CO;2)

- Soulsby, R.L., Dyer, K.R., 1981. The form of the near-bed velocity profile in a tidally accelerating flow. *J. Geophys. Res.* 86, 8067–8074.
<https://doi.org/10.1029/JC086iC09p08067>
- Spalding, M., Kainuma, M., Collins, L., 2010. *World Atlas of Mangroves*. Earthscan, London, 319.
- Spalding, M.D., Blasco, E., Field, C.D., 1997. *World Mangrove Atlas*. Int. Soc. Mangrove Ecosyst. 178. <https://doi.org/10.1017/S0266467498300528>
- Spalding, M.D., McIvor, A., Tonneijck, F.H., Tol, S., van Eijk, P., 2014. *Mangroves for coastal defence: guidelines for coastal managers & policy makers*. Wetl. Int. Nat. Conserv. 42. <https://doi.org/Wetlands International and The Nature Conservancy>
- Spenceley, A.P., 1977. The role of pneumatophores in sedimentary processes. *Mar. Geol.* 24, M31–M37. [https://doi.org/10.1016/0025-3227\(77\)90001-9](https://doi.org/10.1016/0025-3227(77)90001-9)
- Staudt, F., Mullarney, J.C., Pilditch, C.A., Huhn, K., 2017. The role of grain-size ratio in the mobility of mixed granular beds. *Geomorphology* 278, 314–328.
<https://doi.org/10.1016/j.geomorph.2016.11.015>
- Stoesser, T., Kim, S.J., Diplas, P., 2010. Turbulent Flow through Idealized Emergent Vegetation. *J. Hydraul. Eng.* 136, 1003–1017.
[https://doi.org/10.1061/\(ASCE\)HY.1943-7900.0000153](https://doi.org/10.1061/(ASCE)HY.1943-7900.0000153)
- Stoesser, T., Salvador, G.P., Rodi, W., Diplas, P., 2009. Large eddy simulation of turbulent flow through submerged vegetation. *Transp. Porous Media* 78, 347–365. <https://doi.org/10.1007/s11242-009-9371-8>
- Struve, J., Falconer, R.A., Wu, Y., 2003. Influence of model mangrove trees on the hydrodynamics in a flume. *Estuar. Coast. Shelf Sci.* 58, 163–171.
[https://doi.org/10.1016/S0272-7714\(03\)00072-6](https://doi.org/10.1016/S0272-7714(03)00072-6)
- Styles, R., Glenn, S., 2002. Modeling bottom roughness in the presence of wave-generated ripples. *J. Geophys. Res.* 107, 1–15.
<https://doi.org/10.1029/2001JC000864>
- Sukhodolov, A., Sukhodolova, T., 2006. Evolution of mixing layers in turbulent flow over submersed vegetation: field experiments and measurement study, in: *River Flow 2006*. 525–534.
- Sumer, B.M., Fredsøe, J., 2006. *Hydrodynamics Around Cylindrical Structures (Revised Edition)*. World Scientific, Singapore.
<https://doi.org/10.1142/9789812772770>
- Sumer, B.M., Fredsøe, J., 1997. *Hydrodynamics Around Cylindrical Structures*. World Scientific, Singapore. <https://doi.org/10.1142/9789812772770>
- Sumer, B.M., Fredsøe, J., Christiansen, N., 1992. Scour Around Vertical Pile in Waves. *J. Waterw. Port, Coastal, Ocean Eng.* 118, 15–31.
[https://doi.org/10.1061/\(ASCE\)0733-950X\(1992\)118:1\(15\)](https://doi.org/10.1061/(ASCE)0733-950X(1992)118:1(15))

- Tam, N.F.Y., Wong, Y.S., 1996. Retention and distribution of heavy metals in mangrove soils receiving wastewater. *Environ. Pollut.* 94, 283–291. [https://doi.org/10.1016/S0269-7491\(96\)00115-7](https://doi.org/10.1016/S0269-7491(96)00115-7)
- Tanino, Y., Nepf, H.M., 2008a. Lateral dispersion in random cylinder arrays at high Reynolds number. *J. Fluid Mech.* 600, 339–371. <https://doi.org/10.1017/S0022112008000505>
- Tanino, Y., Nepf, H.M., 2008b. Laboratory Investigation of Mean Drag in a Random Array of Rigid, Emergent Cylinders. *J. Hydraul. Eng.* 134, 34–41. [https://doi.org/10.1061/\(ASCE\)0733-9429\(2008\)134:1\(34\)](https://doi.org/10.1061/(ASCE)0733-9429(2008)134:1(34))
- Taylor, G.I., 1938. The Spectrum of Turbulence. *Proc. R. Soc. Lond. A. Math. Phys. Sci.* 164, 476–490.
- Temmerman, S., Bouma, T.J., Govers, G., Wang, Z.B., De Vries, M.B., Herman, P.M.J., 2005. Impact of vegetation on flow routing and sedimentation patterns: Three-dimensional modeling for a tidal marsh. *J. Geophys. Res. Earth Surf.* 110, 1–18. <https://doi.org/10.1029/2005JF000301>
- Temmerman, S., Bouma, T.J., Van de Koppel, J., Van der Wal, D., De Vries, M.B., Herman, P.M.J., 2007. Vegetation causes channel erosion in a tidal landscape. *Geology* 35, 631–634. <https://doi.org/10.1130/G23502A.1>
- Temmerman, S., Meire, P., Bouma, T.J., Herman, P.M.J., Ysebaert, T., De Vriend, H.J., 2013. Ecosystem-based coastal defence in the face of global change. *Nature* 504, 79–83. <https://doi.org/10.1038/nature12859>
- Tennekes, H., Lumley, J.L., 1972. *A First Course in Turbulence*. MIT Press, Cambridge, MA, USA.
- Thampanya, U., Vermaat, J.E., Duarte, C.M., 2002. Colonization success of common Thai mangrove species as a function of shelter from water movement. *Mar. Ecol. Prog. Ser.* 237, 111–120. <https://doi.org/10.3354/meps237111>
- Thom, B.G., 1982. Mangrove ecology: a geomorphological perspective. *Mangrove Ecosyst. Aust. Struct. Funct. Manag.* 3–17.
- Thom, B.G., 1967. Mangrove Ecology and Deltaic Geomorphology: Tabasco, Mexico. *J. Ecol.* 55, 301. <https://doi.org/10.2307/2257879>
- Thomson, J., 2012. Wave breaking dissipation observed with “swift” drifters. *J. Atmos. Ocean. Technol.* 29, 1866–1882. <https://doi.org/10.1175/JTECH-D-12-00018.1>
- Thornton, E.B., Guza, R.T., 1983. Transformation of wave height distribution. *J. Geophys. Res.* 88, 5925–5938. <https://doi.org/10.1029/JC088iC10p05925>
- Tinoco, R.O., Coco, G., 2014. Observations of the effect of emergent vegetation on sediment resuspension under unidirectional currents and waves. *Earth Surf. Dyn.* 2, 83–96. <https://doi.org/10.5194/esurf-2-83-2014>

- Tomlinson, P.B., 1986. The botany of mangroves. Cambridge tropical biology series. Cambridge University Press. Cambridge, UK.
- Torrence, C., Compo, G.P., 1998. A Practical Guide to Wavelet Analysis. *Bull. Am. Meteorol. Soc.* 79, 61–78. [https://doi.org/10.1175/1520-0477\(1998\)079<0061:APGTWA>2.0.CO;2](https://doi.org/10.1175/1520-0477(1998)079<0061:APGTWA>2.0.CO;2)
- Trowbridge, J., Elgar, S., 2001. Turbulence Measurements in the Surf Zone. *J. Phys. Oceanogr.* 31, 2403–2417. [https://doi.org/10.1175/1520-0485\(2001\)031<2403:TMITSZ>2.0.CO;2](https://doi.org/10.1175/1520-0485(2001)031<2403:TMITSZ>2.0.CO;2)
- Trowbridge, J., Scully, M., Sherwood, C.R., 2018. The Cospectrum of Stress-Carrying Turbulence in the Presence of Surface Gravity Waves. *J. Phys. Oceanogr.* 48, 29–44. <https://doi.org/10.1175/JPO-D-17-0016.1>
- Trowbridge, J.H., 1998. On a Technique for Measurement of Turbulent Shear Stress in the Presence of Surface Waves. *J. Atmos. Ocean. Technol.* 15, 290–298. [https://doi.org/10.1175/1520-0426\(1998\)015<0290:OATFMO>2.0.CO;2](https://doi.org/10.1175/1520-0426(1998)015<0290:OATFMO>2.0.CO;2)
- Trowbridge, J.H., Madsen, O.S., 1984. Turbulent wave boundary layers: 2. Second-order theory and mass transport. *J. Geophys. Res.* 62, 53–62. <https://doi.org/https://doi.org/10.1029/JC089iC05p07999>
- Tsujimoto, T., 1999. Fluvial processes in streams with vegetation. *J. Hydraul. Res.* 37, 789–803. <https://doi.org/10.1080/00221689909498512>
- Valiela, I., Bowen, J.L., York, J.K., 2001. Mangrove Forests: One of the World's Threatened Major Tropical Environments. *Bioscience* 51, 807–815. [https://doi.org/10.1641/0006-3568\(2001\)051\[0807:MFOOTW\]2.0.CO;2](https://doi.org/10.1641/0006-3568(2001)051[0807:MFOOTW]2.0.CO;2)
- van Rijn, L.C., 1998. Principles of coastal morphology. Aqua Publications. Amsterdam, the Netherlands.
- van Rijn, L., 1993. Principles of sediment transport in rivers, estuaries and coastal seas. Aqua Publications. Amsterdam, The Netherlands.
- van Steenis, G.C., Gerrit, J., 1941. Coastal growth and Mangroves. *Natuurwet. Tijdschr. Ned. Indië* 101: 40–65.
- van Santen, P., Augustinus, P.G.E.F., Janssen-Stelder, B.M., Quartel, S., Tri, N.H., 2007. Sedimentation in an estuarine mangrove system. *J. Asian Earth Sci.* 29, 566–575. <https://doi.org/10.1016/j.jseaes.2006.05.011>
- Vo-Luong, P., Massel, S., 2008. Energy dissipation in non-uniform mangrove forests of arbitrary depth. *J. Mar. Syst.* 74, 603–622. <https://doi.org/10.1016/j.jmarsys.2008.05.004>
- Walles, B., Salvador de Paiva, J., van Prooijen, B.C., Ysebaert, T., Smaal, A.C., 2015. The Ecosystem Engineer *Crassostrea gigas* Affects Tidal Flat Morphology Beyond the Boundary of Their Reef Structures. *Estuaries and Coasts* 38, 941–950. <https://doi.org/10.1007/s12237-014-9860-z>

- Walsh, G.E., 1974. Mangroves: A Review, in: Ecology of Halophytes. Academic Press, New York, NY, USA, pp. 51–174.
- Walsh, J.P., Nittrouer, C.A., 2004. Mangrove-bank sedimentation in a mesotidal environment with large sediment supply, Gulf of Papua. *Mar. Geol.* 208, 225–248. <https://doi.org/10.1016/j.margeo.2004.04.010>
- Walton, M.E.M., Samonte-Tan, G.P.B., Primavera, J.H., Edwards-Jones, G., Le Vay, L., 2006. Are mangroves worth replanting? The direct economic benefits of a community-based reforestation project. *Environ. Conserv.* 33, 335–343. <https://doi.org/10.1017/S0376892906003341>
- Watson, J.G., 1928. Mangrove forests of the Malay Peninsula. *Malayan For. Rec.* 6, 1–275.
- Weitzman, J.S., Zeller, R.B., Thomas, F.I.M., Koseff, J.R., 2015. The attenuation of current- and wave-driven flow within submerged multispecific vegetative canopies. *Limnol. Oceanogr.* 60, 1855–1874. <https://doi.org/10.1002/lno.10121>
- Whitehouse, R., Soulsby, R., Roberts, W., Mitchener, H., 2000. Dynamics of Estuarine Muds. HR Wallingford Thomas Telford, London 210. <https://doi.org/10.1680/doem.28647>
- Wiberg, P.L., Sherwood, C.R., 2008. Calculating wave-generated bottom orbital velocities from surface-wave parameters. *Comput. Geosci.* 34, 1243–1262. <https://doi.org/10.1016/j.cageo.2008.02.010>
- Widdows, J., Friend, P.L., Bale, A.J., Brinsley, M.D., Pope, N.D., Thompson, C.E.L., 2007. Inter-comparison between five devices for determining erodability of intertidal sediments. *Cont. Shelf Res.* 27, 1174–1189.
- Widdows, J., Pope, N.D., Brinsley, M.D., 2008. Effect of *Spartina anglica* stems on near-bed hydrodynamics, sediment erodability and morphological changes on an intertidal mudflat. *Mar. Ecol. Prog. Ser.* 362, 45–57. <https://doi.org/10.3354/meps07448>
- Wikramanayake, P.N., Madsen, O.S., 1994. Calculation of movable bed friction factors. Tech. Rep. DRP-94-5, U.S. Army Corps of Engineers, Coastal Engineering Research Center, Vicksburg, MS, pp 104.
- Wiles, P.J., Rippeth, T.P., Simpson, J.H., Hendricks, P.J., 2006. A novel technique for measuring the rate of turbulent dissipation in the marine environment. *Geophys. Res. Lett.* 33, L21608. <https://doi.org/10.1029/2006GL027050>
- Winterwerp, J.C., Borst, W.G., de Vries, M.B., 2005. Pilot Study on the Erosion and Rehabilitation of a Mangrove Mud Coast. *J. Coast. Res.* 212, 223–230. <https://doi.org/10.2112/03-832A.1>

- Wolanski, E., 2007. Thematic paper: Synthesis of the protective functions of coastal forests and trees against natural hazards, in: *Coastal Protection in the Aftermath of the Indian Ocean Tsunami: What Role for Forests and Trees*. RAP Publication (FAO), pp. 161–184.
- Wolanski, E., 2006. Thematic paper: Synthesis of the protective functions of coastal forests and trees against natural hazards. 157–179. Braatz, S. Fortuna, S., Broadhead, J., and Leslie R., (Eds). *Coastal protection in the aftermath of the Indian Ocean tsunami: what role for forests and trees?* Food and Agriculture Organization (FAO) of the United Nations.
- Wolanski, E., 1995a. Transport of sediment in mangrove swamps, in: *Asia-Pacific Symposium on Mangrove Ecosystems*. pp. 31–42.
- Wolanski, E., 1995b. Sediment transport in mangrove swamps. *Hydrobiologia* 295, 51–58.
- Wolanski, E., 1992. Hydrodynamics of mangrove swamps and their coastal waters. *Hydrobiologia* 247, 141–161. <https://doi.org/10.1007/BF00008214>
- Wolanski, E., Gibbs, R.J., Spagnol, S., King, B., Burnskill, G., 1998. Inorganic sediment budget in the mangrove-fringed Fly River Delta, Papua New Guinea. *Mangroves Salt Marshes* 2, 85–98. <https://doi.org/10.1023/A:1009946600699>
- Wolanski, E., Jones, M., Bunt, J.S., 1980. Hydrodynamics of a Tidal Creek-Mangrove Swamp System. *Mar. Freshw. Res.* 31, 431–450. <https://doi.org/10.1071/MF9800431>
- Wolanski, E., Mazda, Y., King, B., Gay, S., 1990. Dynamics, flushing and trapping in Hinchinbrook Channel, a giant mangrove swamp, Australia. *Estuar. Coast. Shelf Sci.* 31, 555–579.
- Wolanski, E., Nguyen Ngoc Huan, Le Trong Dao, Nguyen Huu Nhan, Nguyen Ngoc Thuy, 1996. Fine-sediment dynamics in the Mekong River estuary, Vietnam. *Estuar. Coast. Shelf Sci.* 43, 565–582. <https://doi.org/10.1006/ecss.1996.0088>
- Wolanski, E., Nhan, N.H., Spagnol, S., 1998. Sediment dynamics during low flow conditions in the Mekong River estuary, Vietnam. *J. Coast. Res.* 472–482.
- Wölcke J., T., Albers, M., Roth, M., Vorlaufer, M., Korte, A., 2016. Integrated Coastal Protection and Mangrove Belt Rehabilitation in the Mekong Delta. *Integr. Coast. Manag. Program. (ICMP)*, Dtsch. Gesellschaft für Int. Zusammenarbeit GmbH 1–236.
- Wooddroffe, C.D., 1985. Studies of a Mangrove Basin, Tuff Crater, New Zealand: III. The flux of Organic and Inorganic Particulate Matter. *Estuar. Coast. Shelf Sci.* 20, 447–461.
- Wooddroffe, C.D., 1992. Tropical mangrove ecosystems. *Coast. Estuar. Stud.* 41, 7–41. <https://doi.org/10.1029/CE041>

- Woodroffe, C.D., 1990. The impact of sea level rise on mangrove shorelines. *Prog. Phys. Geogr.* 1, 412–459.
- Woodroffe, C.D., Davies, G., 2009. The morphology and development of tropical coastal wetlands. *Coast. Wetl. An Integr. Ecosyst. Approach* 65–88.
- Wu, C., 2011. Visual SFM: A visual structure from motion system. <http://Ccwu.Me/Vsfm> 9.
- Wu, W., Perera, C., Smith, J., Sanchez, A., 2018. Critical shear stress for erosion of sand and mud mixtures. *J. Hydraul. Res.* 56, 96–110. <https://doi.org/10.1080/00221686.2017.1300195>
- Wu, W., Wang, S.S.Y., 2006. Formulas for Sediment Porosity and Settling Velocity. *J. Hydraul. Eng.* 132, 858–862. [https://doi.org/10.1061/\(ASCE\)0733-9429\(2006\)132:8\(858\)](https://doi.org/10.1061/(ASCE)0733-9429(2006)132:8(858))
- Wu, Y., Falconer, R.A., Struve, J., 2001. Mathematical modelling of tidal currents in mangrove forests. *Environ. Model. Softw.* 16, 19–29. [https://doi.org/10.1016/S1364-8152\(00\)00059-1](https://doi.org/10.1016/S1364-8152(00)00059-1)
- Yager, E.M., Schmeeckle, M.W., 2013. The influence of vegetation on turbulence and bed load transport. *J. Geophys. Res. Earth Surf.* 118, 1585–1601. <https://doi.org/10.1002/jgrf.20085>
- Yang, J.Q., Chung, H. and Nepf, H.M., 2016. The onset of sediment transport in vegetated channels predicted by turbulent kinetic energy. *Geophys. Res. Lett.* 43(21), 11–261. <https://doi.org/10.1002/2016GL071092>
- Yang, J.Q., Nepf, H.M., 2018. A Turbulence-Based Bed-Load Transport Model for Bare and Vegetated Channels. *Geophys. Res. Lett.* 1–9. <https://doi.org/10.1029/2018GL079319>
- Young, B.M., Harvey, E.L., 1996. A spatial analysis of the relationship between mangrove (*Avicennia marina* var. *australasica*) physiognomy and sediment accretion in the Hauraki Plains, New Zealand. *Estuar. Coast. Shelf Sci.* 42, 231–246.
- Zhang, H.J., Zhou, Y., 2001. Effect of unequal cylinder spacing on vortex streets behind three side-by-side cylinders. *Phys. Fluids* 13, 3675–3686. <https://doi.org/10.1063/1.1412245>
- Zhang, K., Liu, H., Li, Y., Xu, H., Shen, J., Rhome, J., Smith, T.J., 2012. The role of mangroves in attenuating storm surges. *Estuar. Coast. Shelf Sci.* 102–103, 11–23. <https://doi.org/10.1016/j.ecss.2012.02.021>
- Zhang, X., Chua, V.P., Cheong, H.F., 2015. Hydrodynamics in mangrove prop roots and their physical properties. *J. Hydro-Environment Res.* 9, 281–294. <https://doi.org/10.1016/j.jher.2014.07.010>
- Zong, L., Nepf, H., 2012. Vortex development behind a finite porous obstruction in a channel. *J. Fluid Mech.* 691, 368–391. <https://doi.org/10.1017/jfm.2011.479>

